Disordered Optics for Multidimensional Information Processing

by

Xinhao Li

Submitted to the Department of Mechanical Engineering
in partial fulfillment of the requirements for the degree of

Doctor of Philosophy

at the

MASSACHUSETTS INSTITUTE OF TECHNOLOGY

September 2021

Author .....
Department of Mechanical Engineering
July 15, 2021

Certified by .....
Nicholas X. Fang
Professor
Thesis Supervisor

Accepted by .....
Nicolas Hadjiconstantinou
Professor

Disordered Optics for Multidimensional Information Processing

by

Xinhao Li

Submitted to the Department of Mechanical Engineering
on July 15, 2021, in partial fulfillment of the
requirements for the degree of
Doctor of Philosophy

Abstract

Photonic platforms with multiplexing capabilities are of profound importance for high-dimensional information processing. With the rapid expansion of data volume, growing pressure on the sensor and post-processing hardware calls the development of physical pre-processing interfaces. Complex photonic systems aim to address the challenges as the interfaces between raw signals and sensors, which improve the efficiency of information reconstruction. In this thesis, we explore disordered photonic devices for multidimensional information processing and compatible fabrication techniques.

The first part of the thesis is about diffractive optical elements (DOE) for spectral imaging. We designed a spatially modulated DOE filter that can efficiently sample in the Fourier transformed domain and facilitate spectral image reconstruction. The DOE layer distinguishes the main Fourier spectral components, and the second spatial modulation layer mediates spectral aliasing. Unlike conventional snapshot spectral imagers, our design does not require sub-super-pixel-level sensing, which enables the efficient usage of sensor resolution. We further demonstrated a grayscale stencil lithography technique for efficient and customizable manufacturing of DOE or multilayer optics with spatial thickness variation.

The second part of the thesis is about scattering reservoir computers (RC). Complex optical medium shows great potential for large-scale optical RC thanks to the intrinsic parallelism and scalability. We identify the trade-off between the fading memory and non-normality of scattering RC, which determines their memory capacity and resistance to noise. Further, we proposed a transient amplification method to fully harness the high noise resistance and high dimensionality of non-normal scattering RC. We further developed a dynamic hydrogel scatter, and projection lithography method for 2D patterning of gain/loss materials, which are promising for applications in dynamic light modulation and re-configurable optical computing.

Thesis Supervisor: Nicholas X. Fang
Title: Professor

Acknowledgments

First and foremost, I would like to express my science gratitude to Prof. Nicholas Fang for his guidance and support along with my Ph.D. study and work. His broad research scope and advanced vision inspire me to explore the fields of nanophotonics and micro/nanomanufacturing. Every time when I face difficulties, find myself trapped in some details of research works, and lose my direction, it is Prof. Fang who helped me to look at the problems from a higher perspective and find solutions with his enthusiasm and knowledge. He also provides a supportive research environment for me and other group members to work on our own interesting areas, which promotes the diversity of thinking in the group without any restraints.

I would like to thank Prof. Jeehwan Kim and Prof. Juejun Hu as my thesis committee members. Their advice and research expertise helped me to look at my thesis work from the angle of material and information science. I truly appreciate their encouragement throughout the last 2 years of my research and study.

I thank my group members and collaborators Dr. Zheng Jie Tan, Dr. Chang Liu, Dr. Chu Ma, Dr. Seok Kim, Dr. Zhiguang Liu, Mr. Huifeng Du, Dr. Chenkai Liu, Dr. Sang-Hoon Nam, and Ms. Turga Ganapathy. I expanded my research scope through communication and collaboration with them and they have been very patient to teach and help me with their own expertise. I learned a lot of skills on the automation of physic experiments from Zheng Jie. Chang and I worked closely on the thermochromic window project, and her energy always encourages me to refine my research. Chu and Chenkai taught me about acoustic modeling and testing. Seok helped me to complete many sample preparations with 3D printing. Zhiguang provided valuable advice on the optical diffractive optics and the scattering reservoir. I also enjoyed the working experience together with Huifeng, Sang-Hoon, and Durga. And I would like to thank all the other group members, Shahrzad Ghaffari Mosanenzadeh, Ali Ramazani, Kavin Kowsari, and Gina Han for their support along the journey. And a special thank you to Ms. Chevalley Duhart for her continued support and great kindness.

I would thank many MIT technical staff and lecturers including Kurt Broderick,

Gary Riggott, and Dennis Ward at MIT. Nano, Timothy McClure and Yong Zhang at MIT MRL, and Steve Kooi at MIT ISN, and Benita Comeau at MechE. They taught me everything I needed for my research and helped me to find resources to solve the encountered technical problems.

I also thank my friends who went through the graduate study together with me at MIT. Dr. Zhiwei Ding, Dr. Hongzhou Ye, Hejing Huang, Jiayue Wang, Dr. Danhao Ma, Dr. Yifei Zhang, and Dr. Manxi Wu, your accommodation supports me throughout the journey. Every one of you has your own personality that I admire. I wish you all have a wonderful life after the adventure at MIT.

I also thank the funding sources of my Ph.D. study and research, including MIT-HKUST collaboration, OSRAM, MITEI/ExxonMobil, Fujikura, and BASF.

Finally, I would like to thank my parents for their support and understanding. I am truly in debt to them for the moments they need my help and support. I thank my brother, Dr. Xinran Li, for being my support when we are far from home. Special thanks to my girlfriend. We have gone through a memorable three years together. You always believe in me and help me with your kindness and brilliance. I'm truly grateful and looking forward to our next journey together.

Contents

List of Figures

List of Tables

Chapter 1

Introduction

1.1 Background and Motivation

The idea of the optical information process originated in the 1940s when people started to be interested in using all the properties, speed, and parallelism of light to perform computing at high speed and with high efficiency. We briefly introduce the historical view of optical information processing based on Ambs' detailed review.[17] The development of Fourier optics set the foundation for the early stage of research in optical information processing.[18] In 1953, Marechal and Croce invented a spatial filtering technique based on a 4-f optical set up to perform the correlation calculation through a 2 Fourier transform by the lens.[19] The reference information is encoded with a filter inserted after the first Fourier transformation. It paves the way for the development of optical correlators for real-time pattern recognition.

Since then, the development of optical information processing evolves with the advances in materials and manufacturing technologies to fabricate the physical information encoder and brings applications to the field of photonic computing, sensing, and communication. With the invention of the laser in 1960,[20] computer-generated hologram in 1966,[21] and dynamic spatial light modulators in the late 1960s,[22] the field of optical information processing raises with an increase in the degree of freedom for information encoding by the light. The progress in lithography technique in the 1980s-1990s made diffractive optical elements [23] with precise phase

encoding a reliable solution for computer-generated holography and applications as free-space interconnections in optical computing and photonic switching.[24] Coded aperture invented in the late 1970s [25] enables the encoding of spatial amplitude distribution and serves as the Hadamard transformer[26] for optics, which has been widely applied for imaging and spectroscopy applications.[27] While the maturity of dynamic spatial light modulator in the 1990s,[28] optical information processing first achieved the required modulation speed ($>$ 10Hz frame rate), dynamic range ($>$ 5 levels from 0 to 2π), and efficiency ($<$ 50 μJ/cm^2). However, due to the lack of multidimensional sensing and encoding technologies, the interests in optical information processing mainly limited to manipulate a single modality (amplitude or phase) of the optical properties.[17] Then the information is retrieved with 2D sensory arrays in terms of monochromic intensity distribution, for example, the correlation peaks generated with the optical correlator.[19] Meanwhile, the bulky spatial light modulation devices bring limitations to the compact integration of optical information processors.

Entering the 2000s, the engineering of artificial optical materials enabled by advanced micro/nanofabrication technologies opens the possibility for manipulating optical waves in multiple dimensions within a small footprint.[29] Optical metamaterial and metasurfaces have been developed to manipulate single-dimensional (amplitude, phase, polarization, frequency, etc) and multi-dimensional (amplitude/phase, phase/polarization, amplitude/frequency, phase/frequency) properties of the optical wave.[30] The precisely engineered optical response paves the way for encoding information in light with more degree of freedom. It also calls the development of multi-dimensional optical sensing, information reconstruction, and compatible device manufacturing technologies to form the full loop of information processing.

As shown in Figure 1.1, general information sensing includes 3 major components: 1). The raw signal of multiple modalities generated either by reflecting from objects or encoded by artificial apertures. In optics, the light can carry spatial, spectral, temporal, and polarization encoded information. 2). The second part is the sensor that can capture the raw data and convert it into electrical signals and send it to the CPU. 3). The third part includes the computational units and post-processing algorithm

that can retrieve the multidimensional information encoded in the raw data. Aside from optical computing, multidimensional optical sensing itself also have broad applications in 1) Multispectral imaging for remote sensing,[31] biomedical monitoring,[32] etc. 2). Spatial-temporal sensing for volumetric imaging and motion detection.[33] 3). Holographic quantitative phase retrieving for bio-medical imaging,[34] etc. With the increased demand for information processing with higher resolution, larger scale, and a number of modalities, there is continuous pressure on the hardware and algorithms side to support the handling of a mixed deluge of data. However, the physical limitations on the sensor and computational units bring challenges on how to efficiently acquire, store and process multi-dimensional information. First, the amount of resolvable multidimensional information is fundamentally limited by the number of pixels of the sensor array. The state-of-art spectro-polarimetric imaging can reconstruct spatial, spectral, and polarization information (5 modalities).[35] The required sensor resolution grows exponentially with an order of 5 as the increase of sensing resolution along each dimension. To overcome the limitation, compressive sensing has been applied to reduce the dimensionality of the multidimensional information reconstruction.[36] However, the photon-noise and detector-noise acquired along the sensing process compromise the reconstruction accuracy.[37, 38] Maintaining the information accuracy under the influence of noise is then the second challenge for post-processing, especially in recurrent systems with high dimensionality, in which the noise will accumulate repeatedly through the recurrent process.[39]

Previously, innovation is mainly driven by the improvements in the computational back-end, which brings higher demands on the computer's power. Less attention has been paid to the sensing hardware side.[40] In between the raw signal and sensors, physical interfaces perform the front-end processing of the raw signal and have great potential to improve the efficiency of the back-end algorithms. However, conventional sensing interfaces, such as lenses and filters, are often lack of the design for handling multi-dimensional information. This comes from two aspects: (1) The filter design does not consider the character of the multi-dimensional data, which brings more requirements to the post-processing (2). The filter design does not consider the re-

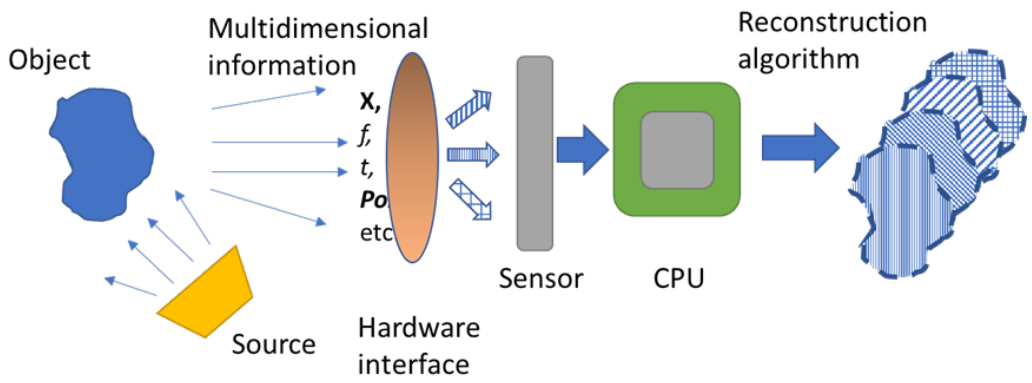

Figure 1.1: Schematic of multi-dimensional information sensing and reconstruction.

quirements it applied to the sensors, which increases the demands on sensors and compromises their efficiency.

The motivation of my thesis works is to design front-end hardware interfaces for efficient and accelerated multi-dimensional information processing. Specifically, we explore new disordered photonic devices and their application for multidimensional information processing. In this thesis, we define generic disordered optics as systems or devices with random and heterogeneous distribution of the refractive index. It can either be diffractive optical elements with spatially variable phase encoding or random optical diffusers commonly used in lighting. The linear operation performed by those random media can be modeled with the transmission equation.[41] In which the transmission matrix T defines how the speckle pattern looks after the medium. More generally, considering the input and output as nodes in a network, the transmission matrix defines the connectivity of the network and how information propagates through it. Due to the complicity, a disordered optical medium can generate distortion between inputs and outputs within a small form factor, which is ideal for signal multiplexing and modes decorrelation. Further, the disordered mediums can perform as universal linear operators,[42] which is the building block for many optical signal processing applications. Given all these features, engineered disordered optical mediums are promising candidates for multi-dimensional information processing. Here we briefly introduce previous demonstrations of disordered medium for spatial, spectral, polarization, and temporal information processing.

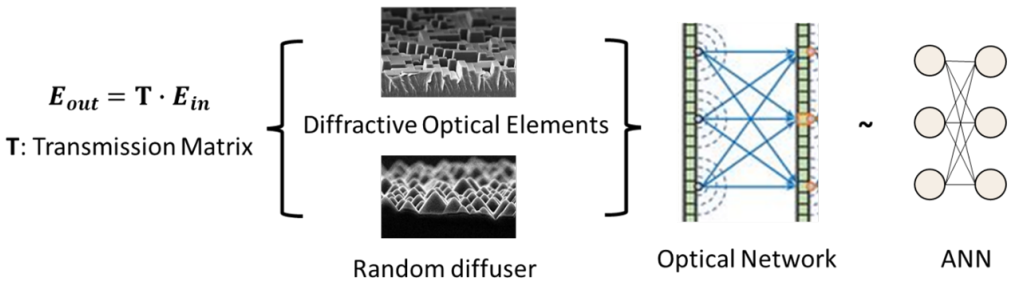

Figure 1.2: Schematic of transmission matrix modeling of the disordered optical medium.

1.1.1 Disordered Optics

Diffractive Optical Elements: DOEs are widely applied optics with microstructure profiles for fulfilling functions including beam splitting, pattern generation, beam homogenization, etc.[24] The structural profile provides the phase modulation at each pixel location on the DOE. Based on classic diffraction theories, the engineered DOE can control the intensity distribution of light propagate through it on the targeted image plane. Due to the customizability of phase profiles by the DOEs, they have been widely applied for compact "flat" optics.[18] For example, Fresnel zone plates with phase wrapping from 0 to 2π can replace the thick optical lens. Further, phase gratings made from DOEs can also fulfill customizable wave-front shaping. Binary phase gratings with controlled inter-cell distance can fulfill functions including angular selective transmission and focusing.[43]

Recently, the extending of DOEs to the field of optical computing further explore their capabilities as diffractive neural networks (DNN).[44, 45] In each layer of the DNN, the micro-structures on the DOE act as the connection between the nodes in the previous layer and the nodes in the next layer, which defines the coupling strength between them. The linear operation of the network is deterministic-ally defined by the diffraction pattern of each DOE layer, while the non-linear activation function is achieved with the intensity readout by the camera sensor array at the read-out layer. The DOE layers are designed by first numerically simulate the light propagation process through it and then adjusting the height profile at each location through

back error propagation based on the target error function. Applications including pattern classification,[44] optical logic operation,[46] and spectral-encoded machine vision [47] have been demonstrated with DNNs. The development of DNN based on DOE opens many new directions for optical computing and sensing with disordered and complex optical mediums.

Multi-scattering Medium: Turbid medium supporting multiple light scattering can generate large distortion between the input and output beam, and serve as the physical platform for different optical operations.[47] Given the knowledge of the transmission function of a disordered medium,[41] the same scatter can act as multi-functional optical elements including lens,[48] beam splitter,[49] and spectrometer,[50] through the wave-front shaping of the input signal. The highly customizable functionality of the scattering medium makes them a fundamental building block for optical linear operations with a small form factor.

Due to the multiplexed design freedom of scattering medium, engineered scattering medium can fulfill multiple functions simultaneously.[42] The recent development in adjoint optimization-based inverse design have demonstrated the reconstruction of spectral, spatial and polarization information with the 3D disordered optical element.[40] The end-to-end optimization method provides guidance to both the design of the physical hardware interface between the raw signal and the sensor array and the reconstruction algorithms to retrieve the multi-dimensional information.

Transmission Matrix modeling: The functionality of the disordered medium is defined by its transmission matrix.[41] In a network point of view, it defines the coupling strength between the nodes in the previous layer and the nodes in the next layer. In the aspect of sense, it defines how the multidimensional information is multiplexed and recorded as the intensity distribution on the sensor array.

For a scattering medium, the transmission matrix can be modeled with the random matrix theory.[51] It can be deduced based on Green's function of the scatter which defines how the radiation emitted by a given source is scattered to a receiver at a certain location.[41] Another approach for coherent scattering is to generate the random scattering matrix S directly which satisfies the requirement of unitary:[52]

$$\mathbf{S} = \begin{bmatrix} \mathbf{r} & \mathbf{t}' \\ \mathbf{t} & \mathbf{r}' \end{bmatrix} \tag{1.1}$$

and

$$\mathbf{t}^\ddagger\mathbf{t} + \mathbf{r}^\ddagger\mathbf{r} = \mathbf{t}'^\ddagger\mathbf{t}' + \mathbf{r}'^\ddagger\mathbf{r}' = \mathbf{1} \tag{1.2}$$

$$\mathbf{t}\mathbf{t}^\ddagger + \mathbf{r}\mathbf{r}^\ddagger = \mathbf{t}'\mathbf{t}'^\ddagger + \mathbf{r}'\mathbf{r}'^\ddagger = \mathbf{1} \tag{1.3}$$

$$\mathbf{r}^\ddagger\mathbf{t}' + \mathbf{t}^\ddagger\mathbf{r}' = \mathbf{t}'^\ddagger\mathbf{r} + \mathbf{r}'^\ddagger\mathbf{t} = \mathbf{0} \tag{1.4}$$

$$\mathbf{t}'\mathbf{r}^\ddagger + \mathbf{r}'\mathbf{t}^\ddagger = \mathbf{r}\mathbf{t}'^\ddagger + \mathbf{t}\mathbf{r}'^\ddagger = \mathbf{0} \tag{1.5}$$

Where the $\mathbf{r}, \mathbf{r}', (\mathbf{t}, \mathbf{t}')$ are the reflection (transmission) of the input modes from the left- and right-hand side of the scattering medium. The scattering matrix can be parameterized with the "polar decomposition" method based on the singular value decomposition of the transmission and reflection blocks:[41]

$$\mathbf{S} = \begin{bmatrix} \mathbf{V} & \mathbf{0} \\ \mathbf{0} & \mathbf{U} \end{bmatrix} \begin{bmatrix} -\sqrt{\mathbf{1}-\tau} & \sqrt{\tau} \\ \sqrt{\tau} & \sqrt{\mathbf{1}-\tau} \end{bmatrix} \begin{bmatrix} \mathbf{V}^\ddagger & \mathbf{0} \\ \mathbf{0} & \mathbf{U}^\ddagger \end{bmatrix} \tag{1.6}$$

Where $\mathbf{U}$ and $\mathbf{V}$ are random unitary matrices defining the input and output modes and the τ is a diagonal matrix with non-negative real diagonal elements. The total transmission T_{total} of the scatter with an N-by-N transmission matrix is determined by τ as:

$$T_{total} = \frac{Tr(\mathbf{t}^\ddagger\mathbf{t})}{N} =< \tau^2 > \tag{1.7}$$

The distribution of the diagonal terms in τ determines the statistical distribution of the eigenvalues of the transmission matrix. More details of constructing the transmission matrix of a scattering medium given the total transmission will be described in Chapter 4.

Knowing the transmission matrix of a scatter means we can control the "speckle" pattern with wave-front shaping of the input beams. Experimentally, the transmission matrix can be directly mapped with the "4-phase-shifting" [48] method requiring a

reference beam for phase retrieve, or reference-less methods. Given the measured transmission matrix, applications for multidimensional information processing can be achieved, as described in the next section.

1.1.2 Multi-dimensional information processing with disordered optics

Spatial information: Once the transmission matrix is measured or designed, the disordered medium becomes deterministic for retrieving or controlling the spatial intensity distribution of the incident beam. Applications including beam focusing,[48] holographic imaging through a turbid medium,[53] and invariant mode transmission[54] have been demonstrated with wave-front control techniques.

For beam shaping and imaging applications, the reconstruction of the spatial information is straightforward by calculating the inverse matrix of the transmission matrix. Compared with conventional optical lenses, which act as spatial frequency filters, the disordered medium can preserve high spatial frequency components to achieve sub-diffraction limit focusing and super-resolution imaging applications.[55, 56] Further, utilizing the correlation in the point spreading functions (PSF) of the speckle patterns, i.e. the "memory effect", a disordered medium can be treated similarly as a conventional imaging system with shift-invariant PSF.[57] As the result, the spatial information can be retrieved after calibrating the transmission matrix of the turbid medium.

Another important application for spatial intensity modulation is the enhanced transmission by coupling into the open eigenmode of the scattering medium.[58] The random matrix theory predicts the existence of eigenmode with the transmission of 100% for the disordered medium. Modulated input signals coupled into the open channel can have unitary transmission, which is preferable for efficient communication through the random medium. On the other hand, eigenmodes without 100% transmission still preserve the spatial distribution with some attenuation factors. Scattering invariant modes have been observed based on this, which are potentially helpful for

imaging through a scattering medium.[54]

Embedding gain and loss materials into the disordered mediums can further help to regulate the spatial intensity distribution of light propagating through it. The transition from ballistic to diffusive and localization transportation has been demonstrated in randomly coupled 1D waveguides embedded with gain and loss.[59] Further, more complex field control in 2D systems including beam splitting steered focusing, and collective resonance have also been proposed.[59] The extended design freedom by modulating the energy level of individual scatters/resonators in a random system opens more possibilities for spatial information processing.

Spectral information: The complex spectral response of DOE and disordered medium described by the spectroscopic transmission matrix can also be measured or designed for spectral information processing. Due to the dispersion of the heterogeneous material with a high disorder level, the speckle patterns for the light of different frequencies with sufficient separation are un-correlated. It requires the frequency difference to be greater than the inverse of the Thouless time [60, 61] $T_{Thouless} = \frac{L^2}{l_t v}$, where L is the thickness of the medium, l_t is the mean free path of light propagating through the medium, and v is the energy velocity of the light. Disordered spectroscopy [50] and spectral imaging [62, 63, 64] systems have been demonstrated utilizing the de-correlation of the wavelength-dependent PSF. However, the spectral reconstruction principle based on this principle induces the trade-off between spectral and spatial resolution.[37] A highly disordered medium is required to improve the spectral resolution by reducing the spacing between separable frequencies, which introduces more distortion to the spatial information and compromises the spatial resolution. Meanwhile, spatial multiplexing with sub-super-pixel level sensing is usually required to retrieve the intensity contribution by different frequency components, which also sacrifices the spatial sensing resolution.

Another application of optical diffusers with low disorder levels for spectral imaging only utilizes its capability to spread the spectral components over the camera pixels covered with different band filters.[65] The spatial-spectral information is then recorded by the multiplexed sensor array and reconstructed with a sparsity-

constrained inverse problem. The method provides a cost-effective solution to balance the spatial and spectral resolution by utilizing the medium NA optics with the optical diffuser. However, the imaging setup restricts the positioning of the object and lens, and the disorder level of the optical diffuser such that the PSF of the objects is wavelength-independent, which brings limitations for flexible applications.

Polarization Information: Vectorized transmission matrix (VTM) of the disordered medium needs to be constructed to describe its polarization response.[66] For example, the polarization state can be represented as the linear combination of the orthogonal basis along the x and y directions for every propagation mode. The transmission matrix for N input and output modes is then expanded to:

$$\mathbf{t} = \begin{bmatrix} \begin{pmatrix} t_{1,1}^{xx} & \cdots & t_{1,N}^{xx} \\ \vdots & \ddots & \vdots \\ t_{N,1}^{xx} & \cdots & t_{N,N}^{xx} \end{pmatrix} & \begin{pmatrix} t_{1,1}^{xy} & \cdots & t_{1,N}^{xy} \\ \vdots & \ddots & \vdots \\ t_{N,1}^{xy} & \cdots & t_{N,N}^{xy} \end{pmatrix} \\ \begin{pmatrix} t_{1,1}^{yx} & \cdots & t_{1,N}^{yx} \\ \vdots & \ddots & \vdots \\ t_{N,1}^{yx} & \cdots & t_{N,N}^{yx} \end{pmatrix} & \begin{pmatrix} t_{1,1}^{yy} & \cdots & t_{1,N}^{yy} \\ \vdots & \ddots & \vdots \\ t_{N,1}^{yy} & \cdots & t_{N,N}^{yy} \end{pmatrix} \end{bmatrix} \tag{1.8}$$

Where $t_{i,j}^{\alpha\beta}$, $\alpha, \beta = x, y$ describe the coupling strength between the polarization directions of different propagation modes. Experimentally, the VTM can be measured by separating the output field into the orthogonally polarized directions and mapping the transmission profile by sending in individual input modes with either one of the polarization directions.[66] After measuring the VTM, the desired magnitude of polarization ratio at the image plane can be achieved by controlling the phase profile of the incident light.

With the adjoint optimization method,[67] the disordered medium can be applied for polarimetry to resolve the polarization states of light emitters. Li et.al,[40] demonstrated the design of a cascade nano-DOE to retrieve the spatial, spectral, and polarization information of a fluorescent molecule. The designed nano-DOE can reconstruct the multidimensional information (36 parameters defining 2 spatial coordinates, 2 spectral channels,s, and 9 polarization states) by multiplexing them onto

100 sensor pixels. It shows great potential for compact microscopy and broadband sensing applications.

Temporal Information: Here we introduce the application of disordered medium for temporal information processing in optical reservoir computing.[68] Reservoir computers (RC) are recurrent neural networks with complex inter-connectivity, which can be applied to memorize or predict temporally encoded information.[69] Details of the mathematical modeling of optical reservoir computers can be found in Chapter 4. The disordered medium can be served as the connectivity matrix for RC. For example, DOE arrays have been applied to a couple of micro VCSEL lasers neurons [70] and optical scatters [71] have been used to distort the spatial-temporal information encoded by pixelated nodes on the spatial light modulator. Thanks to the parallelism and scalability of the optical systems, the disordered medium is promising for large-scale and fast physical reservoir computing.[71] Up to 50,000 optical nodes have been demonstrated for the prediction of chaotic spatial-temporal signals with optical scatter, which is about 4 and 100 times faster than high-end GPU and CPU.

In general, there are many remaining challenges and unexplored areas in applying disordered optical elements for information processing. One of the main questions is how to efficiently utilize the high dimensionality of the scattering medium, in terms of reconstructing information under the influence of noise. The other challenge is how to efficiently and accurately fabricate the complex optical element with a specific design based on the multi-functional purpose. The first aspect of challenges leads to the study of diffractive optical elements for spectral imaging and the scattering reservoir computer of this thesis. While the second aspect of challenges dives into the development of compatible micro/nanomanufacturing techniques, presented in this thesis.0

1.2 Thesis Organization

In this thesis, we present the efforts in developing disordered optical elements for multi-dimensional information processing and we explore the compatible micro/nano-

scale manufacturing techniques for scalable and efficient fabrication of the proposed devices.

In Chapter 2, we developed a Fourier diffractive optical element device (DOE) for a spectral imaging application. Different from conventional snap-shot spectral imaging methods, which rely on the sub-super-pixel sampling of spatial multiplexed spectral information, our method does not require the sacrificing of the sensor's spatial resolution for spectral reconstruction. It is achieved by designing the DOE filter for efficiently sampling the major spectral and spatial information in the Fourier transformed space. We numerically and experimentally demonstrated the working principle of spatial-spectral information reconstruction. The design can also provide guidance to another type of implementation of Fourier transform-based spectral imaging.

In Chapter 3, we invented a grayscale version of stencil lithography to pattern multi-layer optical elements with spatial thickness variation. Creating such kind of structure is highly time- and material-consuming with the conventional lift-off process. We take inspiration from "pinhole" imaging and applied that to eBeam material deposition through a stencil shadow mask. The fine-controlled point spreading function of materials ejected through the mask creates spatially thickness variable deposition with optical-level surface smoothness. Applications of the proposed manufacturing technique include spectral filter and DOE fabrication to overcome the challenges in flexible material choices and structural customizability.

In Chapter 4, we analyzed the memory performance of linear optical scattering reservoirs. We identified the influence of loss and non-normality of a scattering medium on the memory capacity and noise resistance for optical reservoir computing. The scattering strength of a scattering medium determines the total transmission and the distortion between the input and output information. A highly scattering medium will have stronger intercoupling between the transmission modes, which are favorable for information multiplexing. However, the strong scattering medium suffers from the loss of information, especially under the influence of noise. We further proposed a practical amplification method to overcome the intrinsic loss of a strong

scattering medium with high non-normality, which can help to efficiently harness the high dimensionality and high noise resistance of the scattering medium for reservoir computing.

In Chapter 5, we demonstrated a dynamic scattering medium based on thermochromic hydrogel particles. By controlling the particle size through the solution phase manufacturing method, the scattering strength of the gel particle could be controlled over the visible and NIR region. The material is of great potential for applications in reconfigurable optical computing and light modulation. We applied the material as smart windows for solar heat management and achieved high luminous transmission with large solar modulation surpassing commercially available thermochromic windows based on VO¬2 phase transition oxides.

In Chapter 6, we developed a direct projection lithography technique for patterning micro-sized pixelated quantum dots (QDs) / photopolymer composite. The method is promising for the fabrication of gain/loss engineered optical material. We applied it to create color converters for blue μLEDs. Red and green color converters can be directly patterned on top of blue LED pixels, with a broad color gamut, wide view angles, and improved efficiency compared with inkjet-printed QDs color converters.

Chapter 2

Fourier diffractive optical element for spectral imaging

2.1 Introduction

Spectral imaging is the technique to sample both spatial and spectral information stored in the multispectral data cube.[37] As shown in Figure 2.1, spectral imaging can provide more spectral channels compared to conventional RGB color imaging, which carries the intrinsic physical properties of the objects for applications in remote sensing,[31] biochemical production,[72] and healthcare industries,[32] etc.

Spatial or temporal multiplexing methods have been applied to retrieve the spectral information by projecting the monochromic record to higher dimensions and reconstruct the multiple color channels.[37] In the temporal multiplexing method, a scanning mechanism is usually applied to either scan over the 2D image to record the intensities of different color channels at each scanning location or scan over the spectral domain, e.g. a rotational filter wheeler, to record the different color channels over the whole image area. They are equivalent to scan over a single point or a single line in the spatial-spectral data cube, as shown in Figure 2.2 (a). Both methods sacrifice the sampling efficiency for higher spectral and spatial resolution. On the other hand, the spatial multiplexing method can disperse the multiple color channels over multiple sensor pixels to record the whole spatial-spectral data cubic

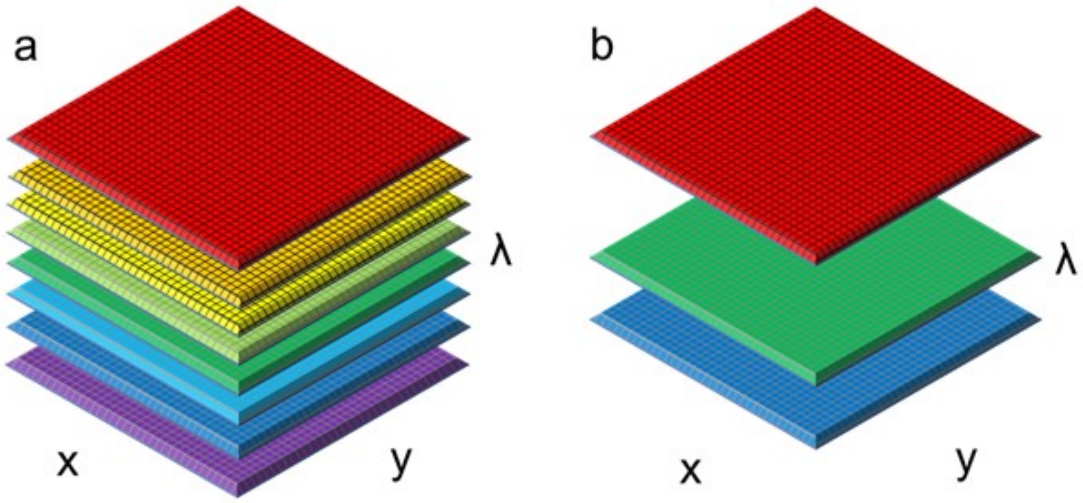

Figure 2.1: (a) Schematic of multispectral channel data cube in spectral imaging. (b) Schematic of conventional three channel RGB color imaging.

within a single snapshot, as shown in Figure 2.2 (b). In snapshot spectral imaging, the spatial-spectral information is collected by a monochromic sensor array which cannot distinguish between different color channels by itself. With the help of filters or dispersive media, the spectral information at a single location can be projected onto a sensor array which selectively records the coefficients for different color channels. Various dispersive elements or filters have been applied as the spectroscopic components for snapshot spectral imaging, as summarized in Table 2.1. For example, optical grating,[73] photonic crystal filter,[74] FP type bandpass filter,[75] quantum dots filter,[76] and complex optical medium [77, 65, 62, 63] have been applied to distinguish different color channels. In those systems, the imaging process can be modeled with the equation here:

$$\boldsymbol{I} = \boldsymbol{T} \times \boldsymbol{S} \tag{2.1}$$

Where **I** is the measured intensity data, **T** is the transmission matrix of the hardware interface, while **S** is the spatial-spectral data cubic. The designing of T determines the efficiency in the use of all sensor pixels and the compactness of the whole spectral imaging system.

In a conventional spatial multiplexing system, the spatial-spectral resolutions are

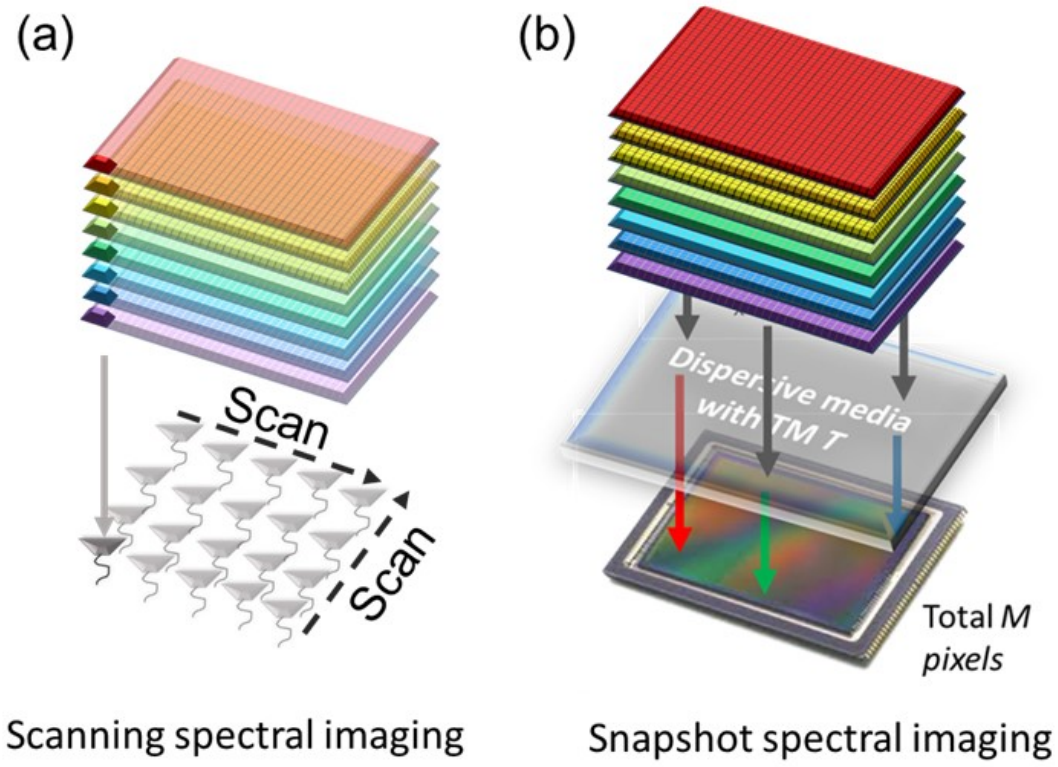

Figure 2.2: (a) Scanning spectral imaging by temporal multiplexing. (b) Snapshot spectral imaging by spatial multiplexing.

coupled and fixed. And the total degree of freedom to represent and reconstruct the spatial and spectral information determines the sampling efficiency.[37] We define the parameter η to represent the efficiency regarding utilizing the physical resolution of the sensor array. $\eta = 2\rho \cdot \sqrt{N_w}$. ρ is the maximum spatial frequency (cycles/pixel) that can be reconstructed. And N_w is the number of retrievable color channels. A system with $\eta > 1$ is more efficient in terms of using the sensor array. However, most conventional spatial multiplexing systems have $\eta < 1$, as shown in Table 2.1. With a finite amount of sensor pixels, the spatial-spectral resolution of the reconstructed image is limited. The sampling efficiency and reconstruction resolution can be improved by choosing a group of basis functions and the corresponding space, in which the majority of the information is stored sparsely, and directly sampling the coefficients against the basis functions instead of measuring each voxel in the data cube.[38] However, information generally cannot be measured in the sparse space with the conventional spatial multiplexing method due to the design of dispersive elements and filters. As the result, the physical resolution of the image sensors cannot be fully utilized, as we will discuss in the following section. Meanwhile, conventional designs also suffer from large footprints or complex filter fabrication, which brings more obstacles for flexible applications.

Recently, compact and small form factor spectroscopy and spectral imaging techniques based on complex or disordered optical mediums have been developed.[77, 65, 62, 63] Thanks to the wavelength-dependent distortion caused by the complex media, the diffractive / scattering pattern of light with different wavelengths on the sensor array could be decorrelated. By sampling the spatial distribution of the "speckle" patterns at the sub-super-pixel level, spectral information could be resolved. Since optical scatters can have high total transmission efficiency compared to bandpass filter arrays for spectral imaging, this method is favorable for low light intensity applications.[78]

However, those methods share the same principle as conventional spatial - multiplexing methods with bandpass filter arrays, while the periodically patterned band filters are replaced by the irregular "speckle" pattern generated by DOE or scattering medium. And the method still requires sub-super-pixel level sensing to resolve the

Table 2.1: Comparison between dispersive media as spectroscopic components for spectral imaging.

Type of spectroscopy	**Examples**	$\eta = 2\rho \cdot \sqrt{N_w}$	**Footprint**
Dispersive elements	Grating[37] & coded aperture[79]	C »1	table-top
Band filter array	FP cavity,[75] QDs,[76] PhCs [74]	C >1	On-chip $\sim \mu$m
Fourier transformation	Fourier FP filter[80]	C >1	On-chip $\sim \mu$m
Complex medium	Scatter,[77, 62, 63] DiffuserCam [65]	C∼1	$\sim$ cm

wavelength-dependent "speckle" pattern and to retrieve spectral information stored in each voxel of the data cube with low efficiency.[64] Meanwhile, sufficient propagation volume is needed to ensure the decorrelation of light with different wavelengths, which limits the compactness of the device. [64, 62] The spectral resolution in terms of separable frequencies is limited by the inverse of Thouless time $T_{th} \approx L^2/(l_t v)$, where L is the thickness of the complex media, l_t is the mean free path of light propagating through and v is the energy velocity of the wave.[60, 61] A larger thickness is required to improve the spectral resolution. However, the lateral expanding of the "speckle" pattern scales with the medium's thickness,[81] which compromises the spatial resolution due to the interference between adjacent light through the propagation. As the result, either the spectral channel number or the spatial resolution will be limited in those designs.[64]

The motivation of this chapter is to design a compact dispersive element for spectral imaging that can efficiently sample the major spatial-spectral information stored in the Fourier transformed space. We developed a Fourier diffractive optical element (DOE) filter and spatial modulation layer (SML) for this purpose. The DOE layer serves as the dispersive element to distinguish the main spectral Fourier components of spectral image data, while the SML effectively reduces spectral aliasing in the Fourier transformed domain to facilitate the spatial-spectral information reconstruction. Compared to conventional spatial multiplexing-based snapshot imaging

techniques and recent developments based on a disordered optical medium, no sub-super-pixel level sensing is required in our system to distinguish between different color channels, and the compactness of the device can be improved since our design does not require the decorrelation between different narrow bands' diffractive patterns. We experimentally demonstrated the designed DOE and SML filter, which can effectively reconstruct spatial and spectral information of color images printed on transparency. After calibration, the filter can achieve a root mean square error (RMSE) of 9% for the spectral reconstruction of 54 different broadband color bands by retrieving the coefficient of the first 5 spectral Fourier components. Meanwhile, the spatial resolution characterization shows that the crosstalk effect is confined to the nearest DOE pixel neighbor, due to the close placement between the DOE and SML at 160 μm, which also helps to improve the compactness of the whole device. The absolution spatial resolution in terms of measured monochromic intensity and the broadband spectral reconstruction can be achieved with patterns of spatial frequency at 0.324 cycles per pixel.

2.2 Sampling spatial and spectral information in Fourier space

To achieve efficient sampling of the spatial and spectral information stored in a spectral cube, we take a closer look at the statistical properties of the real-world spectral image data.[38, 82] Information stored in the spectral cube can be represented in either the real spatial-spectral space or Fourier transformed space. However, the data density distribution may vary depending on the different representations.[83] In real spatial-spectral space, the multispectral information occupies the whole data cube, making spectral sampling difficult due to the spatial overlapping between different color channels. As the result, spatial or temporal multiplexing methods are required to sample the different color channels with the help of the dispersive medium and scanning mechanisms. On the other hand, if we apply Fourier transform to the mul-

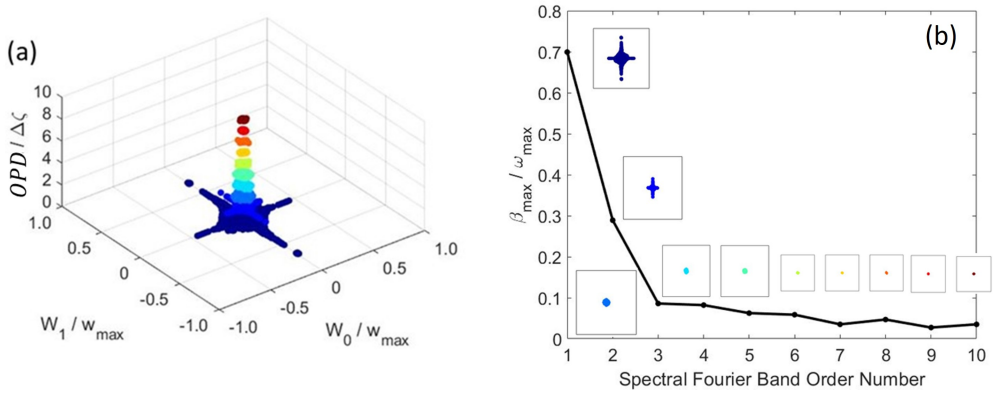

Figure 2.3: (a) Main spatial component support (> - 40 dB) of the first 10 spectral Fourier bands obtained from spectral image data from CAVE data-set. (b) Spatial occupancy of first 10 spectral Fourier bands in Fourier transformed space.

tispectral data cube and represent the information in terms of optical path difference (OPD) and spatial frequencies, we can find out that the spectral information mainly concentrates in the low spatial and spectral frequencies regions in the Fourier transformed space.[83] Figure 2.3 (a) shows the support of the discrete spatial Fourier coefficients of spectral image data obtained from the CAVE multispectral database.[84] The support envelop is drawn as the boundary of information with intensity larger than 40 dB of the averaged intensity. Figure 2.3 (b) shows the occupancy of the spectral bands in the Fourier transformed space. From the 2nd Fourier order, the occupancy is less than 0.3 by 0.3 of the total spatial sensing resolution in the frequency domain.

This observation is coherent with the statistical analysis on the principal components of spectral images in reference,[82] in which the authors pointed out that the main spatial and spectral components of real-world spectral images are of the same feature as the Fourier series, as shown in the adopted images in Figure 2.4.

From this analysis, we can conclude the sparsity of the main spatial and spectral information represented in the Fourier transformed space. This unique distribution can facilitate the efficient sampling of spatial-spectral information for spectral imaging purposes since only finite sampling points are required to obtain the main spatial and spectral components in the discretized Fourier transformed space. Here we compare

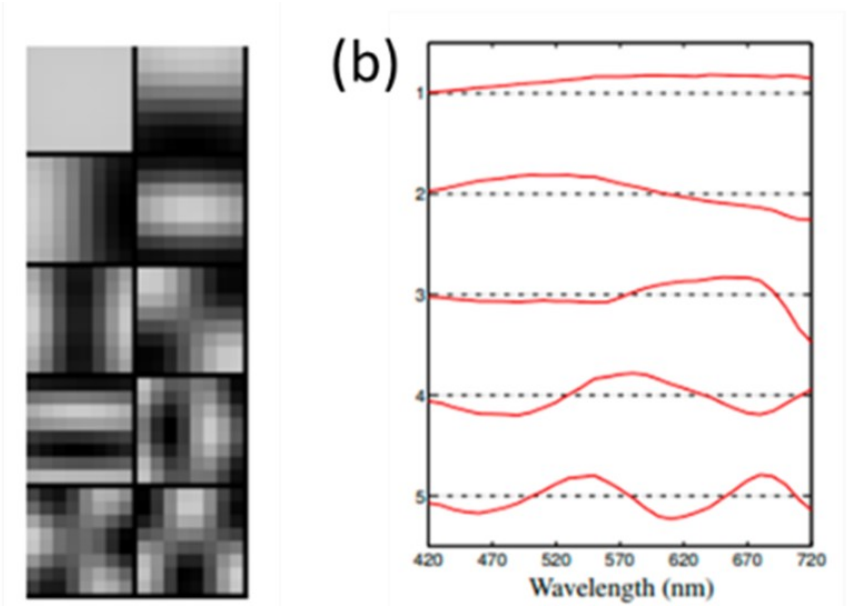

Figure 2.4: (a) First 10 major spatial components of real-world spectral image data. (b) First 5 major spectral components of real-world spectral image data. Figures are adopted from Ref [82].

different sampling methods in terms of their efficiency for data acquisition in the Fourier transformed space.

2.2.1 Sampling with narrowband filters

Narrowband filters are the most widely utilized methods for multispectral imaging applications. Through sampling the spectral intensity at the peak wavelengths of each narrowband filter, the whole spectrum can be approximated by interpolating the measured intensity. Mathematically, the narrowband filter at a center wavelength λ_k can be modeled as $T_k = \delta(\lambda - \lambda_k)$, where δ is a delta function with center at 0. A series of narrow bands with center peak ranging from $\{\lambda_1, ..., \lambda_k\}$ form the whole narrow band's filter array. At sensor pixel $\mathbf{n} = (n_1, n_2)$, the sampled single intensity of the kth narrowband is then:[83]

$$I_k(\boldsymbol{n}) = \langle T_k(\boldsymbol{n}), S(\boldsymbol{n}) \rangle \tag{2.2}$$

If we represent the spectral information against the wavenumber $\sigma = 1/\lambda$, the

above equation transforms to:

$$I_k(\boldsymbol{n}) = \langle \tilde{T}_k(\boldsymbol{n}), \tilde{S}(\boldsymbol{n}) \rangle \tag{2.3}$$

where the $\tilde{}$ represents the spectra in terms of wavenumbers. The transmission function of the filter will be also transformed into $\tilde{T}_k = \delta(\sigma - \sigma_k)$. The above equation is then equivalent to:

$$\tilde{S}(\boldsymbol{n}, \sigma) = \sum_{k=1}^{K} I_k(\boldsymbol{n}) \cdot \delta(\sigma - \sigma_k) \tag{2.4}$$

It is equivalent to direct sampling at each data points in the spectral cube in real spatial-spectral space. As the result, temporal or spatial multiplexing is required to sample different narrow bands of the same spatial location, which sacrifices the sampling efficiency.

Narrowband filters also suffer from spectral aliasing. Sampling narrow bands in the real spectral space are equivalent to sampling with large OPD windows in the Fourier transformed space. We assume that the narrow bands are evenly spaced by 2ϵ in terms of wavenumber. Performing the Fourier transform of the above equation in against to wavenumber and spatial position, we will result in the Fourier coefficient ($\hat{S}$) for $\tilde{S}$, represented in terms of spatial frequency ω and OPD ζ as:

$$\hat{S}(\boldsymbol{\omega}, \zeta) = \frac{1}{\epsilon} \sum_{v \in \mathbb{Z}^+} \hat{S}(\boldsymbol{\omega}, \zeta + \frac{v}{2\epsilon}) \tag{2.5}$$

The sampling windows will have width inversely proportional to the bandwidth of the narrowband filters, as shown in Figure 2.5 (a). Practically, the band filters will have finite bandwidth, which may help to reduce the width of the sampling windows in the Fourier transformed space. However, if the separation between sampling windows whose centers are located at $\frac{v}{2\epsilon}$, $v \in \mathbb{Z}^+$ have overlapped with each other, the spectral aliasing happens. The aliasing not only compromises the sensing efficiency due to the repeated sampling in the overlapped regions in Fourier transformed space but also introduces error during the spectrum reconstruction. As a result, a large number of

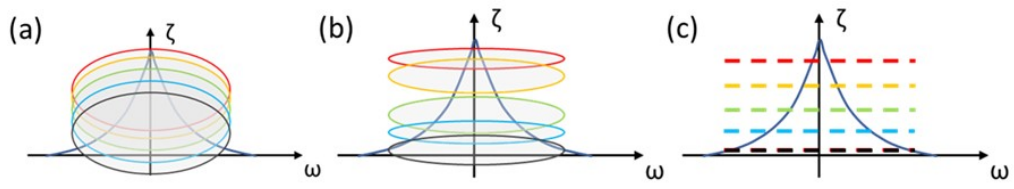

Figure 2.5: Schematic of spatial-spectral sampling with (a) narrow bands, (b) broad bands, and (c) Fourier filters in Fourier transformed domain. The solid black "cone" indicates the support of the major spatial-spectral components as shown in Figure 2.3. The color circles in (a) and (b) indicate the sampling window by narrowband and broadband filters in the Fourier transformed space. The dash lines in (c) represents the "slice" sampling of spectral Fourier components with Fourier transformation filters.

narrowband filters with short enough separation ϵ are usually required to reconstruct the spectral image, which sacrifices the sensing efficiency and spatial resolution.

Previously, scattering medium or DOEs have also been applied as narrowband filters due to the decorrelation between the wavelength-dependent speckle / diffraction patterns of light penetrating through the filter.[62, 64] Because of the high total transmission intensity, optical scatters or DOEs are of high sensing efficiency and preferable for fast imaging/filing applications. However, the previous methods are mathematically equivalent to sampling with narrowband filters. This is because the decorrelation between the wavelength-dependent speckle / diffraction patterns only happens between lights with frequency differences larger than the inverse of the Thouless time of the medium,[60] and the transmission matrix is constructed as a discretized wavelength-dependent matrix. Therefore, the inverse problem is equivalent to reconstructing the spectrum as the linear combination of the principal components of the wavelength-dependent transmission matrix, which is limited to the de-correlated wavelengths. Furthermore, to achieve sufficient dispersion and decorrelation between different wavelengths, it requires a large separation distance between the scattering medium / DOE and the sensor array. And sub-super pixel-level spatial sensing is required to distinguish between the different spectral / diffraction patterns.[64] As the result, the spatial resolution will be largely compromised due to the crosstalk effects and the sub-super pixel sampling.

2.2.2 Sampling with broadband filters

Increasing the bandwidth of filters is an alternative way to avoid spectral aliasing since the broadband filter can capture more color channels compared with the narrowband filters.[83] It is equivalent to a sample with narrow OPD windows in the Fourier transformed space, as shown in Figure 2.5 (b). Various optimized wideband filters for 3 or more channel sensing have been proposed. [85] In these cases, the optimization of the broadband filters is usually based on a pre-defined band shape which is accessible with color filter fabrication techniques, such as Gaussian band filters. However, for compressive sensing purposes, the choice of the broadband filters, i.e. measurement vectors in [38], needs to be uncorrelated to each other, which is not always achieved by the current design [62, 85]. Furthermore, the broadband filter array still suffers from the losses of spatial resolution.[65] Spatial and spectral demosaicking algorithms are usually required to interpolate the missed information at each pixel. [64]

2.2.3 Sampling with Fourier transform filters

A natural choice of base functions for spectral reconstruction would be the Fourier series, i.e. sinusoidal transmission functions since they are of the same characteristics as the spectral principal components. This idea has been widely applied in conventional Fourier transformed spectroscopy, e.g. FTIR, in which the sinusoidal transmission function is obtained through varying the retardation between the OPDs in the two optical arms in the interferometer.[83] By changing the OPDs, the FTIR can directly sample the coefficients of the different spectral Fourier components for reconstruction. Other types of signal transformation, e.g. Hadamard and wavelet transformation, have also been applied for spectroscopic applications. [86, 87] In Hadamard transformation spectroscopy and coded aperture-based spectral imagers, a dynamic/static coded mask is used to scan over the dispersed spectrum to extract spectral information. However, the masks do not necessarily project the spectral information into a sparse space,[88] and multiple scanning is required to reconstruct the data cube.[89] Wavelet transformation is preferable to retrieve spectral information of

a localized signal in time/space. It has the potential for frequency-dependent sensing resolution.[86] While designing optics to implement the physical spectrum wavelet transformer is a challenging topic and deserves further study.

Here we focus on the Fourier transform of the spatial-spectral information and utilized the sparse Fourier transformed space for efficient spectra imaging. Mathematically, we can look at the sampling process in the Fourier transformed space as:[83]

$$I_{\hat{k}}(\boldsymbol{n}) = \langle cos(2\pi\zeta_{\hat{k}}\sigma), \tilde{S}(\boldsymbol{n}, \sigma)\rangle \tag{2.6}$$

Where $\zeta_k = \hat{k}\Delta\zeta$, which is the sampling intervals in terms of OPDs. The above sampling formula is equivalent to modulate the transmission with a sinusoidal spectral filter and we can write it in Fourier transformed space as:

$$\begin{aligned} I_{\hat{k}}(\boldsymbol{n}) &= \tilde{S}(\boldsymbol{n}, \zeta_{\hat{k}}) \text{ and} \\ I_{\hat{k}}(\boldsymbol{\omega}) &= \hat{S}(\boldsymbol{\omega}, \zeta_{\hat{k}}) \end{aligned} \tag{2.7}$$

which represents the coefficient sampled by a slice window at $\zeta_{\hat{k}}$ in the Fourier transformed space. With the measured coefficient, the spectrum information can be reconstructed as:

$$S(\boldsymbol{n}, \sigma) = \Delta\zeta \sum_{k=0}^{\infty} \tilde{S}(\boldsymbol{n}, \zeta_{\hat{k}}) e^{j2\pi\sigma k\Delta\zeta} \tag{2.8}$$

The "slice" sampling by Fourier transformed spectroscopy in Fourier transformed space can effectively avoid spectral aliasing, as shown in Figure 2.5 (c). The result of the spatial Fourier transformation in equation 2.5 can be seen as a special condition of the Wolf mutual coherence function[90] when the image plane is in the scalar diffraction region from the incoherent sources and the two observation points are far away ($>> \lambda$) from each other. [91] Previously, people have discovered that the relationship

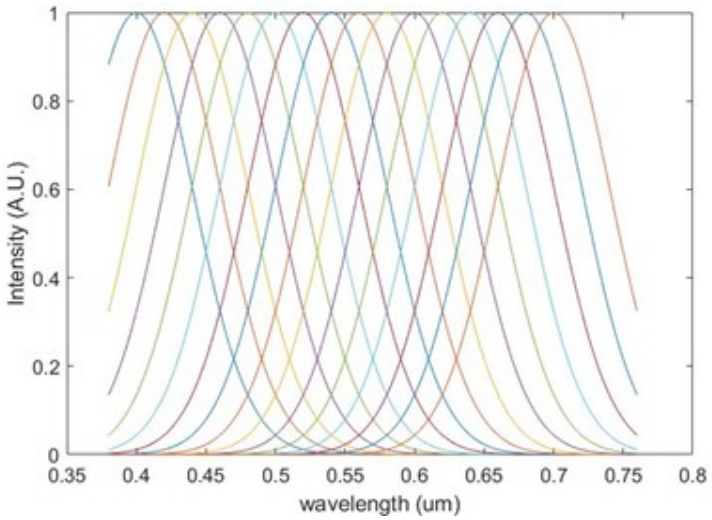

Figure 2.6: Spectrum reconstruction target of 16 Gaussian bands with peaks ranging from 400 to 700 nm at the separation of 20 nm and FWHM of 100 nm.

between the source and field correlation function can be described with Fourier transformation. [91] From this perspective, sampling in the Fourier transformed domain for spectral imaging can be seen as the general principle of the previous design based the measurement of field correlation with volume interferometer.

Here we compare the theoretical spectral reconstruction accuracy between the result obtained with 5 Gaussian filters and 5 Fourier transmission filters. The Gaussian filters have center peaks at 380 to 760 nm and FWHM of 100 nm, while the 5 Fourier filters are correspondingly the first 5 Fourier series. We applied them as the transmission function and applied principal component analysis to retrieve the coefficients associated with the 5 principal components of the filter bands. The target spectrum for reconstruction is 16 Gaussian bands with peaks ranging from 400 to 700 nm at the separation of 20 nm and FWHM of 100 nm, as shown in Figure 2.6.

As shown in Figure 2.7, the reconstruction results show that the Fourier band filters can improve the peak matching accuracy of 16 Gaussian bands by 50% compared with the Gaussian band filters. The mean peak matching error is reduced from 15 nm to 6.7 nm. This result indicates that the Fourier transmission filters are a better choice compared with the commonly used Gaussian wideband filters. With the above consideration, our goal is to design an optical filter that can directly sample the

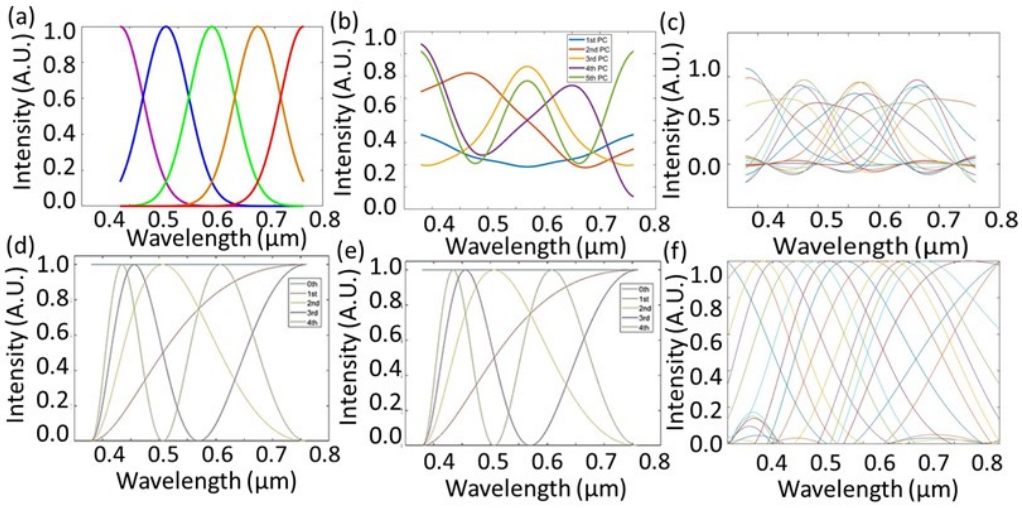

Figure 2.7: Spectral reconstruction based on principle component decomposition. (a-c) 5 Gaussian broadband filters, the first 5 principal components associated with them and reconstructed Gaussian bands as combination of the principal components. (d-f). 5 Fourier broadband filters, whose principal components are the identical spectrum, and reconstructed Gaussian bands.

principal spectral component in Fourier space without the requirements on sub-super pixel-level sensing for a balanced spatial-spectral resolution.

2.3 Working principle of the Fourier DOE filter for spectral imaging

We proposed a Fourier DOE and spatial modulation layer as the optical filter for spectral imaging, which can efficiently sample the principal spatial-spectral components and improve the spatial sensing resolution. The working principle of the cascade filters is shown in Figure 2.8.

1) The spatial-spectral information from the objective is first dispersed by the Fourier DOE layer. In which the randomly distributed phase encoders, i.e. micropillars on the DOE, distinguish the different spectral Fourier components and projects them onto different sub-pixel locations on the spatial modulation layer (SML) with sufficient dispersion volume in between. It needs to notice that the crosstalk effects between neighbor DOE pixels will affect the transmission profile on the SML layer.

2) On different sub-pixel level locations on the spatial modulation layer, we identify the local transmission spectrum which contains the main spectral Fourier components. Then the spatial modulation layer will introduce the extra spatial frequencies to the different spectral components and shift them in the Fourier transformed space to avoid spectral aliasing.[92] It is needed to notice that the spatial modulation is conducted at the sub-pixel level and the modulation is periodic globally across the whole sensor array. Therefore, no sub-super-pixel level sensing is required to sample each of the spectral Fourier components. As shown in Figure 2.8, the spatial modulation layer will generate a periodic pattern on the originally color-uniform area, which represents the introduced spatial frequency.

3) The modulation spatial-spectral information is then sampled by the monochromic sensor array behind the spatial modulation layer. Due to the DOE and SML, the different spectral components are shifted to different locations in the Fourier transformed space, as shown in Figure 2.8. As the result, spectral aliasing can be avoided. From the Fourier transformed intensity profile, we can retrieve the intensity coefficient of the main spectral components.

4) Finally, with the retrieved coefficient, we can reconstruct the spectral information at each pixel location through the inverse Fourier transform of the spectrum. Detailed reconstruction algorithm will be discussed in the later sections.

Here we further describe the mathematical modeling of the imaging and reconstruction process. The transmission function of light going through the DOE and SML on a single sensor pixel is

$$T((n),\lambda) = \sum_{i=0}^{8}\sum_{k=1}^{K} T_{i,k}(\boldsymbol{n},\lambda)\cdot(c_k + \gamma_k \cdot cos(2\pi \boldsymbol{n}\cdot\boldsymbol{\omega_k})) \tag{2.9}$$

Where $T_{i,k}$ is the transmission function of light penetrating through the ith near neighbor (i=0 mean the DOE pixel directly on top of sensor pixel **n**) and projects onto the area belonging to the kth modulation group. As shown in the schematic of Figure 2.8, light propagating through the DOE array will suffer from the crosstalk effect between nearby pixels. Here we consider the effects of the nearest 8 DOE pixels on

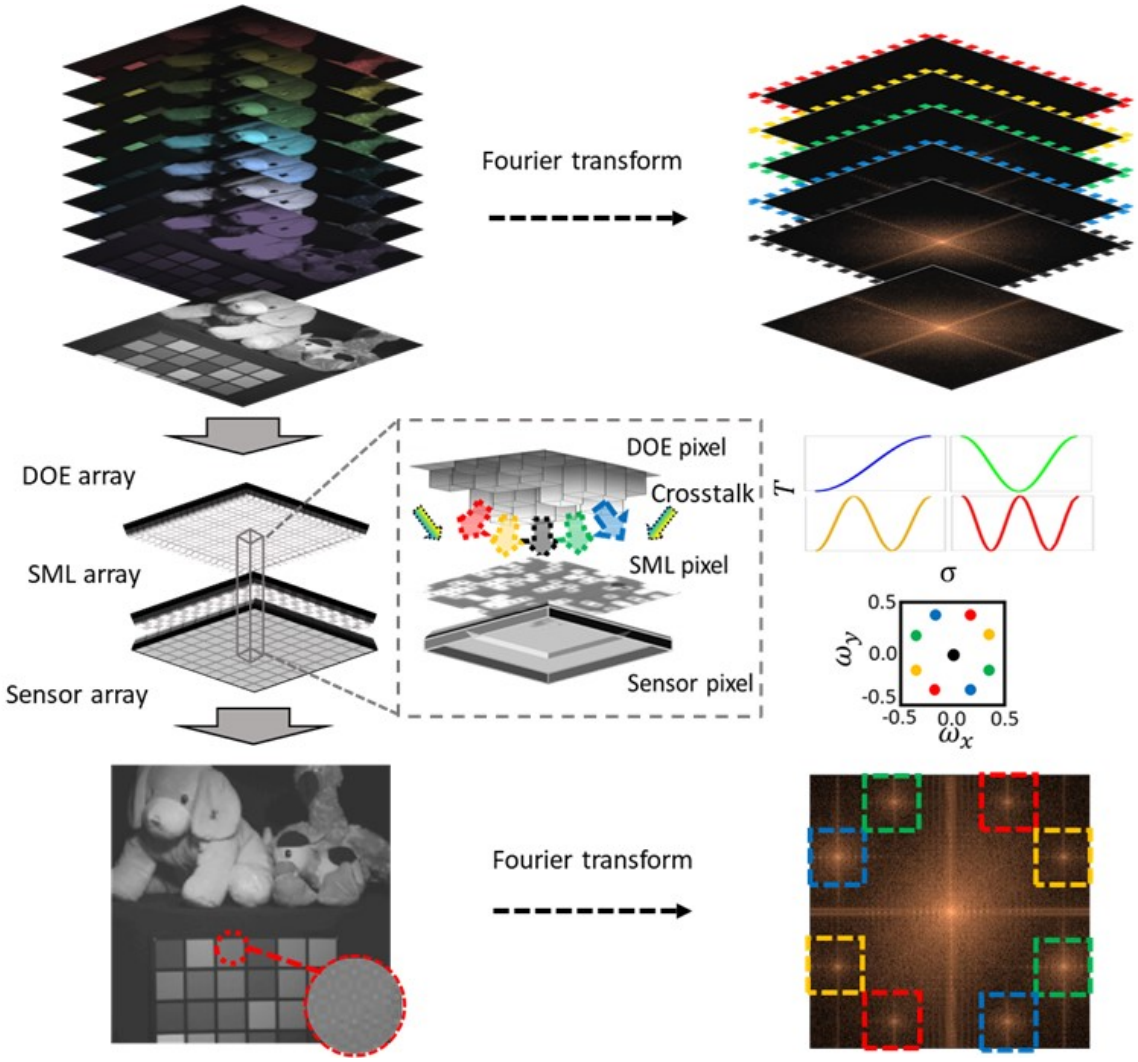

Figure 2.8: Schematic of working principles for the proposed Fourier DOE + SML for spectra imaging. The DOE layer selectively projects the incident beam to sub-pixel locations on the SML and sensory pixel, which contains the first 5 spectral Fourier components. The SML introduces extra spatial frequencies to the transmission spectrum on 4 modulation groups which contains the 2^{nd}-5^{th} major Fourier components (as shown in the inserted plot) and de-alias them in the Fourier transformed domain.

the diffraction pattern. Further, we select K=5 modulation groups containing the first 5 spectral Fourier components to introduce the extra spatial frequency with the SML. γ_k is the modulation coefficient and ω_k is the extra spatial frequency introduced by the SML. Ideally, the spatial modulation on each group will only introduce one extra spatial frequency to fully separate them in the Fourier transformed space. However, due to the fabrication imperfectness, the modulation is mixed in the experimental validation, as we will mention in the following sections. The transmission function $T_{i,k}$ can be decomposed into the form of main spectral Fourier components and represented in terms of wavenumber and OPD:

$$T_{i,k} = \Delta\zeta \cdot \alpha_{0,k} + \Delta\zeta \sum_{m=1}^{\infty} \alpha_{m,k} \cdot cos(2\pi\sigma m\Delta\zeta) \tag{2.10}$$

where $\alpha_{m,k}$ is the sampling coefficient of the mth Fourier bands. Based on our design, for the kth modulation group, the transmission function $T_{i,k}$ will have mainly 2 spectral Fourier components. The sampling process is then equal to:

$$\begin{aligned} I(\boldsymbol{n}) =& \langle T(\boldsymbol{n},\lambda), S(\boldsymbol{n},\lambda))\rangle_\lambda \\ =& \int \sum_{i=0}^{8}\sum_{k=1}^{K} T_{i,k}(\boldsymbol{n},\lambda)\cdot(c_k + \gamma_k \cdot cos(2\pi \boldsymbol{n}\cdot\boldsymbol{\omega_k}))S(\boldsymbol{n_i},\lambda)d\lambda \\ =& \int \sum_{i=0}^{8}\sum_{k=1}^{K} \tilde{T_{i,k}}(\boldsymbol{n},\sigma)\cdot(c_k + \gamma_k \cdot cos(2\pi \boldsymbol{n}\cdot\boldsymbol{\omega_k}))\tilde{S}(\boldsymbol{n_i},\sigma)d\sigma \\ =& \sum_{k=1}^{K}(c_k + \gamma_k \cdot cos(2\pi \boldsymbol{n}\cdot\boldsymbol{\omega_k})) \\ & \cdot \int \sum_{i=0}^{8}[\Delta\zeta\cdot\alpha_{0,k} + \Delta\zeta\sum_{m=1}^{\infty}\alpha_{m,k}\cdot cos(2\pi\sigma m\Delta\zeta)]\tilde{S}(\boldsymbol{n},\sigma)d\sigma \end{aligned} \tag{2.11}$$

We may also decompose the incident wave into the form of its spectral Fourier components with coefficient β_m. The integral of the modulated spectral components is performed against wavenumber from $\sigma = 1/760$ to $1/380\ nm^{-1}$, and we define $\sigma_{max} = 1/380\ nm^{-1}$ and $\Delta\zeta = \frac{1}{\sigma_{max}} = 380$ nm, which is sufficient to reconstruct the spectrum between 380 and 760 nm. Then the integral term of the above equation is

equivalent to the direct sampling of all the Fourier coefficients with some constant determined by the transmission functions $T_{i,k}$. In the following formula, we ignore the crosstalk effects due to the spreading of diffracted light from nearby DOE pixels to simplify the modeling and reconstruction process. We acknowledge the fact that the crosstalk effect will introduce reconstruction error in terms of both spatial and spectral accuracy. While our compact design minimized the crosstalk to nearest neighbor to reduce this error. More detailed discussion will be presented in the following sections. Therefore, the sampling process is transformed to:

$$I(\boldsymbol{n}) = \sum_{k=1}^{K}(c_k + \gamma_k \cdot cos(2\pi \boldsymbol{n} \cdot \boldsymbol{\omega_k})) \cdot \frac{1}{2\sigma_{max}}[\alpha_{0,k} \cdot \beta_0(\boldsymbol{n}) + \sum_{m=1}^{\infty} \alpha_{m,k}\beta_m(\boldsymbol{n})] \quad (2.12)$$

The extra spatial frequency introduced by the SML will then shift the different spectral components in the Fourier transformed space to avoid spectral aliasing, as:

$$\begin{aligned}\hat{I}(\boldsymbol{\omega}) = &\sum_{k=1}^{K}(c_k\delta(\boldsymbol{\omega}) + 0.5 \cdot \gamma_k\delta(\boldsymbol{\omega} - \boldsymbol{\omega_k}) + 0.5 \cdot \gamma_k\delta(\boldsymbol{\omega} + \boldsymbol{\omega_k})) \\ &\cdot \frac{1}{2\sigma_{max}}[\hat{\alpha}_{0,k} \cdot \hat{\beta}_0(\boldsymbol{\omega}) + \sum_{m=1}^{\infty} \hat{\alpha}_{m,k} \cdot \hat{\beta}_m(\boldsymbol{\omega})]\end{aligned} \quad (2.13)$$

Given the extra spatial frequency introduced into the different modulation group, which contains various main spectral Fourier components, the different Fourier coefficients β will be relocated to regions with center at $\omega = \omega_k$, and $\omega = \mathbf{0}$. The intensity of the coefficients will be re-scaled based on the SML (c_k and γ_k) and transmission function of the DOE layer ($\hat{\alpha}_{m,k}$).

We relocated the modulated spectral components to regions in the Fourier transformed space where they have a higher magnitude compared with other components. This can be done by shifting the higher-order spectral Fourier bands to higher spatial frequency regions while keeping the DC spectra component intact.[83] As shown in Figure 2.3, the major components of higher Fourier bands only occupy a small

amount of the Fourier transformed space ($< 0.3\ \omega_{max}$ by $0.3\ \omega_{max}$ of total spatial sensing resolution). Shifting them such that the major components do not overlap with each other can allow effective spectral de-aliasing and facilitate the retrieval of the Fourier coefficients. Based on the measurement in Fourier transformed space, we can reconstruct the Fourier coefficients $\hat{\beta}_m$. Details of the reconstruction method can be found in the following sections. After obtaining the retrieved Fourier coefficients, the spectral information at each sensor pixel location can be reconstructed as:

$$\bar{S}(\boldsymbol{n}, \sigma) = \Delta\zeta \cdot \bar{\beta}_0(\boldsymbol{n}) + \Delta\zeta \sum_{m=1}^{\infty} \bar{\beta}_m(\boldsymbol{n}) \cdot cos(2\pi\sigma m\Delta\zeta) \tag{2.14}$$

Due to the finite band limit of the spectral information, we do not need all the Fourier components to achieve a sufficiently accurate spectral reconstruction. Previous theoretical discussions indicate that reconstruction with the first 5-6 Fourier coefficients is sufficient for spectral imaging in the visible range.[83] Therefore, it is promising to achieve the proposed spectral imaging with relatively small computational loads for the edge sensing system.

2.4 Design of the Fourier DOE filter

The design of the Fourier DOE and spatial modulation layer was conducted under the consideration of fabrication capabilities of the grayscale lithography and eBeam lithography instruments at MIT. Nano, reducing the condition number of the transmission matrix for inverse reconstruction and preventing spectral aliasing between different spectral components.

The fabrication capability determines the physical limitation of the DOE and SML in terms of the DOE's thickness, step height, refractive index, and the area of single spatial modulation spots on SML. We used the MLA-150 direct laser writer to perform grayscale lithography on AZ3312 photoresist. We calibrated the refractive index of AZ3312 by spin-coating it on a Silicon wafer at 1500 RPM to generate 1.40 μm thin film and measuring under a spectroscopic ellipsometer. The rough film thickness is

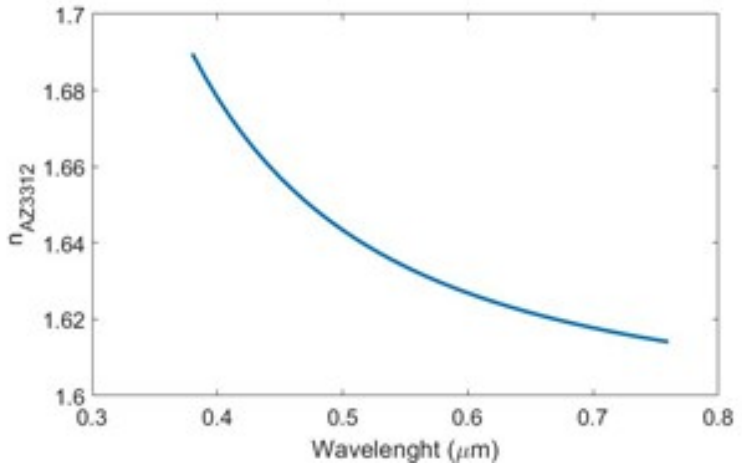

Figure 2.9: Measured refractive index of AZ3312.

measured with a profilometer to fit the refractive index. The fitting result under the Cauchy model is:

$$n_{AZ3312} = 1.59558 + \frac{0.0097174}{\lambda^2} + \frac{0.00055783}{\lambda^4} \tag{2.15}$$

Where λ is wavelength in μm. The plot of the fitting result in the visible range is shown in Figure 2.9.

AZ3312 has a refractive index of around 1.64 in the visible range, which results in a 2pi to 4pi optical path difference for light with a wavelength in the range from 380 to 760 nm when the maximum DOE pillar height is 1.40 μm. Further, the MLA-150 has a theoretical 8-bit grayscale fabrication capability with a lateral resolution at 3 μm. We calibrated the projection dose to generate 8 height steps from 0 to 1.40 μm with a pillar size of 3 by 3 μm. The calibration result is shown in Figure 2.10. We defined the design space for DOE pillars which are 3 by 3 μm pixels with 8 height steps from 0 to 1.40 μm and measured refractive indexes as shown in Figure 2.9.

On the other hand, the spatial modulation layer will be fabricated with eBeam lithography at MIT.Nano as a half-tone-based shadow mask. We pre-defined a squared single modulation spot with the size of 1 by 1 μm. Under this limitation, the intensity modulation is achieved by the "hollow-square" shaped half-tone photomask, as shown in Figure 2.11, which covers 30% to 100% area of the single modulation spot.

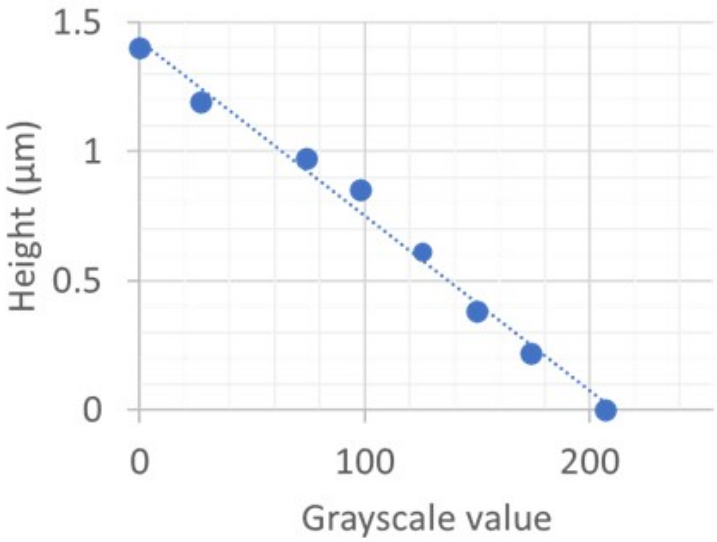

Figure 2.10: Calibrated grayscale value to generate 8 step heights on AZ3321 from 0 to 1.40 μm.

The extra spatial frequencies are introduced to the 4 modulation groups by varying the transmission at each modulation spot periodically across the whole sensing array.

The fabrication restrictions further influence the optimization of the DOE and SML layers. In the optimization, the target function to be maximized is the minimum area of the 4 modulation groups, to increase the transmission efficiency to the main spectral components and reduce the condition number for the spectral reconstruction. A smaller condition number would improve the robustness of the inverse problem and reduce the influence of noises,[65] which could be introduced due to optical misalignment, etc. Further, we also take extra consideration on the separation distance between the DOE and SML/sensor array, to avoid the crosstalk effect beyond the nearest neighbor sensor pixels and ensure the spectral uniformity across a single spatial modulation spot.

The first factor to be considered is the separation distance between the DOE and the SML. A smaller separation distance can help to reduce the crosstalk effects between the nearby DOE pixels and improve the compactness of the whole device for integration. Theoretically, to generate the first 5 Fourier spectral components, the minimum OPD required is 4π, as shown in the schematic in Figure 2.12(b). We

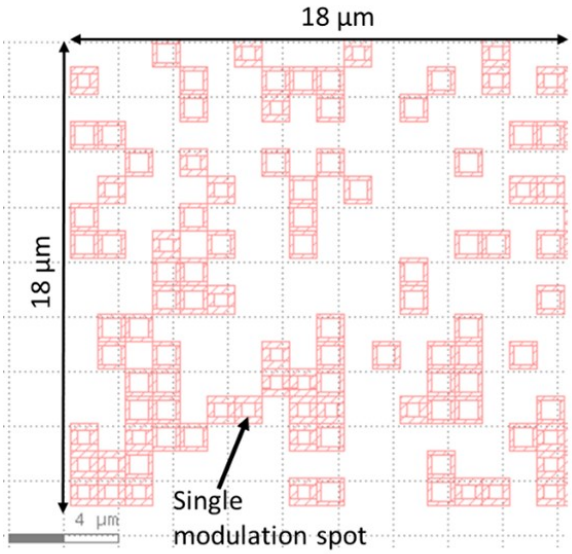

Figure 2.11: Schematic of an 18 by 18 μm half-tone SML pixel with multiple single modulation spot of 1 by 1 μm (red shadow area).

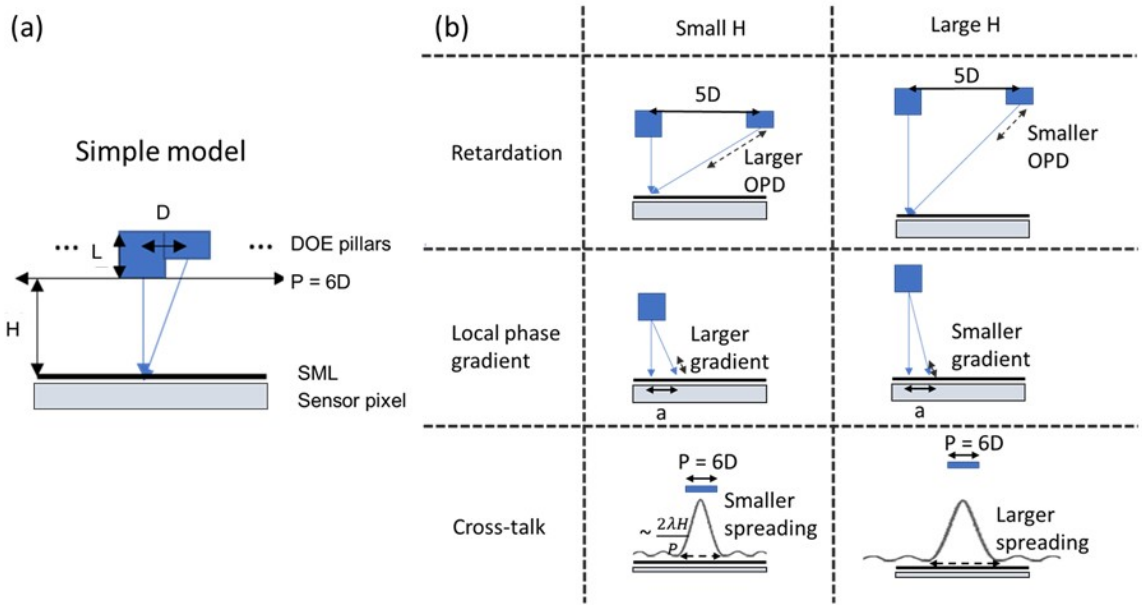

Figure 2.12: Schematic of (a) the simplified diffractive model of DOE+SML layer and (b) considerations to determine the upper and lower bound of the layers' separation distance.

calculate the OPD at the center area of a pillar whose farthest neighbor pillar in the same pixel has the maximum height difference of 1.40 μm. If the OPD across the spectrum from 380 to 760 nm is 4π, i.e.:

$$\begin{aligned} 2\pi(\frac{n_{AZ3312}(0.38)}{0.38} - \frac{n_{AZ3312}(0.76)}{0.76})\Delta L_{max} + \\ [\sqrt{H_{min}^2 + (5D)^2} - H_{min}] \cdot (\frac{2\pi}{0.38} - \frac{2\pi}{0.76}) = 4\pi \end{aligned} \tag{2.16}$$

Where n_{AZ3312} is the refractive index of the DOE material, ΔL_{max} is the maximum height difference of 1.40 μm and D is the width of the single DOE pillar. We could obtain the theoretical upper bound of separation distance is H = 254 μm.

However, it is not practically feasible to have the SML be too close to the DOE layer. There are mainly two reasons for that: (1) When the image plane is close to the DOE, the spatial gradient of transmission spectrum will be large, which restricts the area for intensity modulation, as shown in Figure 2.12(b). In such a case, it requires a very high-resolution fabrication technique to produce the half-tone photomask as the SML. (2). The total transmission efficiency for the high Fourier orders will be small, which will increase the illness of the spectral transmission matrix. As the result, we need to consider the practical lower and upper bound of the separation distance. Practically, if we require the spatial gradient of the OPD to be within 5% over the area of 1 μm by 1 μm, we will need:

$$[\sqrt{H^2 + (P/2 + a)^2} - sqrtH^2 + (P/2)^2] \cdot (\frac{2\pi}{0.38} - \frac{2\pi}{0.76}) < 2\pi \times 0.05 \tag{2.17}$$

Where P=18 μm is the periodicity of the DOE pixel, a = 1 μm is the EBL fabrication resolution of the single modulation spot on SML, and H is the separation distance between the DOE and SML. The practical lower bound of separation distance is then determined as 140 μm. We would like to point out that if we can improve the fabrication resolution of the half-tone photomask fabricated by EBL, we may further improve the compactness of the device. For example, if a = 0.5 μm, we can reduce

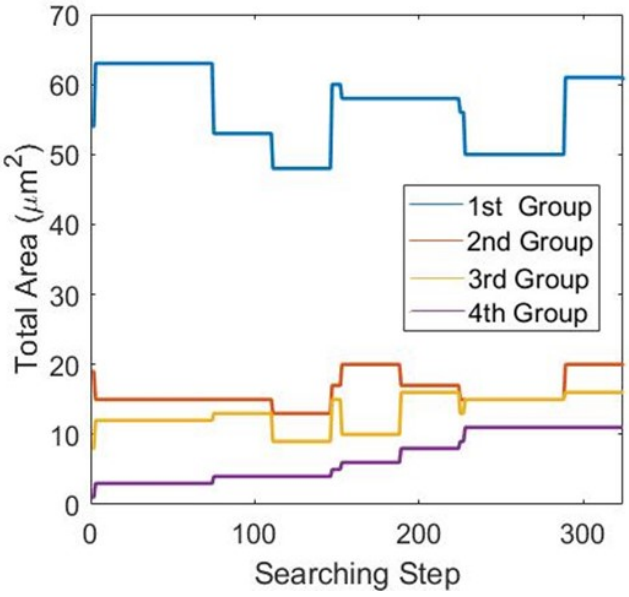

Figure 2.13: Example evolution of the total area of the spatial modulation spots for the groups of the 1^{st} to 4^{th} Fourier bands thorough the optimization process. The minimum area of the 4^{th} order is improved by 10 μm^2 in this example.

the lower bound to 70 μm, and if a = 0.1 μm we can reduce the lower bound to 10 μm.

On the other hand, we would require to only have crosstalk within the first near neighbor DOE superpixel, to use the best of the sensor array's resolution, as shown in Figure 2.12(b). To have the major part (90% of the total diffraction intensity) to have a lateral spreading (L) within a single DOE superpixel area, we need to have:

$$L = \frac{2\lambda H}{P} \leq P \tag{2.18}$$

Given P = 18 μm, we will have the practical upper bound of the separation distance of 231 μm. In summary, the range of choice for the separation distance can be set to 140 230 μm.

A MATLAB code based on Fresnel transformation to predict the diffraction pattern generated by DOEs with a superpixel size of 18 by 18 μm and single pillar size of 3 by 3 μm. The details of the numerical method are described in section 2.8. The optimization was initiated by generating a DOE pixel of 6 by 6 pillars with heights

randomly picked from the 8 height steps characterized in Figure 2.10. Then the diffraction pattern at the certain separation distance behind the DOE is simulated at the resolution of 1 by 1 μm, following by decomposition of the spectral components at each modulation spot and identification of the spots with only 2 major spectral Fourier components, for example, the 0^{th} (DC) and 1^st Fourier series. The threshold we defined to determine the major spectral components is that the Fourier coefficient of the major components should be at least 2 times the Fourier coefficients of the other components. Finally, the total area of modulation spots with the same major spectral components is summed together. After random initialization, we performed a direct binary search method to individually modify (plus or deduce a random step height) the height at each DOE pillar following a random order. After each modification, the diffraction pattern and transmission spectrum are recalculated to evaluate the modified total area of modulation spots for each spectral component. If the minimum area is increased, the modification will be kept and the DOE design will be updated. Otherwise, the modification will be discarded, and the height of the next pillar will be modified to repeat the binary search process. We then performed the optimization algorithm at H = 120, 160 and 200 μm. For each height, a total of 10,800 searches over 30 different initialization was evaluated, and the design with the maximized minimum Fourier coefficient was the design for experimental validation. Here we would like to point out that the optimization method is not the most efficient way and other methods such as adjoint optimization [40] can also be applied for the end-to-end design of DOEs. Figure 2.13 plot a typical evolution of the optimization target as the function of searching steps. In general, the current method can improve the minimum modulation area of the first 5 Fourier components up to 20 μm^2.

We calculated the condition number of the 5 by 5 matrix whose elements are the first 5 Fourier coefficients of the transmission functions over the 4 spatial modulation groups and the rest area of the sensor pixel. Through the optimization process, the condition number of the matrix is 231.2, 105.4, and 104.6 for the 3 different separation distances at 120, 160, and 200 μm, which are of the same order of magnitude. With the current design method, there is no necessity to pick one of the separation distances

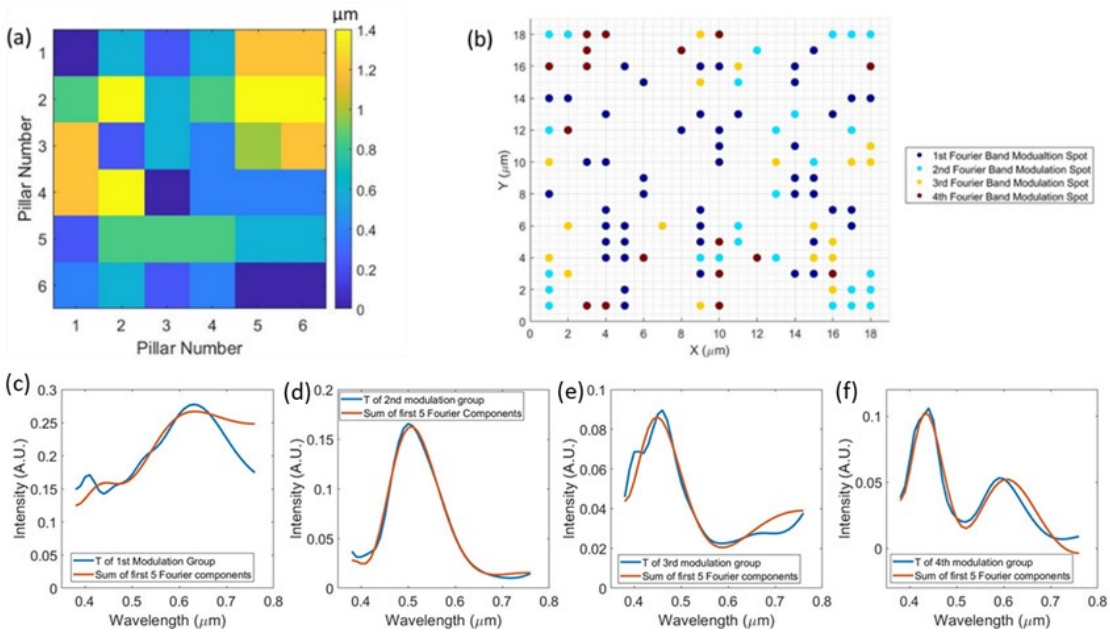

Figure 2.14: (a) Height profile of the designed DOE pixel with 6 by 6 pillars. (b) Locations of the designed 4 groups of modulation spots. (c) to (f) Transmission functions on the 4 groups of modulation spots, and their major components.

in the practical range over another. And we choose the separation distance of 160 μm and the correspondingly optimized design for experimental verification. The details of the DOE pillar height, modulation spot location, and transmission spectrum of the 4 different modulation areas are shown in Figure 2.14.

The second consideration is how many extra spatial frequencies the SML should introduce to shift the spectral components in the Fourier transformed space. We again look at the real-world spectral image data from the CAVE data set.[84] In Figure 2.3 (b), the occupancy area decreases as the Fourier order number increases. And starting from the 2nd band, the area is less than 0.3 by 0.3 of the total spatial sampling frequencies in the Fourier transformed space. To avoid spectral aliasing, the SML needs to introduce extra spatial frequencies to the spectral components and shift them in Fourier space. And in a cubic lattice of the sensor array, the available spatial frequencies are limited. Based on the statistic characteristic of the real-world spectral image data,[82] we can introduce spatial modulation frequencies of $(\frac{1}{\sqrt{5}}, \frac{2}{\sqrt{5}})$,$(\frac{1}{\sqrt{5}}, \frac{-2}{\sqrt{5}})$, $(\frac{2}{\sqrt{5}}, \frac{1}{\sqrt{5}})$,and $(\frac{2}{\sqrt{5}}, \frac{-1}{\sqrt{5}})$ to the 4 higher-order bands, to avoid spectral

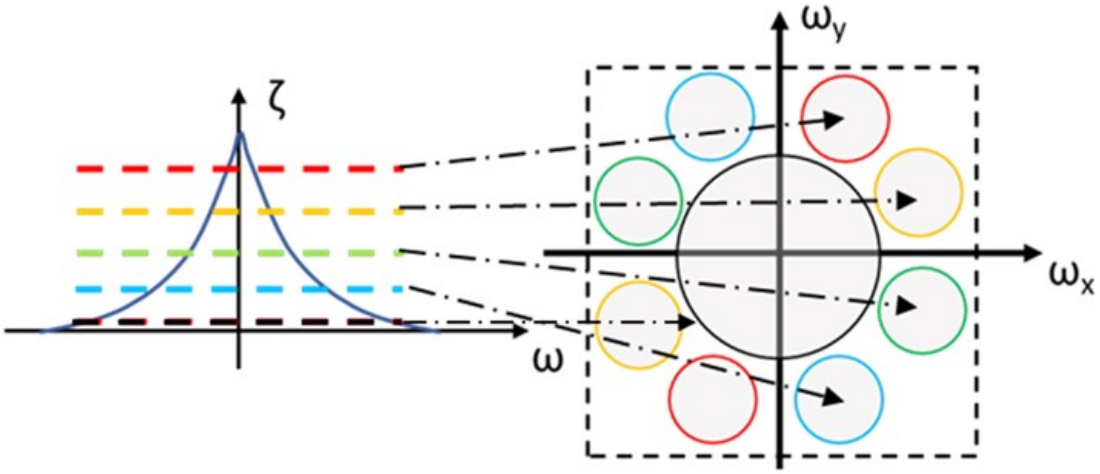

Figure 2.15: Proposed spectral de-aliasing of the first 5 spectral Fourier bands by introducing the extra spatial frequencies through the SML.

aliasing between the first 5 Fourier spectral components. It is equivalent to shifting the four components in the Fourier space as shown in Figure 2.15. As the result, the DOE Fourier filter will have a periodicity of 5 by 5 pixels in both the x and y-direction.

With this design, we may predict the spectrum reconstruction by the Fourier DOE filter and the spectral image reconstruction process. Figure 2.16 (a) and (b) shows the reconstructed 15 Gaussian bands with peak locating at 450 to 700 nm with an RMSE of 7.5 nm. The current design only reconstructs up to the 5^{th} Fourier components of the spectrum, which causes the Gibbs effect [80] on the reconstruction of sharp peaks locating near the edges of the spectrum, and compromises the reconstruction accuracy. Figure 2.16 (c-e) shows the reconstructed "stuffed animal" spectral image in comparison with the RGB ground truth. We will discuss the reconstruction algorithm and spatial-spectral resolution characterization in section 2.7.

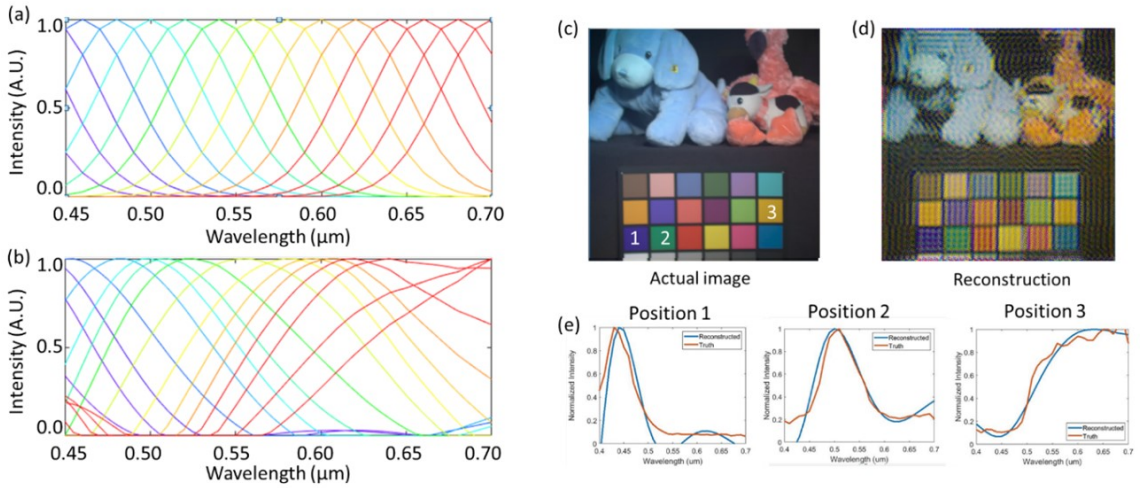

Figure 2.16: (a) Target Gaussian spectrum for reconstruction. (b) Simulated reconstruction results based on the Fourier DOE design. (c) RGB color plot of the spectral input "stuffed animal" (d) Simulated spectral image reconstruction based on the Fourier DOE design. (e) Ground truth (solid orange) and simulated reconstruction result (solid blue) by the designed Fourier DOE at the 3 positions in (c).

2.5 Device fabrication and transmission characterization

The DOE was fabricated through grayscale lithography with MLA-150 at MIT.Nano. Firstly, positive photoresist AZ3312 was spin-coated on 2" fused silica wafer under 1500 RPM for 30 S, which results in about 1.4 μm thickness. Then the wafter was soft baked on a hot plate at 100 °C for 60 S. The grayscale exposure was done in MLA-150 under grayscale mode with 100% intensity of 800 mJ/cm^2. The .bmp file exposure pattern was obtained based on the exposure calibration in section 2.4. The targeted DOE profile is listed in the following table. After exposure, the wafer was post-backed on a hot plate at 110 °C for 90 S, followed by developing in AZ300MIF for 60 S and rinsing with IPA and air-dried. Figure 2.17 shows the fabricated DOE under a white light microscope and the height profile of a single DOE pixel measured by AFM. We could observe that the fabricated DOE does not have a rectangular step profile as the one used in the numerical simulation of the diffraction pattern. This deviation will cause the difference between the generated diffraction pattern and the simulated

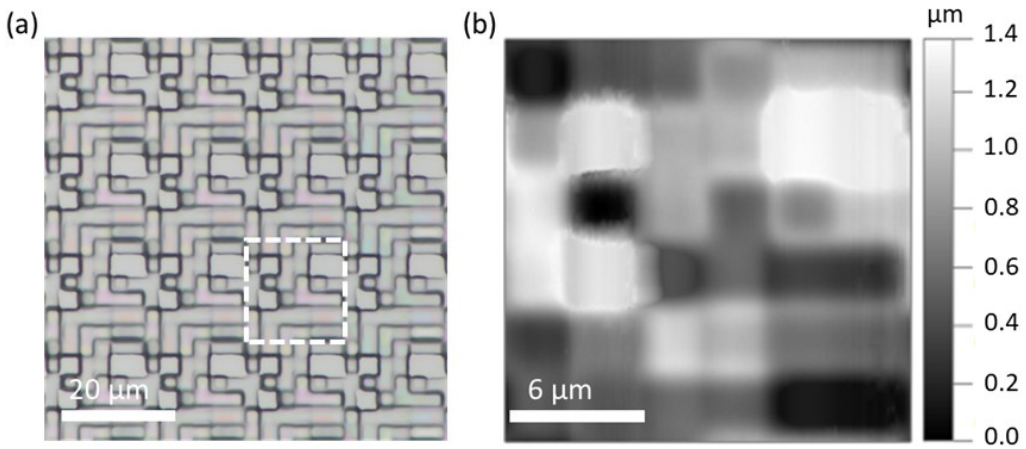

Figure 2.17: (a) Fabricated DOE array under white light microscope. (b) AFM measured height profile of a single DOE pixel.

results. However, the prediction by the simulation results is sufficiently accurate and the fabricated DOE can be applied for spectroscopy and spectral imaging purpose, as we will see in the following sections.

The SML was fabricated with eBeam lithography at MIT. Nano. PMMA450 and PMMA950 were spin-coated (3000 RPM for 45 S) on a 2" fused silica wafer to form double layer resist for easy lift-off. Following that, the wafer was prebaked on a hotplate at 155 °C and 185 °C for 60 S, separately. Then a thin layer of water-based charge relief layer (H_2O Charge) was spin-coated on the fused silica wafer at 1500 RPM for 60 S to reduce the charge accumulation during eBeam lithography. The eBeam pattern was generated based on the simulation results. Figure 2.18 (a) and (b) show the low and high magnification schematic of the SML pattern. After exposure, the wafer was first rinsed with water for 120S to remove the charge relief layer, developed in 3:1 IPA: MIBK for 60 S followed by rinsed with IPA and air dry. Then, 5 nm Ti/60 nm Au/20 nm Cr layers were deposited with eBeam evaporation, followed by lift-off in hot (50 °C) Remover PG. Figure 2.18 (c) shows the white light microscope of the fabricated device.

The designed DOE and SML reduce the fabrication complexity compared to other filter implementations for direct sampling spectral Fourier coefficients.[93] In our case,

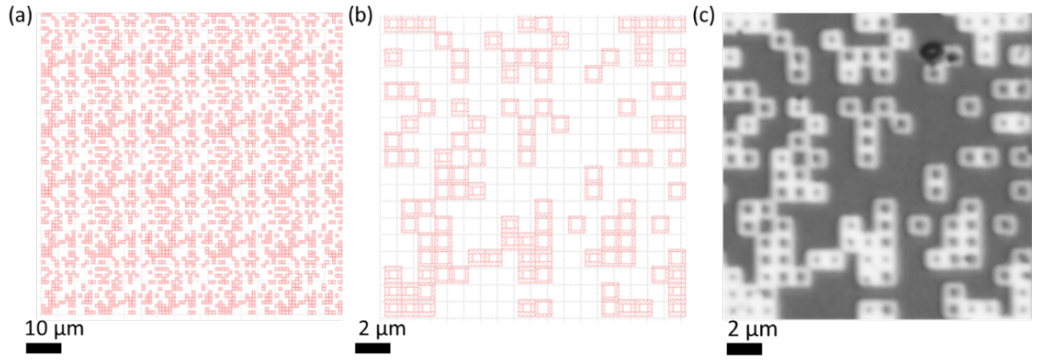

Figure 2.18: (a) and (b) Low and high magnification of the SML's design pattern. (c) Reflective microscopic photo of the one SML pixel. The black defect comes from debris on the fused silica substrate.

only the grayscale lithography and the binary eBeam lithography are required. In contrast, FP-type cavity structures with optical stacks have been proposed to act as the Fourier color filters, which rely on fabricating multi-layer/multi-material structures with spatially variable thicknesses.[93] The complicated fabrication limits the extra spatial frequency that can be introduced to the Fourier components and brings more obstacles for large-scale and flexible applications. Meanwhile, the method cannot avoid the loss in spatial resolution due to the sub-super-pixel-level sensing requirements.

The fabricated DOE and SML were assembled on a home-built optical setup to calibrate the diffraction pattern and spectral response. The schematic and photo of the setup are shown in Figure 2.19, which includes: (1) Super-continuum white laser with AOTF and/or image samples of transparency as a light source. (2) Sample holder with freedoms to adjust the relative translational position (x,y,z), tilting (θ, ϕ), and rotational position (γ) between the DOE and SML. (3) Horizontal object lens with zoom tube lens and monochromic CMOS camera to capture and calibrate the transmission pattern for spectral imaging.

We first installed the DOE onto the sample holder and measured the diffraction pattern at 160 μm behind it. It was done by first focusing on the DOE and moving the sample by 160 μm. Narrowband input beams with peaks from 480 nm to 700 nm, at the step of 10 nm, were captured by the monochromic camera, which is normalized

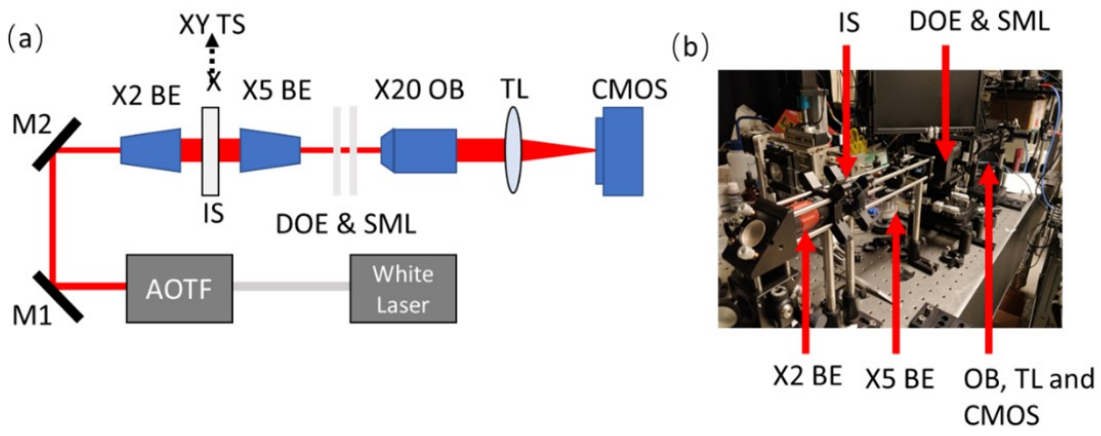

Figure 2.19: (a) Schematic of optic setup for device calibration and spectral imaging. DOE and SML are arranged correspondingly as the schematic in Figure 2.8, with 160 μm separation distance. M1,2: Mirror. X2, X5 BE: Beam expander. XY TS: XY automatic translational stage for image sample scanning. X20 OB: Objective. TL: Tube lens. CMOS: DMM 22BUC03-ML monochromic CMOS. (b) Photo of the optic setup.

against the intensity profile captured without the DOE. Figure 2.20 (a) plots the measured diffraction pattern with the incident beam at 500 nm, 550 nm, 600 nm, and 650 nm, in parallel comparison with the simulated diffraction profile. In the capture profile, pixels on the CMOS were binned together to form the targeted 18 by 18 μm, same as the designed DOE size. We can see that the capture diffraction patterns share similar spatial features as the simulated results, emphasized by the red arrows on the plots. Figure 2.20 (b) shows the self-correlation between the measured diffraction patterns, indicating the wavelength sensitivity of the diffraction pattern. While with the increase of the wavelength, it will be harder to distinguish between the diffraction patterns, due to the less dispersion imposed by the DOE layer to the lights with larger wavelengths. Further, there is certainly deviation between the numerical design and the measurement results due to the fabrication and measurement imperfections. As shown in Figure 2.20 (c), the cross-correlation between the simulated and measured results shows that the deviation is stronger for light with lower wavelengths, since the fabrication imperfectness will affect higher frequency lights more than lower frequency lights.

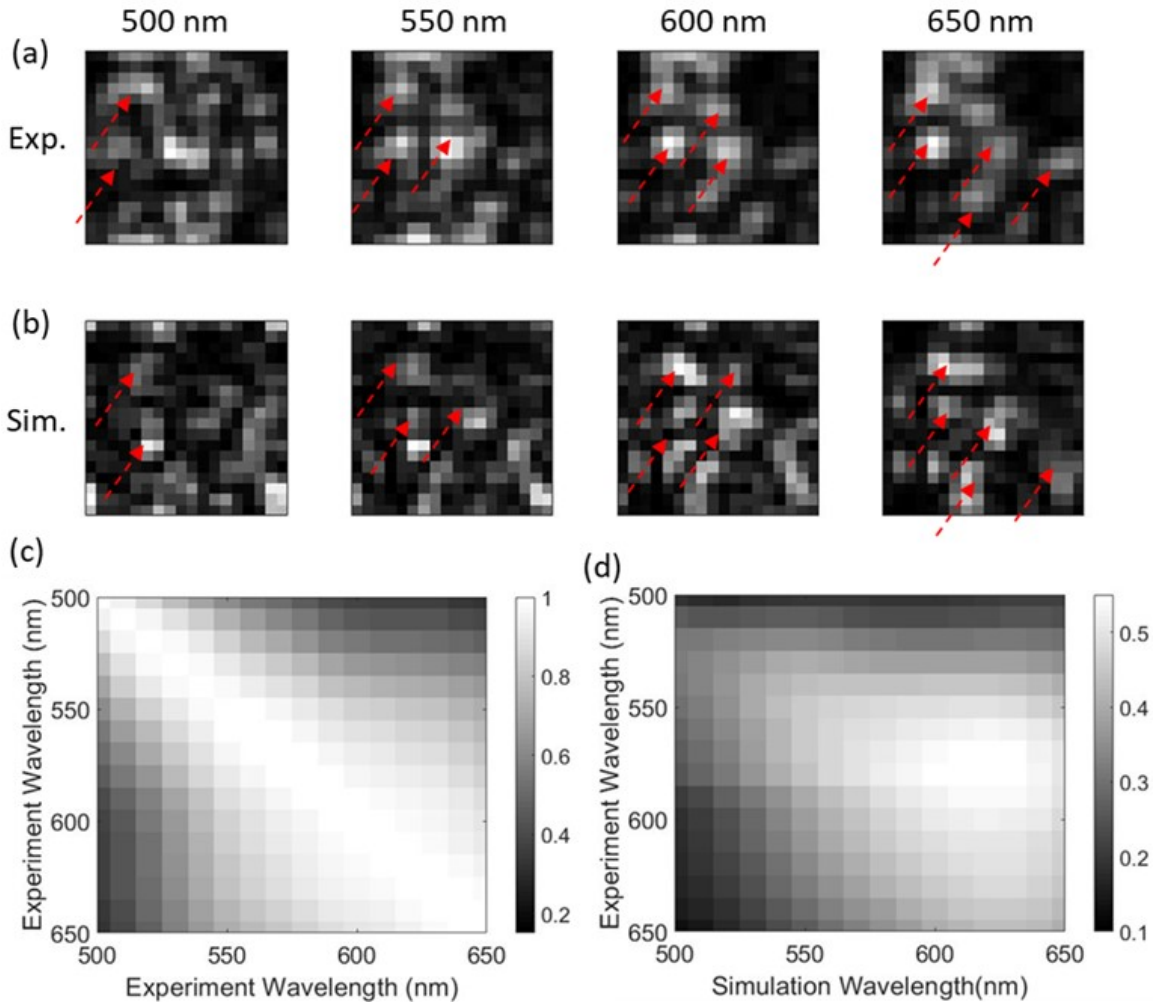

Figure 2.20: (a) Numerical simulation and (b) experimental measurement of the diffraction pattern at 500, 550, 600, and 650 nm. (c) Self-correlation coefficient of measured diffraction patterns from 500 to 650 nm. (d) Cross-correlation between numerical and experimental results of the diffraction pattern from 500 to 650 nm.

To further evaluate the DOE, we extracted the transmission spectrum on the spatial modulation locations and compared them with the simulation results. As shown in Figure 2.21, the measured spectrum on those locations matches well with the linearly re-scaled transmission spectrum on the same locations obtained from numerical simulation. It indicates that the fabricated DOE can effectively capture the spatial-spectral profile of the designed DOE and can be applied for spectroscopic and spectral imaging purposes with linearly re-scaled reconstruction parameters based on the calibration.

Following the characterization of the DOE layer, we assemble the SML onto the sample stage and aligned it with the DOE. The alignment was first conducted by ensuring the parallel separation between the two filter layers at the desired distance of 160 μm. We first focused on the SML and then move the sample stage forward by 160 μm. Then the relative out-of-plane separation between the DOE and SML was adjusted to make the DOE sharply focused under a microscope. Further, we change the relative in-plane position between the DOE and the SML and adjusted the tilting angles of the DOE to ensure that the whole DOE layer is in parallel with the SML layer. After that, we adjusted the DOE and SML to align their relative in-plane positions. To determine the best in-plane alignment condition, we introduced shifting of ($\pm$1 μm, $\pm$1 μm) in relative to the eye-balled "aligned" position. Then the transmission profile was re-measured to determine the spatial modulation over the 5 by 5 pixels area. With the measured result, we could determine the position with the lowest condition number of the transmission matrix, which is (-1,0) μm position in relative to the eye-balled aligned position. Figure 2.21 shows the measured spatially modulated transmission profiles on the 4 groups of modulation spots in the 5 by 5 pixels array.

Due to the imperfectness in fabrication and alignment, the transmission function and spatial modulation is not the same as what we designed. Besides the designed spatial frequencies, the spatial modulation layer together with the DOE also introduced spatial frequencies of $(0, \frac{\pm 2}{\sqrt{5}})$, $(\frac{\pm 2}{\sqrt{5}}, \frac{\pm 2}{\sqrt{5}})$,$(0, \frac{\pm 1}{\sqrt{5}})$, $(\frac{\pm 1}{\sqrt{5}}, \frac{\pm 1}{\sqrt{5}})$,$(\frac{\pm 1}{\sqrt{5}}, 0)$, $(\frac{\pm 2}{\sqrt{5}}, 0)$, $(\frac{\pm 1}{\sqrt{5}}, \frac{\pm 2}{\sqrt{5}})$. Despite this imperfectness, the principle of spectral imaging with the Fourier DOE is not

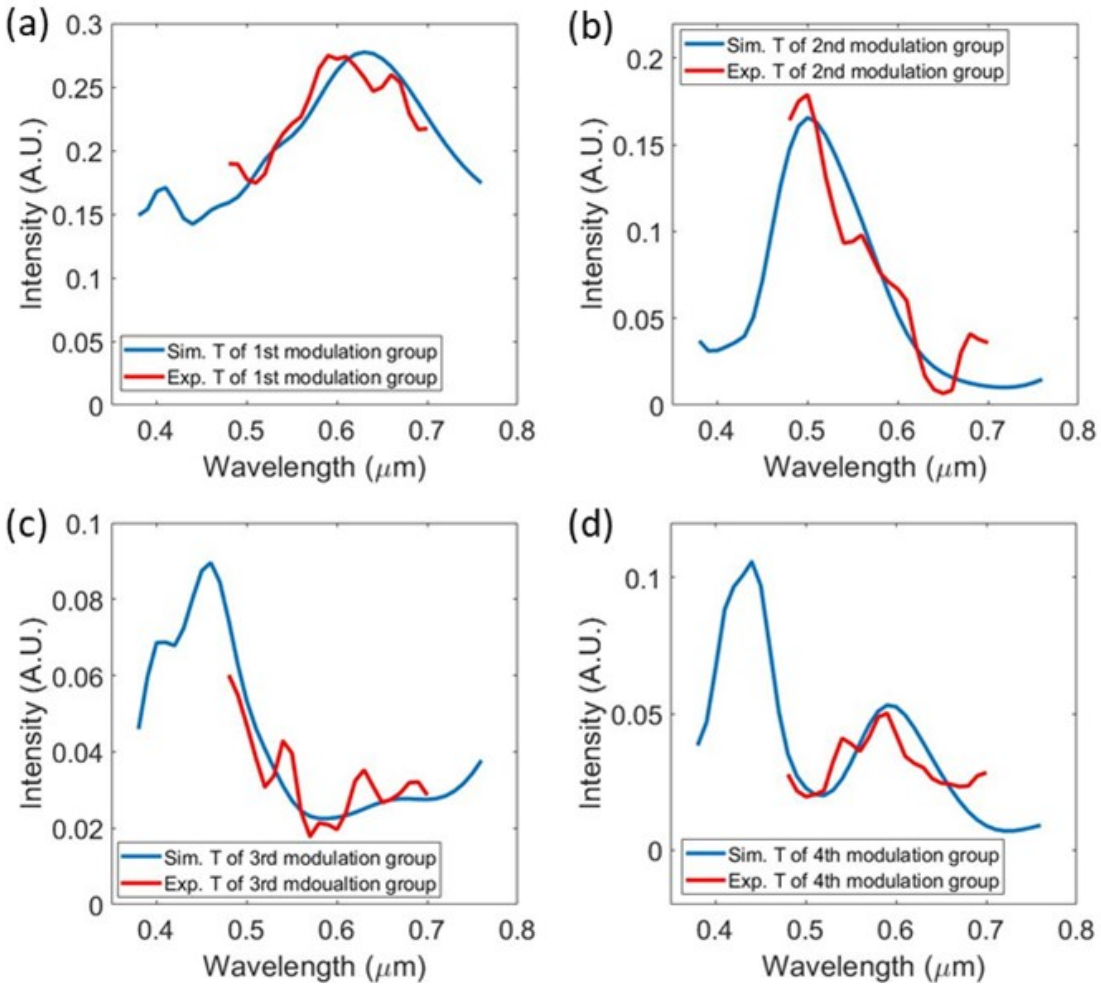

Figure 2.21: Normalized transmission spectrum on the 4 groups of different spatial modulation spots for (a) 0 and 1^{st} Fourier band. (b) 0 and 2^{nd} Fourier band. (c) 0 and 3^{rd} Fourier band. (d) 0 and 4^{th} Fourier band. Blue solid lines: Linearly re-scaled simulation results of the transmission spectrum. Red solid lines: Experiment measured transmission spectrum.

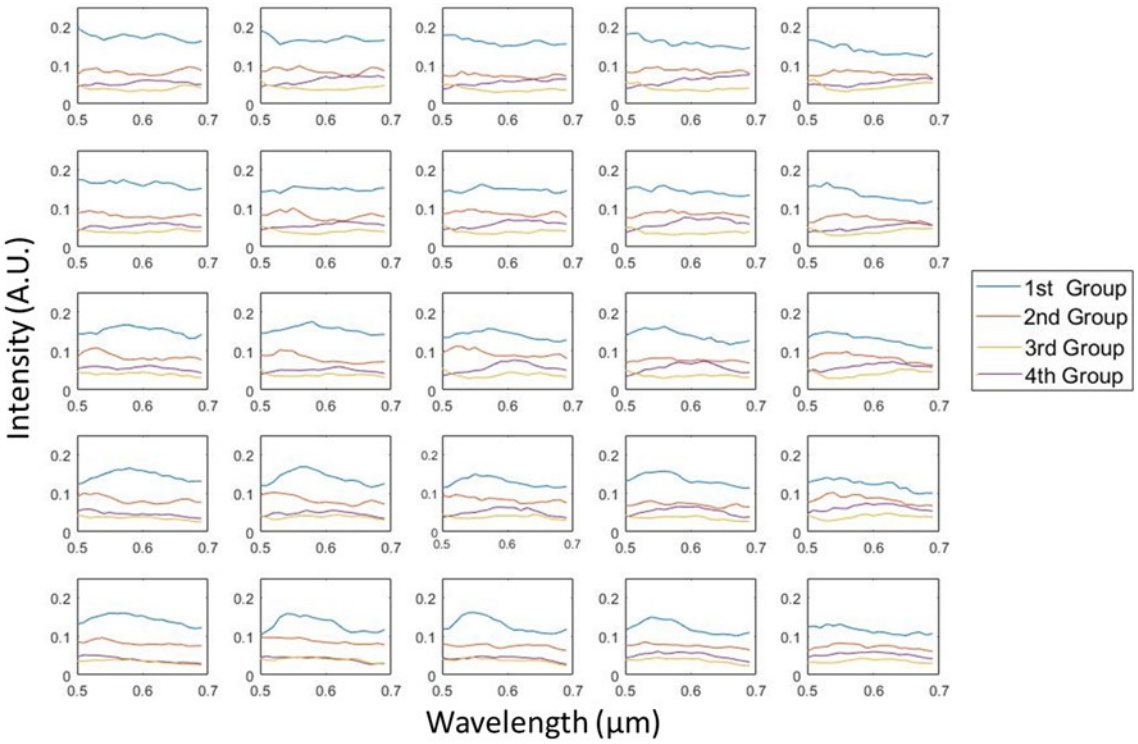

Figure 2.22: Transmission functions on the 4 modulation groups over the 5-by-5 pixel array.

changed and we will see the filter layer can effectively fulfill the designed performance in the following sections. We then fixed the relative position between the DOE and SML and used the assemble filter for further calibration.

2.6 Spectral imaging with the Fourier DOE filter

We first calibrated the reconstruction parameters required to perform the spectral imaging with the designed Fourier DOE. Broad color bands were shinned onto the assembled filter layer, and both the modulated diffraction pattern and the ground truth transmission spectrum were recorded by the monochromic camera (DMM 22BUC03-ML, ImagingSource) and spectrometer (Ocean Optics USB2000+). With this method, we are not limited to narrow bands with discretized center peak locations, which are commonly applied in previously reported spectral imagers with DOE/ scattering medium. On the other hand, the broadband spectral response of the design from 380 nm to 760 nm can be characterized. The broadband color filters were prepared by sandwiching molecular-dye-based PET color filters (Roscolux) in between fused silica and sealed with NOA86 optic adhesive. Figure 2.23 (a) shows the fabricated calibration sample. Then, the capture profiles are repeated in the x and y direction 40 times to form the large scale and uniform images followed by FFT to obtain the reconstruction parameters, as shown in Figure 2.23 (b) and (c). Due to the imperfection in fabrication, the SML introduces more than 1 extra frequency to each group of modulation locations. In Fourier transformed space, the intensity mainly locates on 25 discretized spatial frequency spots, as shown in Figure 2.23 (c). The intensity at each location equals to:

$$\hat{I}(\boldsymbol{\omega_n}) = \begin{cases} \sum_{k=1}^{5} c_k \cdot \frac{1}{2\sigma_{max}} \left[\hat{\alpha}_{0,k} \cdot \hat{\beta}_0 + \sum_{m=1}^{4} \hat{\alpha}_{m,k}\hat{\beta}_m\right], & (\boldsymbol{\omega_n} = [0,0]), \\ \sum_{k=1}^{5} 0.5 \cdot \gamma_{\boldsymbol{n},k} \cdot \frac{1}{2\sigma_{max}} \left[\hat{\alpha}_{0,k} \cdot \hat{\beta}_0 + \sum_{m=1}^{4} \hat{\alpha}_{m,k}\hat{\beta}_m\right], & (\boldsymbol{\omega_n} \neq [0,0]) \end{cases} \tag{2.19}$$

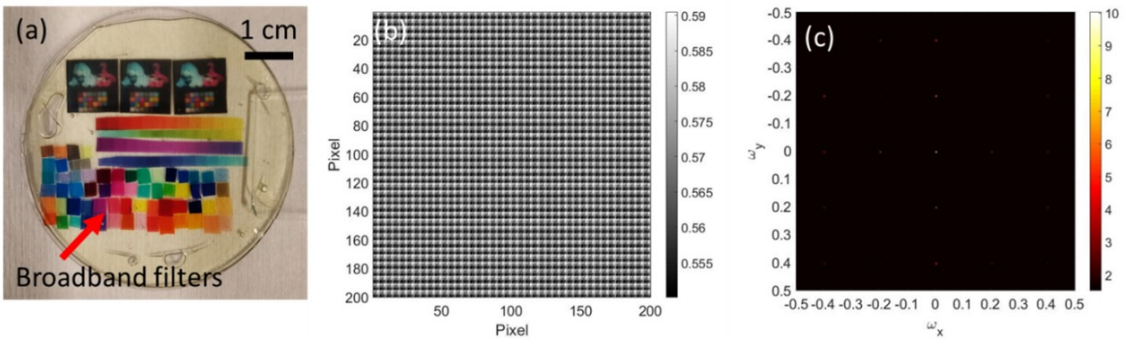

Figure 2.23: (a) Broadband color sample for reconstruction parameter calibration. The 54 color bands are obtained by sandwiching PET-dye filters between fused Silica substrates, which covers the major color regions on CIE diagram. We show examples of 25 transmission spectrum through the filters in Figure 2.23. (b) Example of diffraction pattern of laser beam shinning though the broadband filter, and (c) Log scale plot of the absolute value of Fourier transformation of (b).

Because of the symmetry of intensity locates at $\boldsymbol{\omega}_k$ and $-\boldsymbol{\omega}_k$, we will have 13 independent intensities locates in the Fourier Space, and the pre-knowledge of the Fourier coefficients $\hat{\beta}$ of the 54 broadbands. We choose the intensity at $\boldsymbol{\omega}_n = (0, 0)$, $(\frac{1}{\sqrt{5}}, \frac{2}{\sqrt{5}})$,$(\frac{1}{\sqrt{5}}, \frac{-2}{\sqrt{5}})$, $(\frac{2}{\sqrt{5}}, \frac{1}{\sqrt{5}})$,and $(\frac{2}{\sqrt{5}}, \frac{-1}{\sqrt{5}})$ as the points to calibrate the total 5×5=25 reconstruction parameters in the terms of $\sum_{k=1}^{5} c_k \cdot \hat{\alpha}_{m,k}$ and $\sum_{k=1}^{5} \gamma_{\boldsymbol{n},k} \cdot \hat{\alpha}_{m,k}$ The redundancy in the number of transformed intensities locating in the Fourier space allow us to reconstruct more than the first 5 Fourier coefficient for the spectral imaging. However, due to the higher magnitude of low spectral frequency components in the shifted regions, spectral aliasing may still happen when the introduced spatial frequency, i.e. the amount of shifting in Fourier space is not sufficient. Therefore, we only chose the 5 spots and calibrate the reconstruction parameters.

We extract the reconstruction parameters by least square regression between the measured intensity and the ground truth of the Fourier coefficients of the broadbands. 54 different color filters were used to obtain the reconstruction parameters. Figure 2.24 shows the ground truths and reconstructed spectrum of 25 color bands based on the parameters extracted from the 54 measurements. RMSE of the reconstructed bands in about 9.4%, in comparison with the ground truth. The good match between them indicates the capability of the filter layer for spectral imaging.

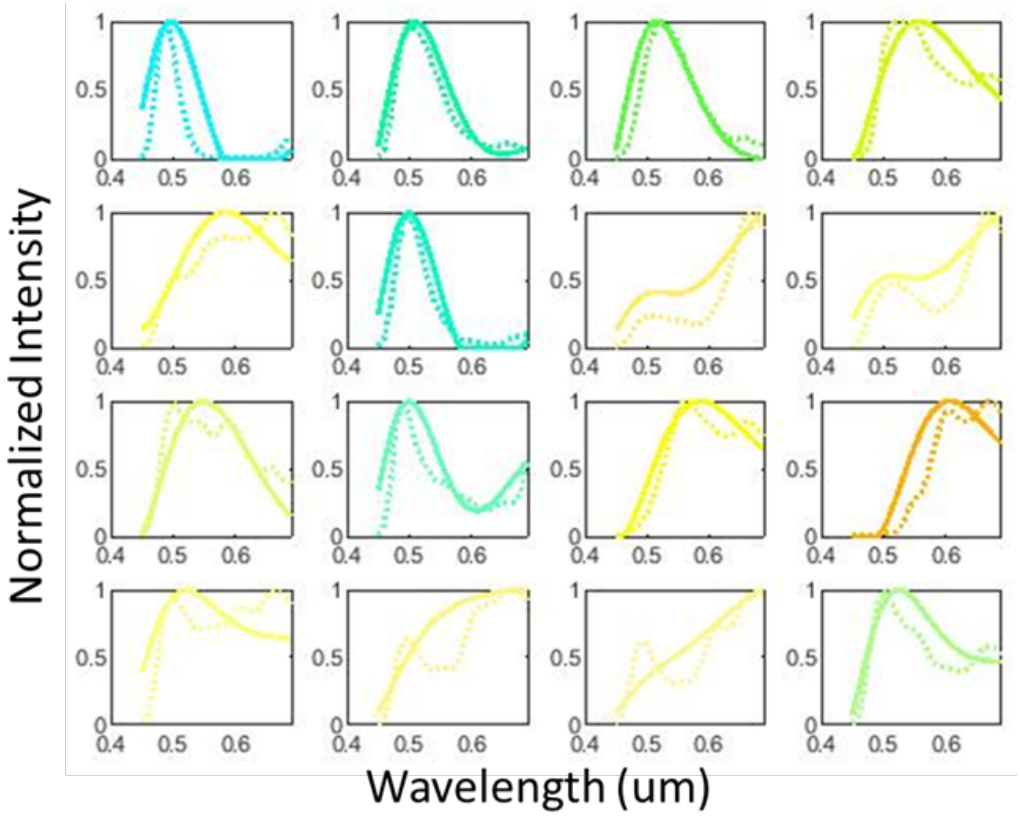

Figure 2.24: Ground truth (solid lines) and reconstruction (dash lines) from the first 5 spectral Fourier components, based on the calibrated reconstruction parameters.

Further, spectral imaging was performed with the same experimental setup. An automatic stage with in-plane translational freedom was used to scan over the spectral samples printed on transparencies. The samples were again sandwiched between fused silica and sealed with NOA86 optical adhesive. The sample was moved by 0.45 mm at each scan location, in corresponding with the 5 by 5 pixels on the DOE and SML layer. Since the actual size of the DOE and SML is larger than 5 by 5 pixels, the crosstalk effects at the end of the recording area are preserved. With this setup, the monochromic images were taken on 4 different samples, which were of 200 by 200 pixels total resolution. Then the image was Fourier transformed and the previously determined reconstruction parameter was applied to retrieve the spectral information. Figure 2.25 (a) and (b) show an example of the fabricated spectral sample and the measured monochromic intensity profile.

We first introduce a simple reconstruction algorithm which will loss the spatial resolution due to the neglect of high spatial frequency information for low spectral Fourier orders. Figure 2.25 (c) show the Fourier transformed image of the measured intensity on the "stuffed animal" sample. We can see the shifted spectral components locating on the 25 different locations as the "cross" shape. We then crop out 0.2 by 0.2 spatial frequencies areas with center at $\boldsymbol{\omega}_n = (0,0)$, $(\frac{1}{\sqrt{5}}, \frac{2}{\sqrt{5}})$,$(\frac{1}{\sqrt{5}}, \frac{-2}{\sqrt{5}})$, $(\frac{2}{\sqrt{5}}, \frac{1}{\sqrt{5}})$,and $(\frac{2}{\sqrt{5}}, \frac{-1}{\sqrt{5}})$ in the Fourier space, as shown in Figure 2.25 (d).

We assume those cropped intensity profiles are corresponding with the calibrated spectral components and the reconstruction parameters and neglected other high spatial frequency information. This is equivalent to construct new FFT images with only the cropped areas at the same locations. Then we performed inverse FFT to reconstruct the intensity distribution of modulated spectral Fourier components at each location in real space. With the 5 cropped areas in Fourier space, we can reconstruct 5 separated images, as shown in Figure 2.25 (e). In each of the images, the intensity distribution equals:

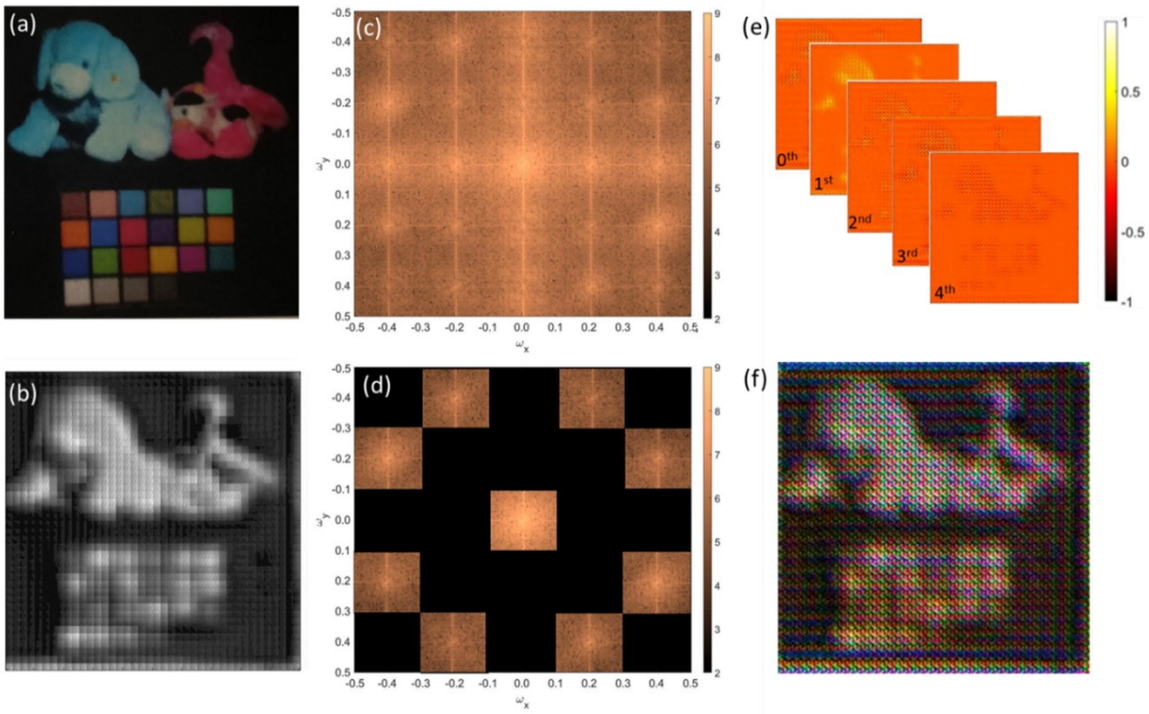

Figure 2.25: (a) Fabricated color image sample on transparency. (b) Measured monochromic intensity through the DOE & SML combination, with 200 by 200 resolution. (c) Fourier transformation of the measured intensity in log scale. (d) Cropped areas in the Fourier Domain for spectral reconstruction, in log scale. (d) Reconstructed Fourier coefficient for the first 5 Fourier bands. (e) Reconstructed RGB image under D65 illumination.

$$I_j(\boldsymbol{n}) = \begin{cases} \sum_{k=1}^{5} c_k \cdot \frac{1}{2\sigma_{max}} \left[\alpha_{0,k} \cdot \beta_0 + \sum_{m=1}^{4} \alpha_{m,k}\beta_m(\boldsymbol{n})\right], & (j=0), \\ \sum_{k=1}^{5} 0.5 \cdot \gamma_{\boldsymbol{n},k} \cdot cos(2\pi \boldsymbol{n} \cdot \boldsymbol{\omega_k}) \cdot \frac{1}{2\sigma_{max}} \cdot \left[\alpha_{0,k} \cdot \beta_0 + \sum_{m=1}^{4} \alpha_{m,k}\beta_m(\boldsymbol{n})\right], & (j=1,2,3,4) \end{cases} \tag{2.20}$$

Since we already calibrated the reconstruction parameters in terms of $\sum_{k=1}^{5} c_k \cdot \hat{\alpha}_{m,k}$ and $\sum_{k=1}^{5} \gamma_{\boldsymbol{n},k} \cdot \hat{\alpha}_{m,k}$, we could solve $\bar{\beta}_m(\boldsymbol{n})$ for m = 0 to 4 from the above 5 equations at each pixel location. Then the whole spectrum is reconstructed as

$$\bar{S}(\boldsymbol{n}, \sigma) = \Delta\zeta \cdot \bar{\beta}_0(\boldsymbol{n}) + \Delta\zeta \sum_{m=1}^{\infty} \bar{\beta}_m(\boldsymbol{n}) \cdot cos(2\pi\sigma m \Delta\zeta) \tag{2.21}$$

Figure 2.24 (f) shows the reconstructed spectral image in the RGB plot, assuming D65 illumination. We can see the simple reconstruction algorithm can effectively retrieve the low spatial frequency components and the color information of the image. We can clearly observe the artificial noises introduced due to the current algorithm with cropped areas in the Fourier transformed space. In the following section, we introduce an approach based on general alternative projection (GAP) [92, 94] to further improve the reconstruction and reduce the artificial spatial noises. The GAP method is widely applied for compressive sensing including hyperspectral imaging, depth imaging, and video reconstruction. Here we applied a GAP-based total variation (GAP-TV) [94] minimization to reduce the spatial noises associated with the previous simple reconstruction method. In the following paragraphs, we describe the specific optimization problem solved in GAP-TV based on [94]:

$$\min_{\boldsymbol{S}} ||TV(\boldsymbol{S})||, \text{ subject to } \boldsymbol{TS} = \boldsymbol{I} \tag{2.22}$$

Where **S** is the spatial-spectral data cube, **T** is the transmission matrix defined by the DOE and SML, and **I** is the measured monochromic intensity. In our case the

above equation is the discretized version of:

$$I(\boldsymbol{n}) = \sum_{k=1}^{K}(c_k + \gamma_k \cdot cos(2\pi \boldsymbol{n} \cdot \boldsymbol{\omega}_k))\cdot \int \sum_{i=0}^{8} \left[\Delta\zeta \cdot \alpha_{0,k} + \Delta\zeta \sum_{m=1}^{\infty} \alpha_{m,k} \cdot cos(2\pi\sigma m \Delta\zeta)\right] \tilde{S}(\boldsymbol{n}, \sigma) d\sigma \tag{2.23}$$

Where all the parameters to build the transmission matrix have been obtained from the calibration process described before. Further, $TV(\boldsymbol{S})$ is the TV norm, which is defined as $TV(\boldsymbol{S}) = \boldsymbol{D}\boldsymbol{S}_1.\boldsymbol{D}$ is the differential operation, and it is performed on all 3 dimensions of $\boldsymbol{S}$. We have obtained the transmission matrix based on the previous calibration of uniform illumination. Then, the above problem could be transferred to an equivalent form of

$$\min_{\boldsymbol{S},C} ||TV(\boldsymbol{S})|| \leq C, \text{ subject to } \boldsymbol{T}\boldsymbol{S} = \boldsymbol{I} \tag{2.24}$$

Where C is the radius of the L1 sphere based on the TV of the signal. The problem can be solved as a series of alternating projection problem:

$$(\boldsymbol{S}^{\boldsymbol{t}}, \boldsymbol{\theta}^{\boldsymbol{t}}) = \text{arg } \min_{x,\boldsymbol{\theta}} \frac{1}{2}||\boldsymbol{S} - \boldsymbol{\theta}||_2^2 + \lambda||TV(\boldsymbol{\theta})|| \quad \text{subject to } \boldsymbol{T}\boldsymbol{S} = \boldsymbol{I} \tag{2.25}$$

where λ is the regularization term and t denotes the iteration number. In the algorithm, we applied the noisy reconstruction as the initial guess of $\boldsymbol{S}$ and set $\lambda = 0.01$ and total iteration number = 2. The GAP-TV allows rapid denoising of the reconstructed spectral imaging after a finite number of iterations.

Figure 2.26 shows 4 color image samples, measured monochromic intensities, reconstructed RGB color images based on the inverse FFT method and GAP-TV method. We could clearly see the reduction of spatial noise after applying the GAP-TV method. Figure 2.26 (b) plots three reconstructed color bands in the "stuffed ani-

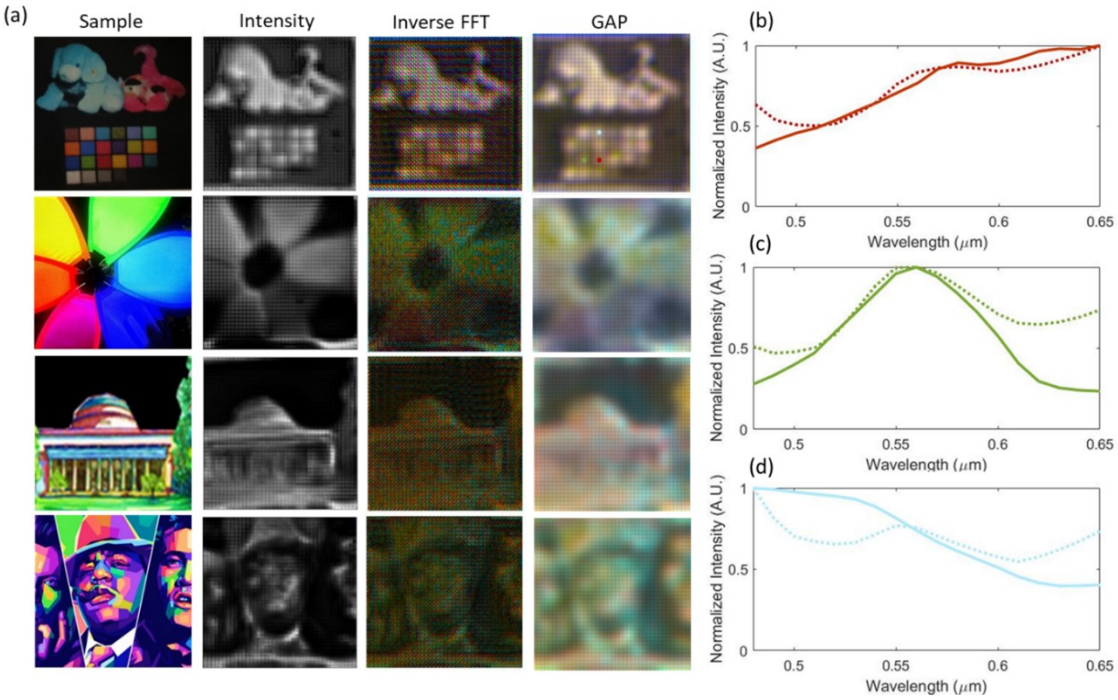

Figure 2.26: (a) Comparison between color image sample, measured monochromic intensity, simple spectral reconstruction, and GAP-TV reconstruction results on 4 color figures. (b) to (d) Reconstructed spectrum over spots covered marked by the three color dots on the reconstructed "stuffed animal" image in (a). Solid lines are ground truth measured by spectroscopy and dash lines are the reconstructed results.

mal" sample. Compared with the printed color figures on the transparency, the spatial resolution of the reconstructed figures drops due to both image shrinkage through the projection lenses and the GAP-TV denoiser. Meanwhile, the color saturation and color temperature of the reconstructed results deviate from the observation of the color printings under white fluorescence light due to the high intensity and "greenish" spectrum of the white laser.

2.7 Spatial-spectral resolution of the Fourier DOE spectral imager

Crosstalk effects between nearby DOE pixels will compromise the spatial resolution.[64] We simulated the diffraction pattern at 450, 550, and 650 nm on top of the SML, as shown in Figure 2.27 (a). When the DOE and SML are separated at 160 μm, the spanning of the diffraction pattern from a single-pixel covers about 3 pixels, which confines the crosstalk effect to the nearest neighbor. As the result, the spatial resolution can in terms of visibility contrast be improved compared to other DOE/scattering-based spectral imagers, whose spectral reconstruction relies on the dispersion of light over multiple pixels. In Figure 2.27 (b), we plotted the visibility contrast at 450, 550, and 650 nm, as the function of the pattern density. Results show that the theoretical visibility can be kept till density equal to 0.5 cycles per pixel. Meanwhile, the lateral spreading is proportional to the light's wavelength. And the visibility drops faster for longer wavelengths.

We experimentally measured the relative contrast against the resolution target (Thorlabs NBS 1963A) with pattern density from 0.18 cycles per pixel to 0.324 cycles per pixel. We first measured the visibility without the DOE and SML layer, then repeat the measurement with the filter installed. The absolute visibility is defined as equation

$$C(v) = \frac{I_{max}(v) - I_{min}(v)}{I_{max}(v) + I_{min}(v)} \tag{2.26}$$

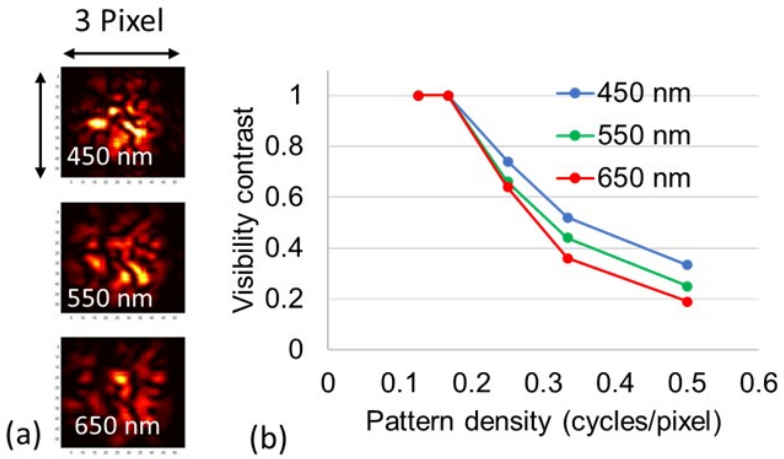

Figure 2.27: (a) Simulated diffraction intensity distribution on SML of light penetrating though single DOE pixel. (b) Simulated visibility of light at 450, 550 and 650 nm as the function of the pattern density.

where $I_{max}(v)$ and $I_{min}(v)$ are the measured maximum and minimum intensity on the sample with pattern density of v. The relative visibility is defined as the ratio between absolute visibility of DOE + optics and the optics itself, $C_{relative}(v) = C_{DOE}(v)/C_{optic}(v)$. The threshold of pattern density with non-zero relative visibility defines the monochromic spatial resolution.

Results show that the relative visibility keeps till 0.324 cycles per pixel, as shown in Figure 2.28. Compared with previous work relying on the de-correlation of diffraction patterns to use DOE for spectral imaging, our method does not require a larger DOE to sensor distance to achieve sufficient wavelength de-correlation. As the result, the monochromic spatial resolution can be improved from about 0.054 cycles per pixel to larger than 0.324 cycles per pixel.

We further evaluated the spatial-spectral resolution by characterizing the spectral image reconstruction of broadband colors shining through the same resolution target. The crosstalk effect determines the absolute spatial resolution in terms of measured monochromic intensity. However, the spatial resolution is meaningless if the spectral reconstruction is totally wrong. For example, in conventional CTIS (computed tomography imaging spectrometer),[95] the minimum and maximum spectral resolution can be achieved when imaging uniform and point-source objects, respectively.

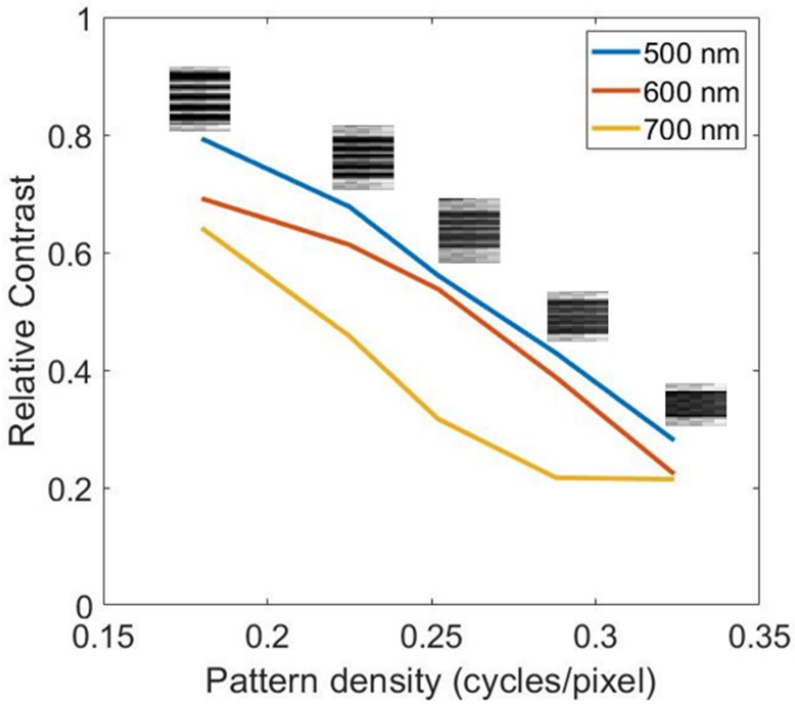

Figure 2.28: Measured relative contrast under 500, 600, and 700 nm illumination, as the function of pattern density.

The object-dependent usefulness limits the application of CTIS for general applications. Therefore, we considered both spatial and spectral reconstruction accuracy when evaluating the performance of spectral imagers. We performed the calibration over 3 color bands with pattern density from 0.18 to 0.32 cycles per pixel. Figure 2.29 (a) and (b) plot the reconstructed intensity, relative contrast, and RGB images for 3 different color bands. The relative contrast decreases with the increase of pattern density. While the visibility is maintained until 0.28 cycles/pixel. However, the spectral reconstruction accuracy also decreases when the image contains high spatial resolution features, as shown in the inserted plots in Figure 2.29 (b), which is partially caused by the crosstalk effects. Evaluation of the spectral RMSE shows that the error grows about 4 times compared with the reconstruction results on uniform samples without any pattern, as shown in Figure 2.29 (c) and (d).

In conventional spatial multiplexed snapshot spectral imaging methods, the spatial-spectral resolutions are coupled and fixed after designing the spectrum of the filters. The channel number of the spectrum's principal component bases and the

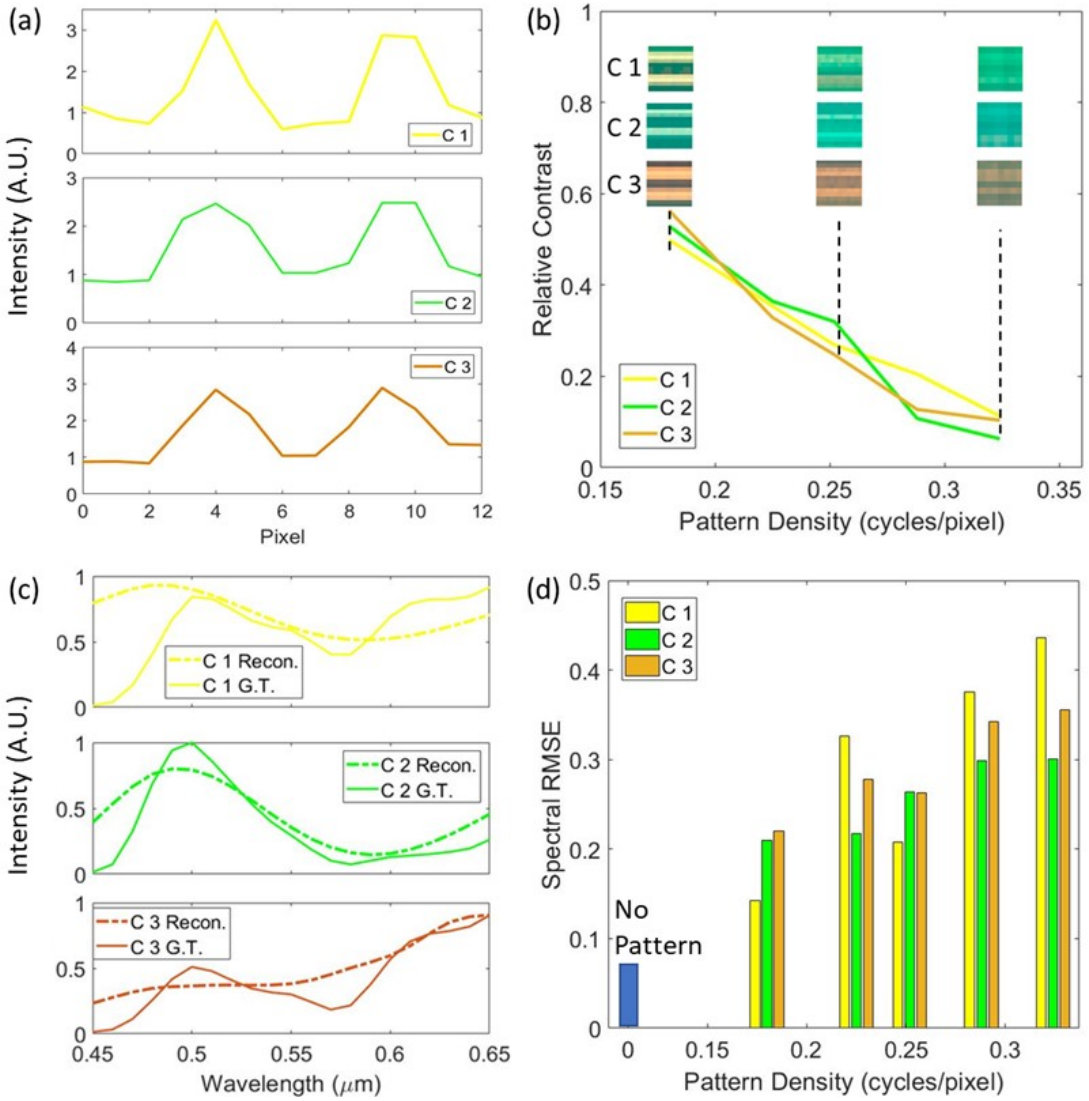

Figure 2.29: (a) Spectral integrated intensities of reconstructed color patterns with 0.18 cycles/pixel density. (b) Relative contrast of reconstructed color patterns as the function of pattern density. Inserted figures are plots of the reconstructed RGB colors of the patterns at 0.18, 0.25 and 0.32 cycles/pixel. (c) Reconstructed spectrum of the color patterns at 0.18 cycles/pixel. (d) RMSE of the reconstructed spectrum of the color patterns, as the function of pattern density.(a) Spectral integrated intensities of reconstructed color patterns with 0.18 cycles/pixel density. (b) Relative contrast of reconstructed color patterns as the function of pattern density. Inserted figures are plots of the reconstructed RGB colors of the patterns at 0.18, 0.25 and 0.32 cycles/pixel. (c) Reconstructed spectrum of the color patterns at 0.18 cycles/pixel. (d) RMSE of the reconstructed spectrum of the color patterns, as the function of pattern density.

de-correlation between the spectrum determine the spectral resolution. In a low-NA system, it means that if the principal basis includes 9 bands, the absolute spatial resolution will be at maximum 3 times smaller than the physical resolution, which is 0.16 cycles per pixel. While in our design, both the reconstructed spectral image maintains the spatial visibility until 0.28 cycles per pixel, while the reconstructed spectrum maintains the spectral features such as peaks and valleys. Our method helps to balance the spatial-spectral resolution for spectral imaging, which does not rely on sub-super pixel lever sensing. Since most of the spatial information locates in the low spectral frequency region, the spatial resolution can be maintained without sacrificing the accuracy in reconstructing the major spectral components. While in conventional spatial - multiplexing - based snapshot spectral imaging methods, the spatial distribution of the low spectral frequency components cannot be resolved at a sub - super - pixel scale due to the different color filters applied on top of each sub-pixel. On the other hand, averaging and interpolation across the super-pixel are applied to reconstruct the sub-pixel level information, which compromises the spatial resolution. Meanwhile, different from the DiffuserCam,[65] the spatial resolution of the Fourier DOE method does not depend on the total area of the sensor array and the number of objects to be recovered. This is because spectral de-aliasing is performed in the Fourier transformed space. When the total image area and the number of objects increase, only the total intensity of the recorded information in the Fourier domain increases, but their relative distribution keeps the same.

In Figure 2.30, we compare our results with previously demonstrated DOE/scatter-based spectral imager and conventional spatial multiplexed spectral imagers. The comparison mainly considers the spatial-spectral resolution in terms of retrievable color channels N_w, spatial resolution ρ (cycles/pixel), and compactness in terms of dispersion volume + filter thickness. The solid line in the plot indicates the condition when the efficiency parameter $\eta = 2\rho \cdot \sqrt{N_w} = 1$. Systems locating above the solid black line are more efficient in terms of utilizing the physical resolutions of the sensor array. Our design can achieve efficient information sampling of the major spectral and spatial components in the Fourier transformed space with a small form factor.

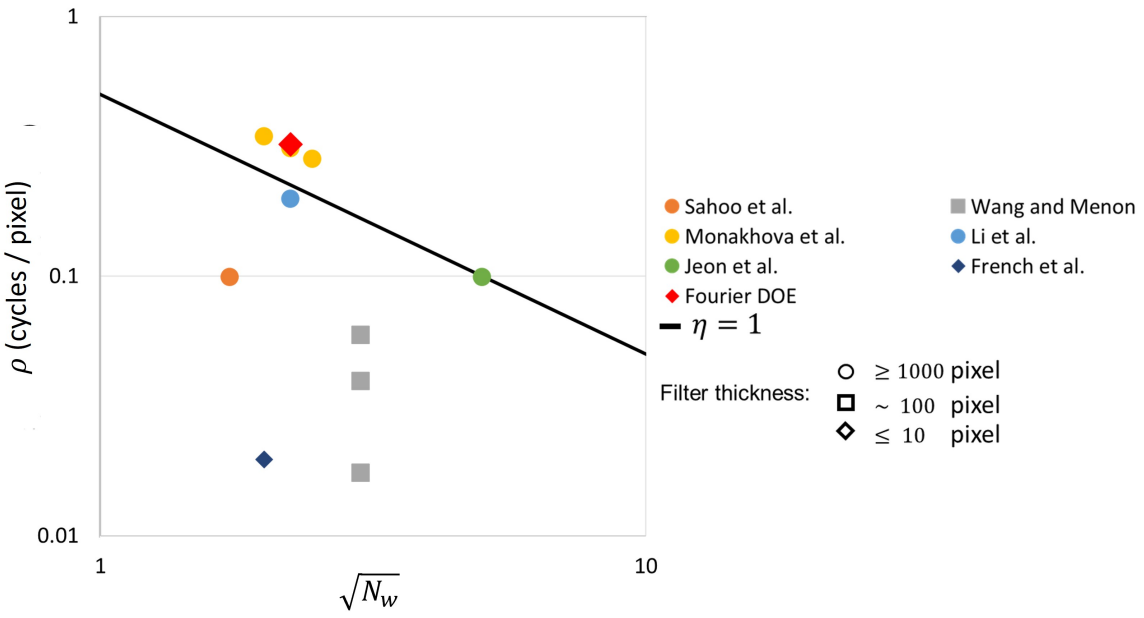

Figure 2.30: Comparison of filter compactness and spatial-spectral resolution between the Fourier DOE design and previous works based on diffractive, scattering, and disordered medium. The shape of the scatter markers indicates the total filter thickness. Solid dash line show the condition when efficiency parameter $\eta = 2\rho \cdot \sqrt{N_w} = 1$.

2.8 numerical methods

2.8.1 Simulation of light diffraction by DOE layer

The numerical simulation of the diffraction pattern generated by the DOE layer is based on the Fresnel transformation method.[18] The DOEs are modeled as square pillar arrays with a size of 3 μm by 3 μm and periodicity of 18 μm in x and y-direction. The simulation has a grid size of $\Delta = 1$ μm. The height profile of the DOE array at position [x, y] can be described as a series of rectangular functions

$$h(x,y) = \sum_m \sum_n h_{m,n} \cdot rect\left(\frac{x - m\Delta}{\Delta}\right) \cdot rect\left(\frac{y - n\Delta}{\Delta}\right) \tag{2.27}$$

where $h_{m,n}$ is the height of the pillar at (m, n) position, within the range from 0 μm to 1.4 μm at 10 steps, based on the experimental calibration results.

The transmission function of light going through the photoresist layers at position

[x, y] is then modeled as

$$T(x,y) = exp(ih(x,y) \cdot (n_{pr} - 1) \cdot k) \tag{2.28}$$

Where n_{pr} is the refractive index of the photoresist material, k is the wavenumber of the light. We ignore the reflections at the DOE/air, DOE/fused Silica, and Fused Silica/air interfaces. Experimental results show that this approximation is acceptable without loss of the spectrum features in the diffraction pattern. The diffracted light field U at position [x', y'] on the image plane with a separation distance of d from the DOE pillar is then modeled with the Fresnel transformation formula

$$\begin{aligned} U(x',y',d) = & \frac{exp(ikd)}{i\lambda d} \int\int g_{illum}(x,y,\lambda) \cdot T(x,y) \cdot \\ & exp(i\frac{k}{2d}[(x-x')^2 + (y-y')^2])dxdy \end{aligned} \tag{2.29}$$

Where $g_{illum}(x, y, \lambda)$ is the on-axis illumination of light with wavelength λ at [x, y] position. Given the height profile, photoresist's refractive index, and illumination distribution, we can simulate the diffraction pattern at the visible range. Based on the analysis, the crosstalk effect is limited to the nearest neighbor of DOE pillars. Therefore, the convolution region cropped to the 3 by 3 DOE pixels in simulation to construct the transmission function.

2.8.2 Binary searching algorithm to improve the diffraction efficiency of Fourier bands

We applied a binary searching algorithm to optimize the transmission efficiency of different Fourier bands onto the spatial modulation spots on the image plane. The DOE design is initialized with randomly generated height profiles ranging from 0 to 1.4 μm at 10 height steps. Then the diffraction pattern on the image plane is evaluated based on the previously described method. From it, we could identify spots where the transmission spectrum mainly contains 2 Fourier band components. It is done by

calculating the Fourier coefficient of the transformed transmission spectrum. If only 1 higher-order Fourier components, e.g k^{th} order, and the 1 order (DC) components have an intensity that is at least 2 times larger than the other Fourier components, the spot is identified as a spatial modulation spot for the k^{th} Fourier order. After evaluation across the whole diffraction pattern, the transmission efficiency of all modulation spots for the k^{th} Fourier order are added up to determine the minimum transmission efficiency to the Fourier orders. Because higher Fourier order requires larger OPD, less area on the image plane will support them, which causes the transmission efficiency to drop as the increase of Fourier order number.

After the initialization, we conducted the binary search starting from the DOE pillar at position [1, 1] to position [6, 6]. In each step, either a positive or negative step height is added to an individual pillar, then the diffraction pattern and transmission efficiency are re-evaluated. If the minimum efficiency is improved, then the design of the DOE will be updated. Otherwise, the searching moves to the next pillar and repeats the process. We conducted the searching over 20 different initialization and searching for 20,000 cycles over the 36 pillars in each initialization to find the optimized design for the highest transmission efficiency.

2.9 Summary

In summary, we designed a Fourier DOE and SML filter for a spectral imaging application. It can efficiently sample the main spatial and spectral information in the Fourier transformed space, thanks to the dispersion of spectral Fourier components by the DOE layer the spectral de-aliasing by the SML. Compared with conventional snapshot spectral imaging techniques, this design does not rely on the spatial-resolved spectral sampling on a sub-super pixel level, which largely compromised the spatial resolution and efficiency of using sensor pixels. We experimentally demonstrated the filter design with DOE fabricated by grayscale lithography and SML fabricated by eBeam lithography. A simple inverse Fourier transform algorithm and a general alternative projection (GAP) algorithm are applied to reconstruct the spectral image. Results

indicate the proposed design can effectively reconstruct the first 5 spectral Fourier bands. Reconstruction results on 54 different broadband color spectra can achieve RMSE of ∼9% after calibration. Meanwhile, the filer is capable to distinguish the peak locations of Gaussian bands with 20 nm $\Delta\lambda$ of the central peak. Spectral imaging was conducted with color images printed on transparency. The GAP algorithm effectively reduced the spatial noise generated due to the artificial spatial frequencies introduced in the simple inverse Fourier transform algorithm. Further, visibility measurement confirms the simulated nearest-neighbor crosstalk between DOE pixels, which helps to improve the absolute spatial resolution of measured monochromic intensity. Spatial-spectral resolution characterization indicates that due to the efficient de-aliasing of main spectral components in the Fourier domain by the DOE filter, we could harness most of the sensor arrays with a balanced spatial and spectral resolution. The device can maintain spatial resolution when imaging with samples of spatial features at up to 0.3 cycles per pixel. Meanwhile, the spectral accuracy in terms of peak preservation and color matching can also be maintained, without dependence on the total number of objects and sensing area. Compared with other designs utilizing DOE or complex optical medium, which relies on the decorrelation of diffraction/scattering patterns at different wavelengths, our design largely improves the spatial-spectral resolution, efficiency of sensor utilization and device compactness. The principle of Fourier spectral imaging with DOE has great potential to be applied with monochromic sensors, with scaled DOE design based on the sensor pixel size, working wavelength and fabrication capabilities.

Chapter 3

Grayscale lithography for flat optics with spatial thickness variation

3.1 Introduction

The push to miniaturize bulky optical elements to go from 3D forms into 2D forms has driven the development of flat optics and metasurfaces [29] for applications in optical filtering and wavefront manipulation [96, 97]. Optical multilayer structures have been applied widely as spectral filters [98, 99, 100, 101] and diffractive elements [102, 103] with a small form factor, in which the thickness variation within the layer structure offers the key customizability. For example, in the 1st Chapter, we demonstrated the Fourier DOEs for spectral imaging, in which the phase modulation is achieved with photoresist micro-pillars arrays with spatially variable thicknesses. Besides, in Fabry-Perot type spectral filters, structures of various layer thicknesses support tunable optical modes, which results in the customizable transmission or reflection. As shown in Figure 3.1(a), pairing arrays of color filters with photo-detectors increasingly draws attention as a promising solution to acquire spatially resolved hyperspectral information in a single snapshot [104]. Metal–dielectric–metal-type optical cavities have been applied widely as reflective or transmissive color filters [105], with high customizability by adjusting the dielectric layer thickness. In both the DOE and multilayer spectral filter, the minimized differences regarding the required physical stack configuration

along with a highly variable spectral function make them a promising candidate for multispectral color filter arrays. However, the major challenge for the application lies in the manufacturing complexity of multilayer structures with different materials and 2D patterning of arrays with spatially variable layer thicknesses responsible for the high spectral customizability.

The conventional method to create thin film patterns with spatial thickness variation usually utilizes patterned photoresists as the shadow mask to define open areas for each material deposition or etching step[106, 107], as shown in Figure 3.1(b). The material thickness generated by each iteration is fixed among all the open areas. By repeated deposition through multiple photoresist hard masks, the pattern of thin films with spatial thickness variation can be created. Notwithstanding the low manufacturing efficiency and hurdles involved with the pattern alignment, lithography, and lift-off, the final number of achievable wavelength bands for color filtering applications is also limited by the number of iteration cycles used [108]. Recently, the grayscale photolithography technique has been applied to overcome the aforementioned obstacles [109, 110, 105]. The development rate of photoresists used for grayscale lithography is sensitive to the exposure dose. As a result, the spatial control of photoresist thickness after development could be achieved by adjusting the dose over the patterning area. Grayscale lithography has been applied to generate Fabry–Perot-type optical stacks by using the resist either directly as the dielectric layer or as the etching mask to transfer the thickness profile onto the underneath dielectric substrate. In the first scenario, despite the improved patterning efficiency and resolution of grayscale lithography, the choice of low-index photoresists limits the design space of optical properties for the dielectric layer, as we discussed in the 1st Chapter. Alternatively, using the grayscale patterned photoresist as etching masks enables a wider choice of materials. However, the need for etching will further increase the manufacturing complexity and cost. While using the photoresist as the optical material itself, as demonstrated in the 1st Chapter, brings limitations to the choice of material and optical index. Therefore, a manufacturing technology that can efficiently generate customizable spatial thickness variation without limited material

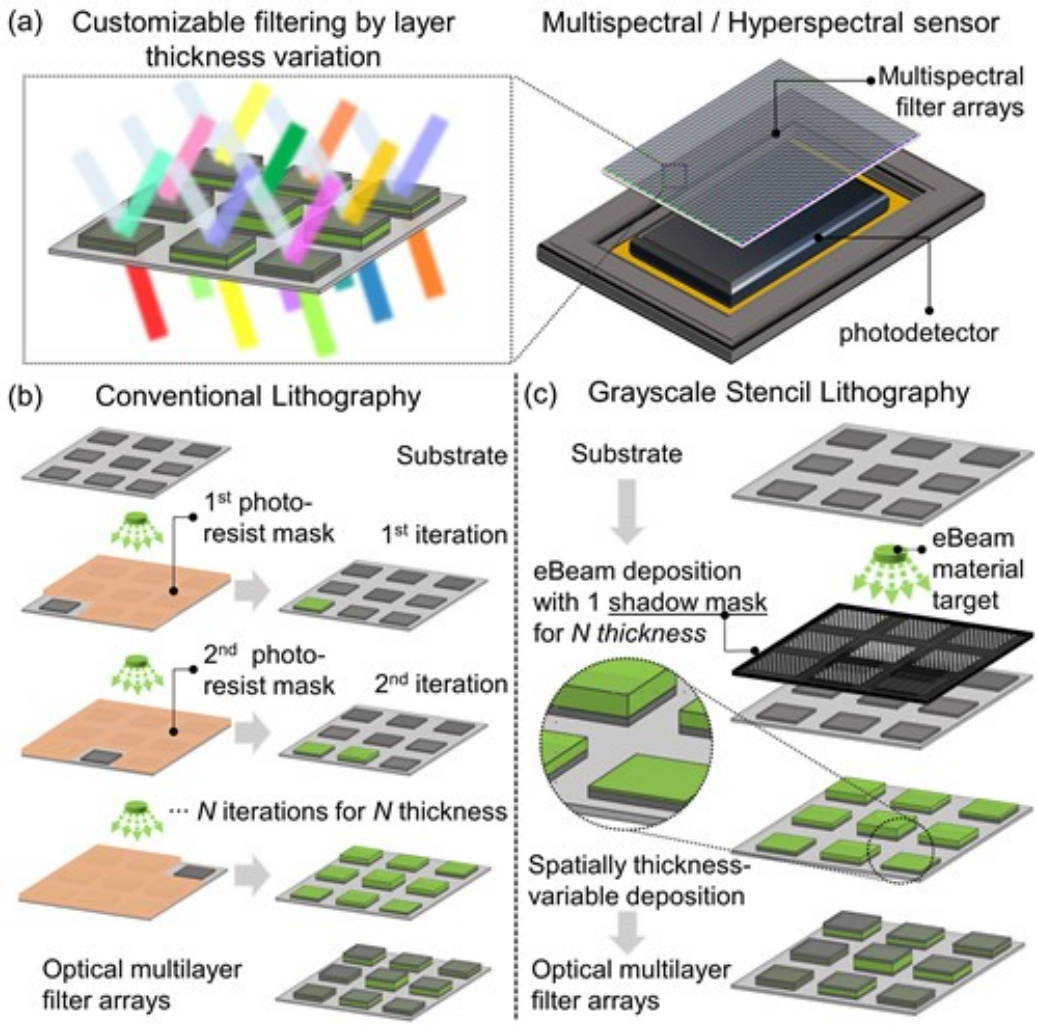

Figure 3.1: (a) Example of optical multilayer structures as customizable filter arrays by spatially varying the middle layer thickness, which can be applied for multispectral or hyperspectral sensing. (b) Schematic of conventional lithography method to generate spatially varying deposition thickness by iterative patterning through multiple photoresist masks. (c) Schematic of the proposed grayscale stencil lithography that can generate patterns of spatially varying deposition thickness with single shadow mask.

choices is needed, which can allow us to find the structural and material design for multispectral color filters with fewer manufacturing requirements and better filtering performance.

In this chapter, we propose grayscale stencil lithography for customizable spatially thickness-variable eBeam material deposition without the iterative patterning process, as shown in Figure3.1(c). Stencil lithography utilizes steady or movable shadow masks, usually made of semiconductors or metals, with apertures defining the open areas for material deposition [111, 112, 113]. The features of resistless-ness and reusability of the stencil shadow mask make it favorable for fabricating micro/nano electro-mechanical systems. In conventional stencil lithography, the transferred deposition pattern has a fixed thickness over the patterns defined directly by the apertures on the shadow mask [111]. We develop a grayscale version of stencil lithography by utilizing the filling ratio of aperture arrays on the customized stencil to define the total amount of deposited materials over certain areas on the substrate. Meanwhile, we design strategies to optimize the point spread function (PSF) of the deposition. Therefore, the materials passing through the shadow mask can be evenly deposited onto the areas defined by the aperture arrays and results in a prescribed spatial thickness profile with a single and reusable shadow mask. This technique allows us to efficiently customize the material stacks for color filtering applications. Even though the current lateral patterning resolution is limited by the commercial stencil used in this work, the size and periodicity of the apertures can approach micro- to nano-meter scale with advanced machining or milling technologies [114, 115], and we foresee great application potentials of the proposed method for micro/nano-scale fabrication.

Further, we demonstrate a proof-of-concept reflective multispectral color filter array with two thickness-variable layers fabricated with grayscale stencil lithography. This offers a broader design space to achieve a wide reflection spectrum on the CIE color space since we are no longer limited to the use of a photoresist as one of the optical layers as in grayscale lithography [109, 110, 105]. This is done by extending conventional stencil lithography from a binary version [111, 112] into a grayscale version so that optically favorable high-index materials can be deposited with arbitrary

thickness across a wafer scale. We also introduce improvements on the material design side, by showing how to extend conventional metal-dielectric-metal stacks [116, 117] into a double cavity or a more advanced stack (as shown later with a Si-containing stack) to capture a large 2D region of the CIE plot with a 2D or even just 1D variation in the stack thickness. We further investigate the dependence of optical performance and reproducibility on the quality control of deposition and materials. The stack designed with a single thickness-variable layer of Si achieves a wide reflective color span with a thinner total thickness and less dependency on the material's deposition quality.

3.2 Grayscale stencil lithography

The grayscale stencil lithography process can be seen as an analogue to optical imaging through arrays of pinhole cameras with finite apertures. The ejection of materials in the eBeam pockets is analogous to the "light" coming from the "source," which passes through the holes on the shadow masks to finally cast the "image" onto the deposition substrate with spatially variable thickness "intensity." We define the thickness distribution of the deposition through an infinitely small hole on the shadow mask as the PSF, which is determined by the depositing strategy described below. The convolution between arrays of apertures with finite size on the shadow mask with the PSF determines the image of customizable 2D patterns of spatial thickness variation. We designed shadow mask patterns using circular apertures on hexagonal arrays and sent them to OSH Stencils for commercial laser cutting onto a 3 mil (76 µm) thick metal stencil. The periodicity and size of the holes determine the spatially customizable filling ratio, which controls the local amount of materials that can be deposited onto the substrate. During deposition, the stencil is mounted onto holders with spacers to create a specific distance between the shadow mask and substrate. To reduce the surface roughness of material deposited through the discrete stencil apertures, we chose a PSF with a Gaussian-shaped distribution and a lateral dimension larger than the periodicity of the apertures on the shadow mask. This is because the

overlap between depositions through adjacent similarly sized apertures will help to homogenize the deposition rate behind this group of apertures. Theoretically, how the materials spread through an infinitely small hole on the shadow mask can be controlled by the shape factor of the source, so that the Gaussian-shaped PSF and the deposition with spatial thickness variation can be achieved within a single step. This can be done by customizing the angular profile of material ejected from the eBeam pockets. Williams and others demonstrated an attempt of this manner to fabricate layered structures with linear thickness variation along only a single spatial direction [118] using rather a complex deposition instrumentation, which is not feasible for most common eBeam evaporators. Due to the limitation on continuously adjusting the material ejection profile, we need to divide the deposition into multiple steps with the substrate tilted at specific angles while rotating the substrate along with the deposition. The combination of circular PSFs defined by each step results in the digitized Gaussian-shaped PSF, in which the PSFs of individual steps is just adjoining. Finally, by performing a convolution between the PSF and the shadow mask, we can predict the 2D spatial variation of the resultant patterned deposition. The numerical simulation of deposition results was performed as follows:

3.2.1 A. Constructing point spread function of deposition

The point spread function (PSF) of each deposition step is the function of deposition time T, substrate tilting angle θ, deposition rate $R = 1$, mask-substrate distance D_{ms}, source-substrate distance D_{ss}=52 cm and material source diameter d_m=15 mm. Deposition at tilted angle will result in annular-shape PSF. The inner and outer radius of the PSF are:

$$r_{in} = D_{ms}tan(\theta) - \frac{1}{2}d_m\frac{D_{ms}}{D_{ss}}cos(\theta) \tag{3.1}$$

$$r_{out} = D_{ms}tan(\theta) + \frac{1}{2}d_m\frac{D_{ms}}{D_{ss}}cos(\theta) \tag{3.2}$$

The total amount of materials deposited inside the annular area is: T×R=T,

which results in the thickness surface density ρ of:

$$\rho = \frac{T}{\pi(r_{our}^2 - r_{in}^2)} \tag{3.3}$$

For deposition at normal incident without tilting, the PSF is circular shape with radius of $r = \frac{1}{2} d_m \frac{D_{ms}}{D_{ss}}$ and thickness surface density of $\rho = T/(\pi r^2)$,The PSF of the single step is then defined by the annular shape with area density $PSF(r_{in}, r_{out}, \rho)$. The total PSF is obtained by combining the PSF of each step.$PSF_{combined} = \sum PSF$.

3.2.2 Convolution between PSF and shadow mask

The shadow masks are defined as 2D binary matrix M, in which 1 represents the open areas that allow material passing through while 0 represents the masked areas. The deposition result H, i.e. spatial distribution of deposition thickness, is then calculated by a convolution between the $PSF_{combined}$ with M.

$$H = PSF_{combined} \otimes M \tag{3.4}$$

Following the model, Figure 3.2(a) shows one specific strategy of a four-step deposition with substrates tilted at θ= 0°, 1.7°, 3.3°, and 5.0°, and deposition times T of 2.7, 14.8, 15.6, and 8.9 (arbitrary unit) at some constant deposition rate. The PSF of an individual step and combined PSF were simulated based on our eBeam evaporator equipment, where the simulation parameters include material source diameter (15 mm), source–substrate distance (52 cm), and mask–substrate distance (10 mm), which results in the Gaussian-shaped PSF with lateral dimension D of 1.01 mm. The convolution between the combined PSF and a shadow mask with apertures of various filling ratios arranged in a 3×3 block array results in the deposition of block patterns with spatial thickness variation. As shown in Figure 3.2(b), simulations with filling ratios ranging from 0% to 50% show that the deposition thickness is linearly proportional to the filling ratio, while the arithmetic average surface roughness (R_a) at each filling ratio is small. In the simulated range, the maximum R_a of the strategy is 0.22 (A.U.) at a filling ratio of 36.4% with a targeted deposition thickness of 16.1 (A.U.).

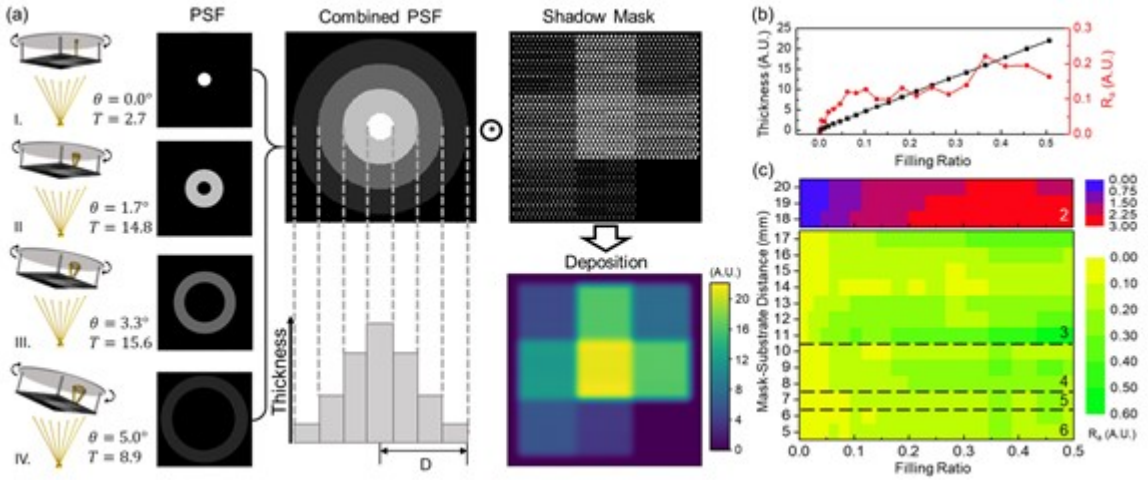

Figure 3.2: (a) The deposition process used combines four substrate tilting angles and deposition time, each of which gives a different PSF of the deposited material. Examples of how the PSF arises is shown for one point in the dot-raster shadow mask. The combined PSF results in the digitized Gaussian-shaped PSF designed to have a span D larger than the periodicity of apertures on the stencil shadow mask. The convolution between the combined PSF and the shadow mask is the predicted deposition thickness. (b) Simulated deposition thickness and surface roughness (Ra) as functions of stencil's filling ratio, following the procedures shown in (a). (c) Simulated Ra at fixed deposition dose of 42 (arbitrary unit) and various filling ratios and mask–substrate distances. The numbers denote the minimum required deposition steps to achieve a combined PSF with lateral dimension larger than 0.75 mm.

We can foresee that a sub-2 nm Ra can be achieved in deposition thicknesses ranging from 0 to 150 nm for color filter applications described in the following sections.

A sufficiently wide combined PSF is required to reduce the deposition surface roughness caused by the unevenly overlapped material flux through adjacent apertures on the shadow mask. Since we cannot continuously customize the material ejection profile from the eBeam pocket in our equipment, we must discretize the analog PSF into multiple deposition steps to achieve the digitized Gaussian PSF shown in Figure 3.2(a). The trade-off between the fabrication complexity, i.e., a number of deposition steps, and the surface roughness is discussed in Figure 3.2(c). The number of required deposition steps is defined as the minimum steps needed to have the lateral dimension D of the combined PSF larger than the periodicity of the apertures on the shadow mask (0.75 mm). Since the source–substrate distance is practically fixed in a deposition chamber, the required number of deposition steps is the function of the only mask–substrate distance. In Figure 3.2(c), we plot the Ra of deposition with various filling ratios and mask–substrate distances, with a fixed total amount of deposition dose of 42 (A.U.). The numbers on the plot indicate the required deposition steps. With increasing mask–substrate distance, the number of required deposition steps decreases since the contributing width of the circular PSF from each deposition step expands. For mask–substrate distance ranging from 5 to 17 mm, the surface roughness is small, as shown in the bottom panel of Figure 3.2(c). However, when increasing the mask–substrate distance to beyond 17 mm, the surface roughness increases dramatically because the two-level digitized PSF then deviates a lot from the perfect Gaussian-like profile required to homogenize the deposition profile beyond the shadow mask. The maximum Ra can be as large as 20 nm for a targeted deposition thickness of 150 nm. For actual depositions demonstrated in the following sections, the mask–substrate distance is chosen to be 10 mm to balance the fabrication complexity, control accuracy of tilting angles (about 0.1°), and surface roughness. A more precisely controlled deposition, e.g., PSF with a hexagonal lateral shape, can help to further minimize the surface roughness. However, it requires computer-numerical control of the substrate rotation motor and the deposition tilting angle, which are

beyond the customizability of the eBeam evaporator we used. Besides, other treatments including substrate temperature control can further reduce surface roughness caused by island effects or surface diffusion, which are neglected in our modeling.

Further, we would like to mention that this strategy can be applied to material deposition methods other than eBeam evaporation, e.g. physical vapor deposition, as long as the material's flux travels in straight lines. However, the effects of the target source shape factor in different deposition methods need to be considered when modeling the PSF. The sharp emission point in the eBeam evaporator simplifies our modeling.

3.3 Patterning multi-spectral color filter array

3.3.1 Two-variable-layer multi-spectral color filter arrays

The grayscale stencil lithography method allows material deposition of customizable 2D patterns with spatial thickness variation. In the following section, we apply the method to fabricate multispectral reflective color filter arrays with two layers of variable thicknesses to achieve a broad span of the color spectrum. The configuration of the multilayer stack structure is shown in Figure 3.3(a), which contains TiO_2/Pt/TiO_2/Ag on Si substrate. The thickness of Pt and Ag layers are fixed at 15 nm and 40 nm, separately, whereas the thicknesses of the top and bottom TiO_2 layers vary from 0 to 150 nm. The stack structure acts as a lossy double optical cavity. The Ag bottom reflection layer is thick enough to prevent light penetration into the Si substrate. Light is absorbed mainly by the middle Pt layer.

Different configurations of the top and bottom TiO_2 layer thicknesses result in the variation of the spectral absorption profile by the Pt layer across the visible range to give rise to multispectral reflective colors. As shown in Figure2.3(b), the achievable colors are simulated by solving the reflection spectrum of the stack structure with variable top and bottom TiO_2 layers at a step of 2 nm. The cross marks on the plot denote the layer configurations of the closest color matching with the representative

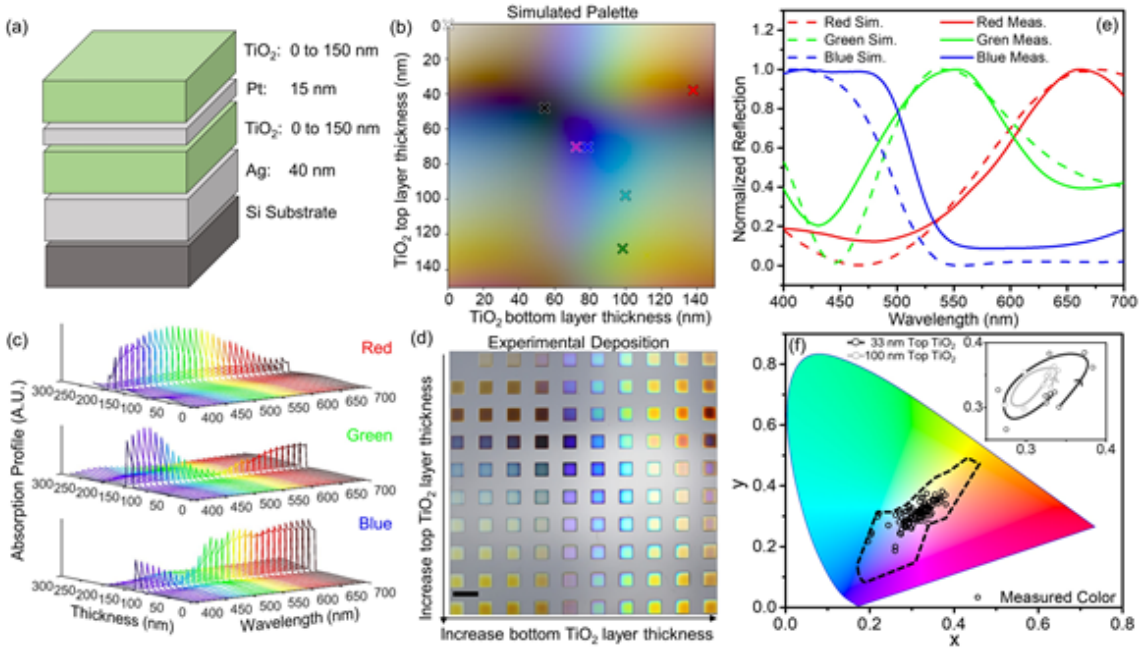

Figure 3.3: (a) Schematic of the multilayer stack structure of TiO_2/Pt/TiO_2/Ag on Si substrate. The top and bottom TiO_2 layers have variable thicknesses from 0 to 150 nm. (b) Simulated reflective colors of the stack structure by varying the top and bottom TiO_2 layer thicknesses, under illuminant D65. The cross marks denote the closest matching with representative colors of red, green, blue, cyan, magenta, yellow, black, and white. (c) Simulated spectral absorption profiles in the stack structures with configurations matching with red, green, and blue colors. The thicknesses of bottom and top TiO_2 layers (t_b, t_t) are (138 nm, 36 nm), (78 nm, 70 nm), and (98 nm, 128 nm), separately. (d) Experimental deposition results of stacks with block patterns of variable reflective colors. The scale bar is 2 cm. (e) Comparison between experimental and simulated reflection spectra of stacks with targeted bottom and top TiO_2 layer thicknesses of (133 nm, 33 nm), (100 nm, 133 nm), and (83 nm, 66 nm), corresponding to red, green, and blue curves, separately. (f) Reflective color span on the CIE plot. The closed black dashed line shows the simulated envelope of achievable color span by the stack structure. The open circular dots show the measured reflective colors on the 10×10 blocks in (d). The inserted plot shows the zoom-in color trajectories of stacks with 33 nm and 100 nm top TiO_2 layers, while the spline curves with arrows show the direction of bottom TiO_2 layer increment.

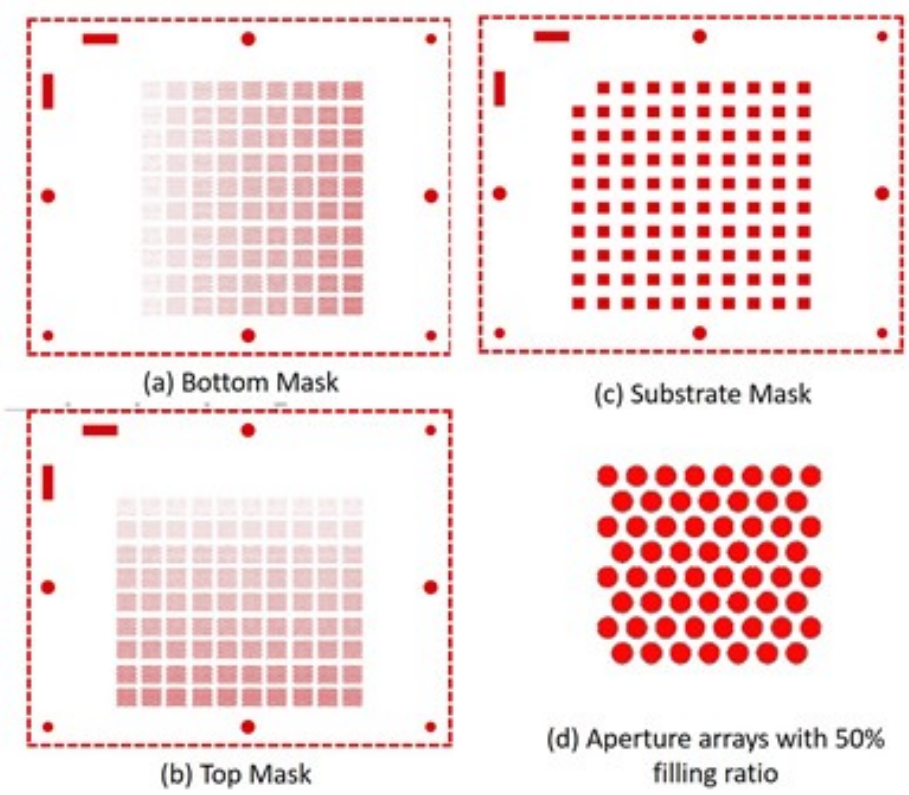

Figure 3.4: Design of stencil shadow masks used for 10-by-10 block deposition. (a) Mask for bottom TiO_2 layer. (b) Mask for top TiO_2 layer. (c) Additional masks are placed on the substrate to define deposition areas. The size of all shadow masks is 87cm by 110 cm. (d) Zoom-in plot of a circular aperture array to define the filling ratio.

colors of red, green, blue, cyan, magenta, yellow, black, and white. In Figure2.3(c), the spatial distribution of absorbed spectral energy inside the stack structure, i.e., spectral absorption profile, of configurations matching with the red, green, and blue colors is plotted. The thickness axis denotes the position inside the stack, from bottom to top. The high absorption region locates in the middle Pt layer. By varying the top and bottom TiO_2 layer thicknesses, the electric field distribution in the stack is altered, resulting in the variation of the spectral absorption profile. Different from conventional lossless Fabry–Perot cavities in which destructive interference causes color filtering, the reflected color here is determined by the spectrum of the least absorbed wavelengths by the middle thin metal layer.

The designed multispectral reflective filter array is fabricated with the grayscale

stencil lithography method. The deposition follows the same steps and angles as in Section 2 and Figure 3.2. Stencil shadow masks for depositing the top and bottom TiO_2 layers are designed with 10 by 10 blocks of varying aperture filling ratios linearly spanning from 0% to 50%. A bottom mask with block holes is placed on top of the substrate through the process to confine the deposition in the areas defined by the blocks. The design of shadow masks n is shown in Figure 3.3. The open apertures are shown as red areas on the figure. The circular and rectangular large openings near the edge of each mask were used as cutting guidance and mounting holes to fix the mask onto the deposition stage. There are totally 3 shadow masks used in the deposition, including (a) Mask for bottom TiO_2 layer (b) Mask for top TiO_2 layer, and (c) An additional mask placed directly on top of the substrate the define the block deposition areas. The filling ratio of open areas on the top and bottom masks are designed to vary from 0 to 50% in 10 steps along with x and y directions, as shown in Figure 3.3. Figure 3.3(d) shows an example of the circular arrays in one of the block areas to define the filling ratio of 50%. The periodicity of the hexagonal circular array is 0.75 mm. The design of shadow masks was manufactured with stainless-steel PCB stencils by OSH Stencils, with 0.001" fabrication tolerance. The fabricated stencils are shown in Figure 3.4.

The stencil shadow mask is fixed together with the deposition substrate on a custom deposition stage, as shown in Figure 3.6. The top and bottom TiO_2 shadow masks were clamped by steel frames to prevent warping during deposition. Aluminum spacers from McMaster Inc. were used to control the mask-substrate distance to 10 mm. When doing eBeam deposition, the substrate stage is attached to the rotation head in the eBeam chamber with magnetic contact, while the substrate and masks face the material source. The depositions were conducted with AJA ATC-E eBeam evaporator with Glancing Angle Deposition Substrate Holder at MIT.Nano. The accuracy of manually controlled stage tilting angle is 0.1°. Ag, Pt, TiO_2, Au, Ti, Si, and Al material target from AJA Inc. were used for deposition. The deposition rate for all materials is fixed at 2 Å/s. The stage rotation speed is fixed at 50 rounds per minute for all depositions. Depositions were conducted with the chamber under a

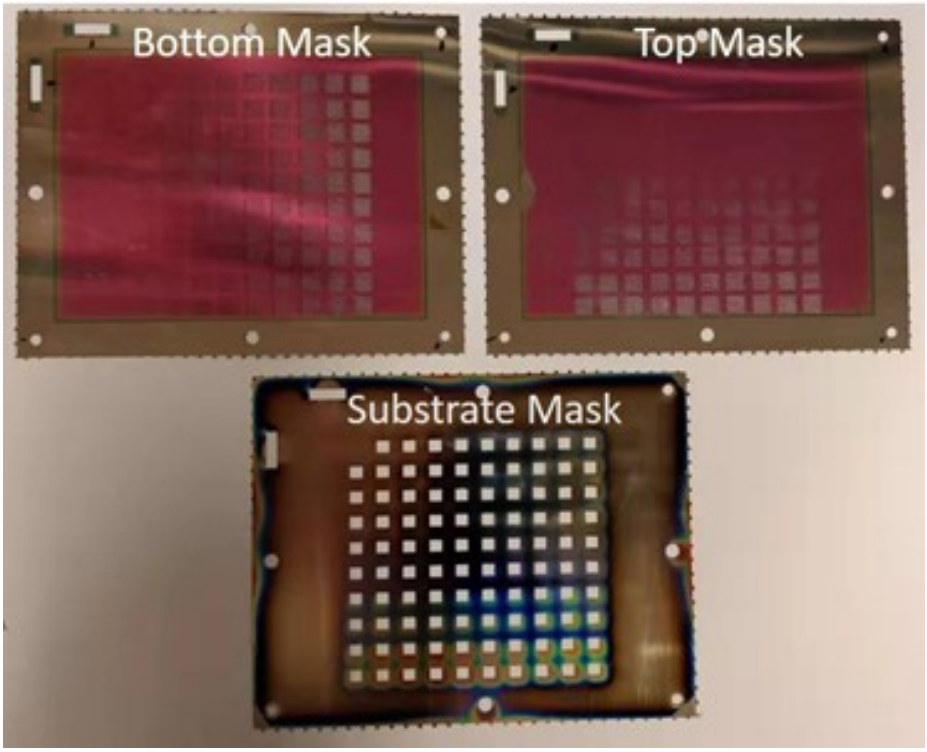

Figure 3.5: Manufactured stainless-steel stencils. The colors on the stencils are resulting from deposition.

high vacuum level above 1×10^{-6} torr. When depositing TiO_2, the substrate is back sputtered with O_2 to improve the oxygen content. Before and after the deposition of layers with spatially variable thickness, the stencil shadow mask was added and removed from the deposition stage. For deposition of other layers, no shadow mask was used.

During the deposition, we only need to use each of the two stencil shadow masks once for each of the two TiO_2 layers. Compared with the conventional lithography-and-lift-off process [119, 107, 106], which needs N times of iterative lithography and deposition with different photoresist patterns to generate N different thicknesses, our grayscale stencil lithography method significantly reduces the fabrication complexity. The deposition result is shown in Figure 3.3(d), with arrows indicating the directions of linearly increasing top and bottom TiO_2 layer thicknesses. A white LED light source is illuminated onto the sample and generates vivid colors properly reproducing the simulation predictions in Figure 3.3(b). Currently, the spatial resolution of

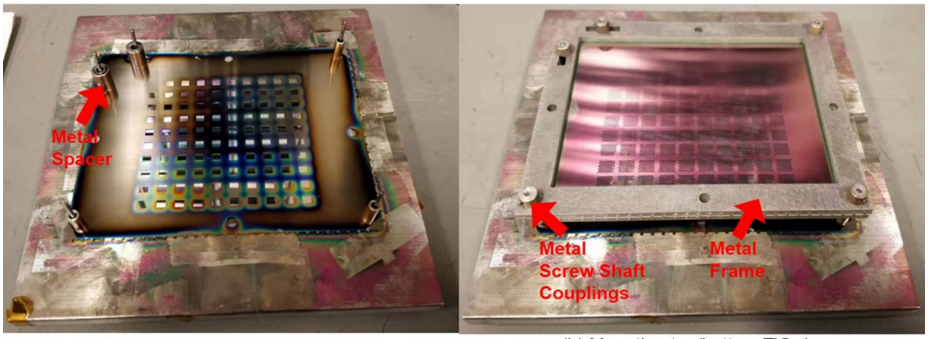

(a) Mounting substrate shadow mask and metal spacers

(b) Mounting top/bottom TiO_2 layer stencil shadow mask with metal frames

Figure 3.6: (a) Mounting substrate mask and metal spacer on top of Si substrate on the custom deposition stage. (b) Mounting top/bottom TiO_2layer mask with metal frames on to the custom deposition stage.

the color patches deposited by this method is limited by the stencil resolution since the material flux must be deliberately expanded and overlapped to uniformly cover the block region behind apertures. The resolution limit of deposited features is determined by the size of these regions, which is in turn determined by the aperture spacing on the stencil. Further advancements in stencil manufacturing and deposition control will improve the fabrication resolution.

Due to the limitation on the manual substrate angle controlling the eBeam evaporator we used, the angle accuracy is about 0.1°. Given the pre-determined deposition steps and angles, the accuracy of substrate angle control will affect the outcome, especially the surface roughness. To investigate the effects of angle control error on the deposition thickness and reflective color, we conducted the following simulation analysis. Following the steps and angles for depositions with the mask-substrate distance of 10 mm as described in Section 2 and Figure 3.2, we simulate deposition of 150 nm and 30 nm thicknesses through the stencils shadow mask with 50% and 10% filling ratio. We introduce random error to the actual angle of each step. The real deposition angle $\theta_{real} = \theta_{target} + rand \cdot w$, where θ_{target} is the target angle of the step, $rand$ is a random number in (-1°,1°), w is the error weight representing the significance of the error. We calculated the mean deposition thickness and surface roughness (R_a) as the function of the error weight. The averaged values of 100 different realizations for each error weight are shown in Figure 3.7. Since the filling ratio of stencil determines the

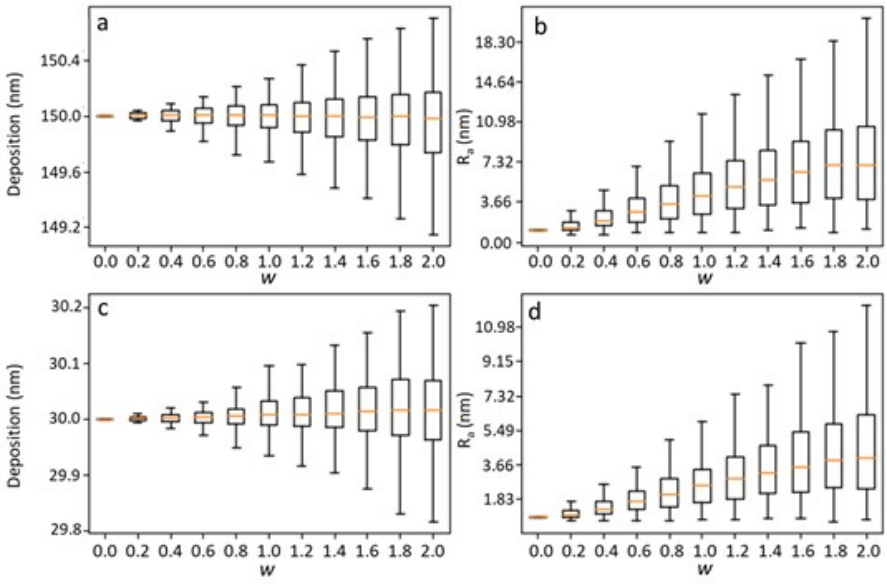

Figure 3.7: (a-d) Mean deposition thickness and surface roughness R_a for targeted thickness of 150 nm (a, b) and 30 nm (c, d), as the function of error weight w. For each error weight, the averaged values are taken over 100 different realizations of deposition angles.

actual amount of materials depositing onto the substrate, the error in angle control does not affect the mean deposition thickness significantly, as shown in Figure 3.7(a) and (c). However, the surface roughness increases as the angle error weight increases, which will affect the color uniformity of the actual deposition. As shown in Figure 3.7 (b) and (d), the maximum Ra under certain angle realization can be higher than 10 nm, which can significantly affect the thin-film interference.

Correspondingly, we simulated the actual colors of depositions with angle errors, through the stencils originally designed for the best-matched red, green, and blue colors. The results with certain angle errors are shown in Figure 3.8. As expected, as the error weight increases, the color uniformity decreases. Interestingly, due to the sensitivities of different colors to the variation in the double TiO_2layer thickness are different, the color uniformity among the red, green, and blue blocks are different. For example, the green color block shows less sensitivity to the surface roughness, due to the relatively large span of green on the pallet in Figure 3(b). On the other hand, the red and blue blocks show larger sensitivity to the surface roughness. Meanwhile,

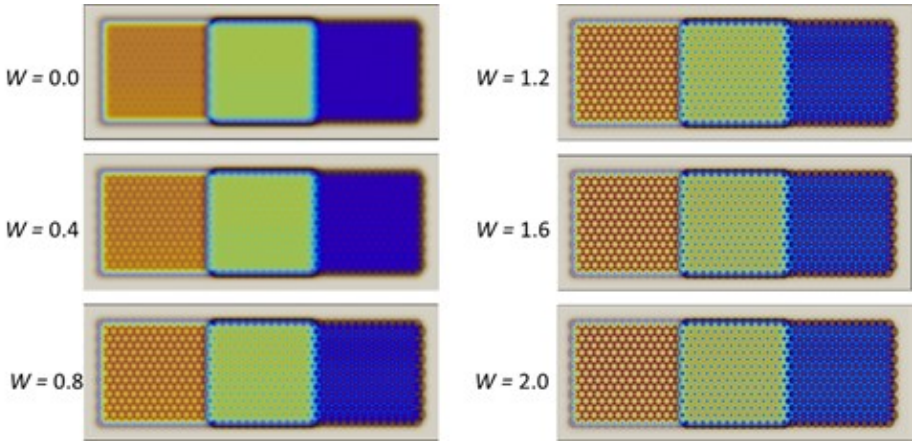

Figure 3.8: (a-d) Simulated the actual colors of depositions with certain angle errors, through the stencils designs for the best-matched red, green, and blue colors on the pallet in Figure 3.3(b). Each of the color blocks is 10 mm by 10 mm. The angular errors used in this simulation are exaggerated with respect to the 0.1° precision of our stage tilt control. The w=0.4 case models a situation where the angle of deposition can only be set with a 0.4° precision

due to the hexagonal periodic pattern of the stencil, the color non-uniformity also shows a hexagonal periodicity. These results imply the importance of angle control in grayscale stencil lithography.

Simulated and measured reflection spectra of configurations matching with red, green, and blue reflective colors in real depositions are shown in Figure 3.3(e). Different from the conventional metal-dielectric-metal structure with single and sharp light absorption peaks [99, 120], the double cavity with two variable high-index dielectric layers generates multiple spectral absorption peaks with relatively wide bandwidth in the visible range [121], which expands the span of the reflective color spectrum. The simulated envelope of reflective colors achieved with the current stack configuration is shown as the dashed line in Figure 3.3(f). We can see that the current design has better color coverage for red and blue compared to green, which is due mainly to the wide bandwidth of reflection peaks located in the green region. The thickness of the middle metal layer plays a crucial role in determining the color span [99], which will be discussed in later sections. The measured colors on the fabricated sample are shown as the circular dots located inside the envelope in Figure 3.3(f). Due to the finite number of top and bottom TiO_2 layer thickness combinations, the

measured colors are a discrete sampling within the area inside the envelopes. The inserted zoom-in plot shows the color trace on the CIE chart of stacks with 33 and 100 nm top TiO_2 layers. The spine curves and arrows show the evolution of reflective colors with increasing the bottom TiO_2 layer from 0 to 150 nm. Even though the color trajectories are similar, the stack with the 100 nm top TiO_2 layer has a wider reflection bandwidth, which causes the trajectory to be closer to the white center. Meanwhile, we would like to point out that the design of this stack is not optimized regarding color space coverage due to our limited searching in materials and structural parameters. Another design with improved CIE coverage but more complex material combinations will be shown in the following section.

3.3.2 Arbitrary 2D patterning

Furthermore, we demonstrate that the grayscale stencil lithography method can be applied to deposit arbitrary 2D patterns. As shown in Figure 3.9, an "MIT Dome" pattern on silicon substrate was deposited following the same aforementioned stack configuration. The stencil shadow masks to deposit the top and bottom TiO_2 layers are shown in Figure 3.9 (a) and (b). The simulated deposition thickness is shown in Figure. .8 (c) and (d). The final deposition result is shown in Figure 3.9 (e). It is obvious that there is an irregular non-uniform color mismatch on the pattern, which may be caused by issues related to the degradation of TiO_2's refractive index due to oxygen deficiency [122, 123] and non-uniform deposition thickness across the wafer substrate. More details will be discussed in the following sections. Besides the material imperfection, the flux spreading at the boundaries between different color regions can also cause thickness and color variations at the boundaries between different color regions. Therefore, the color variation observed in Figure 3.9(e) near the edge of the two large color "blocks" can originate from two other sources. (1) The algorithm to create the stencil pattern. In this algorithm, due to the finite resolution of the stencil, discretized feature sampling is conducted at the boundary between different "blocks", which caused the fine features of distinct apertures sizes near the boundary, as shown in Figure 4(a) and (b). The deposition thickness at these locations

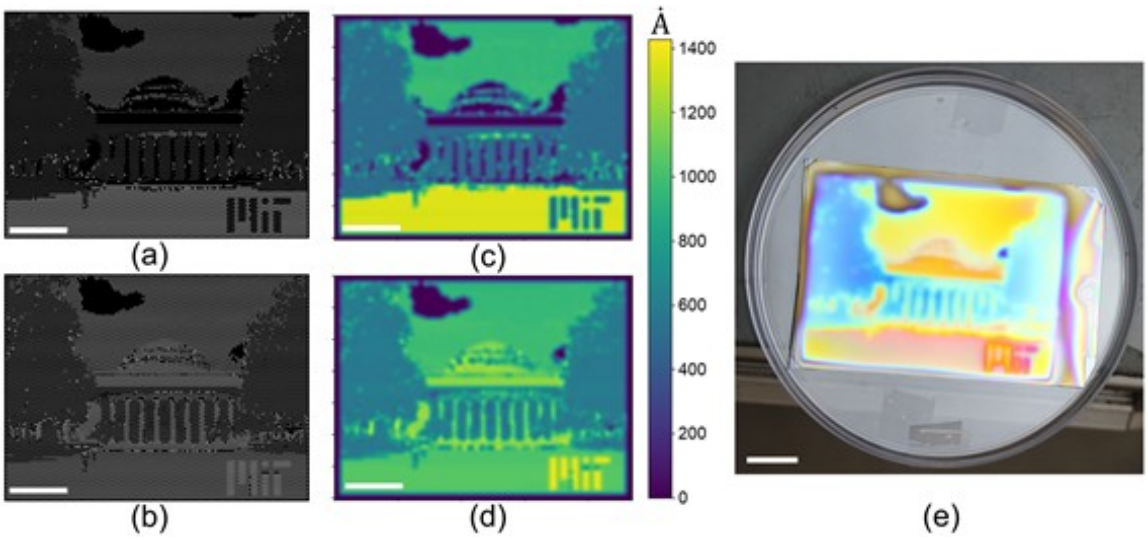

Figure 3.9: (a), (b) Schematic of masks used for top and bottom TiO_2 layer depositions of the "MIT Dome" pattern. (c), (d) Simulated deposition thickness with spatial thickness variation following the strategy in Figure 3.2(a). (e) Deposition results on Si substrate cut from 152.4 mm wafer. All scale bars are 2 cm.

will cause color variation. (2) Due to the deposition strategy, we introduced in Section 2 and Figure 3.2, the finite lateral size of the PSF and the material flux spreading at the boundary of a "block" will cause the thickness variation and an "outline" around the "block" as shown in Figure 3.9 (c) and(d).

3.3.3 Analysis of color mismatch

The first source of the edge color variation can be compensated by further developing the color matching and stencil pattern converting algorithm. While the second source can be compensated by improving the stencil resolution and edge aperture design. Here we show how the flux spreading at the boundary affects the deposition thickness to illustrate this origin of edge color variation. For example, we follow the same deposition steps described in Section 2 and Figure 3.2, with a mask-substrate distance of 10 mm, to deposit two adjoined regions with tar-get deposition thickness of 150 nm and 30 nm through stencils with a filling ratio of 50% and 10%, separately. We calculate the thickness profile at the boundary between the two regions, as shown in Figure 3.10. Due to the flux spreading at the boundary, the thickness at the

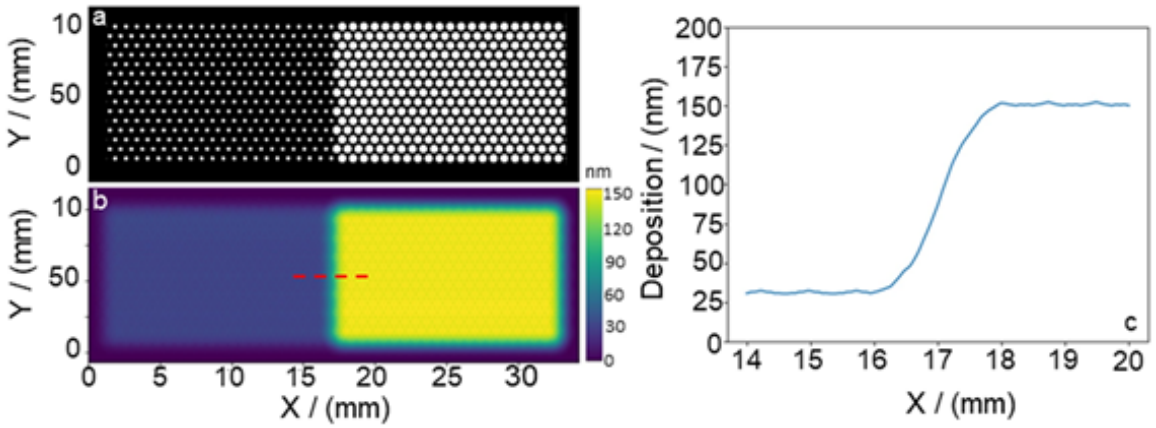

Figure 3.10: (a). Stencil pattern with two blocks of aperture filling ratio of 0.1 and 0.5. (b). Simulated deposition through the stencil mask in (a), following the same steps and angles in Section2 of the main text. The target thickness for the two regions is 30 nm and 50 nm separately. (c). Simulated thickness profile along the red dash line in (b) across the block boundary.

boundary deviates from the targeted deposition thickness at the central area of the blocks, which results in color variation. The boundary spread size is on the level of 1.5 mm in this case. The larger the pinhole size, the larger the flux spreading size. Therefore, regions with larger target thickness may have a thicker "outline" around the blocks, as shown near the boundary of the bottom region in Figure 3.4(c) and (e). Even though this variation exists in the current version of stencil design, it could be compensated by improving the stencil resolution and properly designing the filling ratios and aperture patterns near the boundary, which calls for further optimization.

To investigate the relationship between the reflective color span and the thickness of the middle Pt layer, we compared the numerical simulation of the reflection spectrum and color palettes of stacks with middle Pt layers of 5, 15, and 30 nm, as shown in Figure 3.11 (a). When reducing the Pt layer thickness to 5 nm, the absorption by the metal layer decreases, which causes the shrinkage of the color span as noted by the dashed envelope on the CIE chart. Meanwhile, with the 5 nm Pt layer, the stack structure approaches the configuration with only TiO_2 and Ag layers. As a result, the inserted palette plot shows less dependence on the individual top and bottom TiO_2 layer thicknesses, but stronger dependence on the summation of two TiO_2 layer thicknesses. On the other hand, increasing the Pt layer thickness increases the reflec-

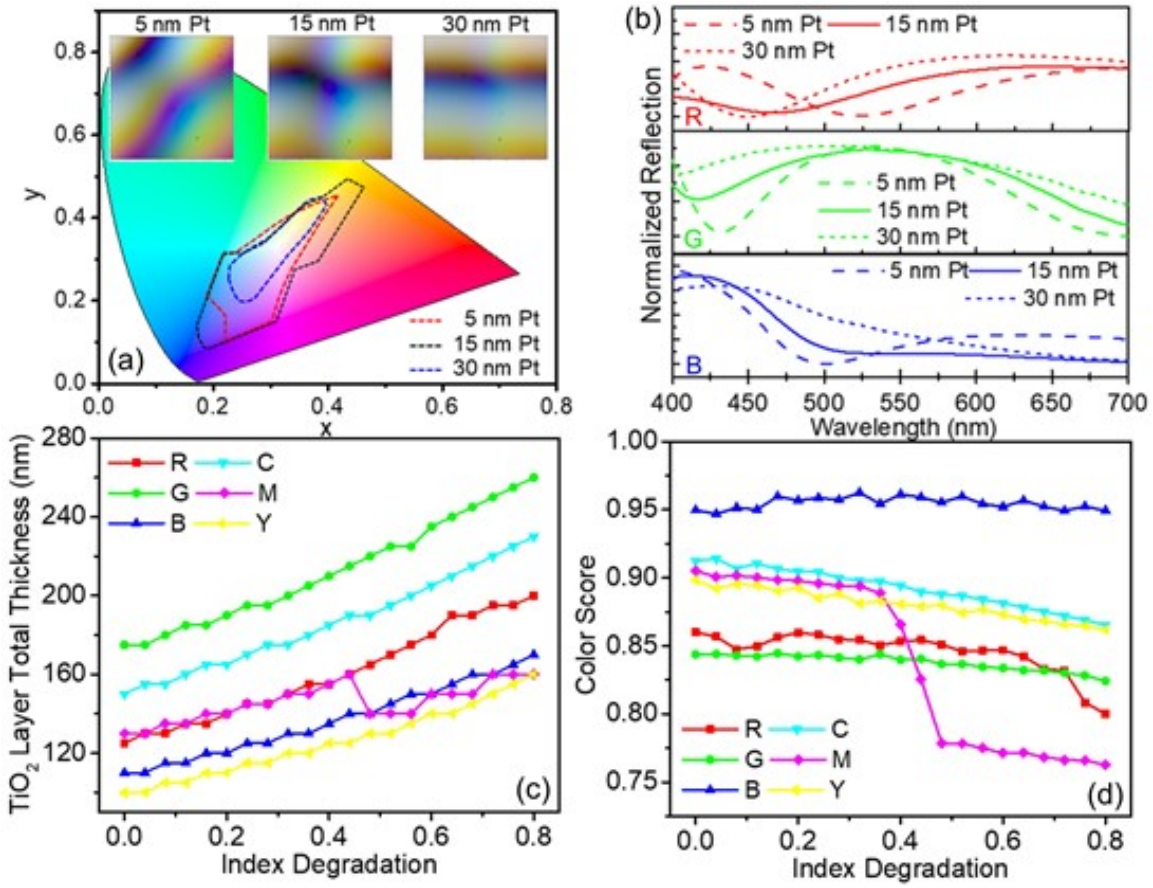

Figure 3.11: (a) Color span and tunability of stacks with middle Pt layers of 5 nm, 15 nm, and 30 nm. The dashed lines in the CIE chart denote the simulated envelope of achievable reflective colors by the stack. The inserted plots show the simulated palettes of stacks with various Pt layer thicknesses, which follow the same coordinates in Figure 3.3(b). (b) Simulated reflection spectra of stacks with various Pt thicknesses. The bottom and top TiO_2 layer thicknesses are (138 nm, 36 nm), (98 nm, 128 nm), and (78 nm, 70 nm), separately, corresponding to the best matching with red, green, and blue colors with 15 nm Pt layer. (c) The required total thickness of TiO_2 layers for matching the six representative colors, as the function of index degradation in TiO_2. (d) Evaluation of color matching scores for the six representative colors, as the function of index degradation in TiO_2.

tion by the Pt layer, and reduces the amount of light that can be coupled into the bottom TiO_2 layer. Therefore, the achievable color spectrum shrinks significantly to the white center on the CIE chart; meanwhile, the palette shows less sensitivity to the bottom TiO_2 layer thickness. Figure 3.11(b) shows the simulated reflection spectrum of stack configurations with 5, 15, and 30 nm Pt layers. When the middle Pt layer is 15 nm, the three configurations correspond to the closest matches with red, green, and blue colors. Similar to a simple metal-dielectric-metal structure, increasing the Pt layer thickness enhances the light confinement in the Pt/bottom TiO_2/Ag layers and sharpens the spectral absorption profile. Along with the effects of complex round-trip phase shifting in the Pt and TiO_2 layers, increasing the Pt layer thickness causes the shifting and broadening of the reflection spectrum. In summary, the middle Pt layer thickness determines the trade-off between the light that can be coupled into the Pt/bottom TiO_2/Ag layers and the amount of light that can be absorbed by the Pt layer. It further determines the achievable reflective color span and the sensitivity against adjusting the top and bottom TiO_2 layers. Based on the consideration, we chose 15 nm as the Pt layer thickness for the previous sample deposition.

Another crucial parameter that affects the reflective color is the complex refractive index of the materials in the multilayer structure. Ag and Pt are relatively stable through the eBeam deposition process. However, the refractive index of TiO_2 is very sensitive to the oxygen content and deposition condition. Oxygen deficiency can cause a lower n of TiO_2.

We measured the materials' refractive index with XLS-100 spectroscopic ellipsometer from J.A.Woollam Inc at Institute for Soldier Technologies, MIT. The reflection spectrum of deposited samples was measured with a USB-2000 UV-Vis spectrometer from Ocean Optics, coupled with a Microscope from AmScope. The100% reflection was calibrated with protected silver mirrors from Thorlabs, Inc. The conversions between reflection spectrum to sRGB and XYZ colors are based on the formulations of CIE color-matching functions under illuminant D65. The reflection spectrum, electric field distribution, and spectral absorption profiles in the stack structures were solved with Lumerical FDTD solutions, [124]. Optical properties of

Ag [125], Pt [126], Al [126], Si [127], Au [125] and Ti [128] used in the simulation were obtained from the literature. The simulated reflective color was again converted with the CIE color matching function under illuminant D65. The evaluation of matching between simulated-color and reference colors was done based on the Delta 1994 color difference standards.

Figure 3.12 shows the measured n of TiO_2depositedunder different conditions. Back sputtering O_2during eBeam evaporation can help to improve the oxygen content in the deposited layer and increase the refractive index. However, the measured n is still about 0.6 lower than the ordinary TiO_2crystals in literature [129].

To investigate the effects of the refractive index differences on the reflective color, we simulated the color palettes of the same stacks with varying top and bottom TiO_2 layers from 0 to 150 nm at a step of 5 nm. The n of TiO_2 is modeled by the fitting equation of DeVore [129], with an additional term δ to quantify the degradation of it:

$$n^2 = 5.913 + \frac{0.2441}{(\lambda/\mu\text{m})^2 - 0.0803} - \delta \tag{3.5}$$

Where λ s the wavelength. The imaginary part of the refractive index is assumed to be negligible in the visible range. Due to the decrease in n the optical path length in the TiO_2 layers is reduced. To achieve the same round-trip phase shifting, the TiO_2 layer thickness needs to be increased. Figure 3.11 (c) plots the summation of top and bottom TiO_2 layer thicknesses of the configurations matching best with the six representative colors with refractive degradation δ ranging from 0 to 0.8. Due to the decrease in n the required total TiO_2 thickness to generate the same field distribution and spectral absorption profile increases for all six colors. It is needed to mention that the drop of the required thickness for magenta between index degradation of 0.4 and 0.5 is because the best layer configuration that generates magenta has shifted to outside of the simulation range (0 to 150 nm TiO_2 layers) with the degradation of the TiO_2 index, and the remaining colors do not match magenta well. Besides the increased cost of depositing more materials, index degradation will also compromise the reflective color quality. We evaluate the closest matching of the size representative

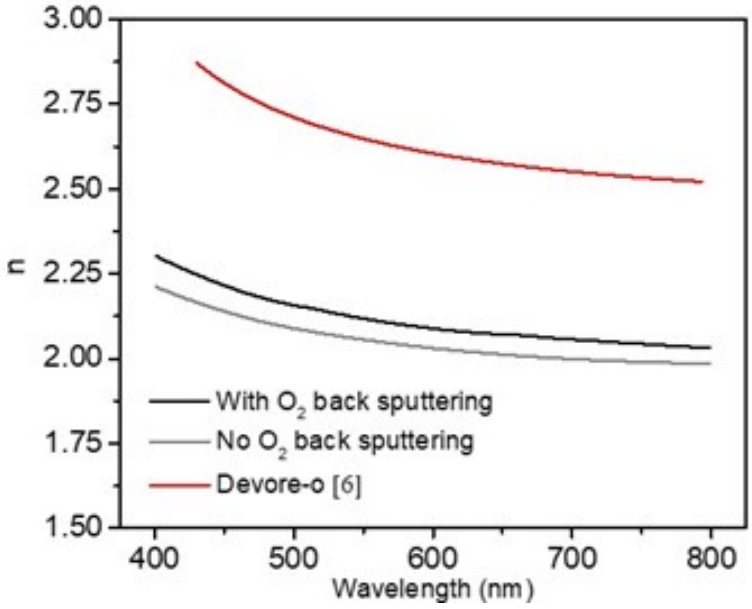

Figure 3.12: Comparison between measured n of TiO_2 deposited with and without O_2 back sputtering and literature data of ordinary TiO_2 crystals.

colors with a self-defined color score:

$$s = 1 - \frac{\Delta E_{94}}{100} \tag{3.6}$$

where the ΔE_{94} is the CIE (1994) color difference [130] between the reference representative color and the best matching on the palette. A better matching will result in a higher score. Figure 2.10(d) plots the influence of index degradation on the defined color scores, which generally decreases with a decrease in n The drop of the color score for magenta between δ= 0.4 and 0.5 is again due to the shifting of the best matching configuration to outside of the simulation range. The differences in TiO_2's optical index cause not only reduced reproducibility between run-to-run depositions, but also a mismatch between the simulated deposition results and real measurements. Furthermore, other possible reasons for the deviation between color pattern prediction and actual deposition include the thickness mismatch caused by non-uniform material ejection due to the not evenly melted material source in the eBeam chamber and the manufacturing error of the apertures on the stencil shadow

mask.

3.4 Summary

In conclusion, we developed a new type of grayscale stencil lithography method to deposit 2D patterns with spatial thickness variation, which improves manufacturing efficiency and removes material limitation compared to conventional iterative lithography-and-lift-off approaches and grayscale lithography methods. We demonstrated the deposition strategy to generate spatial thickness variation with a single stencil shadow mask; meanwhile, the surface roughness can be reduced to less than 2 nm for a deposition thickness of 150 nm. Then, this approach was utilized for a proof-of-concept application to create multispectral reflective color filter arrays with two thickness-varying TiO_2 layers, which produced a wide range of structural color in the visible range. The mechanism of reflective filtering in the lossy Fabry–Perot-type stack structure was studied by investigating the effects of the metal absorbing layer thickness and the degradation of TiO_2 layers' refractive index on the achievable color range and quality. We showed that by tuning the Pt layer thickness, the trade-off between the color span and customizability could be balanced.

The grayscale stencil lithography method demonstrated shows great potential for micro/nano fabrications due to its features of customizable 2D patterning with spatial thickness variation and the freedom of applicable materials for deposition. Manufacturing and processing technologies developed for nano stencil lithography [114, 115] can be applied directly to further improve the patterning resolution of the grayscale stencil lithography technique. As the aperture size becomes smaller, the effects of material clogging and mask thickening during the deposition need to be considered, which is neglected in the current work due to the larger size of apertures compared to the deposition thickness. Meanwhile, methods to prevent aperture clogging with self-assembled molecules on the shadow mask are also appealing [114]. Despite those challenges, the customizability brought by grayscale stencil lithography is beneficial for applications beyond color filtering. It can potentially replace the current design

principles of flat optics, which are limited by the conventional spatially fixed depositions. By using this technique, it would be possible to fabricate flat Fresnel/Kino-like lens [131] or microlens arrays [132]. We also foresee a broad application of it for active and tunable filter arrays [133], and flat diffractive optical elements [64]. Meanwhile, the gentler technological curve of this method is favorable for labs without access to heavily booked eBeam lithography machines in exploring the field of flat optics.

Chapter 4

Optical scattering reservoir computer

4.1 Introduction

A reservoir computer is a high-dimensional dynamic system working as a recurrent network with fixed and random internal connections.[134, 69] It transforms temporal signal series into multiplexed reservoir states, which can be used to memorize or predict complex / chaotic temporal series. As shown in Figure 4.1, a reservoir computer can be decomposed into an input layer, a reservoir, and an output layer. The input temporal signal S is sent into the reservoir with input weight $\boldsymbol{V}$. The status of each node in the reservoir is updated with the connection matrix $\boldsymbol{W}$ at each step n, such that the information from the input layer is propagating through the network and reflected on the multiplexed reservoir states $\boldsymbol{X}$. At each time step, certain nodes in the reservoir can be chosen as the output nodes and a trained output weight $\boldsymbol{u}$ is applied to read out the status as y.

In a traditional artificial neural network (ANN), the connections between the nodes are adjusted through the training process by backward error propagation.[135] This process is time and energy-intensive,[136] especially for larger-scale networks. As the result, hardware acceleration will also depend on the structure of the network and be limited to the scale.[137] On the other hand, the reservoir is usually treated as a fixed box, while only the output weight is trained.[69] Due to the complicity of the reservoir, the RC can handle complex operations with relatively simplified

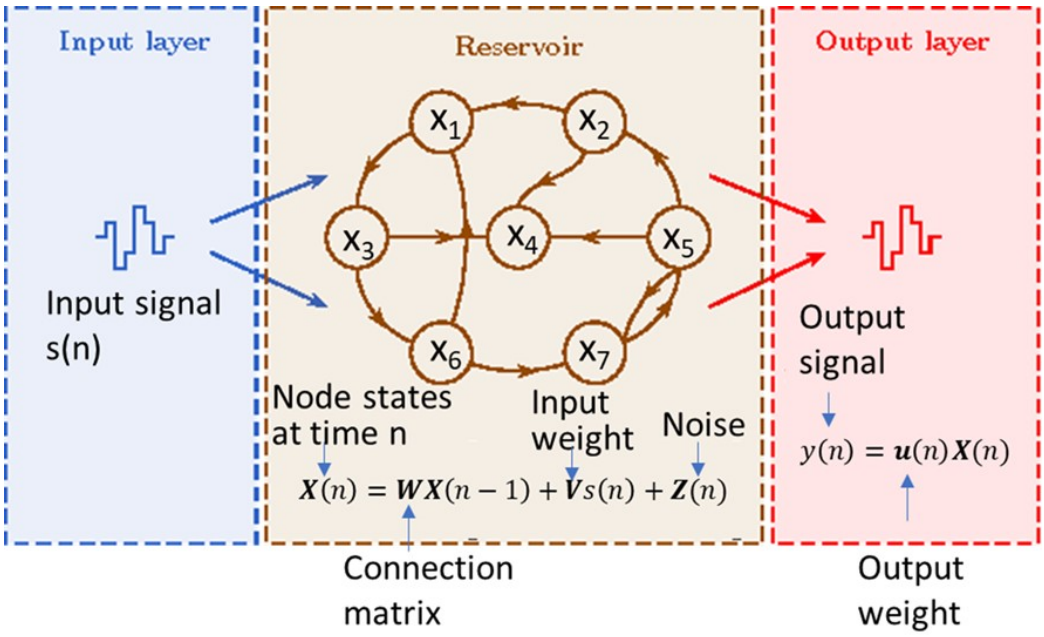

Figure 4.1: Schematic of linear reservoir computer, adapted from Ref [144]

training demands. The way that the reservoir computer performs makes it preferable for general time-series signal processing [138] and ideal for hardware acceleration with fast and large-scale physical reservoirs.[71] There are 3 basic requirements for a physical system to act as an RC [69]: 1). High Dimensionality 2) Fading Memory and 3). Resistance to noise for signal separation. Many physical systems can satisfy those basic requirements, such as optical [139, 140, 141, 71], electronic [142, 143, 144], spintronic [145], etc. Physical RC is continuously drawing attention to combine the advantages of simple implementation, low training cost with the accelerated and parallel capabilities of physical systems.

The optical system shows promising potential for large-scale optical RC thanks to its intrinsic properties of parallelism and scalability.[68] Spatial [70, 71] or temporal [146, 147] multiplexing methods have been applied to form the network of random connections. For example, single microlaser cavities with multiple randomly located probes [140] or multiple microlasers coupled through waveguides or free space [139, 70] have been demonstrated to fulfill functionalities including temporal information reconstruction, chaotic prediction, and pattern classification. Thanks to their intrinsic high dimensionality, large-scale optical scattering reservoir computer for chaotic

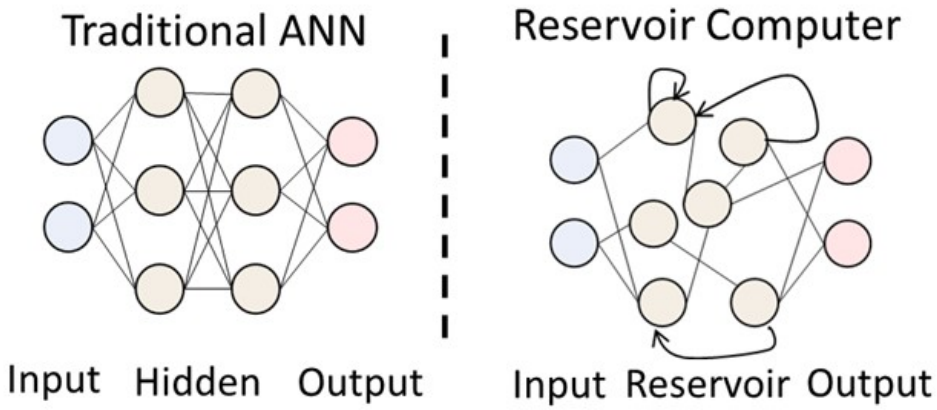

Figure 4.2: Comparison between traditional artificial neural network (ANN) and reservoir computer.

spatial-temporal signal prediction have been developed.[71] The system can achieve high dimensionality with 10^5 embedded nodes and high-speed processing which is about 100 times faster than a conventional CPU. Further, a passive optical system has also been proved to be able to serve as a high-efficiency reservoir computer, in which the non-linear intensity readout provides the non-linearity of the network.[147] Finally, due to the inherent parallel ability of a photonic system, frequency or spatial multiplexed parallel RC has been proposed to improve the total bandwidth. [148]

One of the key metrics to evaluate the performance of RC is the memory capacity, which represents how much past information can be stored in the reservoir and be correctly recovered.[149] The function of memory lay the ground for RC to fulfill other more complex and high-level functions, such as signal pattern classification and prediction. Many attempts have been made to optimize the performance of specific optical reservoir computers. For example, factors including the shape and size of the micro-laser-cavity, and the positioning of the probes, [140] and the interconnection of the laser array have been optimized to improve the MC.[139] However, it still lacks a more general principle for a complex optical medium to be a good physical reservoir. Here we are going to explore the following 3 questions to select a good linear optical reservoir based on random scattering medium: 1). How to design the connectivity matrix to efficiently utilize the high dimensionality for larger MC? 2).

How to maintain the memory performance under the influence of noise? 3). How to choose the optical scattering medium and encode the temporal signals based on the precious considerations?

In this chapter, we investigated the effects of loss and non-normality of a scattering medium on the MC and noise resistance. We modeled the optical scattering reservoir as a linear dynamical system governed by the transmission matrix. Based on that, we studied the linear memory capacity and noise resistance of the scattering reservoir with experimentally measured transmission matrices of ZnO thin films, and virtual scattering reservoirs modeled by the random matrix theory. Through the numerical evaluation, we investigated how information propagates through the reservoir network and its effects on memory performance. The embedded network architecture and the decaying of the information, which is determined by the transmission matrix of the scattering reservoir, defines the linear memory capacity of the system under the influence of noise. We further purposed an amplification method to encode the information to fully harness the high-dimensionality and high noise resistance of the optical scattering reservoir. Future works include the experimental validation of the proposed scattering RC and information encoding method.

4.2 Scattering medium for reservoir computing

In practice, a scattering optical reservoir computer can be built as the schematic shown in Figure 4.3.[71] The input layer consists of a spatial light modulator (SLM) or digital micromirror device (DMD) to encode the spatial-temporal information in terms of the amplitude and phase coupled into the nodes of the reservoir. The signal can be coupled into the scattering medium through lenses for free-space configuration or waveguides for on-chip integration. Finally, the information propagated through the scatter can be recorded with a CCD camera at the readout layer. In each time step, the sensor pixels on the CCD camera probes the status of the 100 nodes embedded in the scattering network, which will then be updated by the modulated inputs through the SLM or DMD.

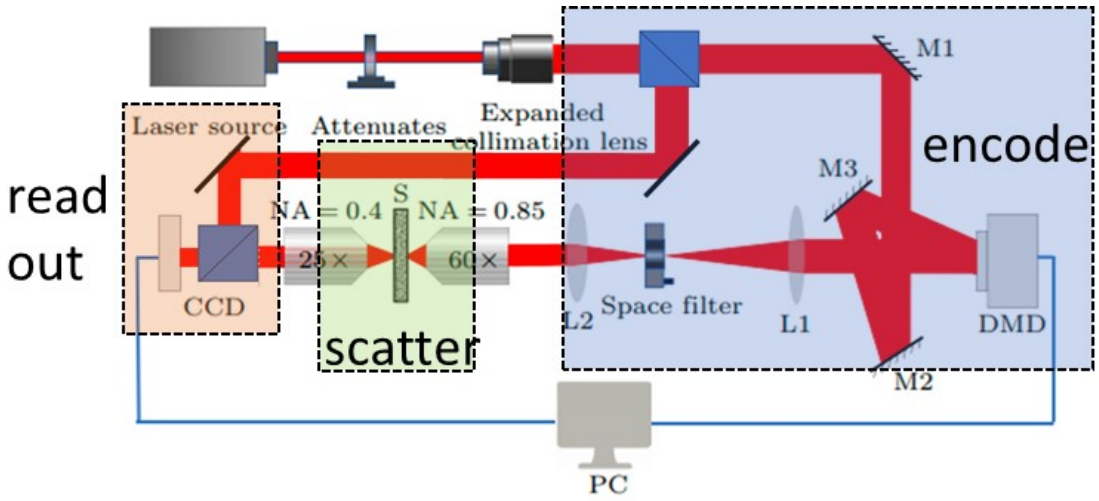

Figure 4.3: Proposed experiment setup for linear optical reservoir computing with scattering medium.

The scattering RC in Figure 4.3 can be modeled with the complex transmission matrix of the medium.[41] In free space, the transmission matrix describes the inter-coupling between different modes, i.e. plane-waves of different wave-vectors, as shown below:

$$E_n^{out} = \sum_m t_{mn} E_m^{in} \tag{4.1}$$

Where E_m^{in} is the complex input field of the m^{th} mode and E_n^{out} is the complex output filed of the n^{th} mode. The elements t_{mn} in the transmission matrix t describes the coupling strength between E_m^{in} and E_n^{out}. The information embedded in each mode through the SLM/DMD and detected by the CCD camera represents the status of the nodes in the scattering reservoir. As demonstrated in the setup in Figure 4.3, the status of the nodes is encoded at time step n as the amplitude and phase on the Fourier plane in front of the 60X object, and retrieved by the CCD on the back Fourier plane at time step $n+1$. Therefore, the transmission matrix defines the connectivity of the RC.

The transmission matrix of a scattering medium can be modeled with the random matrix theory.[41] Following the "Mexico approach",[150] a random unitary matrix M can be applied to describe the scattering medium,[52] in which:

$$\boldsymbol{M} = \begin{bmatrix} \boldsymbol{r} & \boldsymbol{t'} \\ \boldsymbol{t} & \boldsymbol{r'} \end{bmatrix} \tag{4.2}$$

Where $\boldsymbol{r}/\boldsymbol{r'}$ and $\boldsymbol{t}/\boldsymbol{t'}$ are the reflection and transmission matrices, either for the forward or backward direction. In our case, as demonstrated in Figure 4.2, the scattering reservoir will be modeled with the transmission matrix $\boldsymbol{t}$ in the random matrix theory. For modeling purposes, the random complex and unitary matrix M can be drawn from Dyson's circular ensemble[151] to preserve the statistical properties of a scattering medium. Practically, we can generate the transmission matrices following [52]:

Where $\boldsymbol{\tau}$ is a diagonal matrix with real and non-negative diagonal elements. $\boldsymbol{U}$ and $\boldsymbol{V}$ are arbitrary random unitary matrices. The total transmission of the scatter is determined by the matrix $\boldsymbol{\tau}$ as:

$$T_{total} = \langle \boldsymbol{\tau^2} \rangle \tag{4.3}$$

where $\langle\rangle$ is the average operator over the diagonal terms in the matrix $\boldsymbol{\tau^2}$. We further define matrix $\boldsymbol{\Gamma}$ as:

$$\boldsymbol{\tau^2} = sech^2(\boldsymbol{\Gamma}) \tag{4.4}$$

The real diagonal terms in $\boldsymbol{\Gamma}$ can be drawn randomly between 0 and γ_{max}, which is determined by:

$$T_{total} = \frac{\int_0^{y_{max}} sech^2(\gamma/2)\, d\gamma}{\gamma_{max}} \tag{4.5}$$

Random matrices drawn from the above method have been shown to preserve the statistical properties in terms of the distribution of eigenmodes and eigenvalues of the measured and numerical simulated scattering mediums.[52] Further, the real values on the diagonal matrix $\boldsymbol{\tau}$ determines the eigenvalues of the matrix $\boldsymbol{t^{ddagger}t}$, which are correspondingly the decaying rate of the information stored in the eigenchannels through the information propagation. In a passive system, the eigenvalues of $\boldsymbol{t^{ddagger}t}$

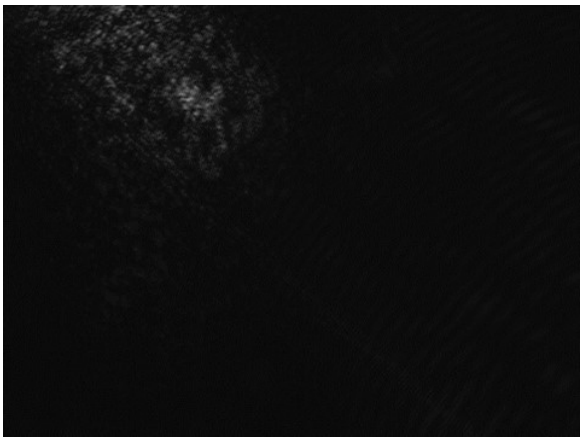

Figure 4.4: Example of measured speckle pattern of a single input modes going through the scattering medium.

≤ 1. The eigenchannel with an eigenvalue of 1 is the "open channel" of a scattering medium,[58, 54] through which the wave / information propagates without any losses.

We further experimentally measured scattering samples made of ZnO powders embedded in transparent photopolymer. ZnO powders (Sigma Aldrich, 99.99%) were first mixed with NOA86 photopolymer at different concentrations (50, 25, and 10 wt%). And 5 μL of the mixture were coated and sandwiched between two 1 cm by 1 cm glass microscope cover slides. Then the samples are photo-polymerized under 365 nm UV light (UVP CL1000) for 5 min (or 120,000 μJ). The measurement setup shares the same architecture as shown in Figure 4.4. A super-pixel-based DMD modulation method is applied to modulate the input modes as the amplitude and phases locating on the Fourier plane in front of the 60X object, and a standard "four-phase method" [48] is applied to retrieve the complex transmission matrix. In the measurement, a known wave-front S_n from the reference beam is used to generate interference with the complex field on the output plane. By shifting the relative phase of the input filed at each mode by a value of α, the intensity a the n^{th} output mode will change by:

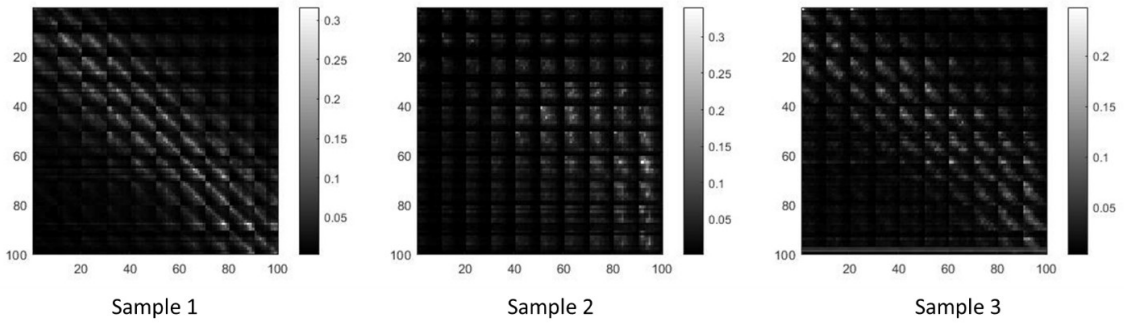

Figure 4.5: Absolute value of the measured transmission matrix of the 3 scatter samples.

$$
\begin{aligned}
I_n^{\alpha} &= |S_n + \sum_m e^{i\alpha} t_{mn} E_m^{in}|^2 \\
&= |S_n|^2 + |\sum_m e^{i\alpha} t_{mn} E_m^{in}|^2 + 2Re(e^{i\alpha} \bar{S_n} \sum_m e^{i\alpha} t_{mn} E_m^{in})
\end{aligned}
\tag{4.6}
$$

Where S_n is the complex reference filed in the nth output mode. With the super-pixel modulation method,[152] we can encode the phase and amplitude at each input free space propagation mode. If we only input one single-mode with normalized amplitude at each time, i.e. flipping on one super-pixel of the DMD, and measure the complex fields at every output mode when $\alpha = 0, \pi/2, \pi$, and $3\pi/2$, we can map the complex transmission matrix as:

$$
t_{mn} = \frac{(I_n^0 - I_n^{\pi}) + i(I_n^{3\pi/2} - I_n^{\pi/2})}{4\bar{S_n}} \tag{4.7}
$$

Figure 4.4 plots the example of measured input filed and "speckle" output filed by the setup. From it, we deduced the transmission matrix of 3 samples of different scattering strengths. Figure 4.5 plots the retrieved transmission matrix. The measurement characterized the combined transmission matrix of both the scattering medium and the optical setup. And Figure 4.6 (a) plots the distribution eigenvalues of the measured matrix. The total transmission calculated as the average of the

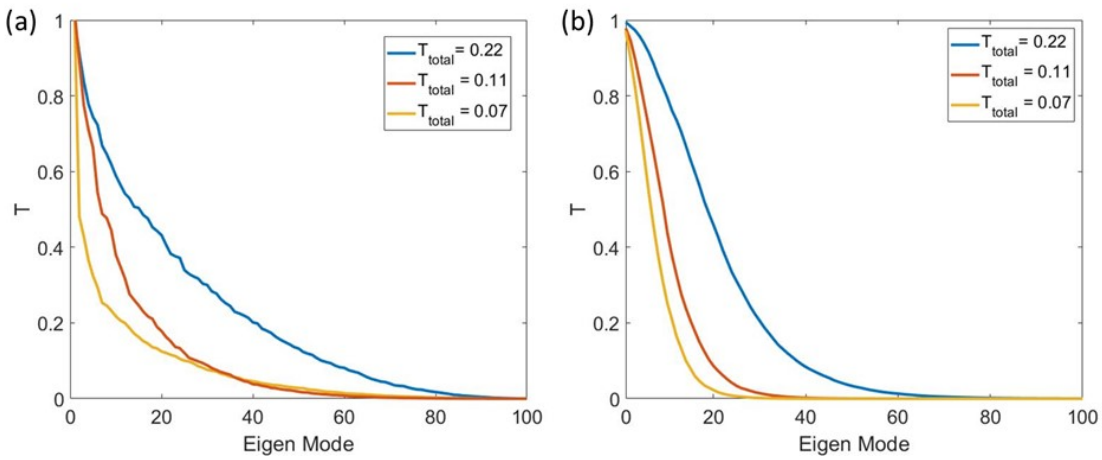

Figure 4.6: The distribution of eigenvalue (T) of $\boldsymbol{t}^{\ddagger}\boldsymbol{t}$ sorted in descending order for (a) Measured samples with the total transmission of 0.22, 0.11, and 0.07, and (b) Calculated value based on random matrix theory.

eigenvalues for the 3 samples is 0.22, 0.11, and 0.07, respectively.

Figure 4.6 (b) plots the eigenvalue distribution of random matrices obtained following the random matrix theory. For each curve, 100 random matrices are generated and the average eigenvalue at each eigenmode index is calculated. The simplified theoretical model can effectively capture the general statistical properties of the measured scattering matrix. However, the eigenvalue of the measured transmission matrix seems to have wider distribution compared with the model. This might be caused by the measurement setup which has extra restrictions on the different modes and the measured transmission matrix.

We evaluated the memory performance of scattering reservoirs based on the measured transmission matrix. The memory capacity is defined as the correlation between the read-out and reconstruction target. In our case, we define the reconstruction target as the input signals in K time steps ago. And the memory function $m(k)$ is then defined as [153]:

$$m(k) = \langle s(n-k)y_k(n)\rangle_n \tag{4.8}$$

Where $s(n-k)$ is the input signal in k time steps ago and $y_k(n)$ is the readout at time step n. In a linear reservoir computer, the readout is obtained with the trained readout weight vector $\boldsymbol{u_k}$:

$$y_k(n) = \boldsymbol{u_k^\dagger X(n)} \tag{4.9}$$

We assume that the input signal are random values between 0 and 1, with Gaussian white noise of covariance ϵ. Then the trained readout weight vector can be deduced as:

$$\boldsymbol{u_k = C^{-1} P_k} \tag{4.10}$$

Where $\boldsymbol{P_k = W^k V}, \boldsymbol{C} = \sum_{\boldsymbol{k}} \boldsymbol{P_k P_k^\dagger} + \epsilon \boldsymbol{C_n}$, and $\boldsymbol{C_n} = \sum_{\boldsymbol{k}} \boldsymbol{W^k W^{k\dagger}}$. Further, the memory function can be expressed as:

$$m(k) = \boldsymbol{P_k^\dagger C^{-1} P_k} \tag{4.11}$$

The memory capacity of the linear reservoir is then defined as:

$$MC = \sum_k m(k) \tag{4.12}$$

The total memory capacity of the linear reservoir describes the capability of the system to reconstruct the past information based on its current memory it. Theoretically, the memory capacity cannot be larger than its dimensionality,[149] which is equal to the number of eigenchannels of the transmission matrix. In our case, the dimensionality (N) of the system is 100.

In Figure 4.7, we plot the memory function of the 3 measured scattering matrices

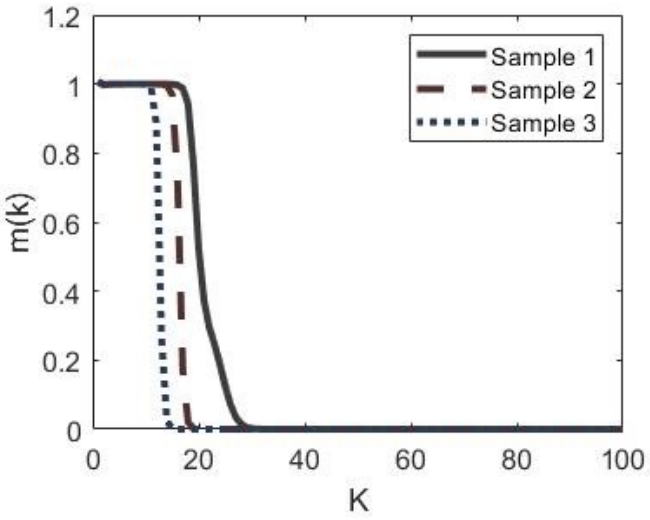

Figure 4.7: Memory function $m(k)$ of the 3 samples calculated with signal to noise ratio (SNR) of 140 dB

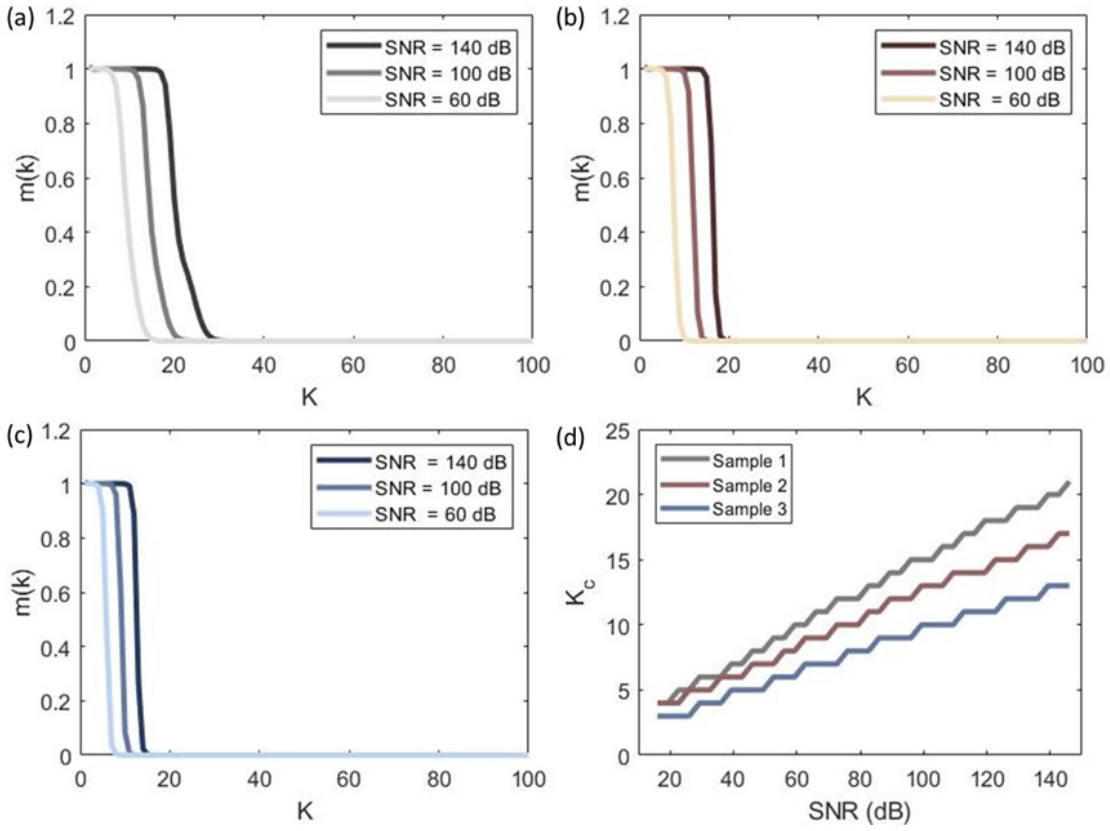

Figure 4.8: (a) to (c) Memory functions of the 3 samples calculated with SNR of 140, 100, and 60 dB. (d) Drop of k_c of the 3 samples as the function of SNR.

as the function of past time step k, when the SNR is 140 dB. For the 3 system, the memory function drops dramatically from 1 to 0 when the k is larger than 29,19, and 15. While the total memory capacity of them is 20,16, and 12, respectively. Further, in Figure 4.8, we plot the memory function of the 3 systems when reducing the SNR from 140 dB to 100 dB and 60 dB. The memory function degrades with the increase of noise intensity. We further define a metric as the temporal capacity k_c:[153]

$$k_c = min\{k|m(k) < 0.5\} \tag{4.13}$$

The larger the k_c, the better the memory performance of the system. Due to the finite dimensionality of a linear reservoir, k_c cannot be larger than the dimension in a passive system. In Figure 4.8 (d), we plot the dropping of k_c as the function of the SNR and we could observe that the dropping rate of the 3 systems is different, indicating different resistance to the noise. These observations raise the question of what factors determine the memory capacity and noise resistance of a linear system. In the following sections, we are going to answer these questions for choosing an optical scattering reservoir.

4.3 Effects of loss on the memory capacity

The fading memory is crucial for RC since a system with finite dimensionality, but long-term memory cannot reconstruct the past correctly. We calculated the memory function of scattering reservoirs with 100 nodes and total transmission from 0.1 to 0.99 based on the random matrix model. In Figure 4.9(a), the memory function at SNR = 140 dB is plot. We could clearly observe the effects of loss on memory capacity. It is straightforward to understand that if all the past information is mixed, the finite system cannot distinguish between short- and long-term memory and retrieve them correctly. Reflected in the memory capacity m(k), we can see that as the total transmission increases, the memory function drops for short-term memory but

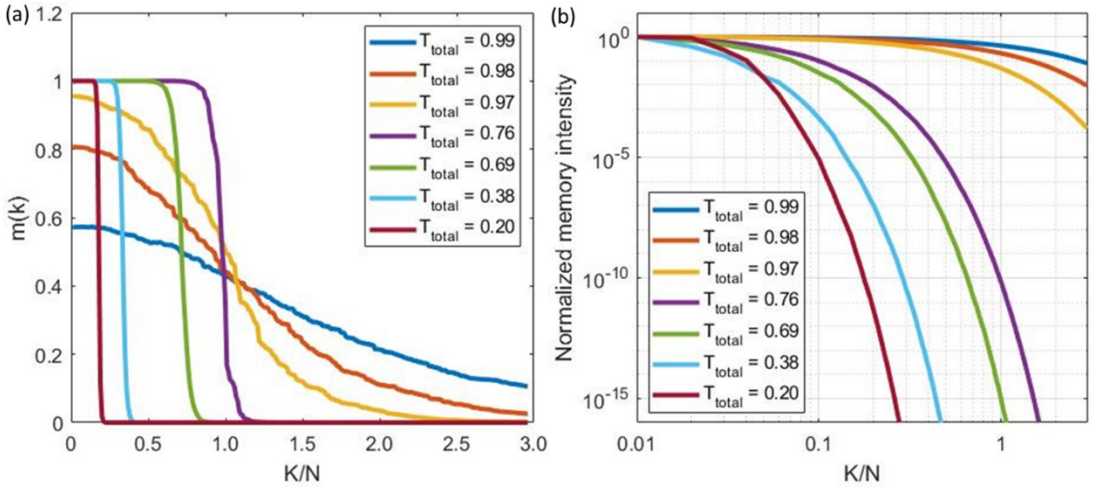

Figure 4.9: (a) Memory function $m(k)$ of 100 nodes scattering RC at various total transmission from 0.99 to 0.20. The SNR is 140 dB, (b). Memory intensity $||W^k V||^2$ in the 7 scattering RC as the function of time step k.

increases for long-term memory with $K/N > 1$, where N is the dimension of the linear system. Therefore, sufficient loss is required to forget the long-term information. In our case, for the 100 nodes scattering reservoir, to reduce the memory intensity of the stored information at 101 time steps ago to be less than 1% of the memory intensity of the stored information at 1-time steps ago, the required transmission is $T_{total} < \sqrt[100]{0.01} = 0.95$.

It is also obvious that if there is no noise, the system should be able to retrieve all information correctly up to $k = N$ when the loss is large.[153] However, under the influence of noise, the memory function of the high loss system drops when the memory intensity drops to the level comparable with the noise intensity. As shown in Figure 4.9 (b), when the memory intensity $||W^k V||^2$ drops to the comparable value of the noise intensity, which is marked as the red dot line for SNR = 140 dB, the system cannot retrieve the past information correct. Correspondingly, the memory function starts to drop at the same k in Figure 4.9 (a). Therefore, we could conclude that in a high loss system, the short-term memory will be compromised when the noise has comparable intensity compared with the signal. We need to choose a system with sufficient loss but also high noise resistance.

In Figure 4.10 (a), we plot the k_c as the function of SNR and total transmission.

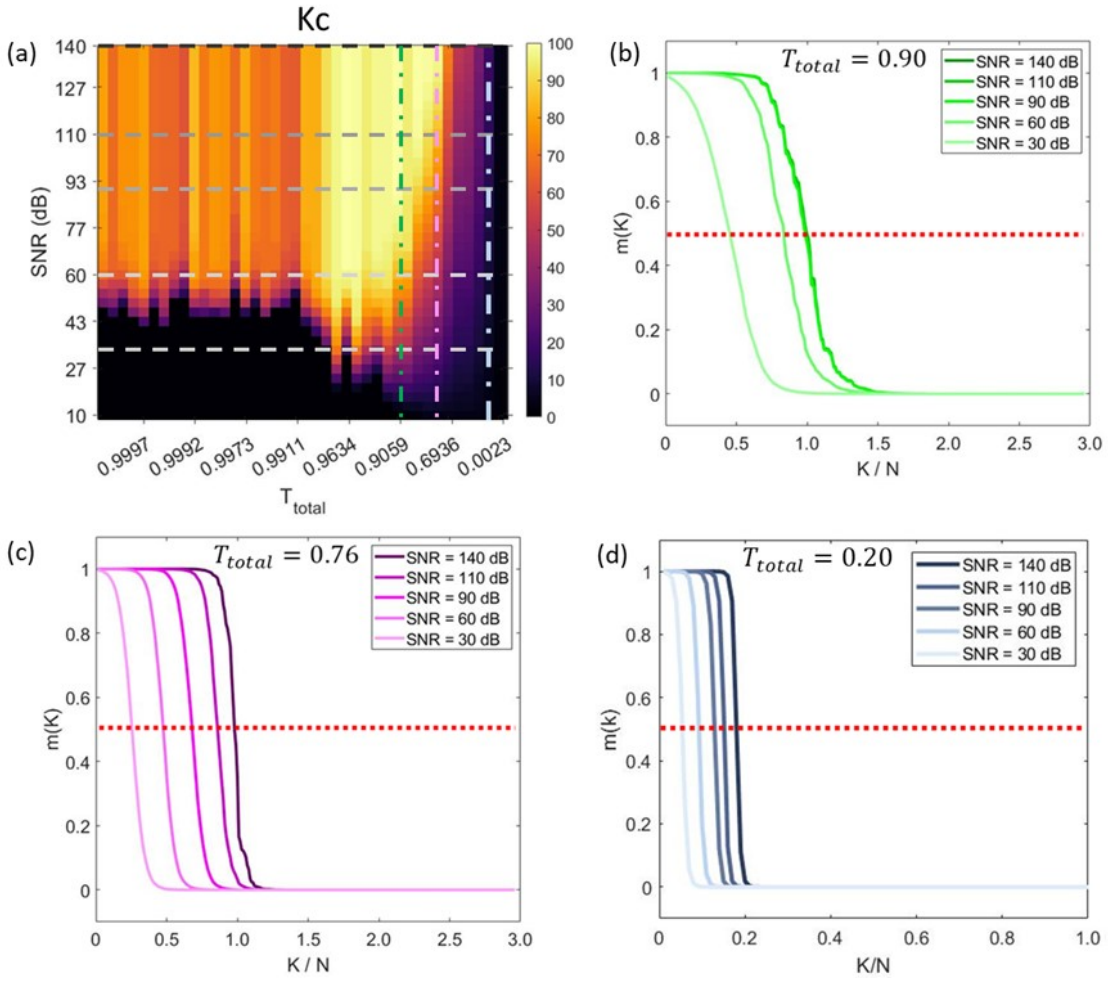

Figure 4.10: (a) k_c as the function of SNR and total transmission T_{total}. (b-d) Evolution of memory function $m(k)$ for scattering RC with total transmission of 0.90, 0.76, and 0.20.

With the increase of noise intensity, we could observe that the degradation of the k_c for systems with the different transmission is not the same. A closer look for systems with the total transmission of 0.76 and 0.90 are shown in Figure 4.9 (b) and (c). The low loss system ($T_{total} = 0.90$) preserves the memory function curve till SNR drops to 90 dB. While the memory function of the relatively high loss system ($T_{total} = 0.76$, and 0.20) cannot be maintained when SNR drops to 110 dB. In the following sections, we will analyze the effects of the non-normality of the transmission matrix on the noise resistance of the system.

4.4 Effects of non-normality on the noise resistance

The connectivity matrix of the RC can be equivalently transformed into either a diagonal matrix (normal matrix) or matrices with off-diagonal components (non-normal matrix).[153] The former transformation means that the network is equivalent to isolated nodes, which are corresponding to the eigenmode of the matrix. Input signal coupled into this system will go through independent decay at each isolated node without interference. On the other hand, inter-coupling happens between the nodes in the non-normal matrix, which is equivalent to a feed-forward network. Previous theoretical studies have proved that a non-normal network is preferable for efficient information propagation by amplifying selective input modes to overcome the effects of noise.[153, 154] We will see that the non-normality also helps to improve the noise resistance of a scattering reservoir in terms of preserving the memory function.

The noise resistance of a linear dynamic system can be evaluated with the metric of the Fisher Memory Curve.[153] It is defined as the diagonal terms of the Fisher Memory Matrix **J**:

$$J_{k,l} = \langle -\frac{\partial^2}{\partial S_k \partial S_l} log P(\boldsymbol{X}(n)|S) \rangle_{P(\boldsymbol{X}(n)|S)} \tag{4.14}$$

Where P is the conditional probability distribution of the current network states

induced by the past signal and noise inputs S. The Fisher Memory Curve measures the ability of the past information to change the present states. Given the transmission matrix and the statistical properties of the noise, we could deduce the Fisher Memory Cure as:

$$J(k) = \boldsymbol{J}_{k,k} = \boldsymbol{V}^{\dagger}\boldsymbol{W}^{k\dagger}\boldsymbol{C}_{\boldsymbol{n}}^{-\mathbf{1}}\boldsymbol{W}^{\boldsymbol{k}}\boldsymbol{V}\frac{1}{\epsilon} \tag{4.15}$$

The total area under the Fisher Memory Curve (FMC) then describes the noise resistance of the system:

$$\begin{aligned} J_{total} &= \epsilon \sum_{k} J(k) \\ &= \boldsymbol{V}^{\dagger}\left[\sum_{\boldsymbol{k}} \boldsymbol{W}^{k\dagger}\boldsymbol{C}_{\boldsymbol{n}}^{-\mathbf{1}}\boldsymbol{W}^{\boldsymbol{k}}\right]\boldsymbol{V} \end{aligned} \tag{4.16}$$

For the non-normal matrix, the total FMC equals 1, indicating that the noise resistance of the normal network does not depend on the input spatial distribution. While for the non-normal network, the total FMC depends on the input weight vector V. While choosing the V as the eigenvector of the largest eigenvalue of matrix $\boldsymbol{V}^{\dagger}\left[\sum_{\boldsymbol{k}} \boldsymbol{W}^{k\dagger}\boldsymbol{C}_{\boldsymbol{n}}^{-\mathbf{1}}\boldsymbol{W}^{\boldsymbol{k}}\right]\boldsymbol{V}$ can help to improve the total FMC and the noise resistance of the network. The previous study shows that the optimized input spatial distribution can increase the total FMC by 4 5 times compared with random input distribution.[153] In the following section, we will always use the optimized input weight vector when calculating the memory functions of the non-normal scattering reservoir.

The non-normality and total FMC of the scattering reservoir network are affected by the total transmission of the scattering medium. In Figure 4.9 (a), we plot two metrics [154] for evaluating the non-normality of a transmission matrix, as the function of the total transmission, which is the distance from commutativity:

$$M_1 = ||\boldsymbol{t}^\dagger \boldsymbol{t} - \boldsymbol{t}\boldsymbol{t}^\dagger||_F \tag{4.17}$$

and Henrici's departure from normality (DFN):[]

$$M_2 = \left[||\boldsymbol{t}||_F^2 - \sum_{z \in \lambda(\boldsymbol{t})} |z|^2 \right]^{0.5} \tag{4.18}$$

Where $||||_F$ is the Frobenius norm and $\lambda(\boldsymbol{t}$ are the eigenvalues of the transmission matrix $\boldsymbol{t}$. The larger the two metrics, the higher the non-normality level of the matrix. Figure 4.11 plots the calculated and measured metrics of non-normality and total area under FMC as the function of the total transmission. The theoretical modeling predicts that the scattering medium with total transmission around 0.4 0.5 has the highest non-normal level. With the increase of the total transmission, the non-normality decreases. When the medium has 100 total transmissions, i.e. a transparent medium without scattering, the incident eigenmodes will not go through any inter-coupling, and the ballistic propagation of the eigenmodes is equivalent to the information stored in the isolated nodes in a normal network.

On the other hand, in an extremely scattering medium, the high scattering loss will also compromise the inter-coupling of information through the eigenmodes. Most of the energy coupling into the network will be lost after few time steps, make the network equivalent to a feed-forward architecture with a large loss in the input node and weak coupling between it and other intermediate nodes. The non-normality of the measured transmission matrices on the 3 samples shows a similar trend as the theoretical prediction. Further, in Figure 4.11 (b), we plot the calculated total FMC of the scattering reservoirs under an optimized input coupling vector. Compared with Figure 4.11 (a), we could see that the value total FMC calculated based on the random matrix theory is highly correlated with the value of non-normality of the matrices, making the non-normality a good metric to characterize the architecture-based noise-

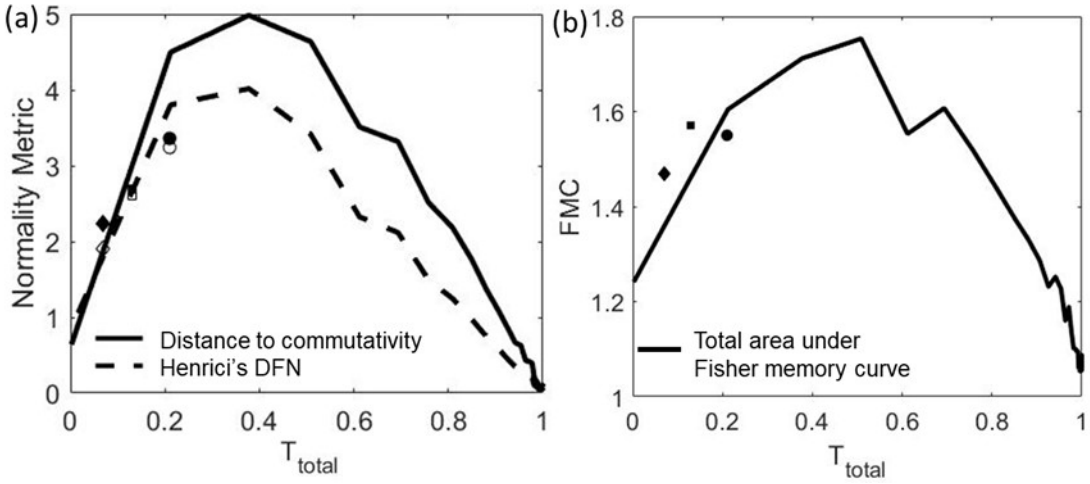

Figure 4.11: (a) Metrics for non-normality of scattering RC as the function of total transmission. Solid (hollow) round, square and diamond markers: Distance to commutativity (Henrici's DFN) of sample 1, 2 and 3. (b) Calculated total area under FMC as the function of total transmission. Solid round, square and diamond markers: Total areal under FMC for sample 1, 2 and 3.

resistance. This is because the embedded feed-forward architecture of the non-normal network ensures the coupling between different modes. Input from the source node can propagate through the feed-forward network, such that the accumulation of the source noise among different time steps can be reduced. However, the experimental measured total area under FMC of the 2^{nd} sample with T_{total} of 0.11 has the highest value of the three, which deviates from the theoretical prediction based on the non-normality metrics. It indicates that there may be more structural factors affecting the noise resistance, or the current two metrics of non-normality cannot characterize the embedded network architecture accurately enough. More experimental works are required to further verify the theoretical prediction for scatters of larger total transmission.

In Figure 4.12 (a), we plot the drop of k_c as the function of the SNR, for scattering mediums with the total transmission of 0.38 to 0.99. Based on the previous analysis, scatters with the total transmission of 0.38, 0.69, and 0.76 should have higher noise resistance compared with other low-loss systems. In Figure 4.12 (a), the dropping rate of k_c of these three scatters is indeed smaller compared with the other 3 scatters.

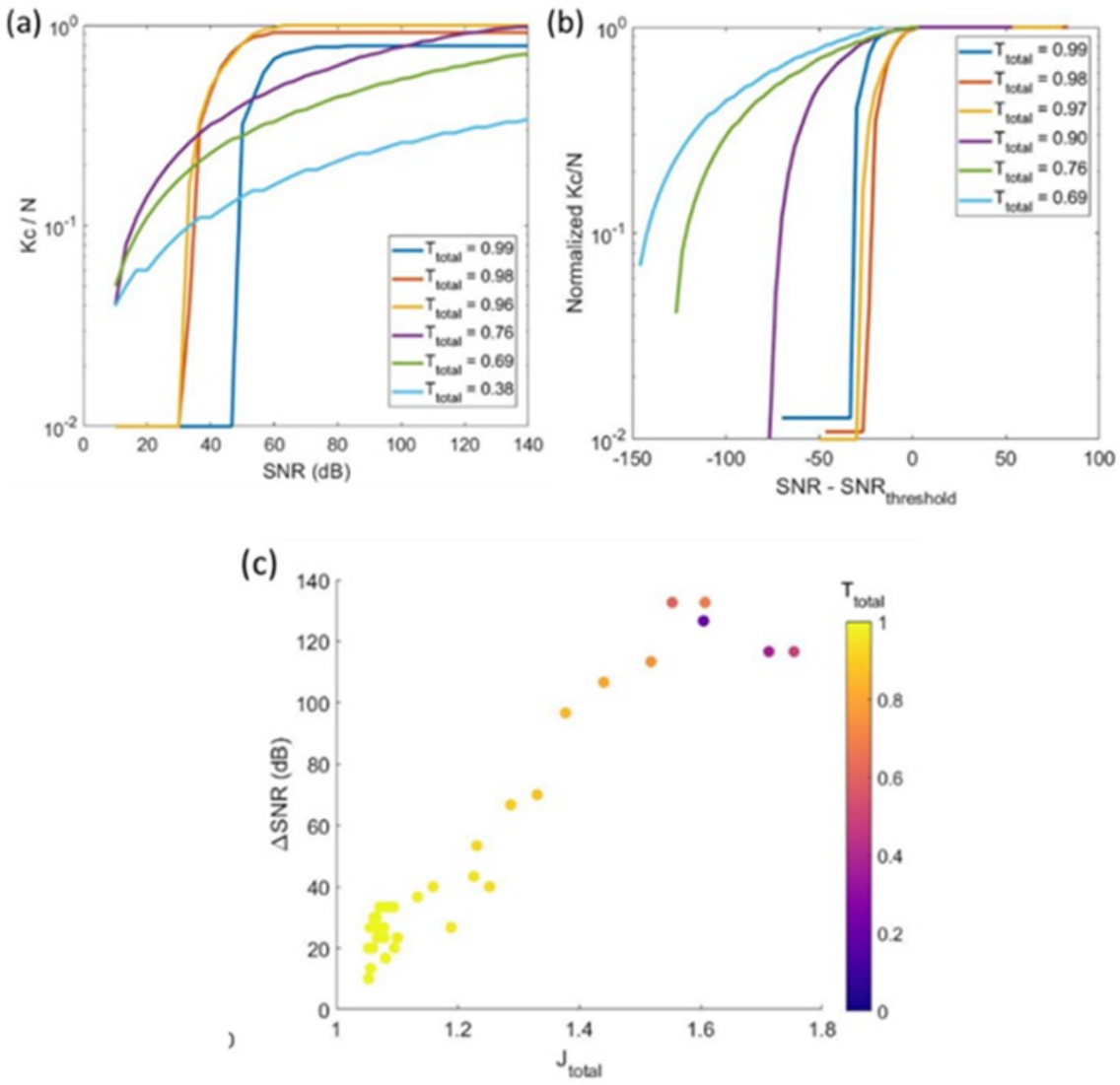

Figure 4.12: (a). Drop of k_c in log scale as the function of SNR for scattering RC with different total transmission. (b) Shifted plot of (a) against the SNR threshold. (c). ΔSNR as the function of total area under FMC. The color map indicates the total transmission of the scattering RCs.

However, due to the high loss, the actual memory performances of them are worse, which are reflected in the lower k_c. To fairly compare the architecture-based noise resistance of different scattering mediums, we could define the threshold SNR as the starting point when the k_c starts to drop and re-draw Figure 4.12(a). In Figure 4.12 (b), we plot the normalized k_c as the function of SNR shifted against threshold SNR for the same size system. It is obvious that the high loss scattering mediums have higher architecture-based noise resistance compared to the other three. In Figure 4.12 (c), we further plot the $\Delta SNR \equiv abs(SNR_{k_c=0.1N} - SNR_{threshold})$ as the function of total FMC. Scatters with higher total FMC show better noise resistance as it can preserve the k_c at higher noise intensity.

We could conclude that the optical scattering reservoir with total transmission around 0.5 will have higher non-normality and better noise resistance. However, the intrinsic loss of the systems will compromise the actual memory function under the influence of noise. In the next section, we will introduce an artificial amplification method to overcome the trade-off between the loss and non-normality of the scattering reservoir, to fully harness the high dimensionality and embedded feed-forward network.

4.5 Artificial amplification for balanced memory capacity and noise resistance

To overcome the issue of losses in a non-normal scattering reservoir and fully utilize the noise resistance, here we propose a practical method to apply artificial amplification to the signals between each time step. It is equivalent to multiply the transmission matrix with a certain amplification factor α while keeping the whole system stable. It can be done in the optical setup in Figure 4.3 with the amplitude modulated by the DMD or SLM in the input layer. Introducing artificial amplification to a high-FMC scattering medium can help to avoid noise resistance drop due to memory loss. Meanwhile, the amplification equally amplifies both signal and noise such that the

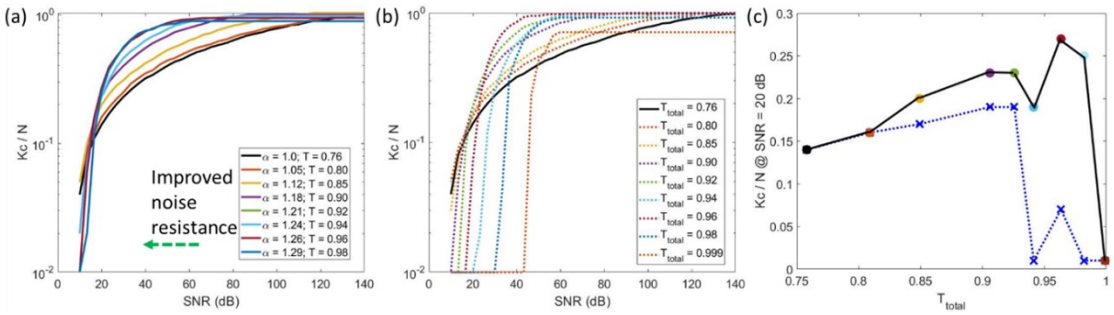

Figure 4.13: (a) k_c as the function of SNR for scattering RC with original T_{total}=0.76 and amplified with different ratios. (b) k_c as the function of SNR for scattering RC without amplification and with different original $Ttotal$, which are the same as the amplified values in (a). (c) Improvement of k_c at SNR = 20 dB through the artificial amplification method.

good memory function quality can be maintained.

In Figure 4.13 (a), we plot the k_c as the function of SNR for a scattering medium with the original total transmission of 0.76 and amplification factor ranging from 1.0 to 1.29. We could see that with the increase of the amplification factor, the value of k_c increases for higher noise conditions, indicating the improvement of the actual noise resistance. In Figure 4.13 (b) and (c), we plot the k_c as the function of SNR for scattering reservoirs without ratification amplification and the comparison between them with the amplified system in Figure 4.11 (a) at the same total transmission. For high noise conditions, e.g. SNR = 20 dB, the system with artificial amplification has higher k_c compared to those low loss systems.

The reason behind the improvement is the artificial transient amplification and the embedded feed-forward architecture of the non-normal system.[153, 154] As shown in Figure 4.14 (a), the amplification shifts the eigenvalues of the system $\boldsymbol{t}^{\dagger}\boldsymbol{t}$ with the original total transmission of 0.76 towards the direction of values greater than 1. Since we keep the system stable, there are still certain eigenvectors with eigenvalue < 1. Due to the coupling between different modes in a non-normal network, the amplified signal will eventually be coupled into the decaying modes and finally fade away. The transient amplification preserves the signal intensity for short-term memory and keeps the SNR, such that the system can have higher noise resistance. As shown in Figure

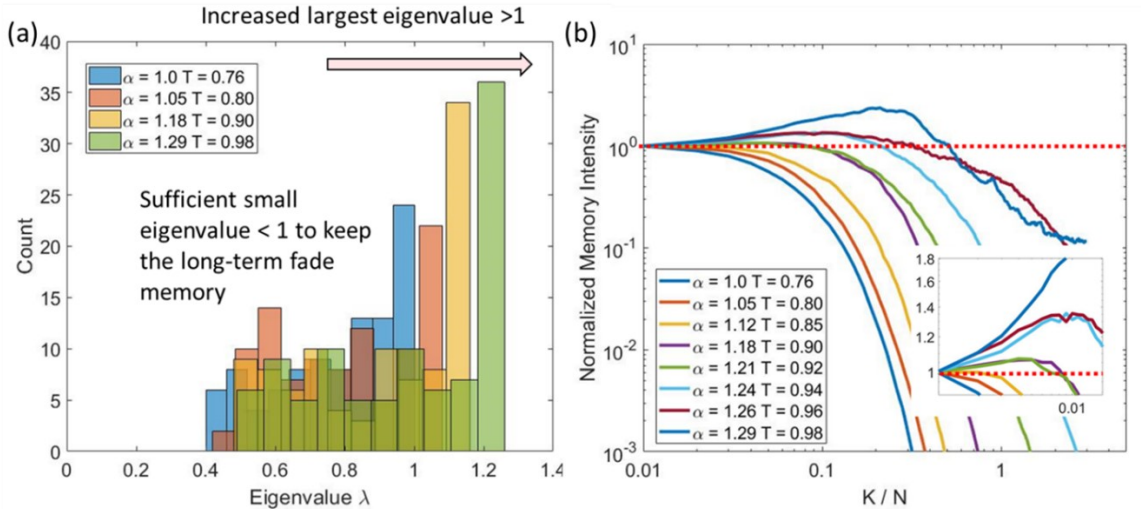

Figure 4.14: (a). Eigenvalue distribution of $\boldsymbol{t}^{\dagger}\boldsymbol{t}$ with different amplification ratios. (b) Transient amplification of the normalized memory intensity $||\boldsymbol{W}^{\boldsymbol{k}}\boldsymbol{V}||^2$ for scattering RC with different amplification ratios. The inserted plot is a zoom-in of the curves near $k/N = 0$.

4.14 (b), we can clearly see the transient amplification of signal intensity when $k < N$. While in the normal matrix the transient amplification is forbidden in a stable system since there is no coupling between different modes. Similar transient amplification by engineering the coupling strength for non-normal networks has been theoretically proposed to improve the read-out noise resistance.[154] In our case, this principle can help to improve the memory performance of a scattering reservoir with some simple modification of the optical setup. Further, it reveals the possibility to engineer the scattering medium with embedded gain/loss regions to achieve an integrated scattering reservoir with non-normality architecture and transient amplification.[155] In Chapter 6, we also proposed a QDs/Photopolymer composite with projection lithography technique, which has the potential to be applied for fabricating gain/loss engineered scattering medium.

4.6 Summary

In this chapter, we identified the two main factors determining the memory performance of a scattering medium as a linear optical reservoir. The first is the loss of

the scatter, determined by the total transmission of the system. We found that sufficient loss is required to efficiently recover the short-term memory while forgetting the long-term memory. However, scatters with large losses will suffer from the influence of noise. The second factor is the non-normality of the scattering medium, which is reflected by the total FMC of the scatter's transmission matrix. We found that the scattering medium with total transmission around 0.5 will have the largest total FMC based on the random matrix theory model, which indicates a higher noise resistance due to the embedded feed-forward network. To overcome the influence of losses on the actual noise resistance, we further proposed an artificial amplification method to fully utilize the dimensionality and noise resistance of a non-normal scattering medium. It is equivalent to transiently amplify the input signals up to N time step while keeping the whole system stable. Therefore, the signal intensity can be preserved while the noise accumulation through the propagation process can be reduced when the information propagates through the embedded feed-forward networks to the decaying nodes. The above findings could be the selection guidance for optical scattering medium or other type of linear physical reservoirs. Future works will focus on numerically and experimentally validating the findings and proposed information encoding methods.

Chapter 5

Micro-sized thermochromic hydrogel particles as tunable scattering medium for light modulation

5.1 Introduction

In the 3rd chapter, we studied the application of an optical scattering medium as a physical reservoir computer. The memory capacity and its resistance to noise of a scattering reservoir are determined by the scattering matrix of the medium, which is reflected in the scattering strength. In this chapter, we developed a dynamic scattering medium based on thermochromic hydrogel particles, which can achieve the controllable transition from a low scattering state to a high scattering state. This dynamic scattering medium is of great potential for applications in light. Here we demonstrated its application as smart windows for solar transmission modulation.

Considerable endeavors have been devoted to light management for energy-efficient buildings to reduce energy use in heating, ventilation, and air conditioning systems, which account for 13% in 2006 and 10% in 2020 (projected) of the total energy consumption in the United States.[10] Light management using advanced smart window technologies is promising as it can theoretically lead to annual energy savings

of more than 1.055×10^{15} kJ in the United States (i.e., 1% of annual total energy consumption).[156] Previous transmittance modulation processes mainly rely on the change of extinction in thermochromic metal oxides or electrochromic active materials.[157] However, this reliance leads to challenges for concurrently achieving a large tuning contrast of refractive index, a broad modulation spectrum, and a near-room-temperature transition. In practical terms, we also need to address several critical claims for large-scale adoption in building technologies, such as luminous transparency, transmittance modulation efficiency, the economics of manufacturing and operation, stability, and scalability.[157, 158]

Electrochromic devices achieve the dynamic modulation of transmittance over visible and infrared (IR) regions based on an electrochemical-cell structure. An operation power is usually required for electrochromic devices, such as in the majority of commercial electrochromic smart windows employing transition metal oxides (e.g., WO_3) as the active material, which switches between oxidized/reduced states during faradic charge injection/extraction,[158] and some emerging electrochromic technologies based on reversible metal electrodeposition and plasmonic nanocrystals.[159, 160] In general, the fabrication of these functional thin films relies on costly physical vapor deposition and a high-temperature process.[158] Up to now, concerns about the cost of production and durability limit the scalability of electrochromic devices.[157, 158, 159] Alternatively, thermochromic devices are considered as autonomous systems with no net energy input because the facade change can be triggered by the temperature change of the environment.[156] The simplicity of the single-component structure holds promise for industrial production and ease of implementation.

Conventional thermochromic devices are generally based on the extinction of IR light by the phase-change medium that can be characterized by a change to the imaginary part of the refractive index. For example, vanadium dioxide (VO_2) varies from an IR transparent state to an IR reflective metallic state at the critical temperature (T_c) of about 68℃.[156] However, such a mechanism of transmittance modulation has two intrinsic limitations. (1) A transparent heating unit is needed for VO_2 to be functionalized as a smart window coating, and the resulting elevated tempera-

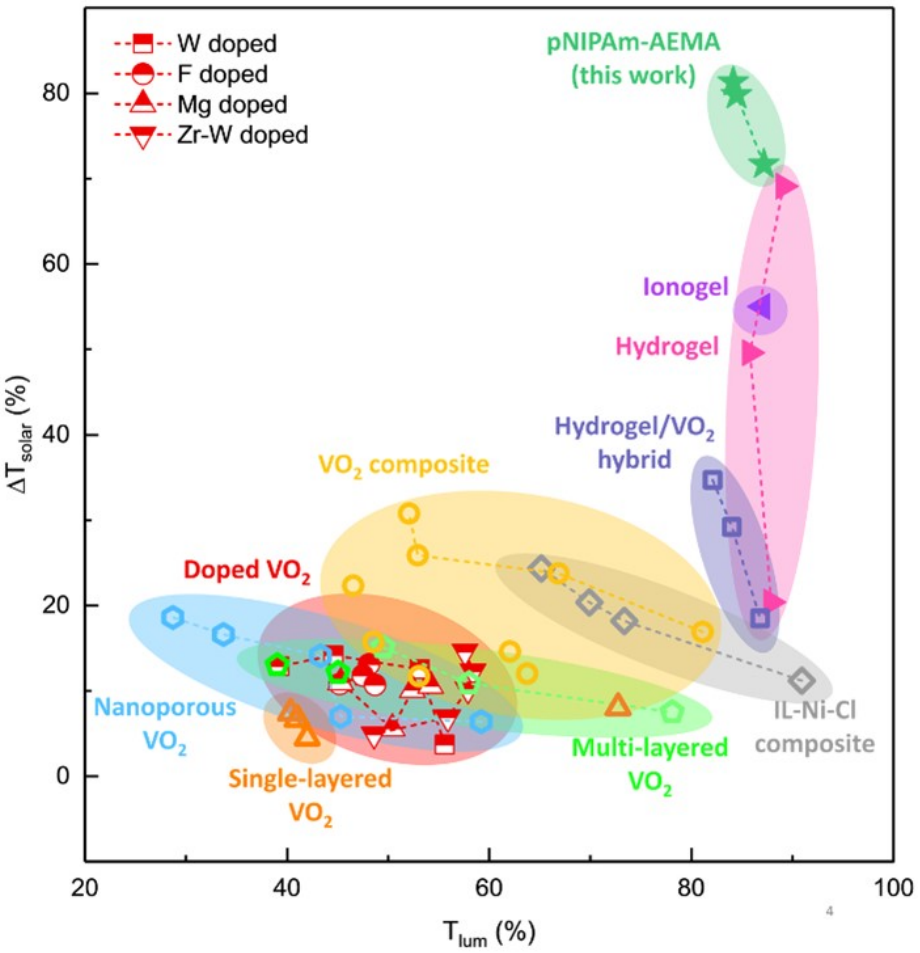

Figure 5.1: Solar transmittance modulation (ΔT_{solar} after phase transition) and luminous transmittance (T_{lum} before phase transition) of different thermochromic films: single-layered VO_2 films [1, 2, 3], multi-layered VO_2 films [1, 2, 4], doped VO_2 films[5, 6, 7, 8], nanoporous VO_2 films [9], VO_2 composite films [10, 11], VO_2/ionic liquid-nickel-chlorine (IL-Ni-Cl) composite films[3], hydrogel films[12], hydrogel/VO_2 composite films[13], ionogel films [14], and the pNIPAm–AEMA films. Hollow symbols indicate the ΔT_{solar} data of VO_2-based thermochromic films at the phase transition temperature from 80℃to 100℃. Solid symbols indicate the thermochromic films with the low phase transition temperature. In particular, the ΔT_{solar} data of hydrogels and ionogels are acquired at the phase transition temperature of 40℃, while, the ΔT_{solar} data of the pNIPAm–AEMA films are obtained at 34℃in our work.

ture of the window surface would diminish the heat-shielding ability. Some of the best-performing VO_2 devices in literature work at 90℃,[10, 9, 161] showing a solar transmittance modulation (ΔT_{solar}) of 22.3% with a luminous transmittance (T_{lum}) of 45.6% before phase transition.[9] Although dopants such as tungsten,[5] niobium,[162] and magnesium,[6] have been used to reduce Tc, the introduction of foreign ions will induce degradation in ΔT_{solar} and T_{lum}.[163, 164, 7] (2) the strong inner-band and inter-band absorption of VO_2 lies in the visible region, leading to the reduced T_{lum}. Strategies such as elemental doping,[7, 165] anT_{IR}eflection coating,[166, 167] porosity tuning,[168, 169] and multilayered structure could improve the T_{lum} of VO_2 thin films to maximal 67.5% while the ΔT_{solar} was limited to 5.4%.13 Furthermore, doping and microscopic structure fabrications noticeably increase the complexity and cost of manufacturing. Current techniques to conquer the obstacles in conventional thermochromic windows are still far from optimal.

In this chapter, we focus our study on a new group of thermochromic materials that achieve light modulation via tunable scattering behaviors. The light-blocking mechanism is elucidated with Mie scattering theory, which predicts efficient scattering in a broad solar spectrum with the aid of co-polymerized hydrogel microparticles of prescribed diameters. In particular, our aim is to achieve efficient transmittance modulation in the IR region (780–2,500 nm) where thermal radiation contributes 53% of the total solar energy (UV 3%; visible 44%).[170] As an example, we fabricated poly(N-isopropylacrylamide) (pNIPAm) and 2-aminoethylmethacrylate hydrochloride (AEMA) co-polymerized pNIPAm-AEMA hydrogel microparticles, whose crosslink uniformity and particle size are manipulated experimentally to attain ultra-high performance in both ΔT_{solar} and T_{lum} as compared with other thermochromic counterparts (Figure 5.1).[161, 6, 1, 2, 3, 1, 8, 12, 13, 171, 14, 172, 173, 174, 175] Besides, pNIPAm-AEMA hydrogel microparticles can undergo phase transition under solar irradiance due to the low critical solution temperature (LCST) of ∼32℃ making them preferable for smart windows.[12] In contrast, an outdoor temperature higher than 50℃is required for the phase transition of VO[]$_2$ under natural convection, which is practically infeasible. Notably, heating-cooling cycles demonstrate the excellent

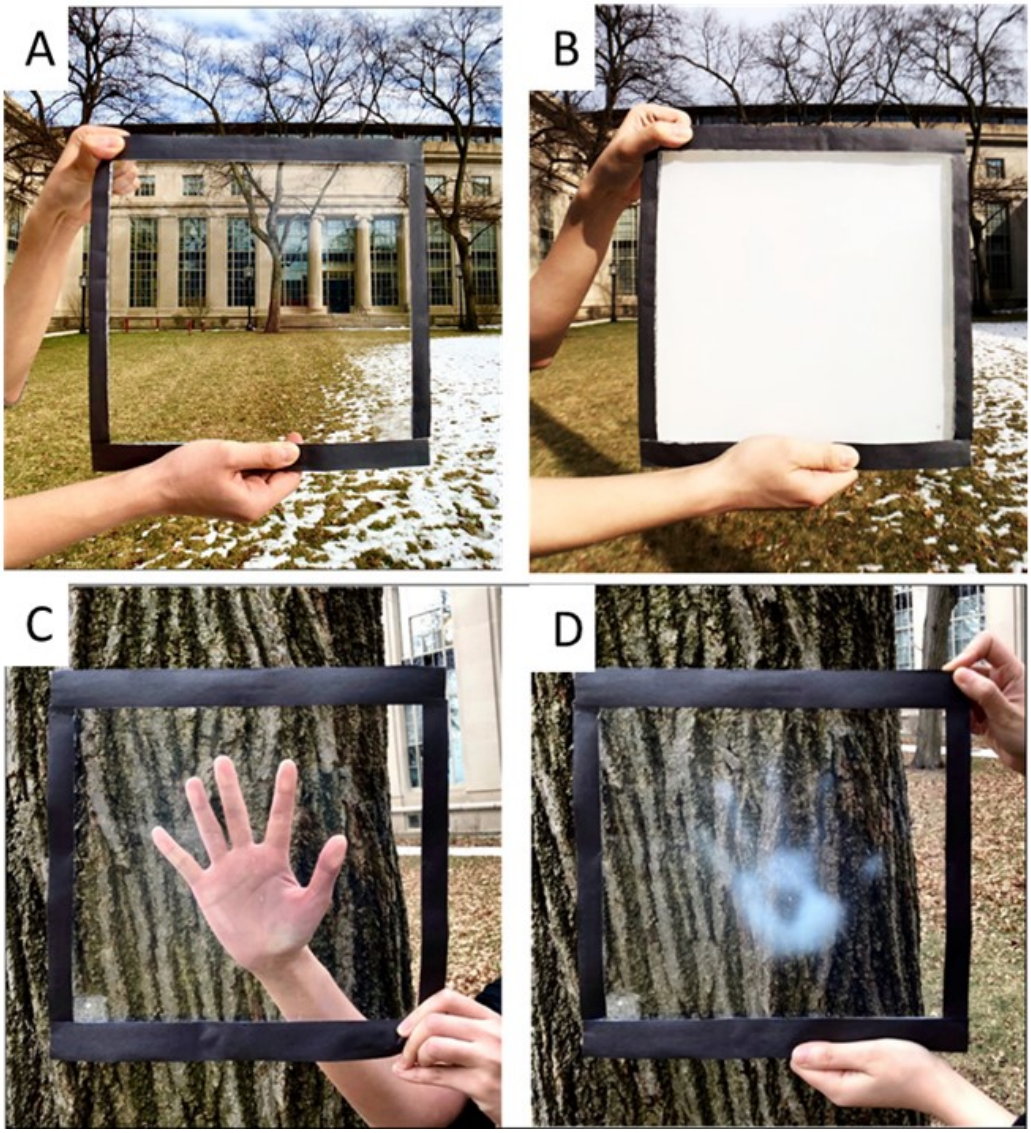

Figure 5.2: (A) Image of a 12" ×12" pNIPAm–AEMA device at an ambient temperature of 5℃. (B) Image of the device after phase transition. (C) and (D) The phase transition of a "hand-shape" area in the pNIPAm–AEMA device was triggered by the hand.

stability of the device. Furthermore, the solution-phase synthesis described herein permits an industrial-scale and cost-effective production, whereby a 12 × 12-inch window device is fabricated to display its scalability and the prospect of practical applications, as shown in Figure 5.2.

5.2 Size and scattering control of PNIPAm-AEMA hydrogel particles

The uniqueness of temperature-responsive pNIPAm hydrogel particles for light management is that their scattering behaviors can be tuned profoundly regarding the particle size, internal structure, and volume fraction of water. A homogeneously low mismatch of refractive index between pNIPAm hydrogel particles and water at the "OFF" state is responsible for high T_{lum} (Figure 5.3 (a)), while the strong optical contrast between pNIPAm hydrogel particles and water is established when the polymer collapses above LCST.[176] The light is scattered at the interface between the dense polymer and surrounding water, regarding the "ON" state. Effective light management for solar heat-shielding purposes requires that the light scattering covers the full solar spectrum, especially the IR region (53% of total solar energy). Problematically, the heterogeneous internal structure of pNIPAm particles made by classical one-pot synthesis results in high turbidity of the hydrogel at the "OFF" state (Figure 3B1).[177] Meanwhile, pNIPAm particles synthesized by radical emulsion polymerization reach the size limit so that the size parameter ($\frac{2\pi r}{\lambda}$) is comparable with 1 only in the visible region,[177, 178, 179] leading to inefficient scattering in the IR region at the "ON" state (Figure 5.3 (b)). To extend the transmittance modulation spectrum and guarantee the high T_{lum}, the synthesis strategy is to enlarge the hydrogel particle size and maintain a homogeneous crosslink density.

The requirements on the scattering behaviors of hydrogel particles were achieved by co-polymerizing pNIPAm and AEMA via a continuous feeding solution-phase synthesis (Figure 5.3 (b)3). Details of the fabrication process are described in the Method

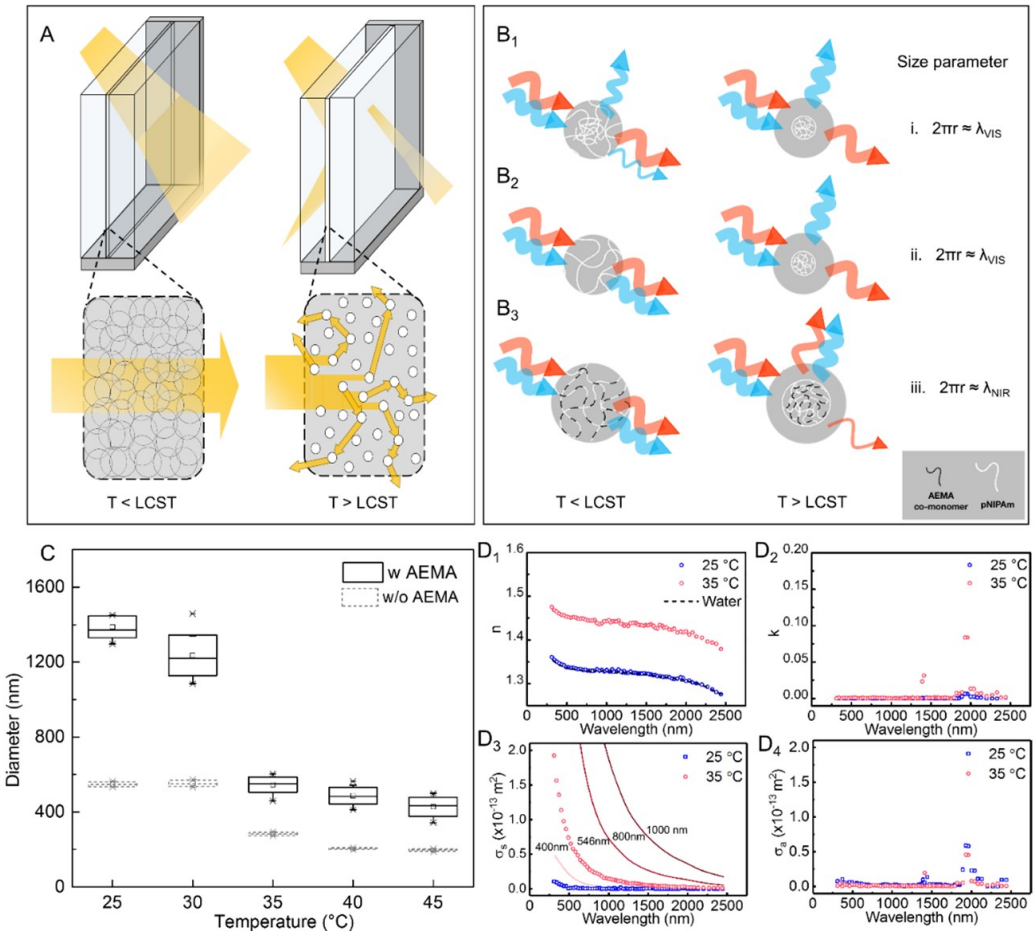

Figure 5.3: Temperature-responsive pNIPAm-AEMA microparticles. (A) Schematic of transmittance modulation based on the tunable scattering behaviors of hydrogel particles. Light manipulating with the aid of the phase transition of (B1) pNIPAm particles produced by one-pot synthesis; (B2) pNIPAm particles synthesized by continuous feeding method; (B3) pNIPAm-AEMA co-polymerized microparticles. Visible light and IR light are presented by blue and red arrows, respectively. (C) Hydrodynamic diameters of pNIPAm-AEMA microparticles (red solid) and pNIPAm particles (green dashed) at different temperatures. (D1 and D2) Real (n) and imaginary (k) refractive index of the pNIPAm-AEMA microparticles at 25℃ and 35℃ respectively. The dashed line in D1 shows the n of water. (D3 and D4) corresponding scattering and absorbing cross-sections of the pNIPAm-AEMA microparticles at 25℃ and 35℃, respectively. Estimated scattering cross-sections of pNIPAm-AEMA with a diameter of 400nm, 800nm and 1000nm at the de-swollen state are illustrated as solid curves.

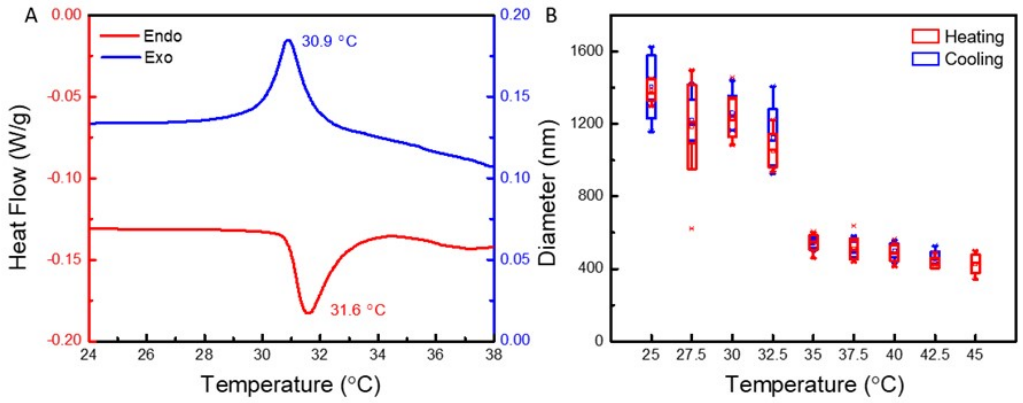

Figure 5.4: Characterization of the LCST of pNIPAm-AEMA microparticles. (A) DSC measurement of normalized heat flow in the endothermic (Endo) and exothermic (Exo) process. (B) Temperature dependence of the hydrodynamic diameter of pNIPAm-AEMA microparticles in heating and cooling operations measured by DLS.

section. The AEMA co-polymer modified the surface charge of particles with the positive terminal primary amine groups.[180] The electrostatic repulsion of the hydrogel particles was diminished, which can be corroborated by the change of the zeta potential from -23.9 mV to -9.0 mV. Thus, the oligomers precipitated on primary particles and consequently increased the particle size. The hydrodynamic diameter (D_h) enlarges to 1,388 nm at 25℃and 546 nm at 35℃ (Figure 5.3(c)), contributing to a size parameter ($frac2\pi r\lambda$) comparable with 1 in the IR region. Meanwhile, the continuous feeding method kept a constant monomer concentration and a reaction rate throughout the enT_{IR}e synthesis. The hydrogel particles were formed with a homogeneous internal structure, contributing to a very low scattering contrast to surrounding water at the swollen state. The temperature response of the pNIPAm-AEMA microparticles was evaluated by differential scanning calorimetry (DSC), revealing an endothermic peak temperature of 31.6℃ and an exothermic peak temperature of 30.9℃ (see Figure 5.4).

Additionally, the strong phase transition from swollen to deswollen state was observed by optical microscopy (Figures 5.5 (a) and (b)). In contrast, the average D_h of pure pNIPAm particles is 548 nm at 25℃and shrinks to 282 nm at 35℃(Figure 5.3 (c)), which reaches its size limitation despite carrying out the polymerization in

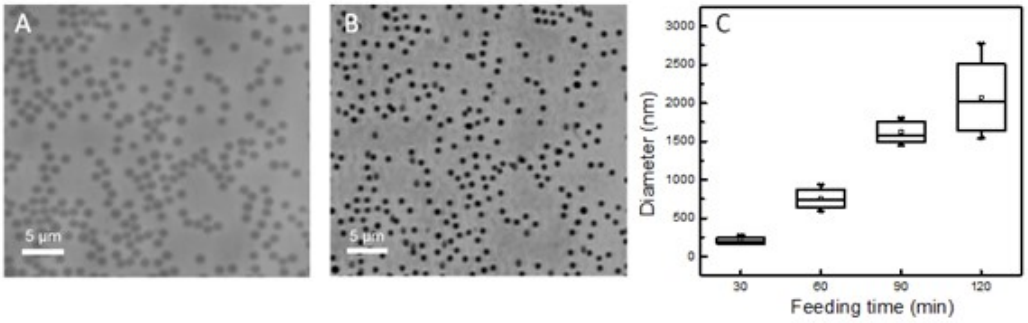

Figure 5.5: Micro-sized pNIPAm-AEMA particles. (A and B) Optical microscope images of the pNIPAm-AEMA microparticles synthesized by continuous feeding for 75min. (A) Before phase transition, D_h is 1388nm at 25℃(B) After phase transition, D_h reduces to 546nm at 35℃(C) Hydrodynamic diameter of the co-polymerized pNIPAm-AEMA particles at 25℃To keep a constant co-monomer concentration for injection, the pNIPAm-AEMA particles grow linearly in dimension with the increasing of feeding time.

a longer period of time and with a larger amount of monomer (see Figure 5.6). Our synthesis achieves the homogeneous crosslink density of particles and the controlled particle size from 200 to 2,000 nm (Figure 5.5 (c)), which simultaneously fulfills the high T_{lum} and the extending transmittance modulation in the IR region for the first time. In addition, compared with the thin-film manufacture of thermochromic VO[]$_2$, such a solution-phase synthesis of hydrogel particles suggests great potential for industrial-scale and cost-effective production.

Tunable scattering behaviors of pNIPAm-AEMA microparticles herein are elaborated in terms of the change of particle size parameter and optical density. Particularly, the scattering cross-section and refractive index were investigated based on Mie theory and Beer-Lambert law,[181, 182] which show that the effective modulation of IR light by scattering could be delivered in response to the size parameter around 1 in the IR wavelength region and a strong enhancement of real part of the refractive index above the LCST. Figures 5.3(d)1 and 5.3(d)2 show the complex refractive index of pNIPAm-AEMA microparticles, which was deduced from the attenuation coefficient (μt) of the diluted suspension, as shown in Figure 5.7. And more details of the characterization process are described in the Method section. The n of particles closes

to the n of water at the swollen state, which is attributed to the large volume fraction of water and a homogeneous crosslinked structure. The small scattering cross-section (σ_s) before phase transition is beneficial for a high T_{lum} (Figure 5.3(d)3). Meanwhile, the small absorbing cross-section (σ_a) indicates a low absorption loss in the pNIPAm-AEMA (Figure 5.3(d)4), where two peaks near 1,450 nm and 1,930 nm are associated with the absorption of water molecules. After the phase transition, the internal structure of pNIPAm-AEMA microparticles changes from a homogeneous water-rich state to a collapsed state. The n approaches that of the bulk polymer with the reduction in the volume fraction of water. The n of pNIPAm-AEMA at the deswollen state increases to approximately 1.45 in the visible region and to 1.40 in the IR region, which is in good accordance with the n of hydrogel particles with similar chemical structures estimated by the effective medium approximation.[181, 182] Figure 5.3(d)3 shows that the σ_s of pNIPAm-AEMA appreciably increases in both the visible and IR regions after the phase transition.

In contrast, the σ_s of pure pNIPAm particles in the IR region is two orders lower due to the size limitation as shown in Figure 5.8 and 5.9, which narrows the transmittance modulation region. The dependence of σ_s on different particle sizes was also investigated (Figure 5.3(d)3), indicating that the enlargement of particle size is responsible for delivering a stronger scattering in the broad solar spectrum. On the other hand, the σ_a of pNIPAm-AEMA microparticles keeps a similar value (Figure 5.3(d)4), indicating that the transmittance is modulated via the enhancement of scattering, with respect to the increases in the real part of the refractive index, instead of absorbing.

5.3 Transmission Modulation by pNIPAm-AEMA hydrogel devices

To fulfill efficient light management for energy-saving purposes, the ideal thermochromic smart window requires a near-room-temperature transition and a sharp gradient of

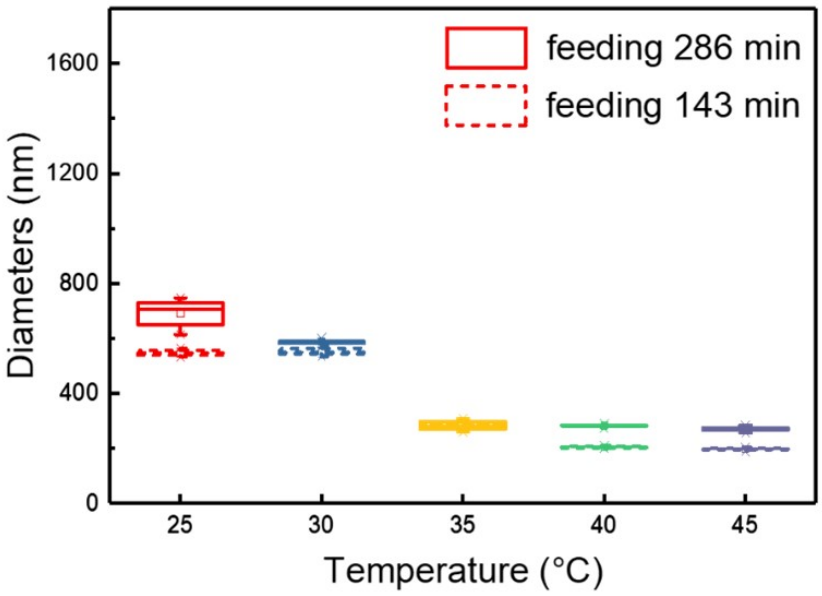

Figure 5.6: Size limitation of pNIPAm particles synthesized by continuous feeding method. Hydrodynamic diameters of pNIPAm particles synthesized by continuous feeding for 143min (dash box) and 286min (solid box) as a function of temperature. To carry out the polymerization for a longer time and a larger amount of monomers (100% increment). There is only 26% increase of D_h at 25℃ and 1.3% increase at 35℃.

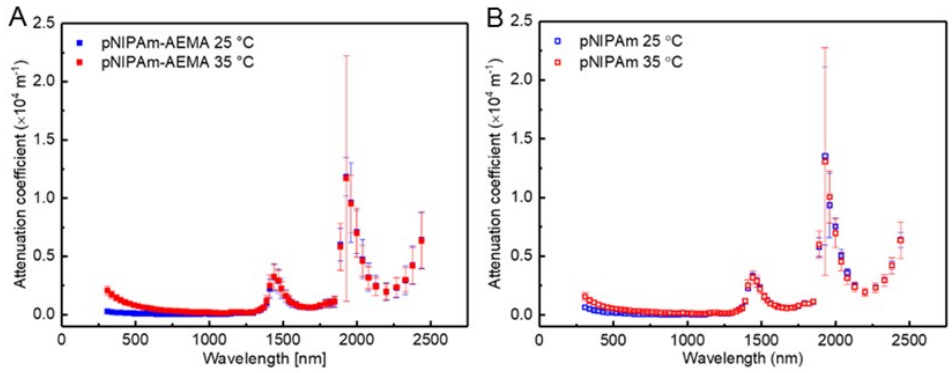

Figure 5.7: Attenuation coefficient of hydrogel particle suspension. (A) The attenuation coefficient of the pNIPAm-AEMA microparticle suspension, obtained from suspension with thicknesses of 130μm, 320μm, 470μm and 620μm. (B) The attenuation coefficient of the pNIPAm particle suspension, obtained from suspension with thicknesses of 130μm, 300μm, 460μm and 670μm. Error bars represent the 95% confidence intervals of fitted attenuation coefficients. Two peaks near 1450nm and 1930nm are associated with the strong absorption of water molecules.[15]

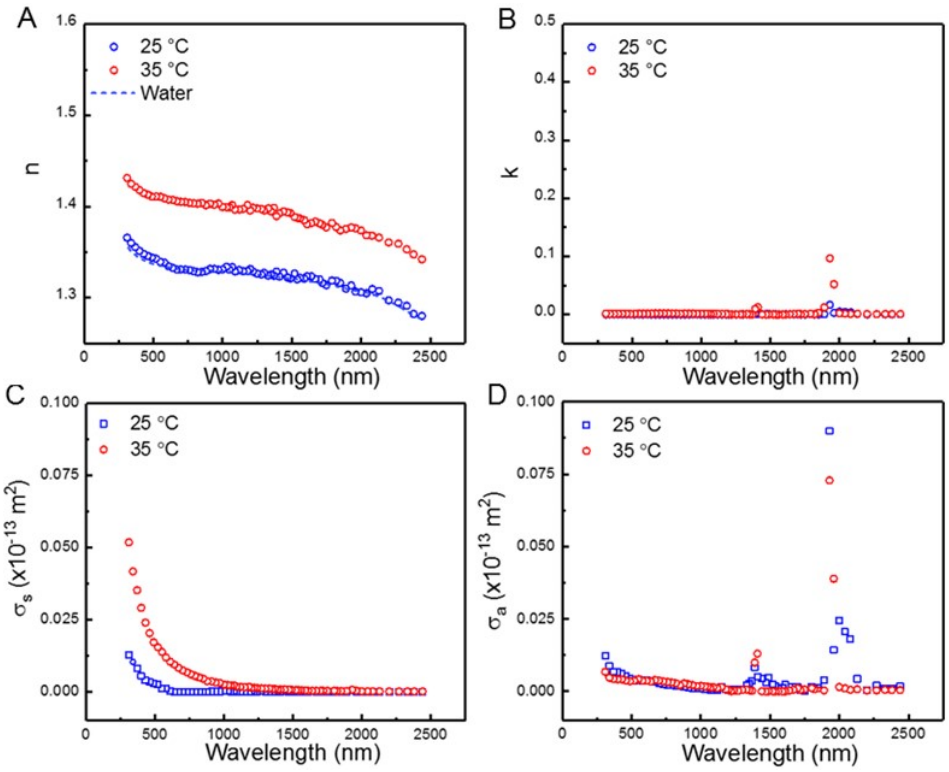

Figure 5.8: Optical properties of pNIPAm hydrogel particles. (A, B) Real (n) and imaginary (k) part of refractive index of the pNIPAm hydrogel particles at 25℃ and 35℃ obtained through the inverse method. The dashed line in (A) shows the n of water. (C, D) Corresponding scattering and absorbing cross-sections of the hydrogel particles at 25℃ and 35℃.

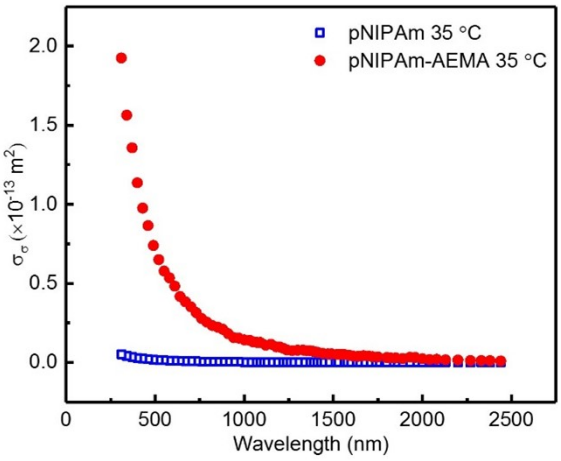

Figure 5.9: Comparison of scattering cross-sections between pNIPAm particles and pNIPAm-AEMA microparticles at 35℃.

transmittance.[183] The transmittance spectra of a pNIPAm-AEMA hydrogel device (250–2500 nm) at the layer thickness of 240 μm are reported in Figure 4A. At temperatures below LCST (22℃ or 25℃), the T_{lum}, T_{IR}, and T_{solar} are as high as 87.2%, 81.6%, and 85.1%, respectively (Figure 5.10). Figure 5.10(b) shows luminous (ΔT_{lum}), IR (ΔT_{IR}), and solar (ΔT_{solar}) transmittance modulations at different temperatures. The phase transition started at 31℃ along with a ΔT_{solar} of 26.2%, implying the strong temperature-responsive nature of pNIPAm-AEMA microparticles. Notably, at 34℃, the T_{IR} was significantly reduced from 81.6% to 6.0%, indicating an unprecedentedly high ΔT_{IR} of 75.6%. As a result, the ΔT_{solar} was boosted to 81.3%. Such a dramatic transition is desired for promptly blocking a large amount of solar irradiance.[183] In contrast, pure pNIPAm particles with small size (D_h = 548 nm at 25℃and 282 nm at 35℃) barely afforded transmittance modulation in the IR region (see Figure 5.11). The pNIPAm hydrogel layer with the same thickness (240 μm) only showed a low ΔT_{IR} of 32.1%, leading to a limited ΔT_{solar} of 59.1%. Although a hybrid of hydrogel with VO2 or antimony-tin oxide nanoparticles has been attempted to improve ΔT_{IR}, [13, 174] the operating temperature of metal oxide nanoparticle/hydrogel composite is as high as 80℃Ȧlso, the complicated fabrication procedures for both nanoparticle doping and composite preparation cause difficulties for practical application. Furthermore, the performance of the pNIPAm-AEMA hydrogel device regarding transmittance modulations is superior to all known VO2-based thermochromic materials and thermochromic films made by hydrogels, hydrogel/VO_2 composites, ionogels, and ligand exchange of thermochromic films.[161, 6, 1, 2, 3, 8, 12, 13, 171, 14, 172, 173, 174, 175]

The excellent light blocking by the pNIPAm-AEMA hydrogel device in the IR spectrum results from microparticles whose dimensionless size parameter ($2\pi r/\lambda$) reaches unity in the IR region. The IR light is effectively scattered by microparticles in the device with the layer thickness from thin (40 μm) to thick (380 μm) (Figure 5.12). By contrast, the transmittance modulation of pNIPAm particles is confined in the visible spectrum and is hardly improved by increasing the layer thickness (see Figure 5.12(b)).

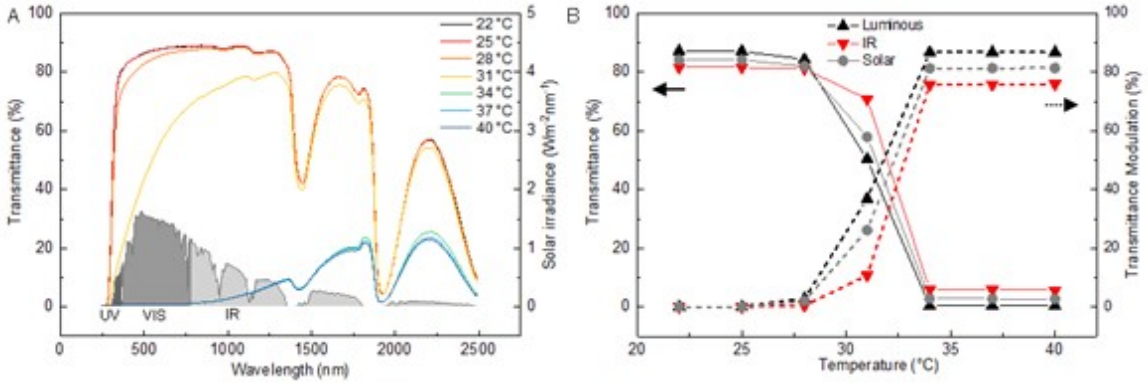

Figure 5.10: Characterization of the pNIPAm-AEMA hydrogel film. (A) Transmittance spectra of pNIPAm-AEMA hydrogel with a layer thickness of 240 μm at different temperatures. The inset is the solar irradiance spectrum (grey area). (B) The luminous (T_{lum}), IR (T_{IR}) and solar (T_{solar}) transmittances (solid line) and corresponding transmittance modulations (ΔT_{lum}, ΔT_{IR}, and ΔT_{solar}) (dash line) in response to the temperature.

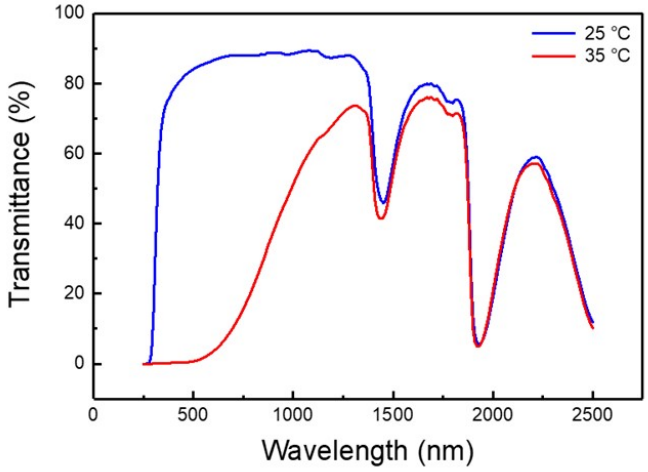

Figure 5.11: Transmittance spectra of the pNIPAm particles with a layer thickness of 240 μm before (25℃) and after phase transition (35℃).

A Monte Carlo simulation of the multiple scattering process based on Mie theory was applied to investigate the dependence of ΔT_{solar} on the layer thickness.[184] More details of the simulation algorithm are described in the Method section. The experimental results of transmittance modulation at different layer thicknesses were well reproduced (Figure 5.12 (c) and (d)), in which the estimated n and k of hydrogel particles were adopted. Owing to the broadband transmittance modulation, ΔT_{solar} of pNIPAm-AEMA hydrogel is higher than ΔT_{solar} of pNIPAm hydrogel for any given layer thickness (see Figure 5.13(a)). Meanwhile, the simulation shows the potential of pNIPAm-AEMA hydrogel of achieving a high T_{lum} and maintaining a decent ΔT_{solar} after phase transition by further reducing the layer thickness (see Figure 5.13(b)).

5.4 Solar energy shielding and device stability

Practical applications of smart windows raise the claims of reducing the solar gain and maintaining stability. A direct solar energy modulation was introduced to characterize the reduction of the heat flux from solar irradiance due to the phase transition of the window device (see Method section). The irradiance from a solar simulator was slashed by 69.5% after passing through a pNIPAm-AEMA device, which is significantly higher than all existing smart window products on the market (Figure 5.14).[185]

The pNIPAm-AEMA device was installed on a chamber, and the temperature change inside the chamber was recorded under 1 sun, air mass 1.5 illuminations (Figure 5.15(a)). The window made by double-glass slides was used as a control experiment, wherein the initial temperature of 25.0℃ rapidly increased to 39.1℃after 20 min and reached a plateau at 30 min (15.1℃ increments); whereas the phase transition of the pNIPAm-AEMA device was spontaneously triggered and completed after 5 min of illumination and the inner temperature only increased by 9.2℃ at 30 min. Notably, the inner chamber temperature rose merely 1.3℃once the phase transition of the pNIPAm-AEMA hydrogel was completed. A slight decline in temperature after the phase transition indicates a net negative heat gain inside the chamber induced by

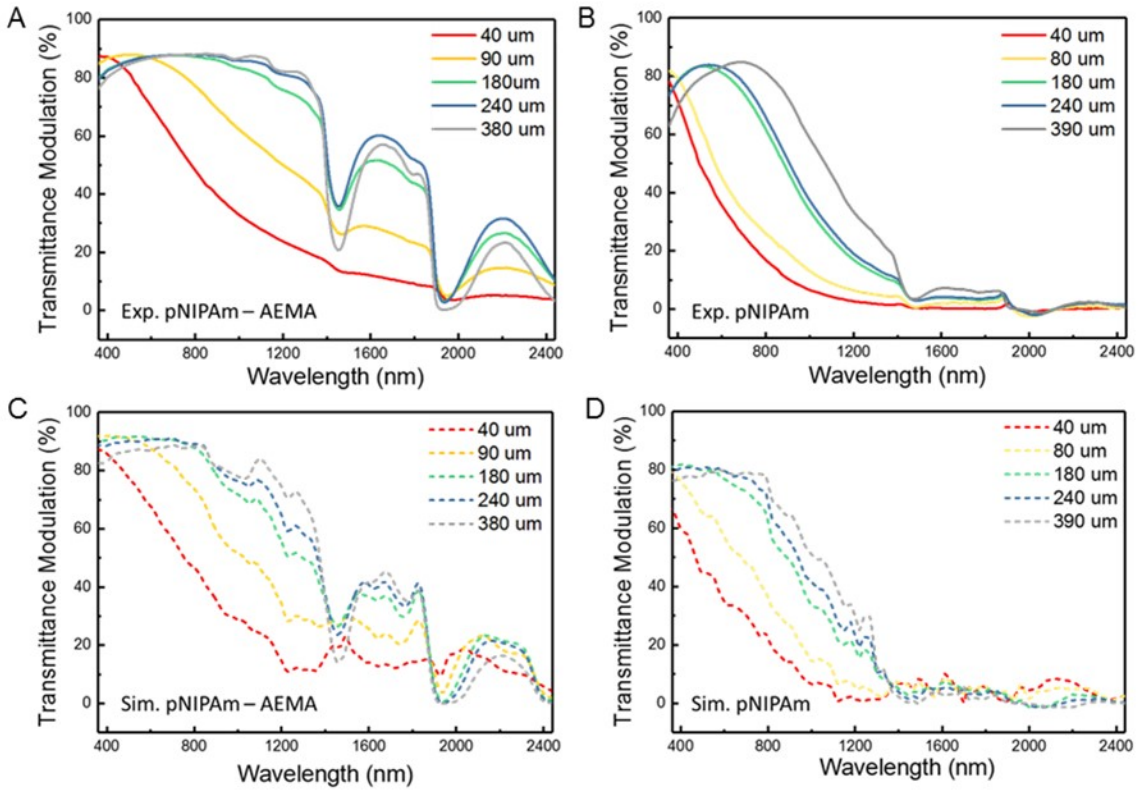

Figure 5.12: Transmittance modulation by pNIPAm-AEMA and pNIPAm hydrogel with different layer thicknesses. Experimental (A and B) and the Monte-Carlo simulation (C and D) results of transmittance modulation ($T_{25^\circ C} - T_{35^\circ C}$) by pNIPAm-AEMA microparticles with the layer thickness from 40 to 380 μm, and pNIPAm particles with the layer thickness from 40 to 390 μm. Large absorption of UV light by the double glass slides at the wavelength range below 360 nm causes the deviation between experiments and simulations, which is excluded in the figure. This deviation is negligible for the estimation of the solar modulation due to the small portion of solar irradiance in the UV region.

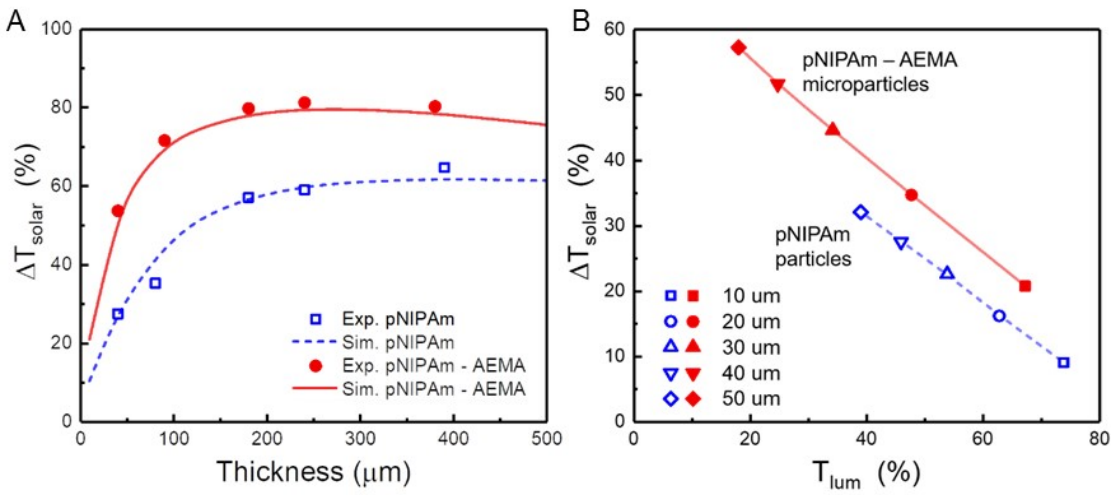

Figure 5.13: Thickness-dependent thermochromic properties of pNIPAm-AEMA and pNIPAm hydrogel. (A) Dependence of ΔT_{solar} on the layer thickness of the pNIPAm-AEMA and the pNIPAm hydrogel, obtained from the experiment and the Monte-Carlo simulation. (B) ΔT_{solar} and T_{lum} at 35℃ (after phase transition) of the pNIPAm-AEMA hydrogel and the pNIPAm hydrogel with the layer thickness from 10 to 50 μm, obtained from the Monte-Carlo simulation.

a sudden opacity change whereby the heat dissipation was more significant than the heat input from illumination. After 10 min of illumination, the outside temperature reached 40.9℃ and the inside temperature increased gradually due to heat conduction and convection. A smaller temperature rising rate of 0.10℃/min was delivered, compared with the rising rate of 0.26℃/min in the control experiment.

Figure 5.15(b)1 demonstrates visible transparency of the pNIPAm-AEMA device before and after phase transition, and Figure 5.15(b)2 shows the corresponding thermal IR images. The pNIPAm-AEMA device became opaque when the temperature rose to 35℃. In particular, the outstanding IR modulation of the pNIPAm-AEMA device was proved by the IR images (Figure 5.15(b)3). At 25℃, the near-IR (NIR) light (850–2,200 nm) passed through an "MIT" logo and was captured by the IR camera, whose intensity was significantly slashed once the phase transition was triggered, indicating an excellent ΔT_{TR}, which is barely obtained by VO_2 thin films and other kinds of thermochromic thin films.1, 9, 27, 30

A heating-cooling test of 1,000 cycles was conducted on the pNIPAm-AEMA de-

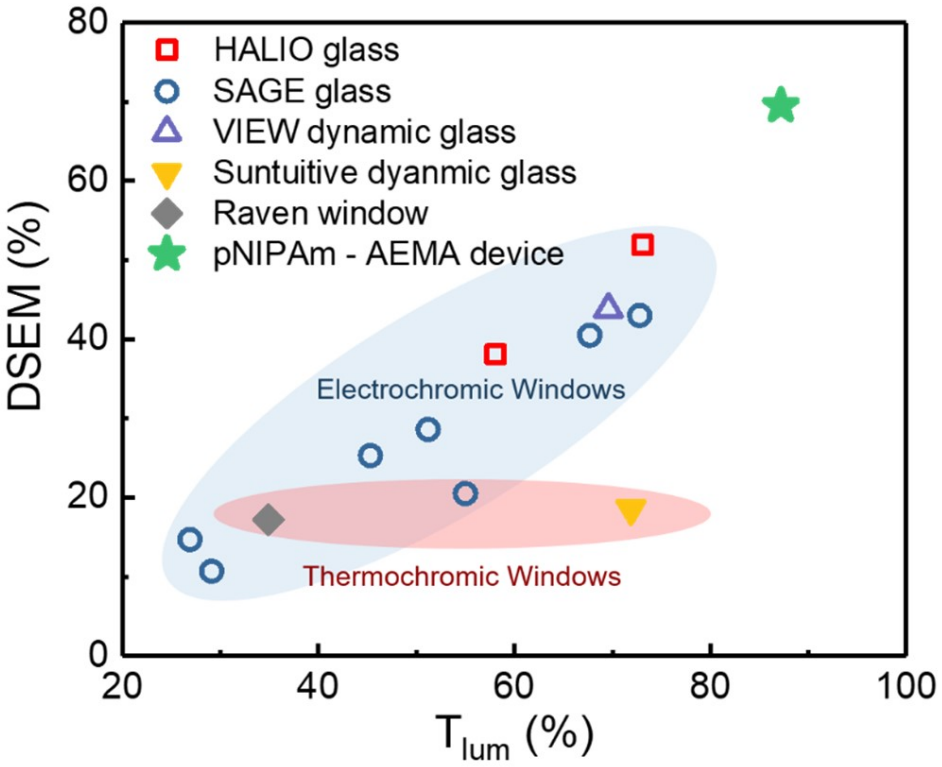

Figure 5.14: Comparison of direct solar-energy modulation (DSEM) and luminous transmittance (T_{lum}) between the pNIPAm-AEMA device with available smart dynamic windows on the market.2 Solid symbols represent thermochromic windows, while hollow symbols represent electrochromic windows.

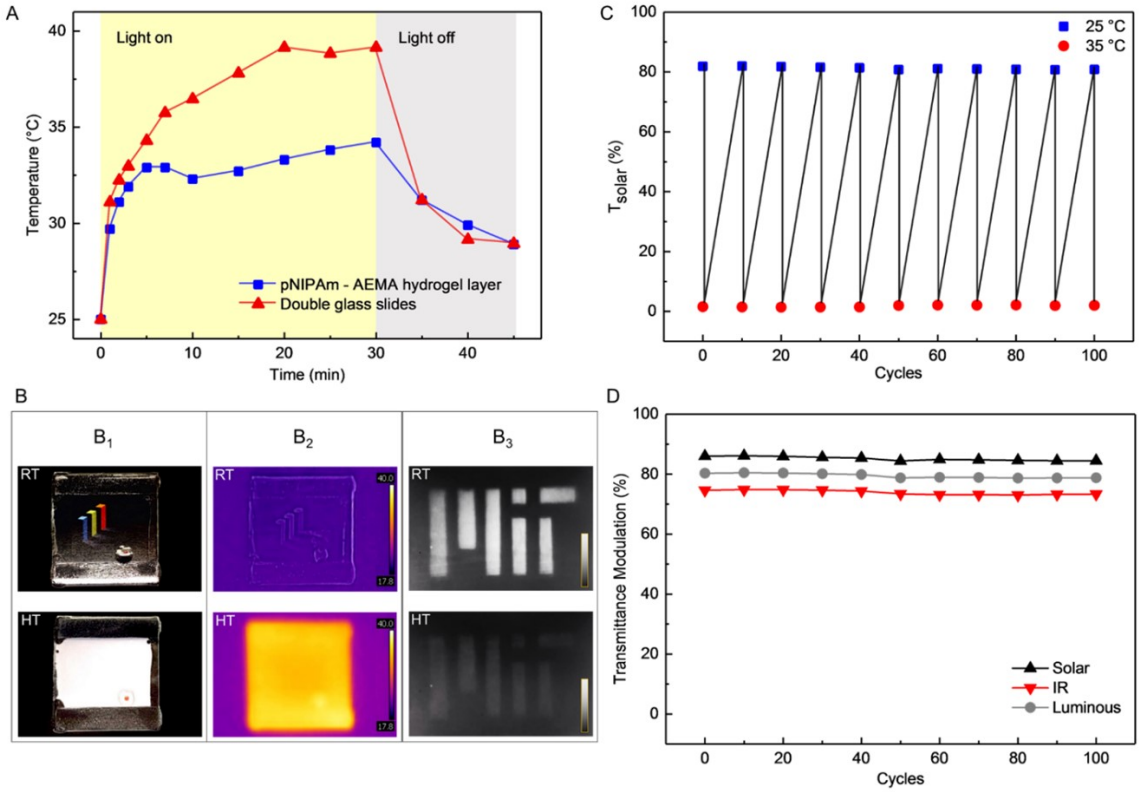

Figure 5.15: Solar-energy shielding performance of the pNIPAm-AEMA device. (A) Temperature profiles of a thermometer inside the model chamber affixed with double glass slides (red) or a pNIPAm-AEMA device as the window. (B1 – B2) Visible images and corresponding thermal infrared images of a 2" × 2" pNIPAm-AEMA device before and after phase transition. (B3) IR images of a pNIPAm-AEMA device under illumination of a NIR source (850 – 2000nm) captured by an IR camera. (C) The solar transmittance (T_{solar}) and (D) transmittance modulations (ΔT_{lum}, ΔT_{IR}, and ΔT_{solar}) of the pNIPAm – AEMA device (380μm layer thickness) measured after every 10 heating-cooling cycles.

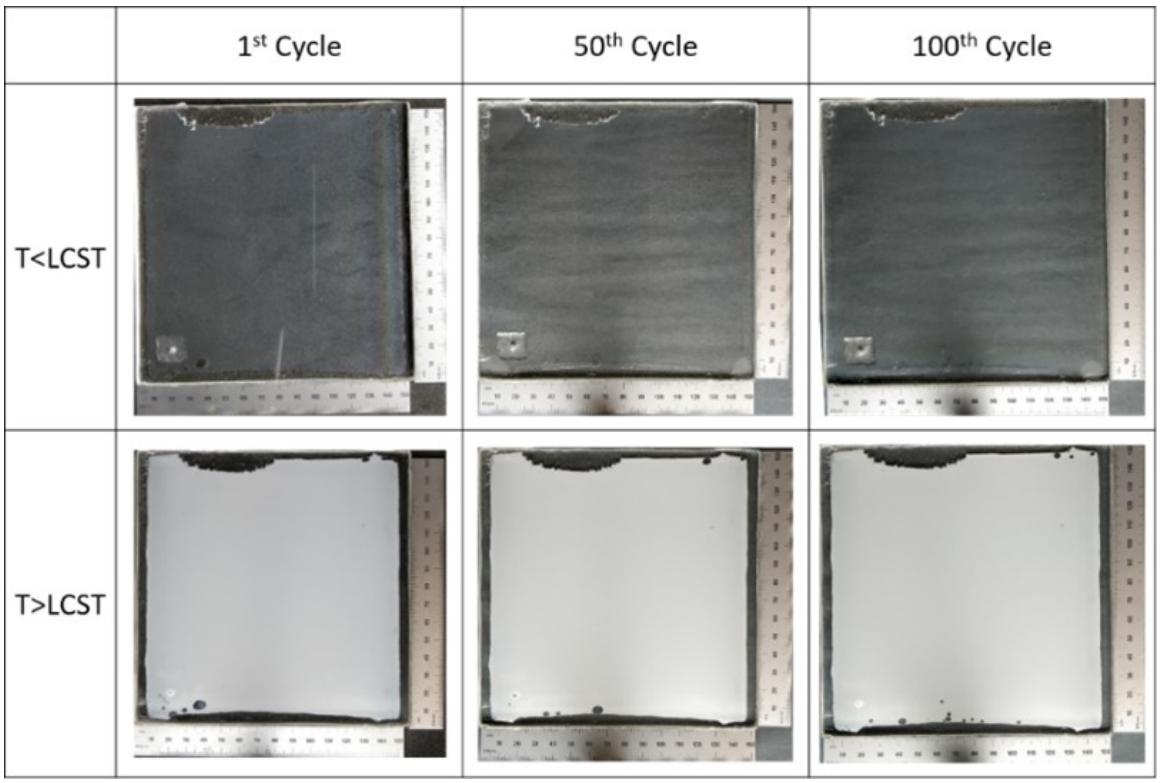

Figure 5.16: Visible Images of a 6" × 6" pNIPAm-AEMA device before and after phase transition captioned during 1st, 50th and 100th heating-cooling cycle.

vice to test its stability for long-term operation, which shows less than a 4% decrease in ΔT_{IR} (Figures 5.15(c) and (d)). Besides, no shrinkage of the hydrogel film was observed during heating-cooling cycles (see Figure 5.16). Such high stability regarding the number of testing cycles has not yet been reported, as most smart windows made by hydrogels suffer severe and non-reversible deformation after cycling tests.27, 30 Additionally, the pNIPAm-AEMA device maintained its transparency at -2.1℃, and the phase transition was reserved when the sample was heated to 32.1℃ (Figure 5.17).

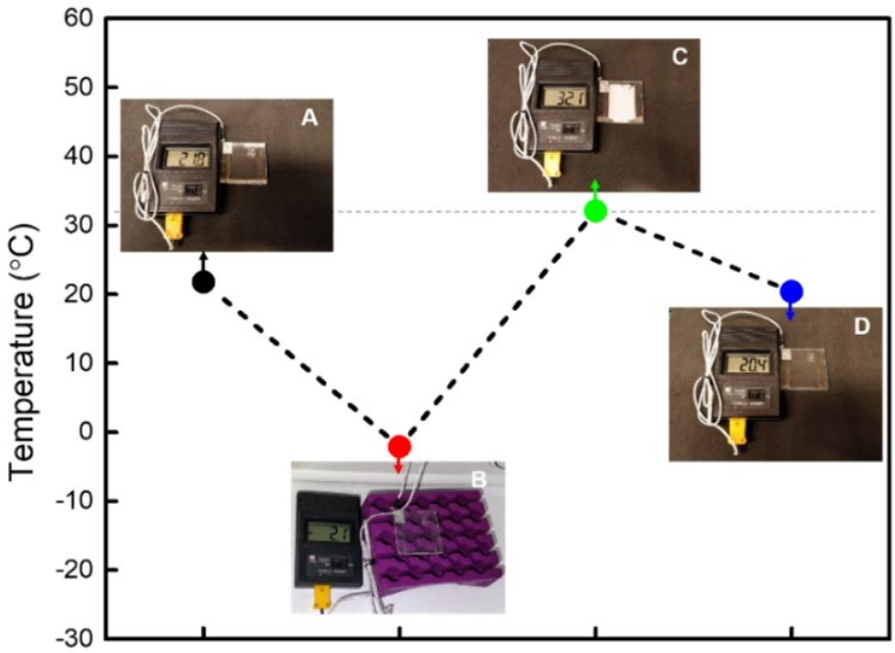

Figure 5.17: Optical images of a pNIPAm-AEMA device at temperature of (A) 21.8℃, (B) -2.1℃ (freezing at -4℃ for 5 min), (C) 32.1℃, and (D) 20.4℃.

5.5 Experiment and simulation methods

5.5.1 Materials

The N-isopropylacrylamide monomer (NIPAm, 98%), N,N'-methylenebis(acrylamide) (BIS, 99%) crosslinker, ammonium persulfate (APS, ≥98%) initiator, and SDS (≥ 98.5%) surfactant were purchased from Sigma-Aldrich. 2-Aminoethylmethacrylate hydrochloride monomer (AEMA, 95%) was purchased from Polysciences.

5.5.2 Synthesis of pNIPAm-AEMA microparticles

The pNIPAm-AEMA particles were synthesized by the continuous feeding of NIPAm and AEMA co-monomers into the reaction vessel. NIPAm (6.00 g), BIS (0.15 g), and AEMA (25.8 mg) were dissolved in 150 mL of deionized (DI) water and purged with N2 for 20 min. The one-fifth as-prepared solution was mixed with 60 mL of DI water and heated to 80℃, and 6 mL of 22.8 mM APS was added to initiate the polymerization. The remaining solution was continuously fed into the reaction vessel

at a rate of 1 mL/min, and the solution was sT_{IR}red intensively during the enT_{IR}e polymerization. The reaction was stopped after 75 min, and the colloidal suspension was quenched rapidly in a freezer. To improve the stability of colloid suspensions, we dissolved 0.87 mM SDS surfactant in the colloid suspension by ultrasonication after synthesis, keeping the temperature of the suspension below 30℃. The size of co-polymerized pNIPAm-AEMA particles was controlled by continuously feeding a constant concentration of co-monomers and predictably stopping the reaction at different feeding times (Figure 5.5).

5.5.3 Synthesis of pNIPAm particles

213ml DI water was heated to 80℃ and purged with N_2 during the enT_{IR}e reaction. Before the polymerization, two monomer solutions were prepared separately and degassed by vacuum at room temperature. The first batch of monomer solution consisted of 0.33g NIPAm and 6.69mg BIS in 13.7ml DI water and injected into the reaction vessel directly; while the second batch of the monomer solution was prepared in 21.75ml DI water with 3.36g NIPAm and 168mg BIS, which was transferred into a syringe. 0.76ml of 0.19M SDS was also injected into the reaction vessel and sT_{IR}red at 1000rpm. Whereafter, the polymerization was initiated by adding 0.76ml of 0.36M APS solution. After one minute, the second batch of the monomer solution was fed into the reaction vessel by a syringe pump at the rate of 200μl/min. The reaction was stopped after all monomers were fed and the suspension was quenched in the same way as for pNIPAm-AEMA microparticles. The effects of applying AEMA co-monomer and SDS surfactant in synthesis were elaborated in Figure 5.18.

5.5.4 Direct Solar-Energy Modulation (DSEM)

The direct solar-energy modulation (DSEM) was introduced to identify the solar-energy shielding ability in this work, which is the magnitude change of the total solar irradiance (mW/cm^2) passing through the window device before and after phase transition. Experimentally, the intensity of a solar simulator was calibrated

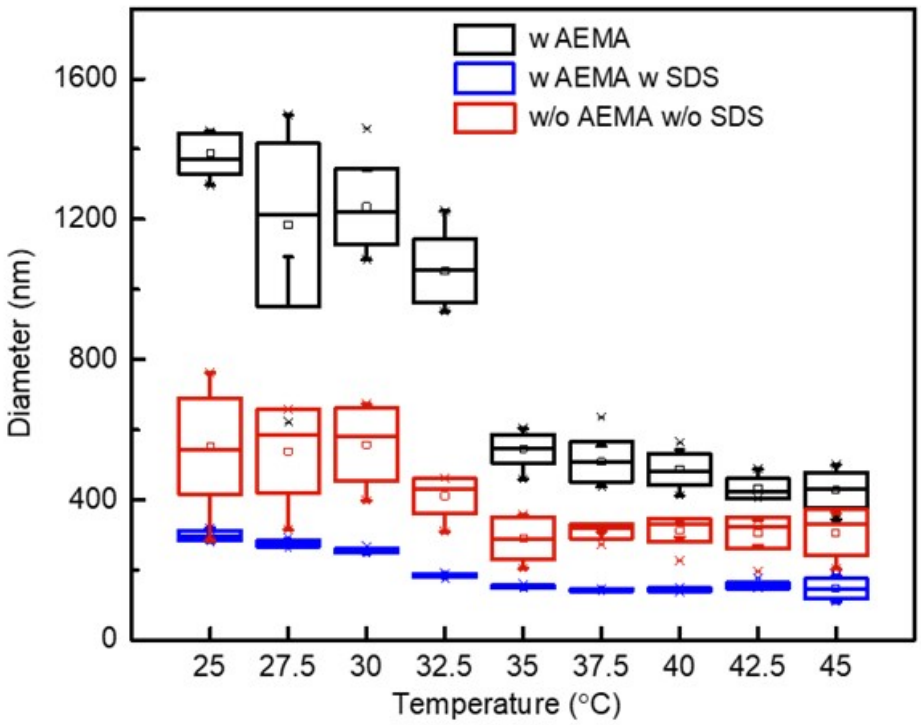

Figure 5.18: Effects of AEMA and SDS on the synthesis of microparticles. Hydrodynamic diameters of pNIPAm-AEMA (black; 1388nm at 25℃; 546nm at 35℃), pNIPAm-AEMA with SDS (blue; 298 nm at 25 ℃; 193 nm at 35 ℃, SDS was added during the continuous feeding polymerization), and pNIPAm (red; 555 nm at 25 ℃; 287 nm at 35 ℃) hydrogel particles. The three different batches were synthesized using the same method as mentioned in the experimental section. Adding AEMA comonomer is responsible for the increase of particle size while adding SDS surfactant during polymerization reduces particle size and avoids aggregation.[16]

to 100mW/cm^2 (one sun) on a crystalline silicon standard solar cell, upon which the pNIPAm-AEMA hydrogel device was installed afterward. A total acquisition of solar irradiance passing through the window device was guaranteed by this configuration.

5.5.5 Device fabrication

The hydrogel particles suspension was centrifuged at 13,000 rpm for 1.5 hr (Mini-iSpin plus, Eppendorf, Germany). The hydrogel thin-film devices were fabricated by injecting close-packed pNIPAm-AEMA or pNIPAm hydrogel particles in between double-glass slides, where the thickness of the layer was controlled by using thermoplastic sealing films (Meltonix 1170, DuPont Surlyn).

5.5.6 Characterization

Dynamic light scattering measurements were performed on a Dynamic Nanostar (Wyatt Technology, USA) with a laser at the wavelength of 658 nm. The hydrogel suspensions were diluted to 50 ppm and injected into UV-vis cuvettes (Eppendorf International). The diffusion coefficient (D) was obtained from the measured autocorrelation function, by which the hydrodynamic diameter (D_h) of a diffusion sphere was determined via the Stokes-Einstein Equation:[186]

$$D_h = \frac{kt}{3\pi\eta D} \tag{5.1}$$

where k is Boltzmann's constant, t is the absolute temperature, and η is the viscosity of the solvent. The temperature was controlled by a thermostat with an accuracy of ± 0.1℃.

DSC analysis was conducted on Discovery DSC (TA Instruments) over the temperature between 20℃ and 45℃ with a heating/cooling rate of 2℃/min under nitrogen flow. The closely packed hydrogel particles after centrifugation were applied to the DSC measurement without further treatment.

The transmittance spectra were collected using a Lambda 1050 UV-Vis-NIR spectrophotometer (PerkinElmer, USA) at normal incidence. The calculations of integral

luminous transmittance T_{lum} (380–780 nm), IR transmittance T_{IR} (780–2,500 nm), solar transmittance T_{solar} (280–2,500 nm), and corresponding transmittance modulations can be found in Equations 5.2 and 5.3, respectively:13

$$T_{lum/IR/solar} = \frac{\int \phi_{lum/IR/solar}(\lambda)T(\lambda)\,d\lambda}{\int \phi_{lum/IR/solar}(\lambda)\,d\lambda} \tag{5.2}$$

$$\Delta T_{lum/IR/solar} = T_{lum/IR/solar}(@LT) - T_{lum/IR/solar}(@HT) \tag{5.3}$$

where $T(\lambda)$ denotes the recorded transmittance at a particular wavelength, ϕ_{lum} is the standard luminous efficiency function for the photopic vision of human eyes,[187] and $\phi_{IR/solar}$ is the IR/solar irradiance spectrum for air mass 1.5.21

The solar energy shielding test was conducted on a model chamber with a dimension of 0.15 × 0.10 × 0.08 m^3, which was covered by rigid melamine insulation sheets. The 0.04 × 0.05 m^2 window devices made by bare double-glass slides or the hydrogel device with a layer thickness of 380 μm were assembled upon the model chamber. The illumination intensity of a standard solar simulator (Peccell PEC-L01, Japan) was calibrated to air mass 1.5 illuminations (100 mW/cm^2) on the top side of the window. The temperatures inside and outside of the chamber were measured simultaneously by a thermometer. The IR thermal images were recorded via a thermal imaging camera (FLIR Systems, USA). The IR images were captured by an IR camera (IR camera 85400, FJW Optical Systems, USA) with sensitivity from 400 to 1,800 nm. A NIR bulb incorporated with a long-pass filter (850–2,200 nm, Throlab FEL0850) was utilized as the irradiation light source for the demonstration of IR modulation

5.5.7 Evaluation of optical properties of hydrogel particles

The scattering cross-sections of the hydrogel particles were evaluated with an inverse method based on Mie theory.[181] On the basis of Beer-Lambert law,[182] the attenuation coefficient (μ_t) of a low-concentration particle suspension could be obtained by determining the linear dependence of $ln(T)$ on the thickness of suspension (d), [182]

$$\mu_t(\lambda) = -\frac{\Delta ln(T(\lambda))}{\Delta d} \tag{5.4}$$

The attenuation coefficient is determined by scattering and absorbing, [182]

$$\mu_t(\lambda) = \mu_s(\lambda) + \mu_a(\lambda) \tag{5.5}$$

$$\mu_s = c\sigma_s \tag{5.6}$$

$$\mu_a = c\sigma_a + \frac{4\pi k_w}{\lambda} \tag{5.7}$$

where μ_s and μ_a are the scattering and absorbing coefficient, respectively, and σ_s and σ_a denote the scattering and absorbing cross-section, respectively. c is the concentration of particles and kw is the imaginary refractive index of water.[188] The transmittance of 10 wt% as-synthesized suspensions with thickness from 130 to 670 μm was measured to determine the attenuation coefficient. We made the assumption that the particles at swollen state are incompressible. The concentration of the hydrogel particles was estimated by measuring the volume of particles after removing the surrounding water by centrifuging and dividing by $1/6(\pi D_h^3)$. The scattering and absorption cross-sections of hydrogel particles were calculated based on a modified Mie scattering code.[181] Here the fitted refractive index was chosen to keep the continuity of the real part (n) through both the visible and IR regions and to achieve a relative error of less than 1% between the fitted and measured attenuation coefficients. Step sizes of 10^{-4} in n and 10^{-6} in the imaginary refractive index (k) for the visible region and 10^{-5} for the IR region were used in the fitting.

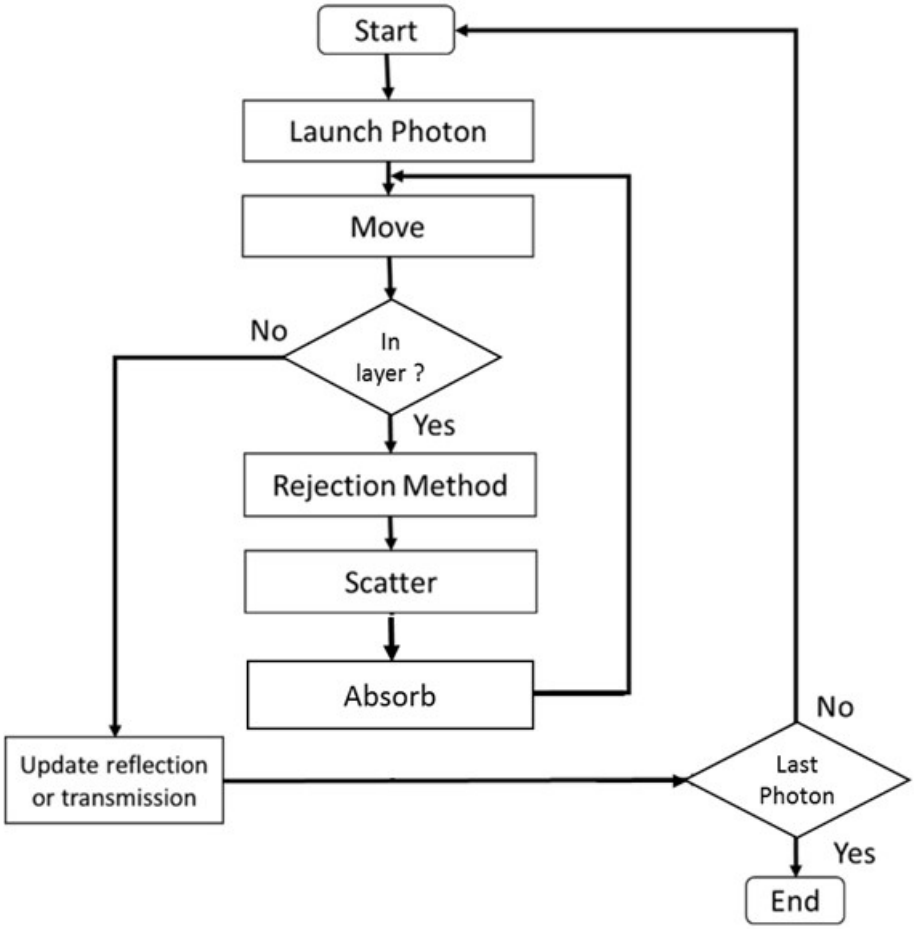

Figure 5.19: Logic flow of the Monte-Carlo simulation.

5.5.8 Simulation of multiple scattering in the thin hydrogel layer

The thickness-dependent ΔT_{solar} of the hydrogel smart window devices was investigated by experiments and a modified Monte-Carlo simulation.[184] ΔT_{solar} of the devices with the layer thickness ranging from 40 to 390 μm were measured. In the simulation, the effect of randomly distributed hydrogel particles on the propagation of light is modeled as multiple scattering and absorbing events. The logic flow of the modified Monte-Carlo simulation is provided in Figure 5.19.

A single photon was launched at the upper boundary of the hydrogel layer in each run, with a normal propagation direction to the surface. Then the photon moves until it is reflected by or transmits through the hydrogel layer. For each moving step, the

photon travels a random distance of ΔS, whose mean value is the same as the mean free path of the photon in this medium:[184]

$$\Delta S = -\frac{ln(\zeta)}{\mu_s + \mu_a} \tag{5.8}$$

where ζ is a pseudo-random number locates in (0,1]. $1/(\mu_s + \mu_a)$ is the mean free path of photons in the hydrogel layer. The concentration of the close-packed hydrogel particles after centrifuging was estimated as $6/(\pi D_h^3)$. The scattering and absorbing cross-sections of pNIPAm-AEMA microparticles and pNIPAm particles estimated through the inverse method were applied to determine the μ_s and μ_a.

The photon changes the propagation direction after each moving step as the scattering occurs. The new propagation direction is determined by a rejection method following the phase function $P(\theta)$ of Mie theory, where θ denotes the scattering angle.[184] Basically, two pseudo-random numbers are generated, which are the random scattering phase function (P_{rand}) and the random scattering angle (θ_{rand}). The random scattering angle is accepted as the propagation direction for the next moving step if $P_{rand} \leq P(\theta_{rand})$. Otherwise, new P_{rand} and θ_{rand} will be generated until the new propagation direction is determined. The light absorption by water inside and outside the hydrogel particles is modeled with a weight function W applied on the photon,[184] where the original weight W_0 before launching is 1. To avoid the inaccuracy near the wavelength of 1450nm and 1930nm, the weight attenuation after nth moving step is accounted as,

$$W_n = W_{n-1} exp(-\frac{4\pi k_w}{\lambda}\Delta S_n) \tag{5.9}$$

where ΔS_n is the nth moving distance. The moving steps repeat until the photon travels out of the upper or lower boundary of the hydrogel layer with a specific weight. Reflectivity (R) of normal incidence at the boundary of two materials with the reflective index of n_1 and n_2 is

$$R = [\frac{n_2 - n_1}{n_2 + n_1}]^2 \tag{5.10}$$

$n_{glass} = 1.5$,$n_{water} = 1.33$ and $n_{air} = 1.0$ were used to estimate the reflectivity at the boundaries between glass and air (R_{ga}) and the boundaries between the glass and the hydrogel layer (R_{gh}). A total transmittance of 92% was obtained, where the multiple reflections between boundaries are negligible.

$$T = (1 - R_{ga})^2(1 - R_{gh})^2 \approx 92\% \tag{5.11}$$

5×10^3 photons were simulated for each wavelength to obtain the ΔT_{solar} with fluctuations less than 0.5%.

The dependence of ΔT_{solar} on the layer thickness for pNIPA-mAEMA and pNIPAm hydrogel was shown in Figure 5.13. The ΔT_{solar} of the pNIPAm-AEMA hydrogel raised with the increasing of the layer thickness, which is apparently higher than that of the pNIPAm due to the extending of scattering into the IR region. The maximum ΔT_{solar} of 81.3% was attained at 240 μm for the pNIPAm–AEMA, while the pNIPAm achieved the maximum ΔT_{solar} of 65.8% at 390μm. Further increase of thickness caused a reduction in ΔT_{solar} Since the transmittance in the visible region is decreased, and the water absorption in the IR range is saturated before the phase transition. A high T_{lum} of the thermochromic layer after phase transition is required in some situations.[12] The thickness of the hydrogel layer needs to be reduced to improve the T_{lum} at high temperatures. Figure 5.13 b shows the Monte-Carlo simulation results of the ΔT_{solar} and T_{lum} at 35℃ for devices with the layer thickness from 10 to 50μm. At the same T_{lum}, the ΔT_{solar} of the pNIPAm-AEMA hydrogel is higher than that of the pNIPAm hydrogel due to the full solar spectrum modulation. Besides, the layer thickness of the pNIPAm-AEMA hydrogel to achieve a specific ΔT_{solar} is smaller than that for the pNIPAm hydrogel. This simulation shows the potential of the pNIPAm pNIPAm-AEMA hydrogel to achieve a high T_{lum} of 50% after phase transition and a decent ΔT_{solar} of 30% by decreasing the layer thickness to 20 μm, which requires precise packaging method and is beyond the scope of this work.

5.6 Summary

In summary, a new type of light-management device based on thermochromic pNIPAm-AEMA microparticles has been demonstrated. The large and broadband transmittance modulation makes the device ideal for energy-saving applications. Especially by tailoring the particle size and internal structure, the pNIPAm-AEMA hydrogel effectively extends light rejection into the IR region, contributing to a significantly enhanced ΔT_{IR} of 75.6% and an ultra-high ΔT_{solar} of 81.3%. Meanwhile, the superiority of hydrogel over conventional VO2-based thermochromic materials are maintained, exhibiting a high T_{lum} of 87.2% and a low phase-transition temperature of ∼32℃. A decline of the indoor temperature of ∼5℃ can be expected by using the pNIPAm-AEMA thermochromic windows, whose excellent stability and scalability also display its prospect of practical applications. Building upon the advancement of light management in the use of pNIPAm-AEMA microparticles over counterpart thermochromic materials, future progress in dynamic transmittance modulation is enabled by pursuing the optimal mechanism that leads to the change in the refractive index. The tunable scattering behaviors of hydrogel particles not only pave a way to revamp energy-saving smart windows but will also be broadly applicable to optical modulators, displays, and invisibility cloaking.[189, 190].

Chapter 6

Projection lithography patterning of pixelated quantum dots / photopolymer

6.1 Introduction

Artificial neural networks with linear connectivity and nonlinear activation functions can model any relations between the input and targeted output [191]. In Chapter 3, we proposed a linear optical recurrent network in the form of a scattering reservoir. However, the nonlinear activation function is missed in the model. In general, optical nonlinearity can be achieved with saturable absorbers [192], electro-optical modulator [193], Fano resonator [194], etc. Integrated photonic circuits with embedded activation units have been developed based on these physical nonlinear effects [195]. On the other hand, free-space optical neural networks still call the development of 2D/3D patterning techniques to embed the non-linear activation layer [196, 197]. For example, a diffractive neural network faces challenges in extending its functionalities with customizable activation functions [44]. In this chapter, we demonstrated a projection lithography method for 2D patterning of QDs/Photopolymer composite. The method can achieve high resolution patterning down to $<$ 10 um scale with the

potential for large-scale manufacturing. We further applied this method to directly patterning QDs color converters on top of blue micro-LEDs for the application of high-resolution displays.

Downconversion of blue/UV micro-LEDs with sub-100 μm pixel size to emit longer-wavelength colors draws increasing attention, for the broad applications including high-resolution wide-gamut display, [198, 199, 200] automotive adaptive front-lighting, [201, 202] high bandwidth visible light communication, [203, 204, 205] and spectral / spatial-sensitive optogenetic stimulation.[206, 207, 208] Quantum dots (QDs) outperform other down-conversion materials due to their high efficiency, tunable narrow-band emission, broad absorption spectra, and fast photoluminescence (PL) decay times. [209, 210, 211] Patterning QDs color converters on blue/UV micro-LEDs can also simplify the manufacturing procedure and reduce product defect rate compared to integrating red, green, and blue-emitting micro-LEDs on a single chip. [147, 212, 213] Ink jet, [214, 215] aerosol jet [212, 216] and photo-lithography [213, 217, 218] methods have been applied to pattern QDs converters on blue/UV micro-LEDs with sub-100 μm pixel size. However, challenges still remain to generate high-resolution color-selective patterns compatible with the advanced III-Nitride blue/UV micro-LEDs with pitch and pixel size approaching $\sim$10 μm, [219, 220, 200] meanwhile to mitigate the drop of photoluminescence (PL) due to aggregation at high QDs loads and host material effects. [221]

Inkjet and aerosol jet printing rely on solvent-based drop-casting with nozzles followed by solvent removal. These methods have only been able to pattern QDs pixels with la limited size of $\sim$50 μm. [212, 216] Meanwhile, the aggregation of QDs and coffee-ring effects after solvent evaporation lowers the light conversion efficiency and emission uniformity. [216, 221] Due to the fluidity of the solution-phase QDs ink, the patterned pixels are usually limited to circular shapes, [215, 214] and color crosstalk may happen during the patterning process. [212] Furthermore, ink jet and aerosol jet printing are not efficient, for the low patterning speed (up to 200 μm/s) of these serial methods. [214]

Conventional photo-lithography patterning requires multiple steps of thermal treat-

ments and developer washing to pattern QDs/photoresists composites with high-resolution of ∼20 μm pixel size. [213, 217, 218] High QD loading in thin films is required to achieve full conversion of blue/UV light. [222, 223] However, the aggregation of highly concentrated QDs during polymerization of the polar photoresists can increase scattering and non-radiative decay mechanisms, which reduces the PL efficiency. [213, 222] Besides, the incompatibility between QDs and photoresists, also known as host material effects, can cause the degradation of QDs' surface passivation, [224] which further reduces the PL efficiency and lowers the re-usability of QDs suspended in uncured photoresists. Furthermore, the omnidirectional emission of QDs raises the issue of color crosstalk due to unintentional excitation from light leakage and coupling through the sides of nearby pixels. [225]

The aforementioned issues call the careful choice for patterning techniques along with host materials for QDs color converters. In this paper, we demonstrated direct projection lithography of pixelated red and green QDs/thiol-ene photo-polymer composite with a UV digital light processing (DLP) printer for color down-conversion of blue LEDs. The DLP projection lithography provides a scalable and air-processing patterning procedure with high resolution. We were able to achieve sub 25 μm square pixels array with 30 μm pitch and sub 10 μm thickness. The smallest pixel size can go down to 6 μm with the DLP printing setup. Meanwhile, a wide view angle approaching the Lambertian emission profile and 95% color gamut coverage of DCI-P3 standard is achievable. The choice of thiol-ene photo-polymer as the host material and quantum dots capped with amine surface groups facilitates the uniform dispersion of QDs in the cured polymer matrix, reduces aggregation, and partially mitigates the drop of PL efficiency. Compared with the drop-casting method, the QDs/NOA86 composite improves PL quantum yield (PLQY) by 0.5-1 times at high QDs loads (25 to 100 mg/mL). Furthermore, we also demonstrated color crosstalk reduction through projection lithography patterning of light-absorbing walls between nearby pixels.

6.2 Projection lithography method & choice of QDs / supporting matrix

6.2.1 Synthesis of QDs/photopolymer composite

NOA86 from Norland Optics was used as the photo-polymer matrix in this study. Green (QSP-520) and red (QSP-620) emission CdSe/ZnS core-shell QDs powder capped with octadecylamine surface group were purchased from Ocean Nanotech. QDs powder was firstly dispersed in chloroform ($\geq$ 99%, Sigma Aldrich) to 5 mg/mL. Then NOA86 were added to form QDs/NOA86 composite with final concentrations of 25, 50, 75, and 100 mg/mL after chloroform removal under reduced pressure.

6.2.2 Direct patterning with projection lithography

The components schematic of the projection lithography printing system are shown in Figure 6.1(a). It contains an inverted optical microscope (IX71, Olympus) with a 2-axis motorized stage system (ProScan III, Prior Scientific) of sub 0.1 μm positioning resolution, a DLP projector (PRO4500, Wintech) with 405 nm UV LED, and a high-resolution digital micro-mirror device (DMD) as the light source and dynamic mask. Patterns reflected by the DMD were guided by the optics and focused through the 20X/0.25 objective lens (Olympus) onto the 2-axis printing stage. The optics were aligned so that the optical path between the DMD and the objective lens is the same as the optical path between the observing CCD and the objective lens. Therefore the system could fulfill pattern alignment and UV projection simultaneously.

Figure 6.1(b) shows the schematic of patterning procedures of red and green QDs color converters on the blue micro-LEDs array. QDs/NOA86 composite (5 μL in the experiment) is drop-cast onto the substrate, followed by chloroform removal under reduced ambient pressure. The QDs/NOA86 composite forms a thin layer of liquid film over the printing area, as in subplots II and IV. UV exposure of the pixel pattern cures the thin layer of the QDs/NOA86 composite under the projected area. The uncured composite is rinsed away with IPA and the substrate is blow-dried with air, resulting

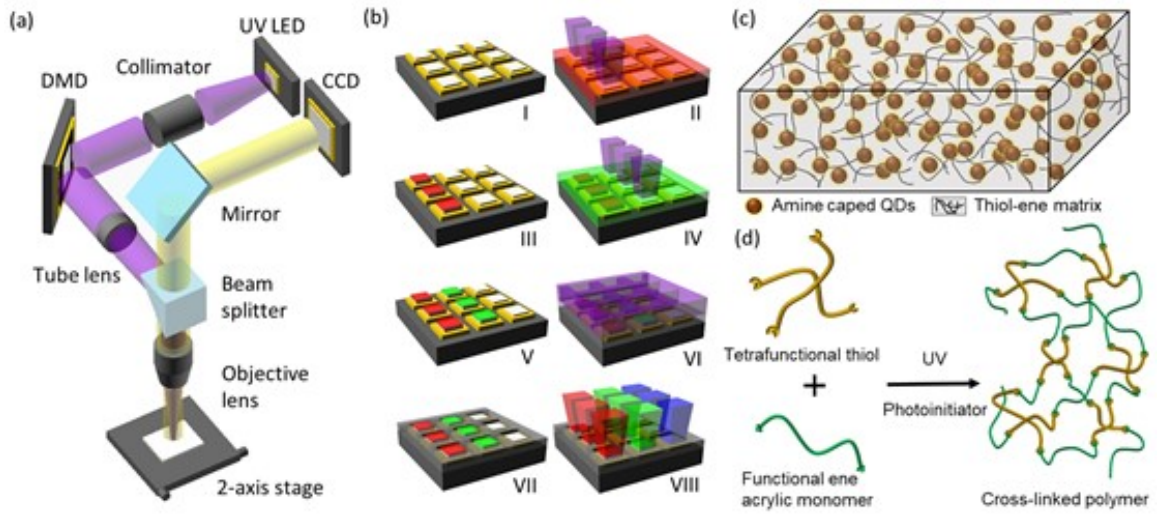

Figure 6.1: (a) Schematic of the UV DLP projection lithography printing system. (b) Schematic of patterning procedure of red (I-III) and green (IV-V) color converters on blue micro-LED array with black matrix (VI-VII) for RGB full color display (VIII). UV pattern projections are shown as the purple square beams. (c) Schematic microstructure of QDs/NOA86 composite films, consisting of cross-linked thiol-ene polymer matrix and amine capped QDs. (d)Schematic of thiol-ene reaction under UV initiation to form the polymer matrix.

in the pixelated color converters, as shown in subplots III and V. Figure 6.1(c) shows the microstructure of cured NOA86 thin films with high QDs load. The thiol-ene reaction process is shown in Figure 6.1(d). NOA86 contains tetrafunctional thiol, acrylic monomers with at least 2 -ene functional groups, and UV/visible sensitive photoinitiator (proprietary formula/ingredients). The thiol-ene reaction is initiated with the 405 nm UV projection. Then it propagates with bonds formation between thiyl radical and ene functional groups and eventually forms the cross-linked polymer matrix. Due to the amine surface group, the QDs are not likely to be involved in the thiol-ene polymerization, which prevents the phase separation and QDs aggregation. [222] Here we further demonstrate the patterning of light-blocking walls between pixels as "black matrix" for color crosstalk reduction, as shown in Fig. 1(b) subplots VI-VIII. The details of exposure time and intensity are listed in the following result sections.

6.2.3 Instrumentation and characterization

Fluorescence and white light photos of the printed pattern were taken under a microscope (OMFL600, OMANO) with a 100W mercury arc lamp as the UV source. The dimensions of the patterned pixel array were measured with a profilometer (DektakXT, Bruker). Fluorescent emission spectra, peaks, and full width at half maximum (FWHM) was measured by spectrofluorometer (Fluorolog-3, Horiba) with integration sphere (Quanta-phi, Horiba) at 400 nm excitation (FWHM of 4 nm). PLQY was calculated following the method developed by de Mello and others. [226] Absorption spectra of the QDs/NOA86 composite were measured with a UV-VIS-NIR spectrophotometer (Lambda 1050, Perkin Elmer).

The angular emission intensity was measured with a homemade setup. An optical fiber adapter (SM1SMA, Thorlabs) on a rotation stage was placed 5 cm away from the samples of blue LEDs covered with pixelated color converters, which was centered at the rotation stage. Fluorescent emission collected by the small aperture on the adapter was guided through an optical fiber (QP600-1-VIS-NIR, Ocean Optics) into a spectrometer (USB2000+, Ocean Optics). The angular emission was measured at a step of 5° from -90° to 90° relative to the normal of the sample plane.

The evaluation of color crosstalk reduction was done by comparing the intensity of fluorescence signals (red or green channel values) before and after patterning the light-blocking walls between pixelated color converters. The signals were collected by a digital camera (EOS60D, Canon) with fixed shutter speed, aperture, and ISO.

6.3 Full-color conversion layer patterning on blue micro-LEDs

Figure 6.2 shows the pixelated QDs/NOA86 color converters patterned by the projection lithography method. The concentration of red and green quantum dots is 100 mg/mL. The exposure time is 1.0 s, and the exposure intensity is 63 mW/cm^2. The white light and UV fluorescent microscope pictures show the high patterning

resolution with a pitch size of 30 μm and pixel size of 21 μm for red pixels as shown in Figs. 2(a)–2(b), and 22 μm for green pixels as shown in Figs. 2(c)–2(d). The size and shape of the pixels could be tuned by adjusting the projected pattern. As shown in Fig. 2(e), square pixels with a size of about 40 μm to 6 μm could be achieved. The patterning resolution of the presented mask-less projection lithography system is limited by the pixel size of the DMD chip and the de-magnification factor of the scaling lens system, i.e. the ratio between the equivalent focal lengths of the collimator tube lens and the objective lens. [227] On the other hand, the imaging quality is affected by multiple factors including optical aberration, [227] non-uniformity of the light source illumination on the DMD, [228] exposure dose control over the projected pattern, [229] etc. Applying the same printing procedure with a scaling lens system of smaller de-magnification factor and DMD with smaller pixel size can improve the patterning resolution. Meanwhile, aberration-correction, [227] illumination uniformity improvement [228] and gray-scale DMD exposure dose modulation [229] could help to compensate for the loss of image quality at a lower de-magnification factor. Figure 2(f) shows the capability of patterning pixels with a wide range of shape choices, including star, hexagon, circle, triangle, and square. All pixels shown in Figs. 2(a)–2(f) were patterned on top glass slides. Figures 2(g)–2(h) demonstrate the capability of multi-material printing for full-color conversion with red and green QDs on a blue LED substrate. Figure 2(h) was taken with a 500 nm long-pass filter (FEL0500, Thorlabs), under the back illumination of the blue LEDs. Size and color conversion efficiency variance across the patterned pixels could be observed in Figs. 2(g)–2(h). The limitation on uniformity may be caused by the aforementioned factors affecting the image quality. Challenges remain for mass production with the full-color conversion of such systems despite being demonstrations of blue micro-LED pixels down to 1-2 μm. [230] Further, pixel-level calibration and correction of electrical driving current and optical leakage are required to reduce the overall color conversion variance. [200]

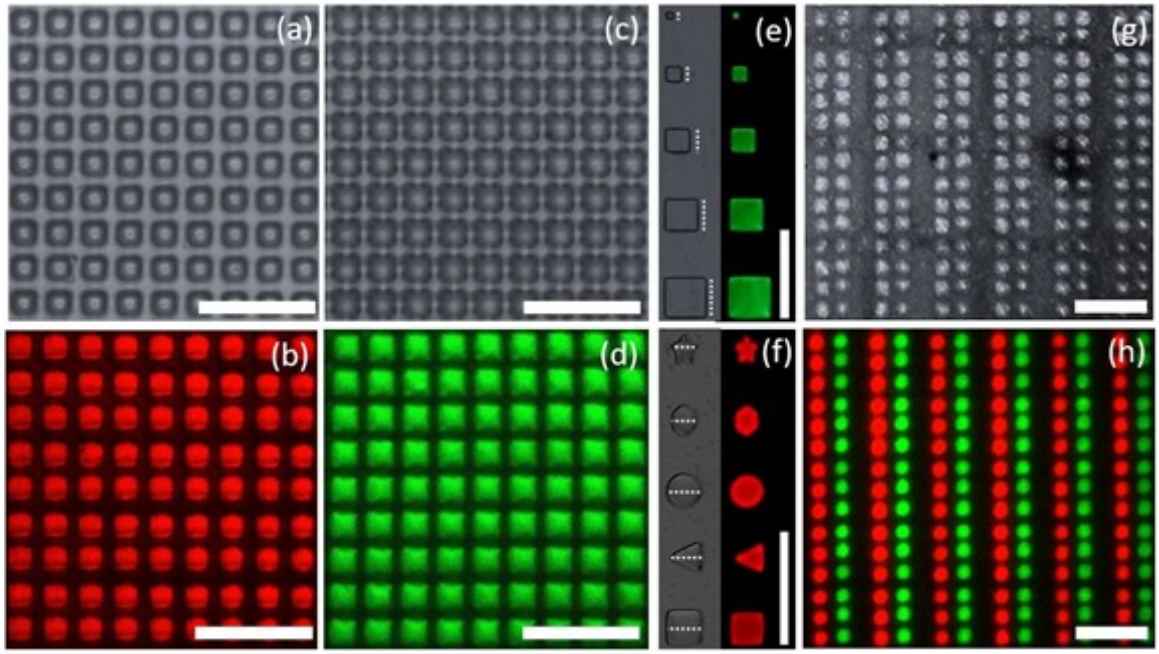

Figure 6.2: Microscope photos of QDs/NOA86 pixels patterned by projection lithography. (a-d)White light and UV fluorescent images of red as and green square pixels. (e, f) Patterned pixels with various sizes and shapes. The representative feature dimensions are marked by the white dash lines in Figs. 2(e)-2(f). In (e), the dimensions are: 43 μm, 30 μm, 22 μm, 15 μm and 6 μm, from large to small. In (f), the dimensions are: Star: 26μm; Hexagon: 27 μm; Circle: 30 μm; Triangle: 28 μm and Square: 30μm. (g, h) Direct patterning of multi-color pixels on blue LED substrate. All scale bars are 100 μm.

6.4 Integration of QDs onto blue LED for color down conversion

We patterned pixelated red and green QDs/NOA86 (QDs concentration of 50 mg/mL) color converters directly on 0.5 mm by 0.5 mm blue LED chips, as shown in Figure 6.3(a)–(b). The fluorescence photos of the red and green pixels excited by the blue LED were taken with a 500 nm long-pass filter (FEL0500, Thorlabs). The aforementioned patterning procedure resulted in a low-profile shape with thickness below 10 μm for both the red and green pixels. The different thickness of the two types of pixels may come from the miss focusing of the object lens. Along with the omnidirectional emission properties of QDs, the low-profile pixel shape and the high pixel density benefit the wide angular emission distribution.

As shown in Figure 6.3(c), the normalized angular emission of both the red and green pixels excited by the blue LED chips approaches the Lambertian emission profile of an ideally diffusive radiator. [231] Figure 6.3(d) shows that the fluorescent emission intensity of the red and green pixels can be adjusted by tuning supply voltage to the blue LED chip. The PL intensity was measured with the angular emission measurement setup at 0° emission angle, without long-pass filtering. Due to the overlap at the range from 475 nm to 500 nm between the emission spectrum of the blue LEDs and green QDs/NOA86 pixels, the PL spectrum of the green QDs/NOA86 composite was fitted with Lorentzian function. On the other hand, the emission spectrum of the blue LED was measured without patterning color converters on it. Figure 6.3(d) indicates that QDs/photo-polymer color converters could be utilized for full-color conversion on the blue micro-LEDs array by controlling the supply voltage of the nearby micro-LEDs. The wide range of choices for QDs further offers tunability of color gamut for blue LED color down conversion. Figure 6.3(e) shows the CIE chart of the QDs color converters with the current choice of QDs and photo-polymer matrix, under the assumption of full light conversion from the blue LED. [232] 95% color gamut coverage of the DCI-P3 color space is achievable. [233]

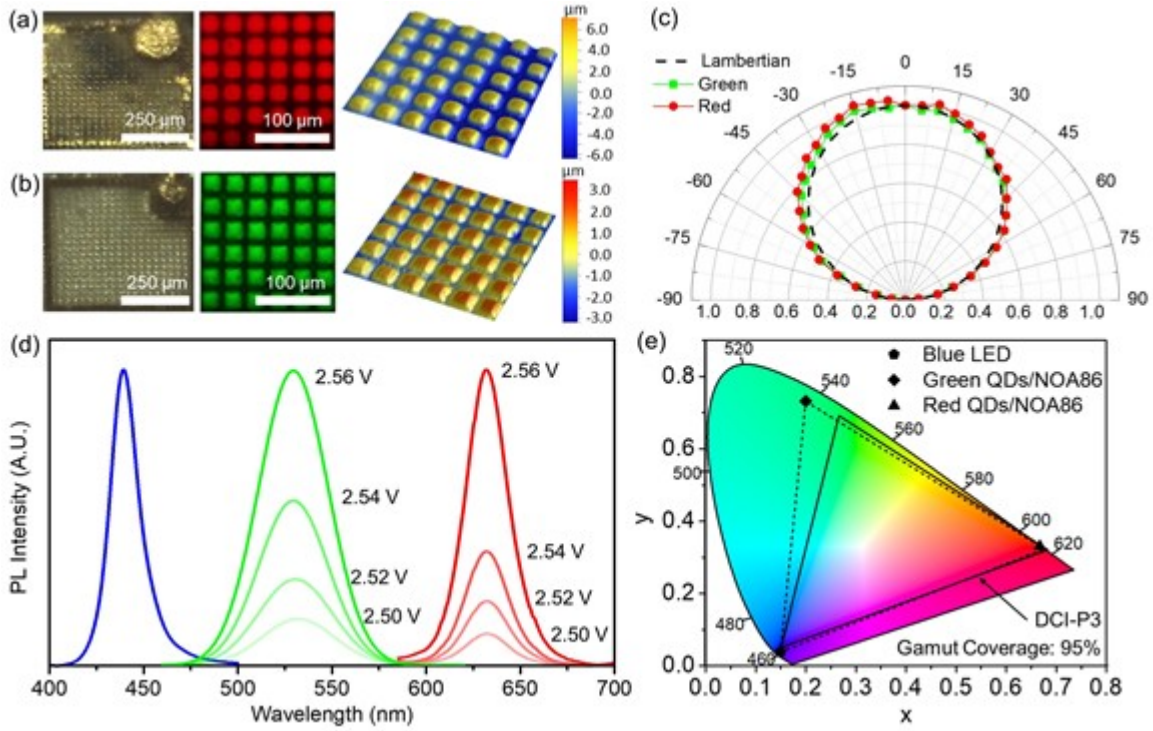

Figure 6.3: Direct patterning of QDs/NOA86 pixels on blue LEDs for color down conversion.(a, b) White light and PL images and pixelated array profiles of red and green pixels. (c)Angular emission profiles of red and green color converters from blue LED excitation. (d)Blue LED emission spectra (Blue solid line) and PL intensities of green (green solid lines)and red (red solid lines) QDs/NOA86 pixels as increasing the supply voltage on the blue LED chip. (e) Color gamut coverage of the blue LED with red and green QDs color converters.Numbers along the boundary of the chart indicate spectral wavelength of the local colors

6.5 Comparison between QDs/photo-polymer, drop-cast, and solution-phase QDs for color down conversion

The phase separation of QDs/photopolymer composites at high QDs concentration causes the aggregation of QDs, which increases the non-radiative decay, scattering and re-absorbing of emitted light. [213, 224] Those mechanisms result in reduced PL efficiency, shifted emission peak, and expanded emission bandwidth. The rapid thiol-ene photo-polymerization reaction can provide a fast cross-linking process during exposure. [234] It has been shown that QDs/thiol-ene photo-polymer could achieve uniformly dispersed QDs in the polymer matrix at high QDs loads, without phase separation and QDs aggregation. [222] The NOA optical photo-polymer is also robust for long-term operation. [222] In the following section, we compare the photoluminescence of QDs color converters fabricated by conventional solvent drop-casting and projection lithography. The drop-cast QDs were initially dispersed in chloroform of the same QDs concentrations as the QDs/NOA86 composite. Meanwhile, solution-phase QDs/chloroform suspensions were also measured as references.

Figures 6.4(a)–6.4(b) show the absorption of QDs / chloroform suspensions with QDs concentration of 25 mg / mL, as well as the PL emission spectrum of solution-phase QDs, QDs / NOA86 composite and drop-cast QDs at concentration of 25 mg/mL. The PL peaks of drop-cast QDs and QDs / NOA86 composites show redshifts compared to the solution-phase QDs. In Figure 6.4(c)– (d), we further compare the PL emission peaks and FWHM between the three groups of samples at high red or green QDs loads from 25 mg / mL to 100 mg / mL. The PL peaks of solution-phase red and green QDs locate at ∼630 nm and ∼525 nm separately. The drop-cast QDs show the largest redshifts of the PL peaks (red: ∼640 nm and green: ∼535 nm), and the widest FWHM (red: ∼37 nm and green: ∼45 nm), due to the large aggregation after solvent evaporation. [221] On the other hand, the PL peaks of red and green QDs/NOA86 shifted less, at ∼632 nm and ∼527 nm, with FWHM of ∼35 nm and

∼40 nm separately, due to the uniform dispersion of QDs in the polymer matrix.

The QDs aggregation and host material effects also result in the degradation of PL efficiency. As shown in Figure. 6.4(e)–(f), the drop-cast QDs have the lowest PLQY (red: ∼11% and green: ∼20%) compared to solution-phase (red: ∼20% and green: ∼40%) and QDs/NOA86 composite (red: ∼15% and green: ∼35%). We could conclude from this comparison that the photo-lithography patterning of QDs/photo-polymer method outperforms the conventional inkjet or aerosol jet patterning methods by forming a more uniformly dispersed QDs in a polymeric matrix. The PLQY of QDs/NOA86 is improved by 0.5-1 times compared to drop-cast QDs. The higher PL efficiency of solution-phase QDs indicates liquid solvents may exceed photo-polymers as the host material, which is partly due to the inhibited degradation of QDs passivation. [224, 221] Other possible reasons include the light scattering from the non-uniform refractive index of the polymer matrix and the high index mismatch between NOA86 (n=1.55) and air. It is suggested that strategies like "Stokes-shift-engineered" giant QDs and silica-coated QDs could combat the host material effects for QDs/photopolymer composites. [235, 224] On the other hand, liquid phase color conversion pixels are not practical for high-resolution display applications, due to challenges in both manufacturing and maintenance for long-lifetime operation. On the other hand, as shown in Figs. 4(e)–4(f), the absorbance coefficient μa of QDs/NOA86 composites (∼0.1/μm) are comparable with solution-phase QDs at a high QDs concentration, which is preferable for full blue light conversion within a thin conversion layer. Furthermore, applying optical bandpass filters to reflect un-converted blue light back to the luminescence layer can further reduce blue light leakage and increase the color gamut for full-color conversion. [212]

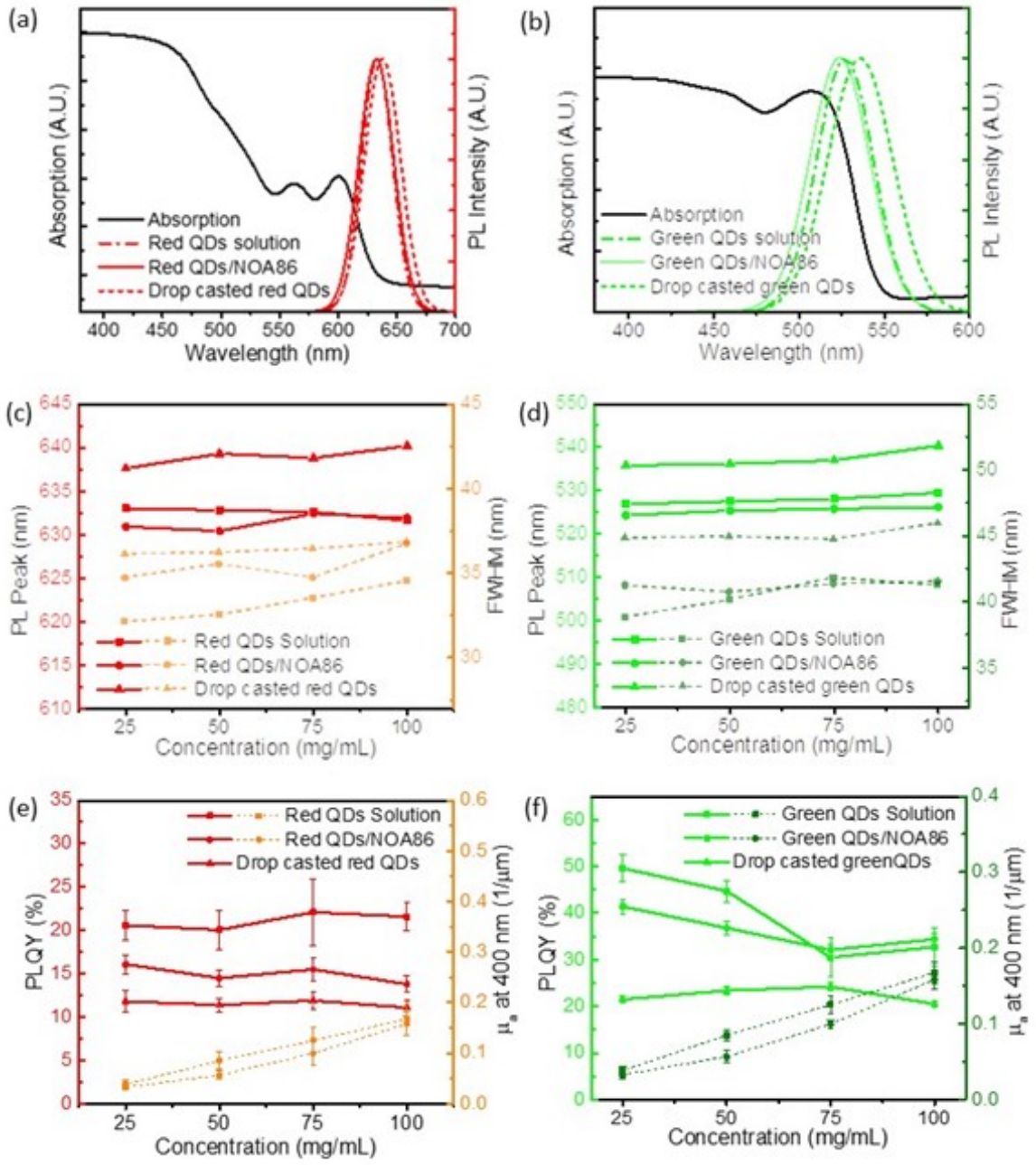

Figure 6.4: Comparison between QDs / chloroform, QDs / NOA86 composite and drop-cast QDs. (a, b) Absorption and PL emission spectra, with red and green QDs concentration of 25 mg / mL. (c, d) PL peaks and FWHM of the 3 sample groups as increasing the red and green QDs concentration from 25 mg / mL to 100 mg/mL. (e, f) PLQY and absorbance coefficient μ_a of the 3 sample groups as increasing the red and green QDs concentration from 25 mg / mL to 100 mg / mL

6.6 Color crosstalk reduction with projection lithography patterned black matrix

Color crosstalk may happen due to the blue light leakage between nearby pixels or the unintentional excitation of red QDs by the nearby green QDs. Both of these two mechanisms originate from the coupling of light emitted from pixels into the other nearby pixels. One widely applied technique to reduce color crosstalk due to unintentional excitation is inserting light-blocking walls or "black matrix" between pixels. [216, 236] Here we further demonstrate that the projection lithography method could be applied to directly pattern red and green QDs color converters with "black matrix" to reduce color crosstalk.

A black photopolymer (PR - 57 Black, Autodesk) containing light-absorbing molecules was used as the black matrix material. First, we followed the previously described procedures to pattern straight lines of red and green color converters (with QDs concentration of 50 mg / mL) on transparent glass substrates. Then the black photo-polymer was applied and exposed with a parallel lines pattern to fill the gap between the nearby pixels. The exposure time is 1.0 s and the intensity is 52 mW/cm^2.

We compared the color crosstalk of the patterned pixels with and without the black matrix. Figures 6.5(a)–(b) show the white light microscope photos in reflection mode of the patterned lines of red and green color converters. The patterned "black matrix" is shown as the white dash rectangular areas in Figure 6.5(b). This process can also pattern black matrix walls around square pixels by projecting a grid pattern at the gaps between red and green pixels. It requires a finer alignment between multiple exposure steps, which is limited by the lack of rotational accuracy of the current setup. Figures 6.5(c)–(d) show the fluorescence images of the patterned color converters under 405 nm excitation from the UV DMD digital light projector over the whole area. While in Figure. 6.5(e)–(f), the excitation only covers the green color converters. The four fluorescence photos were recorded with the same digital camera (EOS60D, Canon) with fixed shutter speed, aperture, and ISO. Figure 6.5(g)-(h) show the extracted red and green channel intensities from the fluorescence photos, along the

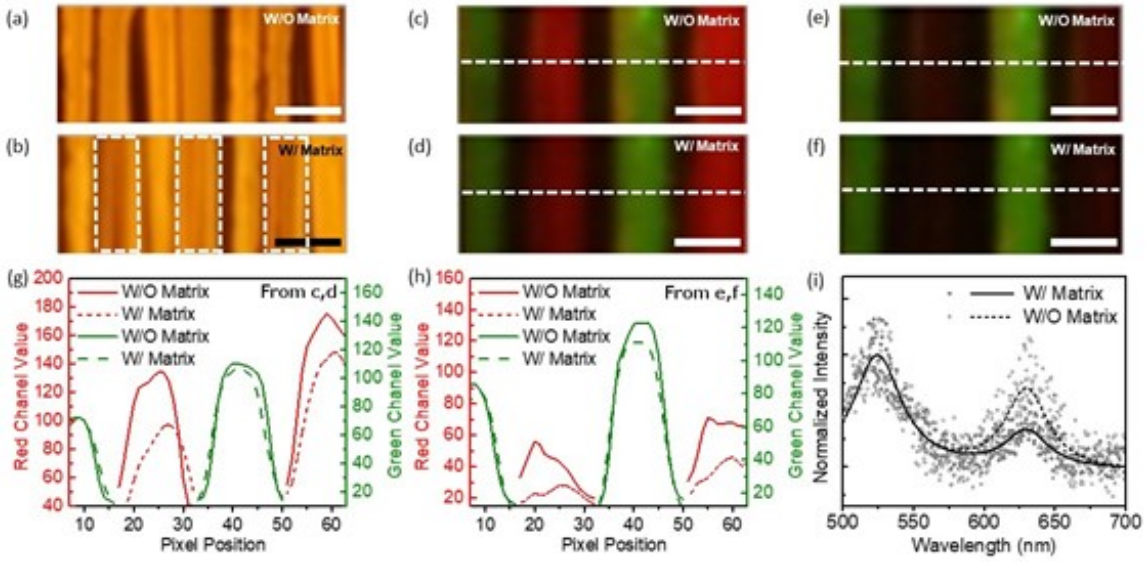

Figure 6.5: Color crosstalk reduction by projection lithography of "black matrix" in between red and green QDs color converters. (a, b) White light microscope photos of color converters with and without the black matrix. The patterned light absorbing photo-polymer composite is shown as the white dash rectangular areas in (b). (c-f) Fluorescence images of color converters excited by 405 nm light from the UV DLP projector. Figures 5(c) and 5(e)show pixels without black matrix. Figures 5(d) and 5(f) show pixels with black matrix. The UV projection covers the whole area in Figs. 5(c)-5(d), while only covers the green color converters in (e)-(f). (g) Red and green channel intensities along the white dash lines in (c)-(d). (h) Red and green color channel intensities along the white dash lines in (e)-(f). All scale bars are 25μm. (i) Normalized PL intensity and fitted PL spectrum of areas with and without black matrix.

white dash lines shown in Figure 6.5(c)–(f). Before and after patterning the black matrix, the green fluorescence emission intensity profiles in both Figure 6.5(g)–(h) keep a similar value, which indicates no direct coverage of the color converters by the black matrix. Furthermore, applying the black matrix in between the red and green color converters effectively reduces the un-intentional excitation of red pixels due to the mitigated coupling of green light emission from a nearby green pixel into the red pixel. As shown in Figure 6.5(h), the red channel intensity caused by color crosstalk is reduced by 40% with the black matrix. Further, PL spectrum measurements over larger areas with and without black matrices were conducted by projecting 405 nm excitation light only onto the green color converters. Normalized PL intensity and fitted spectrum with PL centers at 525 nm and 630 nm in Figure 6.5(i) confirm that the drop of red PL intensity after adding the black matrix walls, which indicates the color crosstalk reduction. The Projection lithography of the black matrix can be a promising solution to prevent color crosstalk between high-resolution QDs converters. However, the continuous decreasing of LED pixels size and pitch distance call the development of new material composites to diminish light coupling between pixels.

6.7 Summary

In summary, we demonstrated the direct patterning of QDs/thiol-ene photo-polymer composite as high-resolution pixelated color converters with DLP projection lithography method. Square pixels array of 21 μm size, 30 μm pitch, and sub 10 μm thickness was demonstrated. The smallest pixel size of 6 μm printed by this method has not been achieved by ink-jet or aerosol jet methods. The fast thiol-ene photo-polymerization reaction facilitates the uniform dispersion of highly concentrated amine capped QDs in the polymer matrix, which improves PLQY by 0.5-1 times compared to solvent drop-cast QDs. Meanwhile, the advantages of QDs as color converters for wide viewing angles and wide gamut are maintained. A nearly ideal diffusive angular emission with 95% gamut coverage of DCI-P3 standard is achievable. The DLP projection lithography method also offers promising solutions to resolve the color

crosstalk due to the leakage of omnidirectional emission from QDs. The combination of QDs/photo-polymer with projection lithography patterning method presents great potential for high-resolution and efficient color conversion in applications like high-end lighting and display, visible light communication and optogenetic neural controls.

Chapter 7

Summary and Outlook

7.1 Summary

We explored the application of disordered optical elements for multidimensional information processing and developed micro/nanofabrication methods that are compatible with patterning engineered disordered optics.

A Fourier DOE with SML has been designed and demonstrated for a spectral imaging application. The compact filter design could efficiently sample the major spectral Fourier components in the Fourier transformed space. The DOE layer serves as the dispersive element to selectively project the major spectral Fourier components to the sub-pixel level locations. The SML layer then introduces the extra spatial frequency to the different spectral components to avoid spectral aliasing in the Fourier transformed space. As the result, the design can achieve balanced spatial-spectral resolution compared with the previous spatial multiplexing-based method. We fabricated the designed DOE and SML with grayscale photolithography and beam lithography. Experiment results show 9% RMSE for the spectral reconstruction of 54 different broadband color bands in the visible range, and 0.324 cycles per pixel spatial resolution, thanks to the efficient sampling of the major spectral components in the Fourier transformed space without the requirement of sub-super-pixel level sensing. This design principle could be scaled with the sensor pixel size and manufacturing capability while the Fourier spectral imaging method can also be applied to other

implementations such as QDs spectroscopy.

One of the limitations on the manufacturing of optical DOE is the efficiently patterning of micro/nanostructures with spatial thickness variation. Grayscale photolithography improves the patterning efficiency compared to conventional lithography and a lift-off method. However, the material choices are limited to the low index photoresists. For example, in our Fourier DOE design, this restriction limits the achievable OPD retardation within a compact dispersion volume and reduces the amount of separable spectral Fourier orders. To overcome this issue, we developed a grayscale version of stencil lithography for efficient patterning of materials with spatial thickness variation. By controlling the PSF of materials ejected through the stencil mask by varying the deposition dose and tilting angle, we could control the local deposition thickness with stencils of different filling ratios and improve the deposition surface roughness to 7 nm. We demonstrated the fabrication method with a 10 by 10 multi-layer spectral filter array. The proposed method can be adapted to micro/nano stencil lithography to further improve the patterning spatial resolution.

In the second part of the thesis, we focused on the application of scattering medium for linear optical reservoir computing, which relies on the memory of spatial-temporal information for temporal signal processing. We identified the effects of loss and non-normality of a scattering medium on its memory capacity and noise resistance when serving as the optical reservoir. We found that sufficient loss ($T_{total} < \sqrt{N}0.01$) is required to efficiently memorize the short-term information up to the N time steps back, where N is the dimensionality of the system. And scatters with a total transmission of around 0.5 have the highest architecture-based noise resistance due to their non-normality. However, the high losses in that system compromise the actual memory performance and noise resistance. By introducing an artificial amplification method, we proposed a practical input encoding method to overcome the loss issue and fully harness the high dimensionality and high noise resistance of the scattering medium for linear reservoir computing.

A dynamic scattering medium based on thermochromic pNIPAM hydrogel particles has been developed for the application of solar modulation, which also has the

potential for a controllable scattering reservoir. Through fine-tuning of the gel particle's size before and after phase transition, we could control the scattering strength over the visible to NIR region. When working as the smart window, the material can achieve $> 80\%$ solar modulation at the "on" state with high luminous transmission $>85\%$ at the "off" state. The large contrast of scattering strength makes it an ideal candidate to validate the dependence of memory performance on the total transmission in the scattering optical reservoir. Meanwhile, the material also shows great stability for long-term usage and the solution-phase manufacturing method is of potential for large-scale production.

Finally, we developed a projection lithography technique to pattern pixelated high-resolution micro-sized QDs/photopolymer composites. We applied this method to package blue μLEDs with QDs color converters for full RGB display. Meanwhile, the same fabrication technique could be applied to introduce gain/loss materials to a passive disordered medium, which can bring non-linear functionalities to the proposed disordered optical network.

7.2 Outlook

The great potential in the engineered disordered optical elements may lead to many future research directions.

Inverse design of disordered optical elements: The complex optical medium can project aliased information to higher dimensions for multi-dimensional information processing. As we demonstrated in the Fourier DOE for spectral imaging and scattering optical reservoir, the designing of the transmission matrix determines the functionality and efficiency of the disordered optical element. Given the material information and targeted functions, inverse design can facilitate the optimization of the transmission matrix and open more design freedom for multi-dimensional information processing. For example, recently an end-to-end adjoint optimization method [40] has been proposed to design 3D printed optical elements for spatial, spectral, and polarization information reconstruction in some special application cases. Following

this direction, designs for more general imaging applications [237, 238] without pre-knowledge of the objects can be developed, which may further extend the application of disordered optical mediums.

Gain/loss engineering in complex optical medium: In the Fourier DOE and scattering optical reservoir, the disordered optical medium only serves as a linear operator modeled by the transmission matrix. Embedding gain/loss materials into the complex medium can achieve unprecedented functions for applications in an optical neural network. [196, 197] Transient signal amplification has been observed in the gain/loss embedded waveguide. [155] Transforming the z-dimension of the waveguide into the temporal dimension can make it equivalent to the transient amplification of signals in an optical reservoir. Further, engineering the gain/loss distribution can facilitate and control the information transportation in complex medium with high scattering strength. [59, 239, 240] This development requires the techniques of temporal modulation of the gain/loss medium with feedback functionality. On the other side, the development of an optical neural network also calls the discovery of optical materials to serve as the non-linear element, such as the activation function at the readout layer. Currently, the most of diffractive neural network and scattering based optical reservoir relies on the non-linearity of the intensity sensors to fulfill the non-linear function. [71, 141] Engineering gain/loss materials with non-linearity, for example, saturable absorbers and Kerr optical materials, can further extend the capability of the disordered optical medium in handling non-linear tasks.

Event-based information processing with disordered optical medium: The capability of disordered optical reservoir for temporal signal processing opens the direction of event-based information encoding and processing. Spiking-based neurons and networks could be a potential candidate for this application. [241, 242, 243] A spiking neuron contains coupled gain and loss elements that define the threshold for stimulated amplification of the input signal, in other words, the "spike" output.[244] Semiconductor lasers with saturable absorbers have been demonstrated as the optical implementation of the biological spike neuron, with great potential for event-based information processing. [245] Integrating multiple spike neurons with randomness

into a network may fulfill more complicated network functionalities. [70] The analysis of the linear optical reservoir computer in this thesis could be further developed to model the spike optical reservoir. Another possible direction is to combine the disordered optical reservoir with event-band neuromorphic CCD, [246] which records the "event" happening as dramatic intensity differences measured by the sensor pixels. The development in the "event" camera opens the direction for fast temporal information processing with lights. [247] While coupling it with the disordered optical medium can further engineering the connectivity between the individual nodes in the network formed by the camera pixels.

3D micro/nanomanufacturing techniques: The development of disordered optical designs requires compatible manufacturing techniques to transform them from blueprints to real working devices. For example, micro-stereolithography-based 3D printing technologies are a promising candidate to further miniaturize the diffractive optical elements, overcome the limitations in step height control, and even fabricate multi-layer cascade DOE with high efficiency and large scale. [248, 249, 250] Challenges remain in improving the patterning resolution and field-of-view by projection lithography and embedding of multi-material. Experiment works based on micro-lens array for large-scale and high-resolution micro-stereolithography have been developed in our lab and paved the way for applications in fabricating engineered disordered optical elements. [251]

Bibliography

[1] Nuru R Mlyuka, Gunnar A Niklasson, and Claes G Granqvist. Thermochromic vo2-based multilayer films with enhanced luminous transmittance and solar modulation. *physica status solidi (a)*, 206(9):2155–2160, 2009.

[2] Zhang Chen, Yanfeng Gao, Litao Kang, Jing Du, Zongtao Zhang, Hongjie Luo, Hongyan Miao, and Guoqiang Tan. Vo2-based double-layered films for smart windows: optical design, all-solution preparation and improved properties. *Solar energy materials and solar cells*, 95(9):2677–2684, 2011.

[3] Jingting Zhu, Aibin Huang, Haibin Ma, Yunxiang Chen, Sanpei Zhang, Shidong Ji, Shanhu Bao, and Ping Jin. Hybrid films of vo2 nanoparticles and a nickel(ii)-based ligand exchange thermochromic system: excellent optical performance with a temperature responsive colour change. *New J. Chem.*, 41:830–835, 2017.

[4] Chang Liu, Shancheng Wang, Yang Zhou, Haibo Yang, Qi Lu, Daniel Mandler, Shlomo Magdassi, Chor Yong Tay, and Yi Long. Index-tunable anti-reflection coatings: Maximizing solar modulation ability for vanadium dioxide-based smart thermochromic glazing. *Journal of Alloys and Compounds*, 731:1197–1207, 2018.

[5] Yijie Zhou, Shidong Ji, Yamei Li, Yanfeng Gao, Hongjie Luo, and Ping Jin. Microemulsion-based synthesis of v 1- x w x o 2@ sio 2 core–shell structures for smart window applications. *Journal of Materials Chemistry C*, 2(19):3812–3819, 2014.

[6] Jiadong Zhou, Yanfeng Gao, Xinling Liu, Zhang Chen, Lei Dai, Chuanxiang Cao, Hongjie Luo, Minoru Kanahira, Chao Sun, and Liuming Yan. Mg-doped vo 2 nanoparticles: hydrothermal synthesis, enhanced visible transmittance and decreased metal–insulator transition temperature. *Physical Chemistry Chemical Physics*, 15(20):7505–7511, 2013.

[7] Lei Dai, Shi Chen, Jianjun Liu, Yanfeng Gao, Jiadong Zhou, Zhang Chen, Chuanxiang Cao, Hongjie Luo, and Minoru Kanehira. F-doped vo 2 nanoparticles for thermochromic energy-saving foils with modified color and enhanced solar-heat shielding ability. *Physical Chemistry Chemical Physics*, 15(28):11723–11729, 2013.

[8] Nan Shen, Shi Chen, Zhang Chen, Xinling Liu, Chuanxiang Cao, Bingrong Dong, Hongjie Luo, Jianjun Liu, and Yanfeng Gao. The synthesis and performance of zr-doped and w–zr-codoped vo 2 nanoparticles and derived flexible foils. *Journal of Materials Chemistry A*, 2(36):15087–15093, 2014.

[9] Litao Kang, Yanfeng Gao, Hongjie Luo, Zhang Chen, Jin Du, and Zongtao Zhang. Nanoporous thermochromic vo2 films with low optical constants, enhanced luminous transmittance and thermochromic properties. *ACS applied materials & interfaces*, 3(2):135–138, 2011.

[10] Yanfeng Gao, Shaobo Wang, Litao Kang, Zhang Chen, Jing Du, Xinling Liu, Hongjie Luo, and Minoru Kanehira. Vo 2–sb: Sno 2 composite thermochromic smart glass foil. *Energy & Environmental Science*, 5(8):8234–8237, 2012.

[11] Jingting Zhu, Aibin Huang, Haibin Ma, Yining Ma, Kun Tong, Shidong Ji, Shanhu Bao, Xun Cao, and Ping Jin. Composite film of vanadium dioxide nanoparticles and ionic liquid–nickel–chlorine complexes with excellent visible thermochromic performance. *ACS applied materials & interfaces*, 8(43):29742–29748, 2016.

[12] Yang Zhou, Yufeng Cai, Xiao Hu, and Yi Long. Temperature-responsive hydrogel with ultra-large solar modulation and high luminous transmission for "smart window" applications. *Journal of Materials Chemistry A*, 2(33):13550–13555, 2014.

[13] Yang Zhou, Yufeng Cai, Xiao Hu, and Yi Long. Vo 2/hydrogel hybrid nanothermochromic material with ultra-high solar modulation and luminous transmission. *Journal of Materials Chemistry A*, 3(3):1121–1126, 2015.

[14] Heng Yeong Lee, Yufeng Cai, Sadiye Velioglu, Chengzhong Mu, Chen Jian Chang, Yi Ling Chen, Yujie Song, Jia Wei Chew, and Xiao Matthew Hu. Thermochromic ionogel: A new class of stimuli responsive materials with super cyclic stability for solar modulation. *Chemistry of Materials*, 29(16):6947–6955, 2017.

[15] Xiaoyan Ma, Jun Q Lu, R Scott Brock, Kenneth M Jacobs, Ping Yang, and Xin-Hua Hu. Determination of complex refractive index of polystyrene microspheres from 370 to 1610 nm. *Physics in medicine & biology*, 48(24):4165, 2003.

[16] Wayne McPhee, Kam Chiu Tam, and Robert Pelton. Poly (n-isopropylacrylamide) latices prepared with sodium dodecyl sulfate. *Journal of colloid and interface science*, 156(1):24–30, 1993.

[17] Pierre Ambs. Optical computing: A 60-year adventure. *Advances in Optical Technologies*, 2010:1–15, 2010.

[18] Joseph W Goodman. *Introduction to Fourier optics*. Roberts and Company Publishers, 2005.

[19] André Maréchal and Paul Croce. A spatial frequency filter for improving the contrast of optical images. *WEEKLY REPORTS OF THE MEETINGS OF THE ACADEMY OF SCIENCES*, 237-12:607–609, 1953.

[20] T.h. Maiman. Stimulated optical radiation in ruby. *Essentials of Lasers*, page 134–136, 1969.

[21] B. R. Brown and A. W. Lohmann. Complex spatial filtering with binary masks. *Applied Optics*, 5(6):967, 1966.

[22] K. Preston. Coherent optical computers. *McGraw-Hill*, 1972.

[23] Fang Xu, Chuan-Cheng Cheng, Axel Scherer, Rong-Chung Tyan, Pang-Chen Sun, and Yeshayahu Fainman. Form-birefringent computer-generated holograms. *Optics Letters*, 21(18):1513, 1996.

[24] M.r. Taghizadeh, J.m. Miller, P. Blair, and F.a.p. Tooley. Developing diffractive optics for optical computing. *IEEE Micro*, 14(6):10–19, 1994.

[25] E. E. Fenimore. Coded aperture imaging: predicted performance of uniformly redundant arrays. *Applied Optics*, 17(22):3562, 1978.

[26] Kunz. On the equivalence between one-dimensional discrete walsh-hadamard and multidimensional discrete fourier transforms. *IEEE Transactions on Computers*, C-28(3):267–268, 1979.

[27] Martin Harwit. Hadamard transform optics. *Academic Press*, 1979.

[28] Uzi Efron. Spatial light modulator technology: materials, devices, and applications. *CRC Press*, 1994.

[29] Nanfang Yu and Federico Capasso. Flat optics with designer metasurfaces. *Nature materials*, 13(2):139–150, 2014.

[30] Shuqi Chen, Zhancheng Li, Wenwei Liu, Hua Cheng, and Jianguo Tian. From single-dimensional to multidimensional manipulation of optical waves with metasurfaces. *Advanced Materials*, 31(16):1802458, 2019.

[31] Gary A Shaw and Hsiaohua K Burke. Spectral imaging for remote sensing. *Lincoln laboratory journal*, 14(1):3–28, 2003.

[32] Guolan Lu and Baowei Fei. Medical hyperspectral imaging: a review. *Journal of biomedical optics*, 19(1):010901, 2014.

[33] Liang Gao and Lihong V. Wang. A review of snapshot multidimensional optical imaging: Measuring photon tags in parallel. *Physics Reports*, 616:1–37, 2016.

[34] Teresa Cacace, Vittorio Bianco, and Pietro Ferraro. Quantitative phase imaging trends in biomedical applications. *Optics and Lasers in Engineering*, 135:106188, 2020.

[35] E. L. Dereniak. From the outside looking in: developing snapshot imaging spectro-polarimeters. *Fifty Years of Optical Sciences at The University of Arizona*, 2014.

[36] Meenu Rani, S. B. Dhok, and R. B. Deshmukh. A systematic review of compressive sensing: Concepts, implementations and applications. *IEEE Access*, 6:4875–4894, 2018.

[37] Nathan A Hagen and Michael W Kudenov. Review of snapshot spectral imaging technologies. *Optical Engineering*, 52(9):090901, 2013.

[38] Rebecca M Willett, Marco F Duarte, Mark A Davenport, and Richard G Baraniuk. Sparsity and structure in hyperspectral imaging: Sensing, reconstruction, and target detection. *IEEE signal processing magazine*, 31(1):116–126, 2013.

[39] Kam-Chuen Jim, C.l. Giles, and B.g. Horne. An analysis of noise in recurrent neural networks: convergence and generalization. *IEEE Transactions on Neural Networks*, 7(6):1424–1438, 1996.

[40] Zin Lin, Charles Roques-Carmes, Raphaël Pestourie, Marin Soljačić, Arka Majumdar, and Steven G Johnson. End-to-end inverse design for inverse scattering via freeform metastructures. *arXiv preprint arXiv:2006.09145*, 2020.

[41] Stefan Rotter and Sylvain Gigan. Light fields in complex media: Mesoscopic scattering meets wave control. *Reviews of Modern Physics*, 89(1):015005, 2017.

[42] Maxime W. Matthès, Philipp Del Hougne, Julien De Rosny, Geoffroy Lerosey, and Sébastien M. Popoff. Optical complex media as universal reconfigurable linear operators. *Optica*, 6(4):465, 2019.

[43] Chu Ma, Xinhao Li, and Nicholas X. Fang. Acoustic angle-selective transmission based on binary phase gratings. *Physical Review Applied*, 14(6), 2020.

[44] Xing Lin, Yair Rivenson, Nezih T Yardimci, Muhammed Veli, Yi Luo, Mona Jarrahi, and Aydogan Ozcan. All-optical machine learning using diffractive deep neural networks. *Science*, 361(6406):1004–1008, 2018.

[45] Onur Kulce, Deniz Mengu, Yair Rivenson, and Aydogan Ozcan. All-optical information-processing capacity of diffractive surfaces. *Light: Science & Applications*, 10(1), 2021.

[46] Chao Qian, Xiao Lin, Xiaobin Lin, Jian Xu, Yang Sun, Erping Li, Baile Zhang, and Hongsheng Chen. Performing optical logic operations by a diffractive neural network. *Light: Science & Applications*, 9(1), 2020.

[47] Jingxi Li, Deniz Mengu, Nezih T. Yardimci, Yi Luo, Xurong Li, Muhammed Veli, Yair Rivenson, Mona Jarrahi, and Aydogan Ozcan. Spectrally encoded single-pixel machine vision using diffractive networks. *Science Advances*, 7(13), 2021.

[48] Sébastien M Popoff, Geoffroy Lerosey, R Carminati, Mathias Fink, Albert Claude Boccara, and Sylvain Gigan. Measuring the transmission matrix in optics: an approach to the study and control of light propagation in disordered media. *Physical review letters*, 104(10):100601, 2010.

[49] Simon R. Huisman, Thomas J. Huisman, Sebastianus A. Goorden, Allard P. Mosk, and Pepijn W. H. Pinkse. Programming balanced optical beam splitters in white paint. *Opt. Express*, 22(7):8320–8332, Apr 2014.

[50] Brandon Redding, Seng Fatt Liew, Raktim Sarma, and Hui Cao. Compact spectrometer based on a disordered photonic chip. *Nature Photonics*, 7(9):746–751, 2013.

[51] C. W. J. Beenakker. Applications of random matrix theory to condensed matter and optical physics, 2009.

[52] Wonjun Choi, Allard P Mosk, Q-Han Park, and Wonshik Choi. Transmission eigenchannels in a disordered medium. *Physical Review B*, 83(13):134207, 2011.

[53] Kyeoreh Lee and Yongkeun Park. Exploiting the speckle-correlation scattering matrix for a compact reference-free holographic image sensor. *Nature Communications*, 7(1), 2016.

[54] Pritam Pai, Jeroen Bosch, Matthias Kühmayer, Stefan Rotter, and Allard P Mosk. Scattering invariant modes of light in complex media. *Nature Photonics*, 15(6):431–434, 2021.

[55] Youngwoon Choi, Taeseok Daniel Yang, Christopher Fang-Yen, Pilsung Kang, Kyoung Jin Lee, Ramachandra R. Dasari, Michael S. Feld, and Wonshik Choi. Overcoming the diffraction limit using multiple light scattering in a highly disordered medium. *Phys. Rev. Lett.*, 107:023902, Jul 2011.

[56] Donald B. Conkey, Antonio M. Caravaca-Aguirre, Jake D. Dove, Hengyi Ju, Todd W. Murray, and Rafael Piestun. Super-resolution photoacoustic imaging through a scattering wall. *Nature Communications*, 6(1), 2015.

[57] Xiangsheng Xie, Huichang Zhuang, Hexiang He, Xiaoqing Xu, Haowen Liang, Yikun Liu, and Jianying Zhou. Extended depth-resolved imaging through a thin scattering medium with psf manipulation. *Scientific Reports*, 8(1), 2018.

[58] Ivo Micha Vellekoop and AP Mosk. Universal optimal transmission of light through disordered materials. *Physical review letters*, 101(12):120601, 2008.

[59] Sunkyu Yu, Xianji Piao, Jiho Hong, and Namkyoo Park. Metadisorder for designer light in random systems. *Science advances*, 2(10):e1501851, 2016.

[60] Jung-Hoon Park, Jongchan Park, KyeoReh Lee, and YongKeun Park. Disordered optics: Exploiting multiple light scattering and wavefront shaping for nonconventional optical elements. *Advanced Materials*, 32(35):1903457, 2020.

[61] Allard P Mosk, Ad Lagendijk, Geoffroy Lerosey, and Mathias Fink. Controlling waves in space and time for imaging and focusing in complex media. *Nature photonics*, 6(5):283, 2012.

[62] Sujit Kumar Sahoo, Dongliang Tang, and Cuong Dang. Single-shot multispectral imaging with a monochromatic camera. *Optica*, 4(10):1209–1213, 2017.

[63] Xiaohan Li, Joel A Greenberg, and Michael E Gehm. Single-shot multispectral imaging through a thin scatterer. *Optica*, 6(7):864–871, 2019.

[64] Peng Wang and Rajesh Menon. Ultra-high-sensitivity color imaging via a transparent diffractive-filter array and computational optics. *Optica*, 2(11):933–939, 2015.

[65] Kristina Monakhova, Kyrollos Yanny, Neerja Aggarwal, and Laura Waller. Spectral diffusercam: Lensless snapshot hyperspectral imaging with a spectral filter array. *Optica*, 7(10):1298–1307, 2020.

[66] Santosh Tripathi, Richard Paxman, Thomas Bifano, and Kimani C. Toussaint. Vector transmission matrix for the polarization behavior of light propagation in highly scattering media. *Opt. Express*, 20(14):16067–16076, Jul 2012.

[67] Michael Giles and Pierce Niles. An introduction to the adjoint approach to design. *Flow, Turbulence and Combustion*, pages 393–415, 2000.

[68] Guy Van der Sande, Daniel Brunner, and Miguel C Soriano. Advances in photonic reservoir computing. *Nanophotonics*, 6(3):561–576, 2017.

[69] Gouhei Tanaka, Toshiyuki Yamane, Jean Benoit Héroux, Ryosho Nakane, Naoki Kanazawa, Seiji Takeda, Hidetoshi Numata, Daiju Nakano, and Akira Hirose. Recent advances in physical reservoir computing: A review. *Neural Networks*, 115:100–123, 2019.

[70] Daniel Brunner and Ingo Fischer. Reconfigurable semiconductor laser networks based on diffractive coupling. *Optics letters*, 40(16):3854–3857, 2015.

[71] Mushegh Rafayelyan, Jonathan Dong, Yongqi Tan, Florent Krzakala, and Sylvain Gigan. Large-scale optical reservoir computing for spatiotemporal chaotic systems prediction. *Physical Review X*, 10(4):041037, 2020.

[72] Michael Pilling and Peter Gardner. Fundamental developments in infrared spectroscopic imaging for biomedical applications. *Chemical Society reviews*, 45(7):1935–1957, 2016.

[73] R Bacon, G Adam, A Baranne, G Courtès, D Dubet, J-P Dubois, Y Georgelin, G Monnet, E Pecontal, and J Urios. The integral field spectrograph tiger. In *Very Large Telescopes and their Instrumentation, Vol. 2*, volume 30, page 1185, 1988.

[74] Zhu Wang, Soongyu Yi, Ang Chen, Ming Zhou, Ting Shan Luk, Anthony James, John Nogan, Willard Ross, Graham Joe, Alireza Shahsafi, et al. Single-shot on-chip spectral sensors based on photonic crystal slabs. *Nature communications*, 10(1):1–6, 2019.

[75] Neelam Gupta, Philip R Ashe, and Songsheng Tan. Miniature snapshot multispectral imager. *Optical Engineering*, 50(3):033203, 2011.

[76] Jie Bao and Moungi G Bawendi. A colloidal quantum dot spectrometer. *Nature*, 523(7558):67–70, 2015.

[77] Rebecca French, Sylvain Gigan, and Otto L Muskens. Speckle-based hyperspectral imaging combining multiple scattering and compressive sensing in nanowire mats. *Optics letters*, 42(9):1820–1823, 2017.

[78] Peng Wang and Rajesh Menon. Computational multispectral video imaging. *JOSA A*, 35(1):189–199, 2018.

[79] Michael E Gehm, Renu John, David J Brady, Rebecca M Willett, and Timothy J Schulz. Single-shot compressive spectral imaging with a dual-disperser architecture. *Optics express*, 15(21):14013–14027, 2007.

[80] Jie Jia, Chuan Ni, Andrew Sarangan, and Keigo Hirakawa. Fourier multispectral imaging. *Optics express*, 23(17):22649–22657, 2015.

[81] Hasan Yılmaz, Chia Wei Hsu, Alexey Yamilov, and Hui Cao. Transverse localization of transmission eigenchannels. *Nature Photonics*, 13(5):352–358, 2019.

[82] A. Chakrabarti and T. Zickler. Statistics of Real-World Hyperspectral Images. In *Proc. IEEE Conf. on Computer Vision and Pattern Recognition (CVPR)*, pages 193–200, 2011.

[83] Jie Jia, Kenneth J Barnard, and Keigo Hirakawa. Fourier spectral filter array for optimal multispectral imaging. *IEEE Transactions on Image Processing*, 25(4):1530–1543, 2016.

[84] F. Yasuma, T. Mitsunaga, D. Iso, and S.K. Nayar. Generalized Assorted Pixel Camera: Post-Capture Control of Resolution, Dynamic Range and Spectrum. *Technical Report, Department of Computer Science, Columbia University CUCS-061-08*, 2008.

[85] Yuqi Li, Aditi Majumder, Hao Zhang, and M Gopi. Optimized multi-spectral filter array based imaging of natural scenes. *Sensors*, 18(4):1172, 2018.

[86] VJ Barclay, RF Bonner, and IP Hamilton. Application of wavelet transforms to experimental spectra: smoothing, denoising, and data set compression. *Analytical Chemistry*, 69(1):78–90, 1997.

[87] Stephen A Dyer. Hadamard transform spectrometry. *Chemometrics and intelligent laboratory systems*, 12(2):101–115, 1991.

[88] Gonzalo R Arce, David J Brady, Lawrence Carin, Henry Arguello, and David S Kittle. Compressive coded aperture spectral imaging: An introduction. *IEEE Signal Processing Magazine*, 31(1):105–115, 2013.

[89] Qi Yi, Lim Zi Heng, Li Liang, Zhou Guangcan, Chau Fook Siong, and Zhou Guangya. Hadamard transform-based hyperspectral imaging using a single-pixel detector. *Optics express*, 28(11):16126–16139, 2020.

[90] E. Wolf and W. H. Carter. Coherence and radiant intensity in scalar wave fields generated by fluctuating primary planar sources. *J. Opt. Soc. Am.*, 68(7):953–964, Jul 1978.

[91] Kazuyoshi Itoh and Yoshihiro Ohtsuka. Fourier-transform spectral imaging: retrieval of source information from three-dimensional spatial coherence. *J. Opt. Soc. Am. A*, 3(1):94–100, Jan 1986.

[92] Chao Deng, Xuemei Hu, Jinli Suo, Yuanlong Zhang, Zhili Zhang, and Qionghai Dai. Snapshot hyperspectral imaging via spectral basis multiplexing in fourier domain. *Opt. Express*, 26(25):32509–32521, Dec 2018.

[93] Chuan Ni, Jie Jia, Matthew Howard, Keigo Hirakawa, and Andrew Sarangan. Single-shot multispectral imager using spatially multiplexed fourier spectral filters. *J. Opt. Soc. Am. B*, 35(5):1072–1079, May 2018.

[94] Xin Yuan. Generalized alternating projection based total variation minimization for compressive sensing. In *2016 IEEE International Conference on Image Processing (ICIP)*, pages 2539–2543, 2016.

[95] Michael Descour and Eustace Dereniak. Computed-tomography imaging spectrometer: experimental calibration and reconstruction results. *Appl. Opt.*, 34(22):4817–4826, Aug 1995.

[96] Mohammadreza Khorasaninejad and Federico Capasso. Metalenses: Versatile multifunctional photonic components. *Science*, 358(6367):eaam8100, 2017.

[97] Sourangsu Banerji, Monjurul Meem, Apratim Majumder, Fernando Guevara Vasquez, Berardi Sensale-Rodriguez, and Rajesh Menon. Imaging with flat optics: metalenses or diffractive lenses? *Optica*, 6(6):805–810, 2019.

[98] Yanxia Cui, Kin Hung Fung, Jun Xu, Hyungjin Ma, Yi Jin, Sailing He, and Nicholas X Fang. Ultrabroadband light absorption by a sawtooth anisotropic metamaterial slab. *Nano letters*, 12(3):1443–1447, 2012.

[99] Zhongyang Li, Serkan Butun, and Koray Aydin. Large-area, lithography-free super absorbers and color filters at visible frequencies using ultrathin metallic films. *Acs Photonics*, 2(2):183–188, 2015.

[100] Yu Horie, Amir Arbabi, Ehsan Arbabi, Seyedeh Mahsa Kamali, and Andrei Faraon. Wide bandwidth and high resolution planar filter array based on dbr-metasurface-dbr structures. *Optics express*, 24(11):11677–11682, 2016.

[101] Mikhail A Kats, Romain Blanchard, Patrice Genevet, and Federico Capasso. Nanometre optical coatings based on strong interference effects in highly absorbing media. *Nature materials*, 12(1):20, 2013.

[102] Shane Colburn, Alan Zhan, and Arka Majumdar. Tunable metasurfaces via subwavelength phase shifters with uniform amplitude. *scientific Reports*, 7:40174, 2017.

[103] Nathalie Destouches, AV Tishchenko, JC Pommier, S Reynaud, O Parriaux, S Tonchev, and M Abdou Ahmed. 99% efficiency measured in the-1 st order of a resonant grating. *Optics Express*, 13(9):3230–3235, 2005.

[104] Pierre-Jean Lapray, Xingbo Wang, Jean-Baptiste Thomas, and Pierre Gouton. Multispectral filter arrays: Recent advances and practical implementation. *Sensors*, 14(11):21626–21659, 2014.

[105] Calum Williams, George Gordon, Timothy D Wilkinson, and Sarah Elizabeth Bohndiek. Grayscale-to-color: Scalable fabrication of custom multispectral filter arrays. *ACS Photonics*, 2019.

[106] Dingrong Yi, Linghua Kong, Jiwu Wang, and Futing Zhao. Fabrication of multispectral imaging technology driven mems-based micro-arrayed multichannel optical filter mosaic. In *Advanced Fabrication Technologies for Micro/Nano Optics and Photonics IV*, volume 7927, page 792711. International Society for Optics and Photonics, 2011.

[107] Jason M Eichenholz and Yishung Juang. Dichroic filter array multispectral imaging systems. In *Applied Industrial Optics: Spectroscopy, Imaging and Metrology*, page ATuA4. Optical Society of America, 2010.

[108] Patrice Genevet, Federico Capasso, Francesco Aieta, Mohammadreza Khorasaninejad, and Robert Devlin. Recent advances in planar optics: from plasmonic to dielectric metasurfaces. *Optica*, 4(1):139–152, 2017.

[109] Zhengmei Yang, Yiqin Chen, Yanming Zhou, Yasi Wang, Peng Dai, Xupeng Zhu, and Huigao Duan. Microscopic interference full-color printing using grayscale-patterned fabry–perot resonance cavities. *Advanced Optical Materials*, 5(10):1700029, 2017.

[110] Yasi Wang, Mengjie Zheng, Qifeng Ruan, Yanming Zhou, Yiqin Chen, Peng Dai, Zhengmei Yang, Zihao Lin, Yuxiang Long, Ying Li, et al. Stepwise-nanocavity-assisted transmissive color filter array microprints. *Research*, 2018:8109054, 2018.

[111] O Vazquez-Mena, L Gross, S Xie, LG Villanueva, and Jürgen Brugger. Resistless nanofabrication by stencil lithography: A review. *Microelectronic Engineering*, 132:236–254, 2015.

[112] Ke Du, Junjun Ding, Yuyang Liu, Ishan Wathuthanthri, and Chang-Hwan Choi. Stencil lithography for scalable micro-and nanomanufacturing. *Micromachines*, 8(4):131, 2017.

[113] Veronica Savu, Marc AF van den Boogaart, Juergen Brugger, Julien Arcamone, Marc Sansa, and Francesc Perez-Murano. Dynamic stencil lithography on full wafer scale. *Journal of Vacuum Science & Technology B: Microelectronics and Nanometer Structures Processing, Measurement, and Phenomena*, 26(6):2054–2058, 2008.

[114] Marius Kölbel, R Willem Tjerkstra, Gyuman Kim, Jürgen Brugger, Cees JM van Rijn, Wietze Nijdam, Jurriaan Huskens, and David N Reinhoudt. Self-assembled monolayer coatings on nanostencils for the reduction of materials adhesion. *Advanced functional materials*, 13(3):219–224, 2003.

[115] Filiz Yesilkoy, Valentin Flauraud, Matthieu Rüegg, BJ Kim, and Jürgen Brugger. 3d nanostructures fabricated by advanced stencil lithography. *Nanoscale*, 8(9):4945–4950, 2016.

[116] Yeo-Taek Yoon, Sang-Shin Lee, and Byoung-Su Lee. Visible filter integrated with an image sensor fabricated by a 90-nm standard cmos process. In *2010 23rd Annual Meeting of the IEEE Photonics Society*, pages 630–631. IEEE, 2010.

[117] Laurent Frey, Pascale Parrein, Jacques Raby, Catherine Pellé, Didier Hérault, Michel Marty, and Jean Michailos. Color filters including infrared cut-off integrated on cmos image sensor. *Optics express*, 19(14):13073–13080, 2011.

[118] Calum Williams, Girish Rughoobur, Andrew J Flewitt, and Timothy D Wilkinson. Single-step fabrication of thin-film linear variable bandpass filters based on metal–insulator–metal geometry. *Applied optics*, 55(32):9237–9241, 2016.

[119] Peter LP Dillon, AT Brault, JR Horak, E Garcia, TW Martin, and WA Light. Fabrication and performance of color filter arrays for solid-state imagers. *IEEE Transactions on Electron Devices*, 25(2):97–101, 1978.

[120] Xiaoyuan Lu, Rengang Wan, and Tongyi Zhang. Metal-dielectric-metal based narrow band absorber for sensing applications. *Optics express*, 23(23):29842–29847, 2015.

[121] Min Yan. Metal–insulator–metal light absorber: a continuous structure. *Journal of Optics*, 15(2):025006, 2013.

[122] Hans K Pulker, G Paesold, and Elmar Ritter. Refractive indices of tio 2 films produced by reactive evaporation of various titanium–oxygen phases. *Applied optics*, 15(12):2986–2991, 1976.

[123] Özlem Duyar, Frank Placido, and H Zafer Durusoy. Optimization of tio2 films prepared by reactive electron beam evaporation of ti3o5. *Journal of Physics D: Applied Physics*, 41(9):095307, 2008.

[124] *Lumerical Inc*, https://www.lumerical.com/products/.

[125] Peter B Johnson and R-W_ Christy. Optical constants of the noble metals. *Physical review B*, 6(12):4370, 1972.

[126] Aleksandar D Rakić, Aleksandra B Djurišić, Jovan M Elazar, and Marian L Majewski. Optical properties of metallic films for vertical-cavity optoelectronic devices. *Applied optics*, 37(22):5271–5283, 1998.

[127] G Vuye, S Fisson, V Nguyen Van, Y Wang, J Rivory, and F Abeles. Temperature dependence of the dielectric function of silicon using in situ spectroscopic ellipsometry. *Thin Solid Films*, 233(1-2):166–170, 1993.

[128] PB Johnson and RW Christy. Optical constants of transition metals: Ti, v, cr, mn, fe, co, ni, and pd. *Physical review B*, 9(12):5056, 1974.

[129] J Rs DeVore. Refractive indices of rutile and sphalerite. *JOSA*, 41(6):416–419, 1951.

[130] Martin Habekost. Which color differencing equation should be used. *International Circular of Graphic Education and Research*, 6:20–33, 2013.

[131] Jad Salman, Martin Hafermann, Jura Rensberg, Chenghao Wan, Raymond Wambold, Bradley S Gundlach, Carsten Ronning, and Mikhail A Kats. Flat optical and plasmonic devices using area-selective ion-beam doping of silicon. *Advanced Optical Materials*, 6(5):1701027, 2018.

[132] Lei Li and Y Yi Allen. Design and fabrication of a freeform microlens array for a compact large-field-of-view compound-eye camera. *Applied optics*, 51(12):1843–1852, 2012.

[133] Mingyu Sun, Xuewu Xu, Xiao Wei Sun, Xin'an Liang, Vytautas Valuckas, Yuanjin Zheng, Ramón Paniagua-Domínguez, and Arseniy I Kuznetsov. Efficient visible light modulation based on electrically tunable all dielectric metasurfaces embedded in thin-layer nematic liquid crystals. *Scientific reports*, 9(1):8673, 2019.

[134] Herbert Jaeger. Echo state network. *scholarpedia*, 2(9):2330, 2007.

[135] Ian Goodfellow, Yoshua Bengio, and Aaron Courville. *Deep Learning*. MIT Press, 2016. http://www.deeplearningbook.org.

[136] Eva García-Martín, Crefeda Faviola Rodrigues, Graham Riley, and Håkan Grahn. Estimation of energy consumption in machine learning. *Journal of Parallel and Distributed Computing*, 134:75–88, 2019.

[137] Yibo Li, Zhongrui Wang, Rivu Midya, Qiangfei Xia, and J Joshua Yang. Review of memristor devices in neuromorphic computing: materials sciences and device challenges. *Journal of Physics D: Applied Physics*, 51(50):503002, 2018.

[138] Mark J Embrechts, Luís A Alexandre, and Jonathan D Linton. Reservoir computing for static pattern recognition. In *ESANN*. Citeseer, 2009.

[139] Kristof Vandoorne, Pauline Mechet, Thomas Van Vaerenbergh, Martin Fiers, Geert Morthier, David Verstraeten, Benjamin Schrauwen, Joni Dambre, and Peter Bienstman. Experimental demonstration of reservoir computing on a silicon photonics chip. *Nature communications*, 5(1):1–6, 2014.

[140] Satoshi Sunada and Atsushi Uchida. Photonic reservoir computing based on nonlinear wave dynamics at microscale. *Scientific reports*, 9(1):1–10, 2019.

[141] Quentin Vinckier, François Duport, Anteo Smerieri, Kristof Vandoorne, Peter Bienstman, Marc Haelterman, and Serge Massar. High-performance photonic reservoir computer based on a coherently driven passive cavity. *Optica*, 2(5):438–446, 2015.

[142] Lennert Appeltant, Guy Van der Sande, Jan Danckaert, and Ingo Fischer. Constructing optimized binary masks for reservoir computing with delay systems. *Scientific reports*, 4(1):1–5, 2014.

[143] Miguel C Soriano, Daniel Brunner, Miguel Escalona-Morán, Claudio R Mirasso, and Ingo Fischer. Minimal approach to neuro-inspired information processing. *Frontiers in computational neuroscience*, 9:68, 2015.

[144] Piotr Antonik, Anteo Smerieri, François Duport, Marc Haelterman, and Serge Massar. Fpga implementation of reservoir computing with online learning. In *24th Belgian-Dutch Conference on Machine Learning*, 2015.

[145] Jacob Torrejon, Mathieu Riou, Flavio Abreu Araujo, Sumito Tsunegi, Guru Khalsa, Damien Querlioz, Paolo Bortolotti, Vincent Cros, Kay Yakushiji, Akio Fukushima, et al. Neuromorphic computing with nanoscale spintronic oscillators. *Nature*, 547(7664):428–431, 2017.

[146] Lennert Appeltant, Miguel Cornelles Soriano, Guy Van der Sande, Jan Danckaert, Serge Massar, Joni Dambre, Benjamin Schrauwen, Claudio R Mirasso, and Ingo Fischer. Information processing using a single dynamical node as complex system. *Nature communications*, 2(1):1–6, 2011.

[147] Fangwang Gou, En-Lin Hsiang, Guanjun Tan, Yi-Fen Lan, Cheng-Yeh Tsai, and Shin-Tson Wu. High performance color-converted micro-LED displays. *Journal of the Society Information Display*, 27(4):199–206, 2019.

[148] Lorenz Butschek, Akram Akrout, Evangelia Dimitriadou, Marc Haelterman, and Serge Massar. Parallel photonic reservoir computing based on frequency multiplexing of neurons. *arXiv preprint arXiv:2008.11247*, 2020.

[149] Joni Dambre, David Verstraeten, Benjamin Schrauwen, and Serge Massar. Information processing capacity of dynamical systems. *Scientific reports*, 2(1):1–7, 2012.

[150] Harold U Baranger and Pier A Mello. Mesoscopic transport through chaotic cavities: A random s-matrix theory approach. *Physical review letters*, 73(1):142, 1994.

[151] Freeman J Dyson. Statistical theory of the energy levels of complex systems. i. *Journal of Mathematical Physics*, 3(1):140–156, 1962.

[152] Sebastianus A Goorden, Jacopo Bertolotti, and Allard P Mosk. Superpixel-based spatial amplitude and phase modulation using a digital micromirror device. *Optics express*, 22(15):17999–18009, 2014.

[153] Surya Ganguli, Dongsung Huh, and Haim Sompolinsky. Memory traces in dynamical systems. *Proceedings of the National Academy of Sciences*, 105(48):18970–18975, 2008.

[154] Giacomo Baggio, Virginia Rutten, Guillaume Hennequin, and Sandro Zampieri. Efficient communication over complex dynamical networks: The role of matrix non-normality. *Science advances*, 6(22):eaba2282, 2020.

[155] Konstantinos G Makris, Li Ge, and HE Türeci. Anomalous transient amplification of waves in non-normal photonic media. *Physical Review X*, 4(4):041044, 2014.

[156] Joshua Apte and Dariush Arasteh. Window-related energy consumption in the us residential and commercial building stock. 2008.

[157] Yang Wang, Evan L Runnerstrom, and Delia J Milliron. Switchable materials for smart windows. *Annual review of chemical and biomolecular engineering*, 7:283–304, 2016.

[158] Evan L Runnerstrom, Anna Llordés, Sebastien D Lounis, and Delia J Milliron. Nanostructured electrochromic smart windows: traditional materials and nir-selective plasmonic nanocrystals. *Chemical communications*, 50(73):10555–10572, 2014.

[159] Christopher J Barile, Daniel J Slotcavage, Jingye Hou, Michael T Strand, Tyler S Hernandez, and Michael D McGehee. Dynamic windows with neutral color, high contrast, and excellent durability using reversible metal electrodeposition. *Joule*, 1(1):133–145, 2017.

[160] Jongwook Kim, Gary K Ong, Yang Wang, Gabriel LeBlanc, Teresa E Williams, Tracy M Mattox, Brett A Helms, and Delia J Milliron. Nanocomposite architecture for rapid, spectrally-selective electrochromic modulation of solar transmittance. *Nano letters*, 15(8):5574–5579, 2015.

[161] Zhang Chen, Yanfeng Gao, Litao Kang, Chuanxiang Cao, Shi Chen, and Hongjie Luo. Fine crystalline vo 2 nanoparticles: synthesis, abnormal phase transition temperatures and excellent optical properties of a derived vo 2 nanocomposite foil. *Journal of Materials Chemistry A*, 2(8):2718–2727, 2014.

[162] Clara Piccirillo, Russell Binions, and Ivan P Parkin. Nb-doped vo2 thin films prepared by aerosol-assisted chemical vapour deposition, 2007.

[163] Yuanyuan Cui, Yujie Ke, Chang Liu, Zhang Chen, Ning Wang, Liangmiao Zhang, Yang Zhou, Shancheng Wang, Yanfeng Gao, and Yi Long. Thermochromic vo2 for energy-efficient smart windows. *Joule*, 2(9):1707–1746, 2018.

[164] Troy D Manning, Ivan P Parkin, Christopher Blackman, and Uzma Qureshi. Apcvd of thermochromic vanadium dioxide thin films—solid solutions v 2- x m x o 2 (m= mo, nb) or composites vo 2: Sno 2. *Journal of Materials Chemistry*, 15(42):4560–4566, 2005.

[165] Shi Chen, Lei Dai, Jianjun Liu, Yanfeng Gao, Xinling Liu, Zhang Chen, Jiadong Zhou, Chuanxiang Cao, Penggang Han, Hongjie Luo, et al. The visible transmittance and solar modulation ability of vo 2 flexible foils simultaneously improved by ti doping: an optimization and first principle study. *Physical Chemistry Chemical Physics*, 15(40):17537–17543, 2013.

[166] Zongtao Zhang, Yanfeng Gao, Hongjie Luo, Litao Kang, Zhang Chen, Jing Du, Minoru Kanehira, Yuzhi Zhang, and Zhong Lin Wang. Solution-based fabrication of vanadium dioxide on f: Sno 2 substrates with largely enhanced thermochromism and low-emissivity for energy-saving applications. *Energy & Environmental Science*, 4(10):4290–4297, 2011.

[167] Hyun Koo, Dongmin Shin, Sung-Hwan Bae, Kyeong-Eun Ko, Se-Hong Chang, and Chan Park. The effect of ceo 2 antireflection layer on the optical properties of thermochromic vo 2 film for smart window system. *Journal of materials engineering and performance*, 23(2):402–407, 2014.

[168] Xun Cao, Ning Wang, Jia Yan Law, Say Chye Joachim Loo, Shlomo Magdassi, and Yi Long. Nanoporous thermochromic vo2 (m) thin films: controlled porosity, largely enhanced luminous transmittance and solar modulating ability. *Langmuir*, 30(6):1710–1715, 2014.

[169] Shangjun Ding, Zhanqiang Liu, Dezeng Li, Wei Zhao, Yaoming Wang, Dongyun Wan, and Fuqiang Huang. Tunable assembly of vanadium dioxide nanoparticles to create porous film for energy-saving applications. *ACS applied materials & interfaces*, 5(5):1630–1635, 2013.

[170] American standard g173: Standard tables for reference solar spectral irradiances: Direct normal and hemispherical on 37° tilted surface. *American Society for Testing Materials*, 2007.

[171] Yang Zhou, Michael Layani, Shancheng Wang, Peng Hu, Yujie Ke, Shlomo Magdassi, and Yi Long. Fully printed flexible smart hybrid hydrogels. *Advanced Functional Materials*, 28(9):1705365, 2018.

[172] Sai Wang, Zuqiang Xu, Tingting Wang, Tangxin Xiao, Xiao-Yu Hu, Ying-Zhong Shen, and Leyong Wang. Warm/cool-tone switchable thermochromic material for smart windows by orthogonally integrating properties of pillar arene and ferrocene. *Nature communications*, 9(1):1–9, 2018.

[173] H.J. Byker, P.H. Ogburn, Vander Griend, B.S. Veldkamp, and D.D. Winkle. Ligand exchange thermochromic (letc) systems. *US Patent 7542196, filed September 4, 2007, and published May 1, 2008*, 2006.

[174] Heng Yeong Lee, Yufeng Cai, Shuguang Bi, Yen Nan Liang, Yujie Song, and Xiao Matthew Hu. A dual-responsive nanocomposite toward climate-adaptable solar modulation for energy-saving smart windows. *ACS Applied Materials & Interfaces*, 9(7):6054–6063, 2017.

[175] Zhang Chen, Chuanxiang Cao, Shi Chen, Hongjie Luo, and Yanfeng Gao. Crystallised mesoporous tio2-vo2 nanocomposite films with self-cleaning and excellent thermochromic properties. 2014.

[176] Howard G Schild. Poly (n-isopropylacrylamide): experiment, theory and application. *Progress in polymer science*, 17(2):163–249, 1992.

[177] Roberta Acciaro, Tibor Gilanyi, and Imre Varga. Preparation of monodisperse poly (n-isopropylacrylamide) microgel particles with homogenous crosslink density distribution. *Langmuir*, 27(12):7917–7925, 2011.

[178] Jun Gao and Zhibing Hu. Optical properties of n-isopropylacrylamide microgel spheres in water. *Langmuir*, 18(4):1360–1367, 2002.

[179] Alberto Fernandez-Nieves, H Wyss, Johan Mattsson, and David A Weitz. *Microgel suspensions*. Wiley Online Library, 2011.

[180] Tim Still, Ke Chen, Ahmed M Alsayed, Kevin B Aptowicz, and AG Yodh. Synthesis of micrometer-size poly (n-isopropylacrylamide) microgel particles with homogeneous crosslinker density and diameter control. *Journal of colloid and interface science*, 405:96–102, 2013.

[181] Qiang Fu and Wenbo Sun. Mie theory for light scattering by a spherical particle in an absorbing medium. *Applied Optics*, 40(9):1354–1361, 2001.

[182] August Beer. Bestimmung der absorption des rothen lichts in farbigen flussigkeiten. *Ann. Physik*, 162:78–88, 1852.

[183] Michael EA Warwick, Ian Ridley, and Russell Binions. The effect of transition gradient in thermochromic glazing systems. *Energy and buildings*, 77:80–90, 2014.

[184] Jessica C Ramella-Roman, Scott A Prahl, and Steve L Jacques. Three monte carlo programs of polarized light transport into scattering media: part i. *Optics Express*, 13(12):4420–4438, 2005.

[185] Lawrence berkeley national laboratory, international glazing database version 60. *https://windows.lbl.gov/software/igdb.*

[186] Iwao Teraoka. *Polymer solutions*. John Wiley & Sons, Inc, 2002.

[187] G. Wyszecki and W.S. Stiles. *Color Science*. 1982.

[188] Kent F Palmer and Dudley Williams. Optical properties of water in the near infrared. *JOSA*, 64(8):1107–1110, 1974.

[189] Robert Schittny, Muamer Kadic, Tiemo Bückmann, and Martin Wegener. Invisibility cloaking in a diffusive light scattering medium. *Science*, 345(6195):427–429, 2014.

[190] Chia Wei Hsu, Bo Zhen, Wenjun Qiu, Ofer Shapira, Brendan G DeLacy, John D Joannopoulos, and Marin Soljačić. Transparent displays enabled by resonant nanoparticle scattering. *Nature communications*, 5(1):1–6, 2014.

[191] Kurt Hornik, Maxwell Stinchcombe, and Halbert White. Multilayer feedforward networks are universal approximators. *Neural networks*, 2(5):359–366, 1989.

[192] Mario Miscuglio, Armin Mehrabian, Zibo Hu, Shaimaa I Azzam, Jonathan George, Alexander V Kildishev, Matthew Pelton, and Volker J Sorger. All-optical nonlinear activation function for photonic neural networks. *Optical Materials Express*, 8(12):3851–3863, 2018.

[193] Ian AD Williamson, Tyler W Hughes, Momchil Minkov, Ben Bartlett, Sunil Pai, and Shanhui Fan. Reprogrammable electro-optic nonlinear activation functions for optical neural networks. *IEEE Journal of Selected Topics in Quantum Electronics*, 26(1):1–12, 2019.

[194] Thorsten S Rasmussen, Yi Yu, and Jesper Mork. All-optical non-linear activation function for neuromorphic photonic computing using semiconductor fano lasers. *Optics Letters*, 45(14):3844–3847, 2020.

[195] Yichen Shen, Nicholas C Harris, Scott Skirlo, Mihika Prabhu, Tom Baehr-Jones, Michael Hochberg, Xin Sun, Shijie Zhao, Hugo Larochelle, Dirk Englund, et al. Deep learning with coherent nanophotonic circuits. *Nature Photonics*, 11(7):441, 2017.

[196] Albert Ryou, James Whitehead, Maksym Zhelyeznyakov, Paul Anderson, Cem Keskin, Michal Bajcsy, and Arka Majumdar. Free-space optical neural network based on thermal atomic nonlinearity. *Photonics Research*, 9(4):B128–B134, 2021.

[197] Ying Zuo, Bohan Li, Yujun Zhao, Yue Jiang, You-Chiuan Chen, Peng Chen, Gyu-Boong Jo, Junwei Liu, and Shengwang Du. All-optical neural network with nonlinear activation functions. *Optica*, 6(9):1132–1137, 2019.

[198] Bin Xie, Run Hu, and Xiaobing Luo. Quantum dots-converted light-emitting diodes packaging for lighting and display: status and perspectives. *Journal of Electronic Packaging*, 138(2):020803, 2016.

[199] Tingzhu Wu, Chin-Wei Sher, Yue Lin, Chun-Fu Lee, Shijie Liang, Yijun Lu, Sung-Wen Huang Chen, Weijie Guo, Hao-Chung Kuo, and Zhong Chen. Mini-LED and micro-LED: promising candidates for the next generation display technology. *Applied Sciences*, 8(9):1557–1573, 2018.

[200] Kai Ding, Vitaliy Avrutin, Natalia Izyumskaya, Ümit Özgür, and Hadis Morkoç. Micro-LEDs, a manufacturability perspective. *Applied Sciences*, 9(6):1206–1220, 2019.

[201] S. Groetsch, J. Reill, M. Schwind, S. Haneder, and U. Hiller. Illumination vs. visualization in headlamps: Way towards hd light source requirements. In *Proc. SIA VISION 2018*. SIA, 2018.

[202] Darshan Kundaliya, Norwin von Malm, and KC Mishra. Integration of YAG: Ce thin film wavelength converter on III-V blue LED via a laser lift-off process. *ECS Journal of Solid State Science and Technology*, 7(1):R3046–R3051, 2018.

[203] Mohamed Sufyan Islim, Ricardo X Ferreira, Xiangyu He, Enyuan Xie, Stefan Videv, Shaun Viola, Scott Watson, Nikolaos Bamiedakis, Richard V Penty, Ian H White, Anthony E Kelly, Erdan Gu, Harald Haas, and Martin D Dawson. Towards 10 gb/s orthogonal frequency division multiplexing-based visible light communication using a GaN violet micro-LED. *Photonics Research*, 5(2):A35–A43, 2017.

[204] Shiliang Mei, Xiaoyan Liu, Wanlu Zhang, Ran Liu, Lirong Zheng, Ruiqian Guo, and Pengfei Tian. High-bandwidth white-light system combining a micro-LED with perovskite quantum dots for visible light communication. *ACS Applied Materials and Interfaces*, 10(6):5641–5648, 2018.

[205] Dingke Xue, Cheng Ruan, Yu Zhang, Haobin Chen, Xiongbin Chen, Changfeng Wu, Chuantao Zheng, Hongda Chen, and W Yu William. Enhanced bandwidth of white light communication using nanomaterial phosphors. *Nanotechnology*, 29(45):455708–455714, 2018.

[206] Niall McAlinden, David Massoubre, Elliot Richardson, Erdan Gu, Shuzo Sakata, Martin D Dawson, and Keith Mathieson. Thermal and optical characterization of micro-LED probes for in vivo optogenetic neural stimulation. *Optics Letters*, 38(6):992–994, 2013.

[207] Suleman Ayub, Christian Gossler, Florian Engesser, Oliver Paul, and Patrick Ruther. Compact intracerebral probe with yellow phosphor-based light conversion for optogenetic control. In *2017 19th International Conference on Solid-State Sensors, Actuators and Microsystems (TRANSDUCERS)*, pages 1703–1706. IEEE, 2017.

[208] Bowen Ji, Zhejun Guo, Minghao Wang, Bin Yang, Xiaolin Wang, Wen Li, and Jingquan Liu. Flexible polyimide-based hybrid opto-electric neural interface with 16 channels of micro-LEDs and electrodes. *Microsystems Nanoengineering*, 4(1):27, 2018.

[209] Seth Coe-Sullivan, Wenhao Liu, Peter Allen, and Jonathan S Steckel. Quantum dots for LED downconversion in display applications. *ECS Journal of Solid State Science and Technology*, 2(2):R3026–R3030, 2013.

[210] Jonathan S Steckel, John Ho, Charles Hamilton, Jingqun Xi, Craig Breen, Wenhao Liu, Peter Allen, and Seth Coe-Sullivan. Quantum dots: The ultimate down-conversion material for LCD displays. *Journal of the Society Information Display*, 23(7):294–305, 2015.

[211] Marcus J Smith, Chun Hao Lin, Shengtao Yu, and Vladimir V Tsukruk. Composite structures with emissive quantum dots for light enhancement. *Advanced Optical Materials*, 7(4):1801072, 2019.

[212] Hau-Vei Han, Huang-Yu Lin, Chien-Chung Lin, Wing-Cheung Chong, Jie-Ru Li, Kuo-Ju Chen, Peichen Yu, Teng-Ming Chen, Huang-Ming Chen, Kei-May Lau, and Hao-Chung Kuo. Resonant-enhanced full-color emission of quantum-dot-based micro LED display technology. *Opt. Express*, 23(25):32504–32515, Dec 2015.

[213] Hyo-Jun Kim, Min-Ho Shin, Hyun-Guk Hong, Bo-Sun Song, Soo-Kang Kim, Won-Hoe Koo, Jong-Geun Yoon, Soo-Young Yoon, and Young-Joo Kim. Enhancement of optical efficiency in white OLED display using the patterned photoresist film dispersed with quantum dot nanocrystals. *Journal of Display Technology*, 12(6):526–531, 2015.

[214] Bong Hoon Kim, M Serdar Onses, Jong Bin Lim, Sooji Nam, Nuri Oh, Hojun Kim, Ki Jun Yu, Jung Woo Lee, Jae-Hwan Kim, Seung-Kyun Kang, Chi Hwan Lee, Jungyup Lee, Jae Ho Shin, Nam Heon Kim, Cecilia Leal, Moonsub Shim, and John Roger. High-resolution patterns of quantum dots formed by electrohydrodynamic jet printing for light-emitting diodes. *Nano Letters*, 15(2):969–973, 2015.

[215] Bin Bao, Mingzhu Li, Yuan Li, Jieke Jiang, Zhenkun Gu, Xingye Zhang, Lei Jiang, and Yanlin Song. Patterning fluorescent quantum dot nanocomposites by reactive inkjet printing. *Small*, 11(14):1649–1654, 2015.

[216] Huang-Yu Lin, Chin-Wei Sher, Dan-Hua Hsieh, Xin-Yin Chen, Huang-Ming Philip Chen, Teng-Ming Chen, Kei-May Lau, Chyong-Hua Chen, Chien-Chung Lin, and Hao-Chung Kuo. Optical cross-talk reduction in a quantum-dot-based full-color micro-light-emitting-diode display by a lithographic-fabricated photoresist mold. *Photonics Research*, 5(5):411–416, Oct 2017.

[217] Ernie Lee, Shihai Kan, Charlie Hotz, Jeff Yurek, ZhongSheng Luo, Heejae Kim, Jay Yamanaga, and Amanda Carpenter. 67-2: Invited paper: Ambient processing of quantum dot photoresist for emissive displays. In *SID Symposium Digest of Technical Papers*, pages 984–987. Wiley Online Library, 2017.

[218] Seonwoo Lee and Changhee Lee. High-density quantum dots composites and its photolithographic patterning applications. *Polymers Advanced Technologies*, 30(3):749–754, 2019.

[219] M Kneissl, T Kolbe, C Chua, V Kueller, N Lobo, J Stellmach, A Knauer, H Rodriguez, S Einfeldt, Z Yang, N. M. Johson, and M. Weyers. Advances in group III-nitride-based deep UV light-emitting diode technology. *Semiconductor Science and Technology*, 26(1):014036, 2010.

[220] Ludovic Dupré, Marjorie Marra, Valentin Verney, Bernard Aventurier, Franck Henry, François Olivier, Sauveur Tirano, Anis Daami, and François Templier. Processing and characterization of high resolution GaN/InGaN LED arrays at 10 micron pitch for micro display applications. In *Gallium Nitride Materials and Devices XII*, pages 1010422–1010429. International Society for Optics and Photonics, 2017.

[221] Sadra Sadeghi, Baskaran Ganesh Kumar, Rustamzhon Melikov, Mohammad Mohammadi Aria, Houman Bahmani Jalali, and Sedat Nizamoglu. Quantum dot white LEDs with high luminous efficiency. *Optica*, 5(7):793–802, 2018.

[222] Marcus J Smith, Sidney T Malak, Jaehan Jung, Young Jun Yoon, Chun Hao Lin, Sunghan Kim, Kyung Min Lee, Ruilong Ma, Timothy J White, Timothy J Bunning, Zhiqun Lin Lin, and Vladimir V. Tsukruk. Robust, uniform, and highly emissive quantum dot–polymer films and patterns using thiol–ene chemistry. *ACS Applied Materials Interfaces*, 9(20):17435–17448, 2017.

[223] Tingting Zhou, Bin Zhang, Yonglian Qi, Dini Xie, Jikai Yao, Zhanfeng Cao, and Jianshe Xue. P-92: Fabrication and patterning of a wide-color-gamut color filter based on quantum dots. In *SID Symposium Digest of Technical Papers*, pages 1469–1471. Wiley Online Library, 2016.

[224] Hongbo Li, Kaifeng Wu, Jaehoon Lim, Hyung-Jun Song, and Victor I Klimov. Doctor-blade deposition of quantum dots onto standard window glass for low-loss large-area luminescent solar concentrators. *Nature Energy*, 1(12):16157, 2016.

[225] Fangwang Gou, En-Lin Hsiang, Guanjun Tan, Yi-Fen Lan, Cheng-Yeh Tsai, and Shin-Tson Wu. Tripling the optical efficiency of color-converted micro-LED displays with funnel-tube array. *Crystals*, 9(1):39–48, 2019.

[226] John C de Mello, H Felix Wittmann, and Richard H Friend. An improved experimental determination of external photoluminescence quantum efficiency. *Advanced Materials*, 9(3):230–232, 1997.

[227] Yu-Huan Liu, Yuan-Yuan Zhao, Xian-Zi Dong, Mei-Ling Zheng, Feng Jin, Jie Liu, Xuan-Ming Duan, and Zhen-Sheng Zhao. Multi-scale structure patterning by digital-mask projective lithography with an alterable projective scaling system. *AIP Advances*, 8(6):065317, 2018.

[228] Zheng Xiong, Hua Liu, Ronghuan Chen, Jia Xu, Qiankun Li, Jinhuan Li, and Wenjuan Zhang. Illumination uniformity improvement in digital micromirror device based scanning photolithography system. *Optics Express*, 26(14):18597–18607, 2018.

[229] Qinyuan Deng, Yong Yang, Hongtao Gao, Yi Zhou, Yu He, and Song Hu. Fabrication of micro-optics elements with arbitrary surface profiles based on one-step maskless grayscale lithography. *Micromachines*, 8(10):314–325, 2017.

[230] Eric H Virey and Nicolas Baron. Status and prospects of microLED displays. In *SID Symposium Digest of Technical Papers*, volume 49, pages 593–596. Wiley Online Library, 2018.

[231] Frank L Pedrotti, Leno M Pedrotti, and Leno S Pedrotti. *Introduction to Optics*. Cambridge University, 2017.

[232] Thomas Smith and John Guild. The CIE colorimetric standards and their use. *Transactions of the Optical Society*, 33(3):73–135, 1931.

[233] *D-Cinema Quality-Reference Projector and Environment*. SMPTE Recommended Practice, 2011.

[234] Andrew B Lowe. Thiol-ene click reactions and recent applications in polymer and materials synthesis. *Polymer Chemistry*, 1(1):17–36, 2010.

[235] Francesco Meinardi, Annalisa Colombo, Kirill A Velizhanin, Roberto Simonutti, Monica Lorenzon, Luca Beverina, Ranjani Viswanatha, Victor I Klimov, and Sergio Brovelli. Large-area luminescent solar concentrators based on stokes-shift-engineered nanocrystals in a mass-polymerized pmma matrix. *Nature Photonics*, 8(5):392–399, 2014.

[236] Ram W Sabnis. Color filter technology for liquid crystal displays. *Displays*, 20(3):119–129, 1999.

[237] Raphaël Pestourie, Carlos Pérez-Arancibia, Zin Lin, Wonseok Shin, Federico Capasso, and Steven G Johnson. Inverse design of large-area metasurfaces. *Optics express*, 26(26):33732–33747, 2018.

[238] Sean Molesky, Zin Lin, Alexander Y Piggott, Weiliang Jin, Jelena Vucković, and Alejandro W Rodriguez. Inverse design in nanophotonics. *Nature Photonics*, 12(11):659–670, 2018.

[239] Konstantinos G Makris, Andre Brandstötter, Philipp Ambichl, Ziad H Musslimani, and Stefan Rotter. Wave propagation through disordered media without backscattering and intensity variations. *Light: Science & Applications*, 6(9):e17035–e17035, 2017.

[240] Andre Brandstötter, Konstantinos G Makris, and Stefan Rotter. Scattering-free pulse propagation through invisible non-hermitian media. *Physical Review B*, 99(11):115402, 2019.

[241] Alexander N Tait, Mitchell A Nahmias, Yue Tian, Bhavin J Shastri, and Paul R Prucnal. Photonic neuromorphic signal processing and computing. In *Nanophotonic Information Physics*, pages 183–222. Springer, 2014.

[242] Bhavin J Shastri, Alexander N Tait, Mitchell A Nahmias, and Paul R Prucnal. Photonic spike processing: ultrafast laser neurons and an integrated photonic network. *arXiv preprint arXiv:1407.2917*, 2014.

[243] Johannes Feldmann, Nathan Youngblood, C David Wright, Harish Bhaskaran, and Wolfram HP Pernice. All-optical spiking neurosynaptic networks with self-learning capabilities. *Nature*, 569(7755):208–214, 2019.

[244] Wolfgang Maass. Networks of spiking neurons: the third generation of neural network models. *Neural networks*, 10(9):1659–1671, 1997.

[245] Mitchell A Nahmias, Bhavin J Shastri, Alexander N Tait, and Paul R Prucnal. A leaky integrate-and-fire laser neuron for ultrafast cognitive computing. *IEEE journal of selected topics in quantum electronics*, 19(5):1–12, 2013.

[246] Guillermo Gallego, Tobi Delbruck, Garrick Orchard, Chiara Bartolozzi, Brian Taba, Andrea Censi, Stefan Leutenegger, Andrew Davison, Jörg Conradt, Kostas Daniilidis, et al. Event-based vision: A survey. *arXiv preprint arXiv:1904.08405*, 2019.

[247] Annamalai Lakshmi, Anirban Chakraborty, and Chetan S Thakur. Neuromorphic vision: From sensors to event-based algorithms. *Wiley Interdisciplinary Reviews: Data Mining and Knowledge Discovery*, 9(4):e1310, 2019.

[248] Fabian Niesler and Yann Tanguy. 3d printers for the fabrication of micro-optical elements: Disruptive technology enables the way for unprecedented applications. *Optik & Photonik*, 11(4):44–47, 2016.

[249] Zheng Xiong and Pranav Soman. Digital printing of hydrogel based diffractive optical elements. In *Advanced Fabrication Technologies for Micro/Nano Optics and Photonics XIV*, volume 11696, page 116960X. International Society for Optics and Photonics, 2021.

[250] Tien-Jen Chang, Lukas Vaut, Martin Voss, Oleksii Ilchenko, Line Hagner Nielsen, Anja Boisen, and En-Te Hwu. Micro and nanoscale 3d printing using optical pickup unit from a gaming console. *Communications Physics*, 4(1):1–8, 2021.

[251] Seok Kim, Jordan Jerome Handler, Young Tae Cho, George Barbastathis, and Nicholas Xuanlai Fang. Scalable additive manufacturing via integral image formation. *arXiv preprint arXiv:1911.11817*, 2019.